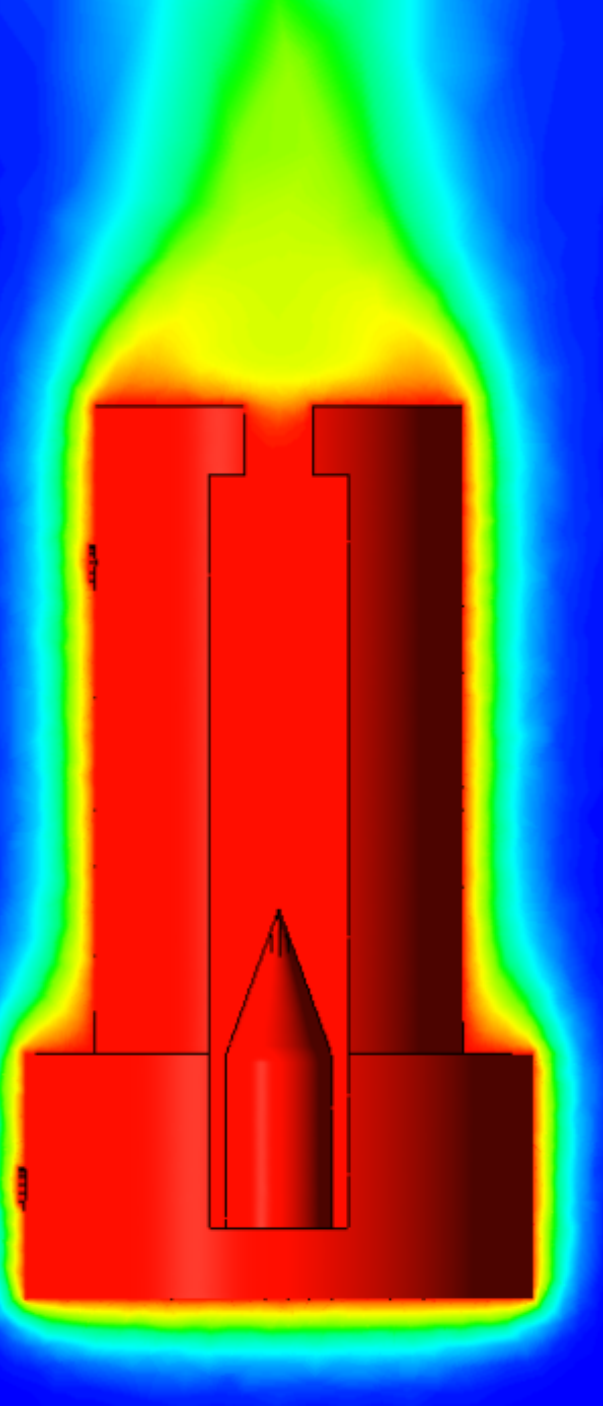


# **Development of high temperature Solar Thermal Propulsion engine**

Master thesis

Aeilt-Jan Takken

Delft University of Technology



# **Development of high temperature Solar Thermal Propulsion engine**

## **Master thesis**

by

**Aeilt-Jan Takken  
4212118**

to obtain the degree of Master of Science  
at the Delft University of Technology,  
to be defended publicly on Tuesday January 19, 2021 at 2:00 PM.

Student number: 4212118  
Affiliation: Chair of Space Systems Engineering, Faculty of Aerospace Engineering  
Supervisor: Ir. B.T.C. Zandbergen  
Thesis committee: Ir. B.T.C. Zandbergen, TU Delft  
Prof. dr. E.K.A. Gill, TU Delft  
Dr. ir. B.C. Root, TU Delft

An electronic version of this thesis is available at <http://repository.tudelft.nl/>.





# Abstract

Miniaturization in spacecraft is an ongoing process in which the launched satellites become smaller and smaller. This trend introduces issues, such as the choice for a reliable and efficient propulsion subsystem. This thesis presents a solution to this problem: a practical **Solar Thermal Propulsion (STP)** thruster which could reach a **Sea Level (SL)** specific impulse of 90.0 s at a continuous mass flow of  $300 \text{ mg s}^{-1}$  and input power of 250 W. Additional requirements were that the propellant should be non-toxic, the thermal efficiency should be at least 70 %, the heat exchanger would have a maximum mass of 0.086 kg and all components should be manufactured and tested using **Delft University of Technology (DUT)** resources. The objective of 90.0 s of **SL** specific impulse was set at this level because it would fall within the constraints set by material, propellant, resources, power input and equipment.

During the project, a thruster named Solar Thermal Thruster 2 was designed and built. It was an indirect absorbing, direct thrusting type of **STP** engine with a copper cylindrical heat exchanger having six spiraling channels and a lid with aperture to reduce cavity heat losses. The total mass, length and diameter was 0.182 kg, 0.051 m and 0.029 m respectively. The heat exchanger featured a spike to scatter the incoming radiation to the inner cavity walls. The predicted thermal efficiency by the tool was 53.7 % with nitrogen as the propellant of choice, which was too low to meet the requirements. Next to that, due to design and manufacturing issues and the COVID-19 pandemic, the thruster could not be used for experiments. In order to continue validation of the preliminary tool, **Computational Fluid Dynamics (CFD)** simulations were used to predict the thermal performance of STT2 which amounted to 61.1 %. The discrepancy was explained by the fact that the simulations could more accurately predict the heat transfer in entrance and exit regions.

Furthermore, with the use of **CFD** a new design was proposed based on the knowledge gained during the project. Solar Thermal Thruster 3 was based on its predecessors, having twelve spiraling channels with a square cross-sectional shape in the heat exchanger. The number of channels was increased to reduce the pressure loss over the heat exchanger. Its total mass, length and diameter was 0.044 kg, 0.038 m and 0.019 m respectively. With nitrogen as the propellant of choice, the thermal efficiency and pressure loss of STT3's heat exchanger reported by the preliminary tool was 61.1 % and 0.02 bar, while the **CFD** simulation showed 68.6 % and 0.43 bar. As such, all requirements were met and the goal was reached, with the exception of the thermal efficiency which was slightly lower than the required 70 %. To validate these values completely, it is recommended to manufacture STT3 and subject it to experiments with and without nitrogen mass flow.

???



# Acknowledgements

The thesis project that I am presenting to you is the final chapter to my years as an Aerospace Engineering student at TU Delft. Although it took longer than expected to finish this work, I am nonetheless proud to show you the results of countless hours of research, debate and considerations. I am happy to count myself among the alumni of this great university.

Via this way I would like to thank my supervisor Barry Zandbergen for his unrelenting support in this challenging part of my master degree. Through his guidance, I was able to conclude the project in a satisfying way with a lot of new insights in the area of experiments and practical research. The weekly meetings were never a bore and always provided me with new material on how to tackle the issues I encountered on the way.

I want to express my sincerest gratitude to my parents who have always been at my side. Their support helped me throughout my whole student life and continues to do so. Next to that, there is an extensive list of people that contributed in some way, both technical and non-technical. There are the countless other staff members at the university that helped me find all the small equipment and the facilities that I desperately needed. There are the fellow students at the master room with whom I had many coffee breaks that unfortunately had to continue online at a later stage. There are my friends in and outside Delft, who served as welcome distraction. There are my siblings who always helped to keep me sharp-witted when I was in their presence. There is Robert, who always offered a listening ear on the walks we suddenly made. And finally, there is Jade, who always provided me with emotional support and kept me sane throughout this endeavour.

It has been a pleasure.

*Aeilt-Jan Takken  
Delft, December 2020*



# Contents

<b>Abstract</b>	<b>iii</b>
<b>Acknowledgements</b>	<b>v</b>
<b>List of Figures</b>	<b>xi</b>
<b>List of Tables</b>	<b>xiv</b>
<b>List of Acronyms</b>	<b>xv</b>
<b>List of Symbols</b>	<b>xvi</b>
<b>1 Introduction</b>	<b>1</b>
<b>2 Research framework</b>	<b>4</b>
2.1 Research background . . . . .	4
2.1.1 Principles of solar thermal propulsion . . . . .	4
2.1.2 Summary of research into solar thermal propulsion . . . . .	5
2.2 Solar Thermal Thruster 1 background . . . . .	5
2.2.1 Design and manufacturing . . . . .	6
2.2.2 Experimental results . . . . .	6
2.2.3 Results discussion . . . . .	8
2.2.4 Main findings . . . . .	9
2.3 Research goal . . . . .	9
2.4 Requirements and constraints . . . . .	10
2.4.1 Functional requirements . . . . .	10
2.4.2 System requirements . . . . .	11
2.4.3 Constraints . . . . .	11
<b>3 Preliminary design tool</b>	<b>13</b>
3.1 Assumptions . . . . .	13
3.2 Verification and validation . . . . .	13
3.2.1 Case 1: no mass flow and no insulation . . . . .	14
3.2.2 Case 2: no mass flow and insulation . . . . .	14
3.2.3 Case 3: mass flow and insulation . . . . .	15
3.3 Conclusions & recommendations . . . . .	17
<b>4 Design theory</b>	<b>19</b>
4.1 Heat transfer overview . . . . .	20
4.2 Convection . . . . .	20
4.2.1 Propellant convection . . . . .	21
4.2.2 Inner cavity convection . . . . .	26
4.2.3 Outer wall convection . . . . .	27
4.3 Radiation . . . . .	28
4.3.1 Inner cavity radiation . . . . .	28
4.3.2 Outer wall radiation . . . . .	31
4.3.3 Area . . . . .	31

4.4 Conduction . . . . .	31
4.5 Pressure loss . . . . .	32
4.6 Thrust . . . . .	33
<b>5 Thruster design</b>	<b>36</b>
5.1 Design process . . . . .	36
5.2 Thruster design . . . . .	37
5.2.1 Propellant choice . . . . .	37
5.2.2 Concentrator subsystem design . . . . .	38
5.2.3 Receiver-Absorber Cavity design . . . . .	39
5.2.4 Nozzle design . . . . .	44
5.3 Solar Thermal Thruster 2 performance . . . . .	45
5.4 Cost . . . . .	46
5.5 Design mistake . . . . .	47
5.6 Hardware . . . . .	47
5.6.1 Receiver-Absorber Cavity hardware . . . . .	47
5.6.2 Connection pieces hardware . . . . .	48
5.6.3 Construction recommendations . . . . .	49
<b>6 Experiment preparation</b>	<b>50</b>
6.1 Planned experiments . . . . .	50
6.2 Locations . . . . .	51
6.2.1 Cleanroom . . . . .	51
6.2.2 Welding facility . . . . .	52
6.3 Equipment hardware . . . . .	52
6.3.1 Thermocouples . . . . .	52
6.3.2 Pressure sensors . . . . .	53
6.3.3 Mass flow sensor . . . . .	54
6.3.4 Propellant supply . . . . .	55
6.4 Test stand hardware . . . . .	55
6.4.1 Test bench AE-TB-1.1 . . . . .	56
6.4.2 Test bench AE-TB-50m . . . . .	57
6.4.3 Test bench conclusions & recommendations . . . . .	64
6.5 Thesis alteration . . . . .	65
6.5.1 Experiment stop . . . . .	65
6.5.2 Plan for continuation . . . . .	66
<b>7 Computational Fluid Dynamics modelling</b>	<b>67</b>
7.1 Computational Fluid Dynamics workings and uses . . . . .	67
7.2 Goal of Computational Fluid Dynamics for this project . . . . .	68
7.3 Verification and validation . . . . .	69
7.4 Computational Fluid Dynamics program choice . . . . .	70
7.5 Quantification of losses to ambient . . . . .	70
7.5.1 Geometry . . . . .	71
7.5.2 Mesh . . . . .	74
7.5.3 Setup . . . . .	74
7.5.4 Post-processing . . . . .	78
7.6 Case 1: Solar Thermal Thruster 1, no mass flow and no insulation . . . . .	81
7.7 Case 2: Solar Thermal Thruster 1, no mass flow and insulation . . . . .	82
7.8 Case 3: Solar Thermal Thruster 1, mass flow and insulation . . . . .	85
7.9 Case 4: Solar Thermal Thruster 1, mass flow and no insulation . . . . .	87
7.10 Case 5: Solar Thermal Thruster 2, mass flow and no insulation . . . . .	89
7.11 Case 6: Solar Thermal Thruster 2, mass flow and no insulation, high power . . . . .	92
7.12 Conclusions & recommendations . . . . .	92
<b>8 Final solar thermal thruster design</b>	<b>94</b>
8.1 Recommendations from previous chapters . . . . .	94

---

8.2	Solar Thermal Thruster 3 design . . . . .	95
8.2.1	Heat exchanger dimensions . . . . .	95
8.2.2	Channel shape and dimensions . . . . .	96
8.2.3	Other changes . . . . .	97
8.2.4	Results . . . . .	98
8.3	Solar Thermal Thruster 3 performance . . . . .	98
8.4	Conclusions . . . . .	99
<b>9</b>	<b>Conclusions &amp; recommendations</b>	<b>101</b>
9.1	Conclusions . . . . .	101
9.2	Recommendations . . . . .	103
<b>Bibliography</b>		<b>104</b>
<b>A Technical drawings Solar Thermal Thruster 2</b>		<b>109</b>
<b>B Technical drawings Solar Thermal Thruster 3</b>		<b>118</b>
<b>C Experiment hardware</b>		<b>123</b>
C.1	Futek LRF400 (L2338) data sheet . . . . .	124
C.2	Futek LSB200 data sheet . . . . .	125
C.3	RS Pro data sheet . . . . .	126
C.4	Pressure sensor data sheets . . . . .	127
C.5	National Instruments USB-6008 data sheet . . . . .	129
C.6	Scaime CPJ Rail data sheet . . . . .	131
C.7	Mettler Toledo AG245 data sheet . . . . .	132
C.8	Zwaluw Fire Sealant 1200 °C data sheet . . . . .	134
C.9	Saffil M-Fil data sheet . . . . .	136



# List of Figures

1.1	Spacecraft launches in the period 2012-2019, split by mass [1]. . . . .	1
1.2	Propulsion concepts and their characteristics [2]. . . . .	3
2.1	Main components of an STP thruster (see footnote). . . . .	5
3.1	Case 1: experimental (in red) and theoretical Matlab (in black) Receiver-Absorber Cavity (RAC) temperatures by Leenders [3]. . . . .	15
3.2	Case 1: theoretical Python RAC temperatures by Takken. . . . .	15
3.3	Case 2: experimental (in black) and theoretical Matlab (in red) RAC temperatures by Leenders [3]. . . . .	15
3.4	Case 2: theoretical Python RAC temperatures by Takken. . . . .	15
3.5	Case 3: experimental (in red) and theoretical Matlab (in black) RAC temperatures by Leenders [3]. The axes labels are time (in min) for the horizontal axis and RAC temperature (in K) for the vertical axis. Note that Leenders' experimental and theoretical values do not match well. . . . .	18
3.6	Case 3: theoretical Python temperatures by Takken. In blue is the RAC temperature, in orange is the outlet propellant temperature. . . . .	18
4.1	Cone with surfaces 1 and 2. Surface 3, the aperture, is not shown. . . . .	30
4.2	Cylinder with surfaces 1 and 2. Surface 3, the bottom wall is not indicated. . . . .	30
5.1	Exploded view of the STT2 heat exchanger. . . . .	45
5.2	Disassembled STT2. . . . .	48
5.3	Assembled STT2. . . . .	48
5.4	STT2 with both machined parts. . . . .	49
6.1	Cleanroom at Faculty of Aerospace Engineering (AE). . . . .	51
6.2	Thermocouples RS Pro 787-7835. In the background, the corresponding NI DAQ device is shown. . . . .	52
6.3	Pressure sensors 3300B16B0A01B000RS and DRTR-AL-20MA-R16B. . . . .	53
6.4	Coiled tube to allow the fluid to cool down for the pressure sensor. . . . .	54
6.5	PCB connected to one of the Brooks mass flow sensors. . . . .	55
6.6	Brooks 5851S mass flow sensor. . . . .	56
6.7	Thrust bench TB-1.1 [4]. . . . .	57
6.8	Thrust bench TB-50m, by Janssens [5]. . . . .	58
6.9	Thrust bench TB-50m, by Krusharev [6]. The LRF400 sensor is clearly shown in the top right corner. . . . .	58
6.10	Thrust bench TB-50m, by Takken. Again, the LRF400 sensor is shown in the bottom. . . . .	59
6.11	Connection of the rotating beam to the sensor. . . . .	59
6.12	The analog amplifier Scaime CPJ Rail. It has three connections: the right to the power grid (230 V), the middle towards the Data Acquisition (DAQ) device and the left to the RS232 cable of the thrust sensor. . . . .	60
6.13	Measuring the weights with the electronic scale Mettler Toledo. . . . .	61
6.14	Measuring the sensor voltage output with the use of the weights. . . . .	61
6.15	Weight on sensor versus voltage. . . . .	62
6.16	Test 1: $F_{EM}$ versus time. . . . .	63

6.17 Test 1: averaged $F_{EM}$ over steps of 1 A.	64
6.18 Test 2: $F_{EM}$ versus time.	65
6.19 Test 2: averaged $F_{EM}$ over steps of 0.5 [A].	66
7.1 Solid domain of Ansys physical model of Solar Thermal Thruster 1 (STT1).	71
7.2 Cross-section of Ansys physical model of STT1. Note the smaller hole at the exit, which is on the right bottom of the picture. Furthermore, both inner walls (cone and circular) can be observed.	71
7.3 Fluid domain of Ansys physical model of STT1.	72
7.4 Air domain containing the RAC and fluid domain.	73
7.5 Cross-section of the meshed ambient, RAC and fluid domain.	75
7.6 Closer cross-section of the meshed RAC and fluid domain. Note the two inner walls: the cone inner wall and the small circular inner wall.	76
7.7 Scaled residuals of the simulation to determine convection losses for a case without insulation at an air speed of $0.001 \text{ m s}^{-1}$ . Note the very small oscillation in the energy equation.	78
7.8 Side view of the heated air domain. Note how the upper part of the air in the cavity has a higher temperature than the lower part, due to buoyancy (gravity is pointed down, in the negative y-direction). Air speed is $0.001 \text{ m s}^{-1}$ .	79
7.9 Front view of the heated fluid domain. Again, a small higher temperature pocket is seen at the top of the cavity, in the positive y-direction. Air speed is $0.001 \text{ m s}^{-1}$ .	79
7.10 Area-weighted average temperatures for inner cone, inner circular and outer walls. Necessary to determine the convection losses for an RAC without insulation. Air speed is $0.001 \text{ m s}^{-1}$ .	80
7.11 Convective heat transfer coefficients for inner cone, inner circular and outer walls, for a case without insulation. Air speed is $0.001 \text{ m s}^{-1}$ .	80
7.12 Case 1: area-weighted average temperatures for inner and outer walls. Note the overlaying Python wall temperature.	82
7.13 Area-weighted average temperatures for inner and outer walls, with insulation. Air speed is $0.001 \text{ m s}^{-1}$ .	83
7.14 Area-weighted average convective heat transfer coefficients for inner and outer walls, with insulation. Air speed is $0.001 \text{ m s}^{-1}$ .	84
7.15 Side view of the heated air domain. Note how the upper part of the cavity has a higher temperature than the lower part, due to buoyancy (gravity is pointing down).	85
7.16 Side view of the heated RAC and insulation domains.	85
7.17 Turbulent subcase. Temperature contour of the fluid domain in side view.	90
7.18 Temperature along both the upper and lower channel, turbulent subcase. Note that the x-axis, which is in the positive Z-direction, is reversed.	91
7.19 Case 5: cross-section of Solar Thermal Thruster 2 (STT2) showing the temperature in RAC and propellant in turbulent flow.	93
8.1 View of STT2.	98
8.2 View of STT3.	98
8.3 Exploded view of the STT3 heat exchanger.	99
A.1 Drawing of STT2 inner cylinder.	110
A.2 Drawing of STT2 outer cylinder.	111
A.3 Drawing of STT2 cap.	112
A.4 Drawing of STT2 spike.	113
A.5 Drawing of STT2 inlet connection piece.	114
A.6 Drawing of STT2 outlet connection piece.	115
A.7 Drawing of STT2 Macor connection piece.	116
A.8 Drawing of the STT2 copper nozzle, from Leenders [3].	117
B.1 Drawing of STT3 inner cylinder.	119
B.2 Drawing of STT3 outer cylinder.	120
B.3 Drawing of STT3 cap.	121

B.4 Drawing of STT3 nozzle. . . . .	122
-------------------------------------	-----

# List of Tables

2.1	STT1 measurements from Leenders's paper [7]. . . . .	7
2.2	STT1 RAC efficiency, enthalpy, propellant and input power, from Leenders's paper [7]. . . . .	8
2.3	Functional requirements for STT2. . . . .	11
2.4	System requirements for STT2. . . . .	11
2.5	Constraints for STT2. . . . .	12
3.1	Case 1 inputs. . . . .	14
3.2	Case 2 inputs. . . . .	16
3.3	Case 3 mass flow and time inputs. . . . .	16
3.4	Case 3 inputs. . . . .	17
5.1	Propellant properties (see National Institute of Standards and Technology (NIST) footnote). . . . .	38
5.2	Material properties (see footnote). . . . .	39
5.3	STT2 tool inputs. . . . .	46
5.4	Component sizes (in mm) . . . . .	48
5.5	Component mass (in kg) . . . . .	49
6.1	Sensor voltage output versus mass. . . . .	61
7.1	STT1 sizes by Ansys DesignModeler. . . . .	71
7.2	Convective heat transfer coefficients per air speed and emissivities. Results of three simulations with the air domain surrounding the RAC domain. . . . .	79
7.3	Inputs and outputs for Ansys case 1. . . . .	81
7.4	Convective heat transfer coefficients, view factors and resulting emissivities for case 2. . . . .	83
7.5	Inputs for verification cases, both laminar and turbulent. . . . .	86
7.6	Comparison between theoretical and Ansys Fluent results, for the laminar test case. . . . .	86
7.7	Comparison between theoretical and Ansys Fluent results, for the turbulent test case. . . . .	86
7.8	Averaged wall temperatures and heat flows for case 4. . . . .	88
7.9	Averaged propellant temperatures and Nusselt numbers for each region, case 4. . . . .	88
7.10	Nusselt number calculations for channel flow, at a Reynolds number of 4550. . . . .	89
7.11	Averaged convective heat transfer coefficients, view factors and emissivities for each surface, case 5. . . . .	90
7.12	Averaged propellant temperatures and Nusselt numbers for each region, case 5. . . . .	92
8.1	Comparison between channel shapes in terms of heat transfer [8]. . . . .	97
8.2	Comparison between channel shapes in terms of pressure loss [8]. . . . .	97
8.3	Properties and results for all three engines. . . . .	100

# List of Acronyms

<b>3mE</b>	Faculty of Mechanical, Maritime and Materials Engineering
<b>AE</b>	Faculty of Aerospace Engineering
<b>AFRPL</b>	Air Force Rocket Propulsion Laboratory
<b>CAD</b>	Computer Aided Design
<b>CFD</b>	Computational Fluid Dynamics
<b>CNC</b>	Computer Numerical Control
<b>COTS</b>	Commercial Off-The-Shelf
<b>DAQ</b>	Data Acquisition
<b>DEMO</b>	Dienst Elektronische en Mechanische Ontwikkeling
<b>DUT</b>	Delft University of Technology
<b>ECTS</b>	European Credit Transfer and Accumulation System
<b>GUI</b>	Graphical User Interface
<b>IRT</b>	Ideal Rocket Theory
<b>LabVIEW</b>	Laboratory Virtual Instrument Engineering Workbench
<b>MEMS</b>	Microelectromechanical Systems
<b>MSE</b>	Materials Science and Engineering department
<b>NI</b>	National Instruments
<b>NIST</b>	National Institute of Standards and Technology
<b>NS</b>	Navier-Stokes (equations)
<b>PCB</b>	Printed Circuit Board
<b>PDT</b>	Preliminary Design Tool
<b>RAC</b>	Receiver-Absorber Cavity
<b>RANS</b>	Reynolds-averaged Navier-Stokes (equations)
<b>S2S</b>	Surface-to-Surface
<b>SL</b>	Sea Level
<b>SSE</b>	Space Systems Engineering
<b>STP</b>	Solar Thermal Propulsion
<b>STT1</b>	Solar Thermal Thruster 1
<b>STT2</b>	Solar Thermal Thruster 2
<b>STT3</b>	Solar Thermal Thruster 3
<b>TRL</b>	Technology Readiness Level
<b>UHF</b>	Uniform Heat Flux
<b>UWT</b>	Uniform Wall Temperature
<b>VTDC</b>	Variable-Turn Density Coil

# List of Symbols

<b>Symbol</b>	<b>Description</b>	<b>Unit</b>
$A_{cs}$	Channel cross-sectional area	$\text{m}^2$
$A$	Area	$\text{m}^2$
$C_d$	Discharge coefficient	—
$C_\mu$	Turbulence model constant	—
$D_{ap}$	Cavity aperture diameter	$\text{m}$
$D_{cav}$	Cavity average diameter	$\text{m}$
$D_c$	Spiral diameter	$\text{m}$
$D_h$	Hydraulic diameter	$\text{m}$
$D$	Cavity (base) diameter	$\text{m}$
$F$	View factor	—
$F$	Thrust	$\text{N}$
$I_{sp}$	Specific impulse	$\text{s}$
$I$	Turbulence intensity	—
$L_{ch}$	Channel length	$\text{m}$
$L_s$	Characteristic length	$\text{m}$
$L$	Cavity length	$\text{m}$
$\text{MM}$	Molar mass	$\text{kg mol}^{-1}$
$M$	Mass	$\text{kg}$
$\text{Nu}$	Nusselt number	—
$\text{Pr}$	Prandtl number	—
$Q_{cond}$	Conduction heat transfer	$\text{W}$
$Q_{conv,T}$	Convective heat transfer per Kelvin	$\text{W K}^{-1}$
$Q_{conv}$	Convective heat transfer	$\text{W}$
$Q_{loss}$	Heat losses	$\text{W}$
$Q_{rad}$	Radiation heat transfer	$\text{W}$
$Q_{res}$	Resultant heat power	$\text{W}$
$R_A$	Universal gas constant	$\text{J mol}^{-1} \text{K}^{-1}$
$\text{Re}$	Reynolds number	—
$R$	Specific gas constant	$\text{J kg}^{-1} \text{K}^{-1}$
$S$	Wetted perimeter	$\text{m}$
$T$	Temperature	$\text{K}$
$U_L$	Limiting velocity	$\text{m s}^{-1}$
$U_{eq}$	Equivalent exhaust velocity	$\text{m s}^{-1}$
$U_e$	Exhaust velocity	$\text{m s}^{-1}$
$C_{RAC}$	RAC heat capacity	$\text{J kg}^{-1} \text{K}^{-1}$
$c_p$	Specific heat at constant pressure	$\text{J kg}^{-1} \text{K}^{-1}$
$f_{DB}$	Darcy-Weisbach friction factor	—
$g_0$	Gravitational acceleration at sea level	$\text{m s}^{-2}$
$g$	Gravitational acceleration	$\text{m s}^{-2}$
$h$	Convective heat transfer coefficient	$\text{W m}^{-2} \text{K}^{-1}$
$k$	Turbulent energy	$\text{m}^2 \text{s}^{-2}$
$k$	Thermal conductivity	$\text{W m}^{-1} \text{K}^{-1}$
$l$	Turbulence length	$\text{m}$
$\dot{m}$	Mass flow	$\text{kg s}^{-1}$
$n$	Total number of channel segments	—

<b>Symbol</b>	<b>Description</b>	<b>Unit</b>
n	Dittus-Boelter equation coefficient	—
n	Sample size	—
p	pitch	m
p	Pressure	Pa
q	Heat flux	W m <sup>-2</sup>
r	Radius	m
t <sub>step</sub>	Time step	s
v	Velocity	m s <sup>-1</sup>
ΔH	Change in enthalpy	J kg <sup>-1</sup>
ΔT	Change in temperature	K
ΔV	Change in velocity	m s <sup>-1</sup>
Γ	Vandenkerckhove function	—
α	Absorptivity	—
α	Thermal diffusivity	m <sup>2</sup> s <sup>-1</sup>
β	Thermal expansion	K <sup>-1</sup>
ε	Emissivity	—
η	Efficiency	—
γ	Specific heat ratio	—
μ	Dynamic viscosity	Pas
ν	Kinematic viscosity	m <sup>2</sup> s <sup>-1</sup>
ω	Specific turbulent dissipation rate	s <sup>-1</sup>
ϕ	Cavity angle	rad
ρ	Density	kg m <sup>-3</sup>
σ	Standard deviation	—
σ	Stefan-Boltzmann constant	W/m <sup>2</sup> K <sup>4</sup>



# 1

## Introduction

Space exploration has been dominated by large spacecraft for decades after the launch of the first satellite, the Sputnik, in 1957. However, from the late 90's onwards the trend has been increasingly turned towards launching small satellites, also called smallsats [9–12]. This shift is mostly explained by the low cost and development time associated with the smaller spacecraft, the availability of [Commercial Off-The-Shelf \(COTS\)](#) technologies and the development of [Microelectromechanical Systems \(MEMS\)](#)-based components [13, 14]. Figure 1.1 illustrates the miniaturization, where the smaller satellites with a maximum mass of 600 kg make up the bulk of the launches [1]. The smallsats come in many forms, of which the CubeSat as nanosatellite (1-10 kg) and its smaller brother the PocketQube as picosatellite (0.1-1 kg) are prime examples [15]. CubeSats consist of one or multiple  $10 \times 10 \times 10 \text{ cm}^3$  cubes and were first envisioned as a low-cost option to perform scientific and technological studies, but are now even considered for use on more sophisticated (commercial) missions [16, 17].

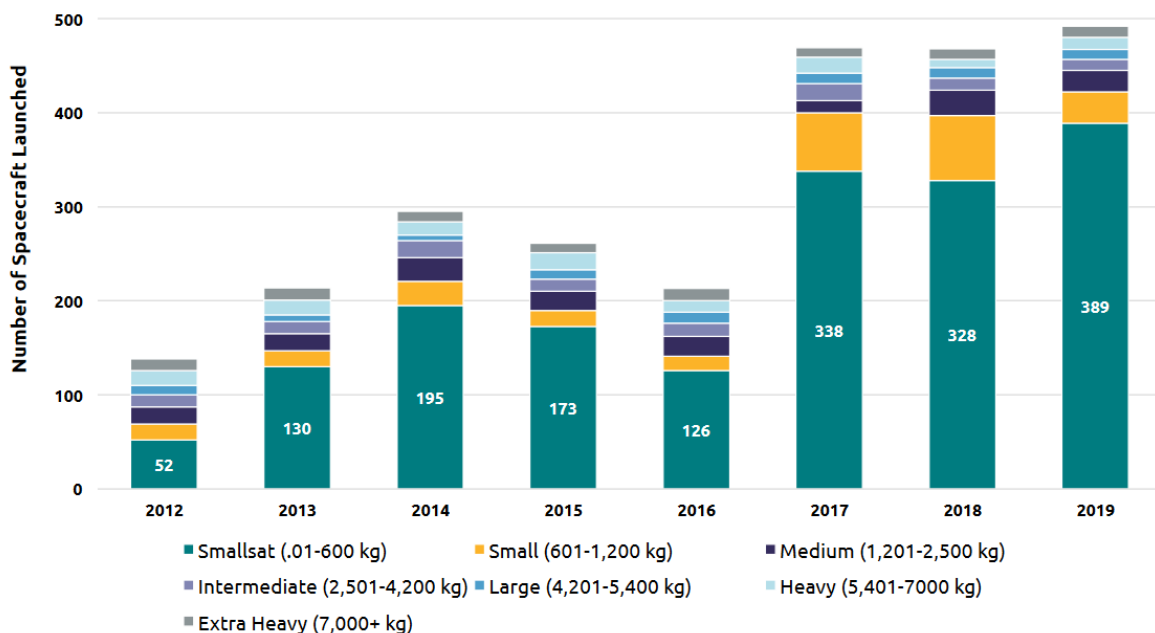


Figure 1.1: Spacecraft launches in the period 2012-2019, split by mass [1].

The shift of the spacecraft mass towards miniaturization is one that is accompanied by challenges. Not all smallsats are deployed on their optimal orbits due to the low number of dedicated launches

[1] and, not unlike other satellite classes, require propulsion for orbit changes, drag compensation, attitude control, station-keeping and other [11]. A dedicated micropropulsion subsystem would thus benefit the mission greatly [18, 19]. A promising candidate for creating thrust on smaller satellites is the concept of solar thermal propulsion [20]. During solar thermal thrusting, a monopropellant is heated by solar irradiation after which it is ejected in order to create thrust [21]. For the heating, large concentrator systems consisting of mirrors and lenses are used. Then, the concentrated beam is led into the RAC or heat exchanger. In the cavity, the thermal energy can be stored or directly used to increase the propellant's enthalpy. Finally, via a nozzle, the heated propellant is expelled.

STP potentially has a higher specific impulse than the conventional monopropellant and bi-propellant thrusters. The latter are known to have a specific impulse around 150-320 s, while STP could reach up to 860 s according to Leverone et al. [11]. This is due to the fact that the most promising monopropellant for solar thermal thrusting, hydrogen, has a very low molar mass when compared to typical chemical propellants [22]<sup>1</sup>. For a similar total impulse, this would mean that less propellant mass needs to be brought into space, implying lower launch costs. Alternatively, the flexibility of the spacecraft mission could be enhanced by bringing the same amount of fuel. Hall effect thrusters and ion thrusters, known as electric propulsion, have even higher specific impulses but are limited by the amount of thrust they produce, which is at most 50 mN for the engines designed until now [16]. STP has been demonstrated to generate thrust (pulses) up to 20 N, which in turn is surpassed by the thrust produced by a chemical engine. Thrust is important in the knowledge that it largely determines the time needed to complete a manoeuvre, e.g. a fast orbit transfer or orbit insertion. Looking at the characteristics, STP thus takes the middle ground between efficient, slow electric propulsion and inefficient, fast chemical thrusting. Compared to a resistojet, where solar light is converted into electrical energy and then converted again to heat, the STP concept cuts out the middle step which sees an efficiency increase in return. These statements are supported by Figure 1.2 [2], which shows various propulsion concepts, their thrust-to-weight ratio and their specific impulses. The figure also shows that the Technology Readiness Level (TRL) of solar thermal thrusting is between 4-6, which indicates that ground tests on the propulsion technology have been conducted [23]. The concept was indeed never flown in space but has been demonstrated successfully in laboratories and in simulations on various occasions, attaining high temperatures up to 2600 K [24]. The largest disadvantage of the concept until now has been the voluminous concentrator system required as well as the vulnerability of this component [25]. However, STP clearly is a viable option for (micro)satellite applications because it delivers specific impulses in excess of chemical thrusters. The challenge is to design a thruster which meets these expectations while tackling the issue of added complexity associated with the large concentrator part.

The research towards STP is of great importance in order to make the concept feasible for (micro)propulsion applications. At the Technical University located in Delft, practical research has been done towards the subject of STP. In 2008, Leenders designed, manufactured and tested an STP thruster consisting of an RAC and nozzle with a 1000 W theater lamp combined with a lens as the heat source [3, 7]. The copper engine, dubbed STT1, attained a maximum RAC temperature of 750 K and maximum propellant temperature of 525 K. The highest performance was reached when the propellant (gaseous nitrogen) reached 494 K at a continuous mass flow of  $167 \text{ mg s}^{-1}$  and RAC input power of 49 W. The highest thrust and specific impulse (both SL) then equalled 81.3 mN and 49.6 s respectively, at a thermal efficiency of 52 %.

The performance reached in those experiments is not competitive in any way: almost half of the inserted heat is lost, while the specific impulse is not close to the aforementioned values in this chapter. The highest possible exhaust velocity (the limiting velocity) for a temperature of 494 K, where the pressure term is ignored, would be  $1013 \text{ m s}^{-1}$ . This gives a specific impulse of 103.3 s, half of which is reached. Leenders's goal was to demonstrate that thrust could be generated with STP technology at DUT, with little attention to mass, size and performance. The current thesis will reach further. For this project the objective is to design, build and successfully test the successor of the STT1, called STT2, at propellant temperatures that are twice the value reached by Leenders. Those temperatures will at that point be limited by the material's melting point and the hard-soldered connections. To achieve these high temperatures, the thesis will hinge on three main ideas or subgoals: increase the temperature

<sup>1</sup><https://webbook.nist.gov/chemistry/>, visited on 20-11-2020.

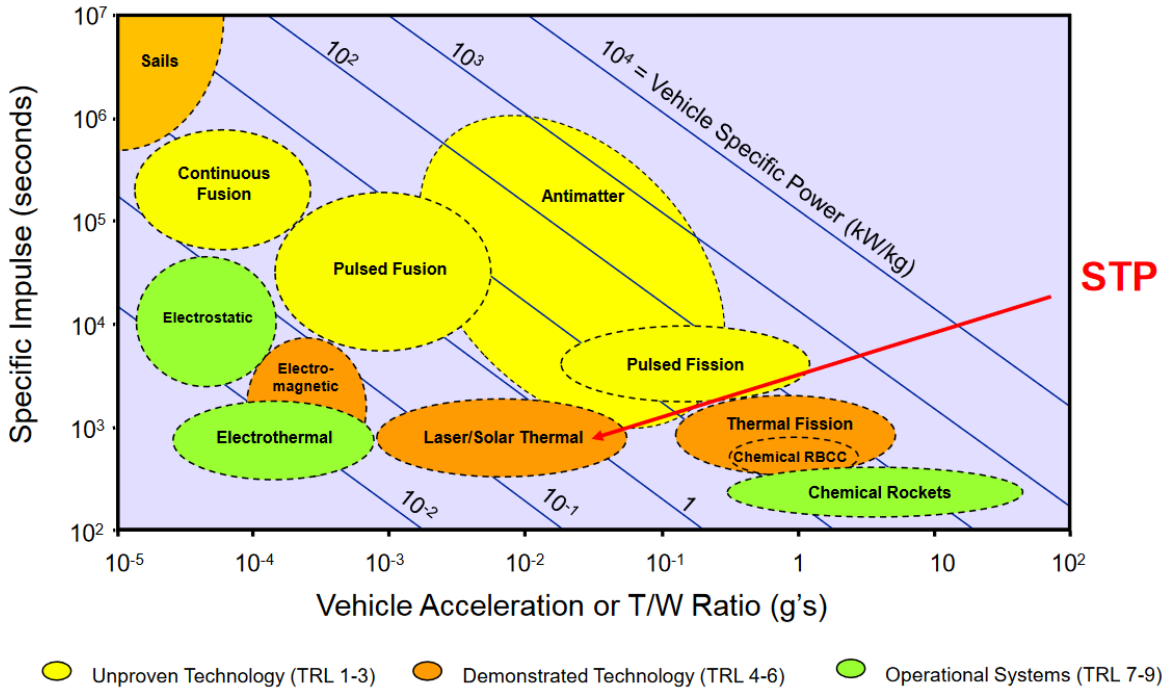


Figure 1.2: Propulsion concepts and their characteristics [2].

of the RAC by increasing the power input from the heat source; increase the thermal efficiency of the heat exchanger by redesigning the piece; and develop a Python tool, the Preliminary Design Tool (Preliminary Design Tool (PDT)), that can predict the STP engine performance as a result of user design choices.

First of all, the research framework of this project will be shown in Chapter 2. It kicks off with a small background on STP, which is followed by a more thorough analysis of STT1 and the research goal, requirements and constraints for STT2. Then, the PDT is presented in Chapters 4 and 3, where the first chapter will focus on the theory and models behind the tool while the second chapter will focus on the tool's capabilities. The tool will be verified by models from both Leenders's and Das's theses [3, 26]. Validation is done using experimental data from Leenders's experiments, combined with the results of experiments on STT2. Because of time constraints, the designed thruster STT2 was already manufactured when the tool was still under development. Chapter 5 will detail this design following from the research goal and requirements. At the end of the chapter the manufactured pieces, both self-made and externally built, are displayed.

Experiment preparations are performed as shown in Chapter 6. After the initial test runs, it was discovered that the thruster had some issues in the channel area, where a small change in the design saw some large consequences. Also, when trying to remedy leakages in the heat exchanger the thruster got damaged, which prevented further experiments on the engine. As such, a drastic change in course was taken and it was decided to replace the actual tests by CFD simulations in order to validate the PDT and see if STT2 would adhere to the set requirements and goal. This analysis is detailed in Chapter 7, which shows the thermal performance of both STT1 and STT2 motors. Finally, now that PDT is validated, a new engine is designed in Chapter 8 which implements the lessons learned from designing and manufacturing STT2. This Solar Thermal Thruster 3 (STT3) engine again has the notable constraint that the engine should be built at DUT. In the end, Chapter 9 gives the conclusions on the research objective and requirements and shows the recommendations for further research into the subject.

# 2

## Research framework

The current chapter will show the research framework of this project. It will kick off with a background on **STP** technology to make the reader familiar with the concept. A small subsection on the research into STP is included in this section as well. It is followed by an extensive section on the performance of the first and up until now only solar thermal thruster built at **DUT** by Leenders, **STT1**. By doing this, the author is able to set a feasible goal for the current project in a next section. In the end the requirements and constraints are derived from the knowledge gained in this chapter.

### 2.1. Research background

This section will give a small background on both the principles of and research towards solar thermal thrusting. The information will be concise, due to the fact that the workings and research were already thoroughly described in the literature study [27] and the thesis proposal [28] from the same author<sup>1</sup>.

#### 2.1.1. Principles of solar thermal propulsion

**STP** is a propulsion concept proposed to be deployed on (nano)satellites [11, 16, 24, 29]. Figure 2.1 displays the main components of an **STP** engine<sup>2</sup>. The concentrator, made up of a combination of (parabolic) mirror(s) or lenses, collects the solar irradiation which is directed towards the heat exchanger or **RAC** [21]. There, the energy is directly or indirectly absorbed by the propellant. The propellant is then collected in the plenum and expelled via a nozzle, thus creating thrust.

There are a few additions that can be made to the thruster system. Fiber optic cables could be used to decouple the thruster attitude from the Sun direction [30]. A heat storage can be added to provide the spacecraft with high-energy thrust pulses [31]. The thruster system can be extended in order to provide power to the spacecraft as well through a thermal-to-electric energy conversion, a so-called bimodal system [24]. That way, (excess) heat is used to provide electrical energy to the spacecraft, thus mitigating the need for solar panels and possibly batteries.

<sup>1</sup>Both documents are retrievable from <https://github.com/AJTRP/AE5810-thesis>.

<sup>2</sup><https://tinyurl.com/y67p194g>, accessed on 29-11-2019.

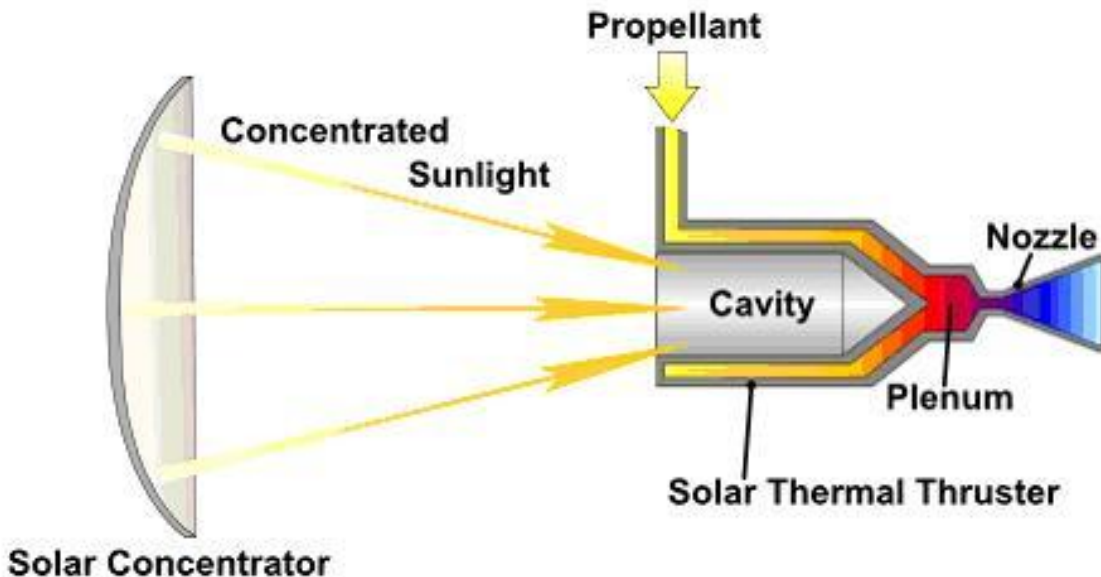


Figure 2.1: Main components of an STP thruster (see footnote).

### 2.1.2. Summary of research into solar thermal propulsion

The concept of solar thermal thrusting was already introduced in 1956 [32]. First it was mainly researched by governmental institutes such as the [Air Force Rocket Propulsion Laboratory \(AFRPL\)](#) [21, 25, 33, 34], but starting in the 2000's researchers from universities also started to explore the technology [24, 35–38]. The thruster first consisted of a concentrator subsystem, heat exchanger and nozzle but was later expanded with fiber optic cables, heat storage and power capabilities [30, 39–41]. Propellants of interest were discussed at criteria such as molar mass, heat capacity, storability and toxicity [28]. Hydrogen, ammonia and water are seen as promising candidates. For the heat exchanger's material, rhenium, tungsten and molybdenum were often considered due to their high melting points [42]. STP has never been flown in space. This is mainly due to the risk associated with the voluminous concentrator subsystem and the storability of cryogenic hydrogen [21].

## 2.2. Solar Thermal Thruster 1 background

Harrie Leenders produced a total of four documents on the subject of solar thermal thrusting in his time at [DUT](#). Together with a fellow student, they modelled the thermal control of an STP-propelled spacecraft in 2006 [43]. In 2007 he finished his literature study [44] and subsequently in 2008 he completed his master thesis [3], which resulted in a paper in association with his supervisor Ir. B.T.C. Zandbergen [7], also the supervisor of the current research. The latter two documents are often cited in this report because of the detailed description of the design methodology, experiment setup and results.

This section will present the design and manufacturing of [STT1](#) and particularly focus on the test results. It will be concise, details and rationale can be found in the document described above. The main findings will be used to improve the current report and prevent the same mistakes from being made twice.

### 2.2.1. Design and manufacturing

Leenders's goal for his master thesis was to develop and test an STP technology demonstrator at DUT. It was designed to heat a propellant flow of  $300 \text{ mg s}^{-1}$  to 373.15 K. The assumption was made that of the incoming 29 W, an arbitrary 80 % would be used to heat the propellant to the aforementioned value without any insulation layer.

Leenders designed a thruster consisting of three main elements: concentrator subsystem, heat exchanger and nozzle. For the concentrator subsystem, he used one converging lens in addition to a 1000 W theater lamp as the irradiation source. The lamp was operated for another STP-related study by Pino [45]. The combination would give a focal spot with a diameter of 2 cm at a focal length of 2 cm.

Two nozzles were intended for use during the tests: a glass and a copper one. Both were previously used in other studies. The glass nozzle has a throat diameter of 6.8 mm, an exit diameter of 7.2 mm and a mass of 16 g. This nozzle was mainly added for demonstration purposes; because the glass cannot exceed 473 K, only a few tests were performed with this nozzle attached to the engine. Because of the temperature limit and the non-optimal dimensions (see later in this section), the results of tests with this nozzle are not used in this report. When results are displayed, these are always produced with the copper nozzle attached.

The copper nozzle was designed with a throat diameter of 0.66 mm, an exit diameter of 0.77 mm and a mass of 4.5 g. The technical drawing can be found in Appendix A. It was reconstructed for unknown reasons and it turned out to have a throat and exit diameter of 0.58 mm and 0.68 mm respectively. The area ratio, which is the ratio of the nozzle throat and exit area, is thus equal to 1.375 [22].

The heat exchanger has the direct propulsion, indirect absorption configuration [27]. It features eight straight rectangular channels around an open-ended cone. It has a ring on the base of cone for distribution of the propellant. It is made of copper and has a total mass of 0.087 kg. The featured propellant is gaseous nitrogen.

The heat exchanger and copper nozzle were both manufactured by the DUT in-house workshop, Dienst Elektronische en Mechanische Ontwikkeling (DEMO). This workshop is equipped with advanced Computer Numerical Control (CNC) mills and lathes, operated by experienced users. The glass nozzle, theater lamp and lens were borrowed or already present at the faculty of AE.

### 2.2.2. Experimental results

All tests on the complete motor were conducted in the cleanroom located at the 8th floor of the faculty of AE. The thruster was tested in different configurations: test were done without and with mass flow and during the latter, insulation was applied around the heat exchanger. Additional equipment used were the test bench TB-AE-1.0 (for more information on this bench, see Jansen [46]), one Futek LSB200 load cell, nine type K thermocouples, two pressure transducers and the Brooks 5851 S mass flow controller. Four of the thermocouples were attached at various points of the RAC and averaged to determine the heat exchanger's temperature, another was inserted in the nozzle to find the propellant temperature. One pressure sensor was attached to the nitrogen feed line, the other was attached to the nozzle chamber.

The highest propellant temperature attained during testing was 525 K for a short period of time at a mass flow of  $50 \text{ mg s}^{-1}$ . The heat exchanger was allowed to heat up to 630-630 K. Thrust and RAC input power for this result are unknown, hence the thermal efficiency cannot be calculated. Next to this, Leenders also tabulated test results from five different mass flow runs, together with thermal efficiency, measured thrust and propellant pressures. These are shown in the upper part of Table 2.1. The lower part shows the calculated specific impulse, exit pressure, exhaust velocities and thrust. The last row shows the theoretical thrust as calculated by Leenders.

Table 2.1: STT1 measurements from Leenders's paper [7].

Measurements					
Measurement number	1	2	3	4	5
$\dot{m}$ [mg/s]	77	103	128	154	167
$F$ [mN]	28.9	43.3	59.7	74.5	81.3
$T_c$ [K]	494	480	466	452	445
$T_{RAC}$ [K]	545	514	490	470	460
$p_{feed}$ [bar]	1.97	2.53	3.07	3.61	3.92
$p_c$ [bar]	1.94	2.48	3.02	3.55	3.87
Calculations					
<b>Resulting <math>I_{sp}</math> [s]</b>	38.3	42.9	47.5	49.3	49.6
<b>Theoretical <math>p_e</math> [bar]</b>	0.37	0.47	0.58	0.68	0.74
<b>Theoretical <math>U_e</math> [m/s]</b>	622	613	604	595	590
<b>Theoretical <math>U_{eq}</math> [m/s]</b>	319	423	480	516	531
<b>Theoretical <math>F</math> [mN]</b>	24.6	43.6	61.5	79.4	88.6
<b>Theoretical <math>F</math> [mN] by Leenders</b>	33.5	53.1	72.6	91.8	103.4

The theoretical values are found using Equations 2.1-2.5 [22]. The involved variables are the propellant temperature in the nozzle chamber  $T_p$ , RAC temperature  $T_{RAC}$ , propellant feed pressure  $p_{feed}$  and propellant chamber pressure  $p_c$ . The assumption is made that the ambient pressure is the standard SL value of 1.01325 bar, while the propellant inlet temperature equals 298.15 K, a value used by Leenders in his calculations. The nozzle dimensions from the previous section were used. Note that the pressure values need to be in Pa for the equations below, the thrust in N and the mass flow in  $\text{kg s}^{-1}$ . The universal gas constant  $R_A$  equals  $8.314 \text{ J mol}^{-1} \text{ K}^{-1}$ , the molar mass MM of nitrogen is  $0.02801 \text{ kg mol}^{-1}$  and the specific heat ratio at 298.15 K is  $1.40^3$ . The resulting Vandenkerckhove function  $\Gamma$  is thus 0.6847.

The equations in this section are derived from the [Ideal Rocket Theory \(IRT\)](#). It hinges on a number of assumptions; the most important are steady, isentropic and one-dimensional nozzle flow, constant propellant heat capacity, homogeneous propellant composition and the propellant obeying the ideal gas law [22]. IRT allows the use of the equations in this chapter and is used in the preliminary design process. Note that IRT does not incorporate the effects of thermal losses, pressure losses, change in propellant composition, throat boundary layers and so on. In a later stage, these can be quantified by consulting literature or conducting experiments.

$$\frac{A_e}{A_t} = \sqrt{\frac{\Gamma}{\frac{2\gamma}{\gamma-1} \left(\frac{p_e}{p_c}\right)^{\left(\frac{2}{\gamma}\right)} \left(1 - \left(\frac{p_e}{p_c}\right)^{\left(\frac{\gamma-1}{\gamma}\right)}\right)}} \quad (2.1)$$

$$\Gamma = \sqrt{\gamma} \left(\frac{2}{\gamma+1}\right)^{\frac{\gamma+1}{2(\gamma-1)}} \quad (2.2)$$

$$U_e = \sqrt{2 \frac{\gamma}{\gamma-1} \frac{R_A}{MM} T_c \left(1 - \left(\frac{p_e}{p_c}\right)^{\left(\frac{\gamma-1}{\gamma}\right)}\right)} \quad (2.3)$$

<sup>3</sup><https://webbook.nist.gov/>, accessed on 11-03-2019.

$$U_{eq} = U_e + \frac{p_e - p_{amb}}{\dot{m}} A_e \quad (2.4)$$

$$F = \dot{m} U_{eq} \quad (2.5)$$

Table 2.2 shows the thermal efficiency  $\eta_{thermal}$  of the RAC for each of the five measurements, as written down in the paper. Combining this with the mass flow and propellant temperature from Table 2.1 and Equation 2.6, the power input from the thermal lamp to the RAC can be calculated, see the last row of the table. Note that the enthalpy change  $\Delta H$  is derived from NIST properties<sup>4</sup>.

Table 2.2: ST1 RAC efficiency, enthalpy, propellant and input power, from Leenders's paper [7].

Measurement number	1	2	3	4	5
$\eta_{thermal}$ [-]	0.32	0.40	0.45	0.50	0.52
$\Delta H \cdot 10^5 \text{ J/kg}$	2.05	1.90	1.75	1.61	1.53
$Q_p [\text{W}]$	15.8	19.6	22.4	24.7	25.6
$Q_{in} [\text{W}]$	49.2	49.0	49.8	49.4	49.2

$$\eta_{thermal} = \frac{\dot{m} \cdot \Delta H}{Q_{in}} \quad (2.6)$$

### 2.2.3. Results discussion

From Chapter 1, it was clear that the attained propellant temperature and specific impulse were low in comparison to results from literature. This can be attributed to three main reasons: low thermal efficiency (at most 52 %), low amount of input power (approximately 49 W) and the nozzle not being adapted. The latter can be derived from the fact that the nozzle exit pressure does not equal the ambient pressure for the measurements in Table 2.1. When it does, thrust is maximized in which case the nozzle has a so-called optimum expansion ratio [22]. The exit pressure is dependent on the chamber pressure, which is not a control variable; it cannot be set during the experiments, but it is a result from the combination of propellant properties, mass flow, nozzle throat area and propellant temperature, see Equation 2.8. So despite the temperature decreasing over the measurements (see Table 2.1), the specific impulse does increase because the exit pressure approaches the optimum of 1 atmosphere.

The influence of an adapted nozzle is large. For the fifth measurement, the nozzle exit area would equal  $2.74 \times 10^{-7} \text{ m}^2$  if the nozzle had an optimum expansion ratio to ambient (Equation 2.1). The equivalent exhaust velocity would then be  $542.4 \text{ m s}^{-1}$  (Equation 2.4) which would result in a specific impulse of 55.3 s, which is 11.4 % higher than the value attained during the test run. The highest possible exhaust velocity would be an expansion to vacuum, which is called the limiting velocity  $U_L$  in  $\text{m s}^{-1}$ , see Equation 2.7. For the fifth measurement that would be  $98.1 \text{ m s}^{-1}$ .

Another thing that was noticed was that the 1000 W theater lamp outputted an irradiation beam of approximately 240 W. Of that number, Leenders estimated that 61 W would be focused by the lens towards the heat exchanger's cavity. However, only 49 W did reach the RAC (see Table 2.2), of which 25.6 W did increase the propellant's enthalpy (for the fifth measurement). So the total system had a thermal efficiency of 2.6 %.

$$U_L = \sqrt{2 \frac{\gamma}{\gamma - 1} \frac{R_A}{MM} T_c} \quad (2.7)$$

<sup>4</sup><https://webbook.nist.gov/>, accessed on 11-03-2019.

The equations in this section are valid for choked flow only. Choked flow, where the flow becomes supersonic in the divergent part of the nozzle, is reached once the ratio of ambient pressure to nozzle chamber pressure is lower than a value which is dependent on propellant properties, see Equation 2.9. This value is 0.528 at nitrogen's specific heat ratio of 1.40. At a standard SL ambient pressure of 1 atmosphere, a chamber pressure of a minimum 1.92 bar is sufficient, which is barely satisfied in the first measurement.

$$\dot{m} = \frac{\Gamma p_c A_t}{\sqrt{\frac{R_A}{M_M} T_c}} \quad (2.8)$$

$$\left(\frac{p_{amb}}{p_c}\right)_{cr} = \left(\frac{2}{\gamma + 1}\right)^{\left(\frac{\gamma}{\gamma - 1}\right)} \quad (2.9)$$

A few issues arose from the results. Table 2.1 shows the theoretical thrust in the last row as calculated by Leenders. These values could not be reproduced and do not match the calculated values in this report, which are displayed in the second to last row. Furthermore, both rows are also not equal to the measured thrust, shown in the second row. Especially the large differences in both the last rows are an issue; apparently Leenders inserted other properties and measurements in the IRT equations than the current author.

A few explanations can be given for the differences between the three rows: first of all, it is not confirmed that the pressure and temperature at RAC exit are equal to the values in the chamber of the nozzle; there could be some heat and pressure loss in the connecting channel, but this is not substantiated in either thesis or paper. Secondly, the nozzle could suffer from a boundary layer in the throat, which is quantified by the discharge factor. This factor is mentioned in the thesis but could again not be checked. Thirdly, the ambient pressure, ambient temperature and/or inlet propellant temperature could be different than the values stated in this section. A fourth explanation would be that the velocity of the propellant in the chamber was not close to 0.

#### 2.2.4. Main findings

What becomes clear from this section is that documentation of methodology and results is of the utmost importance to any successors who would like to reproduce the obtained values and continue research with those results. It is recommended to clearly state all inputs, results, properties and dimensions when an experiment is conducted, preferably tabulated for a quick overview. In this report, this method will be followed to allow the report to be used in future research.

Furthermore, another lesson learned is that the efficiency of the theater lamp is minor, even with a lens. Only 4.9 % of lamp's rated power of 1000 W reached the RAC after which almost half was lost to the surroundings by convection and radiation in the heat exchanger. There is room for improvement here, both in RAC input power as in thermal efficiency of the heat exchanger itself. Next to that, optimizing the nozzle can also add significantly to the specific impulse. If the budget allows so, constructing a new nozzle for STT2 is preferred over using the copper nozzle from Leenders. The last finding is that DEMO can produce very detailed pieces out of copper. For the design of the new thruster, they will be consulted regarding the possibilities and pricing.

### 2.3. Research goal

The objective was briefly explained in Chapter 1 as follows: design, build and successfully test the successor of the STT1, called STT2, at propellant temperatures that are deemed to be the maximum

that can be reliably achieved at this university. In the thesis project plan<sup>5</sup> [28], this goal was quantified: STT2 should reach a SL specific impulse of 62.8 s. However, the specific impulse can be increased beyond that value. With the information from the previous sections, the following research goal is set:

*Demonstrate the feasibility of the Solar Thermal Thruster 2 by having a minimum specific impulse at sea level conditions of 90.0 s at a continuous mass flow level of 300 mg s<sup>-1</sup>.*

A small calculation was performed to see if the specific impulse of 90.0 s could be attained under the requirements and constraints. Using IRT and setting the mass flow at 300 mg s<sup>-1</sup>, about 250 W of input power at a thermal efficiency of 70 % is needed to heat the propellant to 835.3 K (with a propellant inlet temperature of 298.15 K). Then, for an optimally expanded nozzle a pressure ratio of 8.05 (Equation 2.4) and subsequently an area ratio of 1.71 (Equation 2.1) are found. Then, the chamber pressure is 8.2 bar (provided that the ambient pressure is 1 atm) and the nozzle throat diameter and exit diameter are 0.58 mm and 0.76 mm respectively. The thermal efficiency is derived from Leenders. When taking the increase in thermal efficiency in Table 2.2 as a linear trend (which it certainly is not, it has a decreasing increase rate), the thermal efficiency equals 0.72.

Chapter 1 showed that this research goal is hinging on three main pillars or subgoals: increasing the power input, increasing the thermal efficiency and creating a preliminary design tool to allow for accessible evaluation of design choices. These three aspects will be addressed in the next chapters. The goal still allows for changes in the design and experiment outlay: the power source can be altered, additional lenses can be used, more insulation can be applied or another propellant can be used. The mass flow chosen is arbitrary but is set at this level in order to make comparisons to Leenders thruster, as he chose a similar mass flow for his thesis.

## 2.4. Requirements and constraints

The research goal stated above is subject to requirements and constraints, which are given in this section. Two types of requirements will be discussed: functional requirements, which outline the direction of this thesis project, and system requirements, which detail the performance the system has to adhere to. The difference between the two types is that the latter can be quantified, while the earlier cannot.

### 2.4.1. Functional requirements

Table 2.3 shows the functional requirements that were identified in this chapter.

<sup>5</sup>Retrievable from <https://github.com/AJTRP/AE5810-thesis>.

ID	Requirement	Rationale
REQ-F-1	An STP thruster system, called STT2, shall be designed.	The goal for this project is to demonstrate a high-temperature STP thruster at DUT.
REQ-F-2	STT2 shall consist of three primary components: the concentrator subsystem, the heat exchanger or RAC and the nozzle.	In order to reduce the complexity of the thruster, no fiber optic cables, thermal storage and/or power subsystem are implemented.
REQ-F-3	STT2 shall heat propellant through the use of concentrated irradiation.	The requirement of solar irradiation is relaxed, because testing when dependent on the Sun adds complexity.
REQ-F-4	STT2 shall generate a thrust force by expelling heated propellant.	The principle of STP is to expel heated propellant via a nozzle.
REQ-F-5	STT2 shall be manufactured and subjected to experiments.	In order to validate the PDT, the designed thruster needs to be built and tested.
REQ-F-6	STT2 shall be manufactured and tested using DUT resources.	Presently, the time allocated to a thesis is 9 months or 42 ECTS, excluding the literature study. The money available is 500 Euros.
REQ-F-7	STT2 shall be designed with a non-toxic propellant.	The cleanroom at AE does not allow testing with toxic propellants.

Table 2.3: Functional requirements for STT2.

### 2.4.2. System requirements

Table 2.4 shows the system requirements that were identified in this chapter.

ID	Requirement	Rationale
REQ-S-1	STT2 shall have a SL specific impulse of at least 90 s at a mass flow of $300 \text{ mg s}^{-1}$ .	See the research goal.
REQ-S-2	STT2's heat exchanger shall reach a temperature of at least 900 K, without propellant flow.	This temperature is necessary in order to heat the propellant to a sufficient degree.
REQ-S-3	STT2's heat exchanger shall heat the propellant to a temperature of at least 850 K at a mass flow of $300 \text{ mg s}^{-1}$ .	This temperature is necessary in order to reach the specified specific impulse.
REQ-S-4	STT2's heat exchanger shall have a maximum mass of 0.087 kg.	This is the mass of Leenders's heat exchanger.

Table 2.4: System requirements for STT2.

### 2.4.3. Constraints

The system requirements are interconnected and are based on constraints found in Table 2.5, which are mostly sensor-related and derived from the literature study<sup>6</sup> [27].

<sup>6</sup>Retrievable from <https://github.com/AJTRP/AE5810-thesis>.

<b>ID</b>	<b>Constraint</b>	<b>Rationale</b>
CON-1	STT2 shall have a maximum heat exchanger temperature of 933 K.	That is the maximum value that hard-soldered connections can withstand according to the <a href="#">DEMO</a> workshop.
CON-2	STT2 shall experience a maximum propellant pressure of 10 bar.	Although some of the pressure sensors that were tested in the literature study could reach up to 16 bar, literature suggests that high-pressure vessels above 10 bar are not recommended in micropulsion [47].
CON-3	STT2 shall have a maximum propellant mass flow of $861 \text{ mg s}^{-1}$ .	This is the maximum amount the Brooks 5851S Smart Mass Flow, present at the AE cleanroom, can measure.
CON-4	STT2 shall have a maximum thrust of 1000 mN.	This is the maximum amount various thrust sensors and benches developed at AE can support. See also Chapter <a href="#">6</a> .

Table 2.5: Constraints for STT2.

All these values fall within the constraints. There is some room left in the temperature range and the pressure range to accommodate for heat and pressure losses in each component and for nozzle correction factors. After the design for [STT2](#) is finalized in Chapter [5](#), it will be inputted in the preliminary tool built in Chapter [3](#). This will show if the design can actually reach the set specific impulse of 90.0 s.

Note that no  $\Delta V$  requirement nor volume requirement is given in this chapter. This is purely due to the lack of a dedicated mission for which the thruster is designed. Because the thruster needs to be manufactured at low cost, it can most likely not adhere to any (nano)satellite mission standards.

# 3

## Preliminary design tool

### 3.1. Assumptions

Here, the assumptions for the theoretical model are listed.

1. The RAC has a constant temperature throughout the system, as only high-conductive materials (such as copper) and small thicknesses will be used. So, the outer wall of the RAC will be assumed to have a similar temperature as the inner wall and the walls next to the channels.
2. The surroundings of the RAC will be air which is at a wind still and at a uniform temperature.
3. When insulation is applied, its conduction will be taken into account. In that case, the outer wall heat flows will be from the insulated outer wall. Naturally, the inner insulation wall temperature will not be equal to the outer insulation wall temperature.
4. The propellant is treated as a single phase (gaseous) fluid.
5. The convection from RAC to propellant will be modelled as a series of  $n$  (to be defined) segments, where the propellant has a higher temperature the further it flows downstream.
6. The cylindrical RAC (STT2) will have no inner wall losses, because there is only a small aperture where the irradiation falls through. Absorptivity is not also not applicable.
7. No heat is lost to the surroundings in the transportation of the propellant from RAC to nozzle. The channel(s) have a uniform cross-section.
8. The nozzle is assumed to have ideal expansion, i.e. the exit pressure equals the ambient pressure.
9. There are neither heat nor pressure losses in the nozzle.
10. The model is conservative in the sense that it does not take into account entrance and exit heating in the RAC.
11. The RAC is oriented horizontally, with the aperture opening to the side.

### 3.2. Verification and validation

In this section, the thermal model will be verified and validated. It will be done using three cases described by Leenders [3]. He inputted these cases in his Matlab script (which is unfortunately lost),

of which the results will be used for verification. Furthermore, he obtained experimental data which in turn is used for the validation of the thermal part of the tool.

The first case is a conical cavity with no propellant flow and no insulation, the second a similar case with insulation on the outer sides and the third one a similar case with insulation and mass flow. All three will be inputted in the Python model (inputs are found in his thesis) and will be discussed here. Please note that only the thermal aspect of the model will be reviewed. Unfortunately, only graphs are available in Leenders' thesis. The raw data from the tests and the results from his Matlab model were not tabulated. The comparison will thus be made to the graphs, which depict the experimental data and Matlab model data.

Leenders used a 1000 W theater lamp to heat up his RAC. He applied four thermocouples at the outer walls of the RAC and took an average to deduce the RAC temperature. The propellant temperature was only measured at the nozzle, so the measured propellant temperature will be lower than the value to which it is heated in the RAC, due to heat losses in the connection pieces and nozzle.

### 3.2.1. Case 1: no mass flow and no insulation

The irradiance was present from 0 to 16 min. No propellant was flowing and no insulation was applied. See Table 3.1 for the inputs for this case.

Table 3.1: Case 1 inputs.

Name	Symbol	Value	Unit
RAC type	-	"Conical"	-
RAC material	-	"Copper"	-
Insulation	-	"No insulation"	-
RAC length	$L_{cav}$	0.05014	m
RAC inner diameter	$D_{inner}$	0.025	m
RAC outer diameter	$D_{outer}$	0.031	m
RAC aperture diameter	$D_{ap}$	0.025	m
RAC half angle	$\phi$	14	deg
RAC inner cavity area	$A_{RAC,i}$	2.267e-3	$m^2$
RAC outer cavity area	$A_{RAC,o}$	3.897e-3	$m^2$
RAC mass	$M_{RAC}$	0.066	kg
Irradiation time	$n_i$	16	min
Incoming power	$Q_{in}$	60	W
Incoming power efficiency	$\eta$	0.50	-
Absorptivity oxidized copper	$\alpha_M$	0.70	-
Emissivity oxidized copper	$\epsilon_M$	0.65	-
Ambient temperature	$T_{amb}$	298.15	K
Ambient pressure	$p_{amb}$	101325	Pa

A maximum RAC temperature of 542.3 K was calculated by the Python script. The results fit each other nicely, see Figures 3.1 and 3.2. Only the maximum temperature is slightly higher than Leenders' values. However, during his experiments, Leenders utilized four thermocouples, which indicated maximum temperatures in the range of 530-555 K. As such, the Python thermal model is deemed to be verified and validated for this case, as the graphs match very well (so the 10 % criterion is passed).

### 3.2.2. Case 2: no mass flow and insulation

The irradiance was present from 0 to 28 min. No propellant was flowing and M-Fil Saffil insulation was applied at the outer sides of the RAC, together with aluminium foil at the outer side to lower the outer wall emissivity. See Table 3.2 for the inputs for this case.

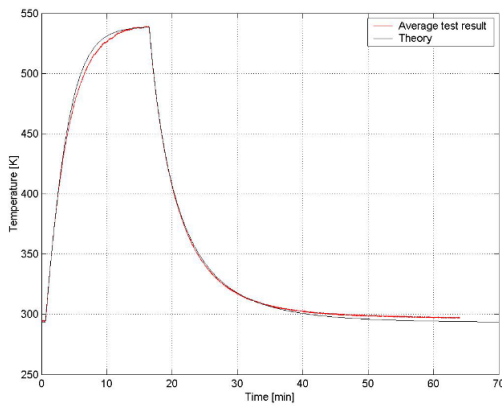


Figure 3.1: Case 1: experimental (in red) and theoretical Matlab (in black) RAC temperatures by Leenders [3].

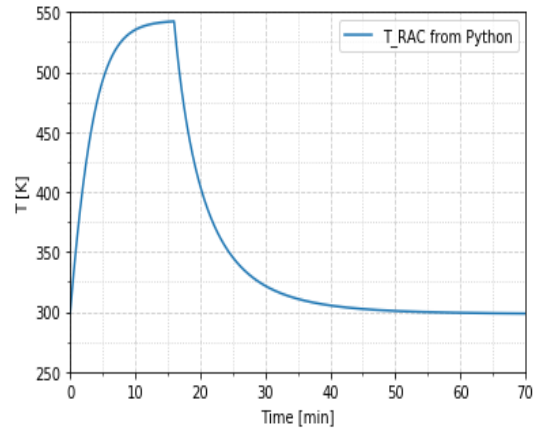


Figure 3.2: Case 1: theoretical Python RAC temperatures by Takken.

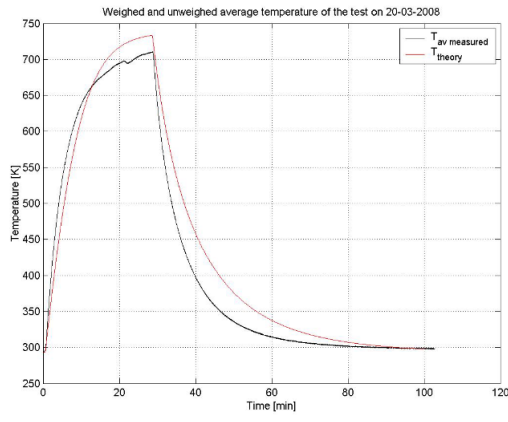


Figure 3.3: Case 2: experimental (in black) and theoretical Matlab (in red) RAC temperatures by Leenders [3].

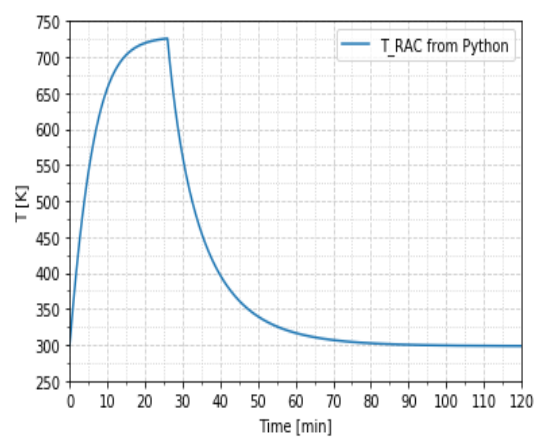


Figure 3.4: Case 2: theoretical Python RAC temperatures by Takken.

The dent at minute 23, Leenders stated, is due to movement of the irradiation source. The maximum RAC temperature calculated by the Python script is 725.9 K. Both results are shown in the graphs in Figures 3.3 and 3.4. Again, the graphs match but the resulting temperature is a bit on the high side. Leenders reported that one of the thermocouples indicated a maximum temperature of 725 K. It could be due to a number of things, such as the incoming radiation being lower (or having a lower efficiency), slightly different area sizes, the thermal conductivity of the Saffil M-Fil being different than Equation 4.46 suggests. Again, the model is deemed to be verified for case 2, as the maximum heat exchanger temperature does not differ for more than 10 % of the Matlab value found by Leenders. Validation is also passed, but with the side note that the final RAC temperature is slightly lower in the experimental data, but still within the 10 % limit of the experimental value.

### 3.2.3. Case 3: mass flow and insulation

The third case will evaluate the influence of propellant mass flow through the RAC. The goal of the heat exchanger is to heat up the propellant as much as possible to create the highest thrust and increase the efficiency  $I_{sp}$  of the thruster. Insulation is applied at the outer wall, see Table 3.4 for the inputs for this case. Furthermore, in Table 3.3, the mass flows and their start and end times are shown.

The graphs in Figures 3.5 and 3.6 do not match as well as they should. This has multiple reasons.

Table 3.2: Case 2 inputs.

Name	Symbol	Value	Unit
RAC type	-	"Conical"	-
RAC material	-	"Copper"	-
Insulation	-	"Saffil M-FIL"	-
RAC length	$L_{cav}$	0.10	m
RAC inner diameter	$D_{inner}$	0.025	m
RAC outer diameter	$D_{outer}$	0.11	m
RAC aperture diameter	$D_{ap}$	0.025	m
RAC half angle	$\phi$	14	deg
RAC inner cavity area	$A_{RAC,i}$	2.267e-3	$m^2$
RAC outer cavity area	$A_{RAC,o}$	5.373e-2	$m^2$
RAC mass	$M_{RAC}$	0.066	kg
Irradiation time	$n_i$	26	min
Incoming power	$Q_{in}$	60	W
Incoming power efficiency	$\eta$	0.50	-
Absorptivity oxidized copper	$\alpha_M$	0.70	-
Emissivity oxidized copper	$\epsilon_M$	0.65	-
Emissivity insulation	$\epsilon_{insu}$	0.09	-
Ambient temperature	$T_{amb}$	298.15	K
Ambient pressure	$p_{amb}$	101325	Pa

Table 3.3: Case 3 mass flow and time inputs.

Mass flow [mg/s]	Start time [min]	End time [min]
75	22	33
100	35	44
125	46	57
150	60	71
175	73	84
200	86	96

The first one also noticed by Leenders is that the flow appears to be turbulent, also at lower mass flows where the Reynolds number should drop below 2300. This is mainly due to the sharp turns at the inlet of the flow. The equations used for convection heat transfer are very much dependent on the Reynolds number and the fact that the flow is laminar or turbulent, so this induces great errors. Next to that, the connection pieces, to propellant feed and nozzle, will also start to heat up during the experiments, which is not taken into account in the model. The last possible explanation is the fact that Leenders noticed a variable radiation input from the theater lamp during this case. This is already noticeable before the first mass flow is applied at minute 22, as the curve of the RAC temperature decreases, while in case 2 it was steeper, towards the maximum temperature of about 710 K. For this reason, the input power was decreased to 45 W in the Python model. This case can thus not be verified nor validated, as only the "trend" of applied mass flow is shown, but the temperature values hold no real value (and differ more than the criterion of 10 %).

Note that the equations used were allowed to be used, as the Prandtl number ranged from 0.719 to 0.728 while the Reynolds number was inbetween 816.5 and 2852.6. Indeed, for the lower mass flows, the Reynolds number is low, which probably means that laminar flow is present. Furthermore, using Equation 4.12, the laminar entrance region proved to be around 50 %, which means that the Nusselt number varies along the channel. Note also that both the Matlab as the Python model overpredict the convection heat transfer to the propellant, indicated by the steep downwards slopes.

Table 3.4: Case 3 inputs.

Name	Symbol	Value	Unit
RAC type	-	"Conical"	-
RAC material	-	"Copper"	-
Insulation	-	"Saffil M-FIL"	-
Propellant	-	"Gaseous nitrogen"	-
Channel layout	-	"Linear"	-
Number of channels	$n_{ch}$	8	-
RAC length	$L_{cav}$	0.10	m
RAC inner diameter	$D_{inner}$	0.025	m
RAC outer diameter	$D_{outer}$	0.11	m
RAC aperture diameter	$D_{ap}$	0.025	m
RAC half angle	$\phi$	14	deg
RAC inner cavity area	$A_{RAC,i}$	2.267e-3	$m^2$
RAC outer cavity area	$A_{RAC,o}$	5.373e-2	$m^2$
RAC mass	$M_{RAC}$	0.066	kg
Irradiation time	$n_i$	95	min
Incoming power	$Q_{in}$	45	W
Incoming power efficiency	$\eta$	0.50	-
Absorptivity oxidized copper	$\alpha_M$	0.70	-
Emissivity oxidized copper	$\epsilon_M$	0.65	-
Emissivity insulation	$\epsilon_{insu}$	0.09	-
Ambient temperature	$T_{amb}$	298.15	K
Ambient pressure	$p_{amb}$	101325	Pa
Propellant pressure	$p_p$	200000	Pa
Channel diameter	$D_{ch}$	0.0006	m

### 3.3. Conclusions & recommendations

The theoretical tool has been validated for cases 1 and 2, where the tool approached the experimental temperature values well. However, when mass flow is applied, the model struggles with the convection heat transfer to the propellant, because the flow appears to be turbulent when the Reynolds number predicts laminar flow. Furthermore, the power input is not constant at the third case and the connection pieces start to heat up due to the length of the experiment.

Applying the tool to the case of STT2 under the inputs from Chapter 5 proved to be insightful: the heat exchanger could meet the requirements and goal from Chapter 2 when insulation was applied or when the power input was raised significantly. However, the performance should be checked in real-life, with experiments (see Chapter 6). Another option is to use CFD simulations, as those can most likely more accurately predict the heat transfer to the propellant, an area where the preliminary tool performs poorly. This statement will be explored in Chapter 7. However, for preliminary design choices, the tool from this chapter can still aid the designer in aspects such as RAC dimensions, power input, channel layout and so on.

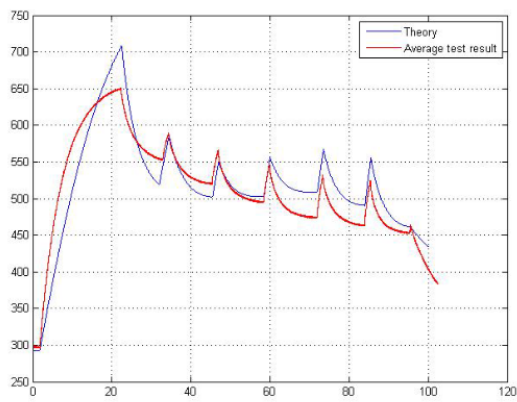


Figure 3.5: Case 3: experimental (in red) and theoretical Matlab (in black) RAC temperatures by Leenders [3]. The axes labels are time (in min) for the horizontal axis and RAC temperature (in K) for the vertical axis. Note that Leenders' experimental and theoretical values do not match well.

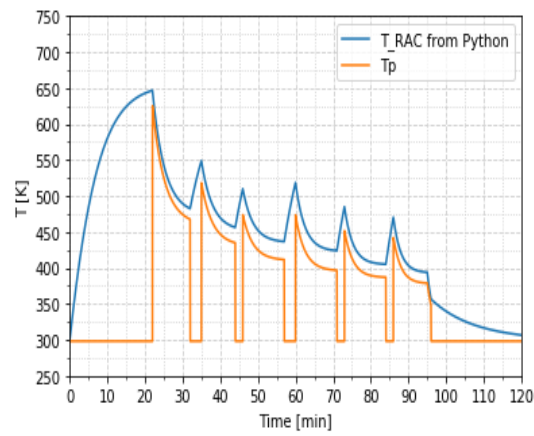


Figure 3.6: Case 3: theoretical Python temperatures by Takken. In blue is the RAC temperature, in orange is the outlet propellant temperature.

# 4

## Design theory

In order to get a better estimate of the performance of the **RAC** design, a **PDT** was built in Python. It consists of three models: a thermal model, pressure loss model and thrust model. The first has been built in great detail, while the other two serve as a means to get a ballpark estimate. The first model will be verified and validated in this chapter as well.

The goal of the tool is to see the impact of design choices on the thermal performance, such as the channel layout, number of channels, propellant, power radiation input, paint and so on. Remember that this design evaluation is one of the three main ideas to bring this thesis to a successful end, see Section 2.3. Assessing the performance will aid the designer in most of the **STP** thruster design decisions. For the thermal model in the **RAC**, the output propellant temperature is the most important output of the tool, as it will indicate the efficiency of heat transfer from solar irradiation to propellant in the **RAC**, thus being a major indicator of the success application of **STP**.

As stated before, the tool will be built in Python and will have three main themes: heat transfer in the **RAC**, pressure loss in the **RAC** and resulting thrust in the nozzle. The tool will be transient (time-dependent) and will mainly focus on the heat transfer from **RAC** to propellant. Much of the model is based on equations also found in Leenders [3] and Das [26]. Where applicable, they will be cited.

At first, the assumptions that are used in the model are given. Then, a heat transfer overview is shown, where the heat flows are explained. Afterwards, the three governing heat transfer aspects (convection, radiation and conduction) are discussed, followed by a section on pressure losses in the **RAC**. The propellant temperature and pressure are then inputs to calculate the thrust which will be produced in the nozzle. **IRT** will be applied to calculate the thrust from the heated propellant.

Afterwards, the model will be subjected to three cases for verification and validation. These cases are described in the thesis by Leenders [3]. He had both experimental as theoretical results, which will be compared to the Python model constructed here to verify and validate the tool. For both aspects, the maximum temperature reached by the **RAC** will be used as the primary criterion. The specific impulse  $I_{sp}$  is proportional to the square root of the propellant temperature. A propellant temperature error of 10 % will thus translate into an error of 3.2 % in the specific impulse, which is deemed well for a preliminary design.

In the one but last section, a **STT2** case will be inserted in the tool with the properties listed from Chapter 5. In the end, conclusions and recommendations will be presented to show the reader how the tool performs. The Python code is retrievable from <https://github.com/AJTRP/AE5810-thesis> and is not added to the report as an appendix because of the large amount of scripts involved. It is encouraged that others use the script as well to assess their design choices.

## 4.1. Heat transfer overview

The RAC will experience heat transfer in the form of three aspects: convection, conduction and radiation. Convection will account for the losses on both inner and outer walls, while it is also the driving force for the heating of the propellant. Conduction will not be taken into account for the RAC (see previous section), but it will be if insulation is applied because it has a low thermal conductivity. Radiation is both present on inner and outer walls as well, while it is also the heat input in the RAC.

The heat transfer part of the model will be transient (time-dependent) and show the heat gain and losses for each time-step  $t_{step}$  in s. These heat flows summed, there will be a resultant heat power  $Q_{res}$  (in W), which either will heat up the RAC if positive or lower its temperature if negative as Equation 4.1 shows.

$$\Delta T_{RAC} = \frac{Q_{res} \cdot t_{step}}{M_{RAC} \cdot c_{RAC}} \quad (4.1)$$

Where  $M_{RAC}$  is the RAC mass (without insulation) in kg and  $c_{RAC}$  is the material's heat capacity in  $\text{J kg}^{-1} \text{K}^{-1}$ . The resultant power is calculated via Equation 4.2.

$$Q_{res} = Q_{in} - Q_{loss} \quad (4.2)$$

Where  $Q_{loss}$  are the power losses, which leave the system in five forms, see Equation 4.3.

$$Q_{loss} = Q_{conv,cavity} + Q_{rad,cavity} + Q_{conv,outerwall} + Q_{rad,outerwall} + Q_{conv,propellant} \quad (4.3)$$

All these variables are in W. Note that the fifth and last form is not really a loss, but the driving principle of the heat exchanger. More information about convection, conduction and radiation is to be found in the subsequent sections.

## 4.2. Convection

Convection is defined as the heat transfer between a solid and a moving fluid [22]. There are two forms of convection discussed in this section, free (or natural) and forced. The first occurs without the 'forced' motion (e.g. by a pump) of the fluid, for instance when a hot wall is exposed to wind-still cold air. The air heats up, expands, has a lower density and rises, essentially creating its own motion. Forced convection is the other aspect and is the governing principle in e.g. refrigerators, where gas is pumped around to cool down the system.

For this theoretical model, both free and forced convection are encountered. The RAC will experience free convection at the outer walls (either the RAC itself or the surrounding insulation) and in the cavity. It is thus assumed that the surrounding medium (which is air) will be at rest. Forced convection is the driving heat transfer principle to heat up the propellant in the channels. Note that part of this section was already discussed in Section 5.2.

Convection is governed by Equation 4.4.

$$Q_{conv} = h \cdot A \cdot \Delta T \quad (4.4)$$

Where  $Q_{conv}$  is the convective heat transfer in W,  $h$  is the convective heat transfer coefficient in  $\text{W m}^{-2} \text{K}^{-1}$ ,  $A$  is the applicable area in  $\text{m}^2$  and  $\Delta T$  is the temperature difference in K between the hot and cold medium. Note that  $\Delta T$  is dependent on the application, during the subsequent sections it will be clear what temperature difference is meant.

The equation seen above is very straightforward, but the values of  $h$  can range from  $10 \text{ W m}^{-2} \text{ K}^{-1}$  to  $11600 \text{ W m}^{-2} \text{ K}^{-1}$  and beyond, depending on fluid properties, solid dimensions, fluid velocity, fluid viscosity etc. Often these values are based on empirical relations, where the Nusselt number  $Nu$  (dimensionless) is used to determine  $h$ , see Equation 4.5 [22].

$$h = \frac{Nu k}{L_s} \quad (4.5)$$

Where  $L_s$  is the characteristic length in m and  $k$  the thermal conductivity in  $\text{W m}^{-1} \text{ K}^{-1}$ . Numerous equations exist to calculate the Nusselt number. Subsections about propellant convection, inner cavity convection and outer wall convection are given hereafter to explain the equations used for this model.

### 4.2.1. Propellant convection

The driving principle for the RAC, essentially a heat exchanger, is convection from the hot wall to the cold propellant. To calculate the power flowing to the propellant, first the Nusselt number and then the convective heat transfer coefficient are calculated according to set of Equations found in 4.6-4.9.

$$Q_{conv,P} = h_p \cdot A_{ch} \cdot \frac{T_{p,out} - T_{p,in}}{\ln\left(\frac{T_w - T_{p,in}}{T_w - T_{p,out}}\right)} \quad (4.6)$$

$$h_p = \frac{Nu_p k_p}{D} \quad (4.7)$$

$$A_{ch} = \pi \cdot D \cdot L_{ch} \quad (4.8)$$

$$T_b = \frac{T_{p,in} + T_{p,out}}{2} \quad (4.9)$$

Note that  $L_s$  has been replaced by the channel diameter  $D$  in m. Furthermore, the area  $A$  is now the inner wall channel area in  $\text{m}^2$ . Note that the wall temperature  $T_w$  next to the channel is equal to the RAC temperature  $T_{RAC}$ , because it is assumed that the heat exchanger (apart from the insulation) has a uniform temperature due to its high conductivity. The last part of Equation 4.6 is the so-called logarithmic mean and is dependent on the boundary conditions, see further down. Note that  $k_p$  is evaluated at the bulk temperature  $T_b$ , which is the mean of the incoming propellant temperature  $T_{p,in}$  and outgoing propellant temperature  $T_{p,out}$ , all in K.

The Nusselt number equation still missing above is dependent on a number of factors. These aspects are listed below. After they have been discussed, the formulas will be given.

#### Reynolds number

One of the most important aspects that impacts the Nusselt number is the flow type, which exists in three forms: laminar, transitional and turbulent. The type is dependent on the dimensionless Reynolds

number  $Re$ , which is given in Equation 4.10. In this case, its characteristic dimension is the diameter  $D$  in m, which can be applied to e.g. a cylindrical object or tube flow. A flow is, in general, laminar for  $Re_D \leq 2320$ , turbulent for  $Re_D \geq 10\,000$  and transitional inbetween. However, Nusselt number equations for certain flow types often give their own ranges for the Reynolds numbers, see later.

$$Re_D = \frac{\rho v D}{\mu} = \frac{\dot{m} D}{A \mu} = \frac{4 \dot{m}}{\pi D \mu} \quad (4.10)$$

Here,  $\rho$  is the local propellant density ( $\text{kg m}^{-3}$ ),  $v$  the propellant velocity ( $\text{m s}^{-1}$ ),  $\dot{m}$  the mass flow,  $A$  the cross-sectional area of the channel and  $\mu$  the dynamic viscosity ( $\text{Pa s}$ ). Note that the equation for mass flow in a circular channel is applied to convert the density and velocity to other variables. Furthermore,  $\mu$  is evaluated at the bulk temperature  $T_b$  (see Equation 4.9). The subscript "D" indicates that the characteristic length for pipe flow is the pipe diameter  $D$ .

In general, a turbulent flow has a higher convection heat transfer than a laminar flow. A higher mass flow or lower channel diameter is thus beneficial. However, one should take care that the flow velocity is not too high. Zandbergen [22] gives a relation for an upper limit to the channel gaseous propellant velocity to prevent the so-called water hammer, which is given in Equation 4.11.

$$v_{max} = 175 \left( \frac{1}{\rho} \right)^{0.43} \quad (4.11)$$

### Flow regime

Next to the flow type, one also needs to assess whether the flow regime is fully developed or not. Two types of flow development are known: hydrodynamically and thermally. When a flow is hydrodynamically developed, the velocity profile will be constant throughout the pipe. For thermally developed flow, the thermal profile will not change along the axial direction.

In a particular section at the start of the flow, also called the thermal entrance length, the flow has not yet developed and the thermal profile and thus Nusselt number vary. For laminar flow, the entrance length is estimated by Equation 4.12, while for turbulent flow it is given by Equation 4.13 [48].

$$\frac{L_{T,e}}{D} = 0.05 Re_D Pr \quad (4.12)$$

$$\frac{L_{T,e}}{D} = 10 \quad (4.13)$$

Where  $L_{T,e}$  is the thermal entrance length in m and  $Pr$  is the dimensionless Prandtl number. The number connects the temperature and the velocity profiles [48]. The Prandtl number can be considered almost constant over a large range of temperatures. For gases, it can be approached using Equation 4.14, but the latter Equation 4.15 is more precise. In those equations,  $\gamma$  is the specific heat ratio (dimensionless),  $\mu$  the dynamic viscosity (in  $\text{kg m}^{-1} \text{s}^{-1}$ ),  $c_p$  the specific heat at constant pressure (in  $\text{J kg}^{-1} \text{K}^{-1}$ ) and  $k$  the conductive heat coefficient (in  $\text{W m}^{-1} \text{K}^{-1}$ ).

$$Pr = \frac{4\gamma}{9\gamma - 5} \quad (4.14)$$

$$Pr = \frac{\mu c_p}{k} \quad (4.15)$$

In general, convection heat transfer is higher in the entrance regions. Often, equations for the Nusselt number are averages for the whole pipe length, including the entrance length.

### Geometric disturbances

Next to flow type and development of the flow, non-straight aspects such as bends, valves and turns also affect Nusselt number. Often, they create small vortices, causing the flow to enter a turbulent state even at lower Reynolds numbers. Furthermore, the pressure loss is increased in these bends. Leenders suspects that the bend at the entrance caused a turbulent flow in the channels during his experiments, even at lower Reynolds numbers [3]. Meyers [49] argues that the insertion of elements or the roughening of walls could also enhance heat transfer.

### Channel cross-sectional shape

Nusselt number equations are susceptible to the shape of the channel cross-section. However, this is often mitigated by using the so-called hydraulic diameter  $D_h$  (in m). The hydraulic diameter is determined by Equation 4.16, where  $A$  is the cross-sectional area in  $\text{m}^2$  and  $S$  the wetted perimeter in m of the tube.

$$D_h = \frac{4A}{S} \quad (4.16)$$

The hydraulic diameter is used in equations as the characteristic dimension whenever the tube is non-circular. Notice that for circular channels,  $D_h$  will equal the circle diameter  $D$ . Note that, for turbulent flow, the equations will have an error of approximately 10 %, while for laminar flow the error is larger [22]. Regarding the latter, Incropera et al. [8] advise to use the tabulated values from their Table 8.1.

### Boundary conditions

Two main boundary conditions exist for an RAC: Uniform Wall Temperature (UWT) and Uniform Heat Flux (UHF). The former will be assumed for this model, which simply means that the RAC wall temperature will be considered constant for the whole length of the channel. For laminar flow, the Nusselt number can be considered constant when the flow is fully developed. The values can be found analytically and are given in Equation 4.17 by Meyers [49]. Meyers bases his conclusion on Bergman [48].

$$\begin{aligned} Nu_D &= 4.36(UHF) \\ Nu_D &= 3.66(UWT) \end{aligned} \quad (4.17)$$

Note that these values can only be applied for laminar cases and in case that the entrance length is relatively short. For turbulent flow, no such analytical solution exists. In general, the average Nusselt number over the whole pipe will be higher than the values presented here because of the entrance length.

### Channel layout

The channel layout options influence the convection heat transfer as well. Two options will be implemented in this model, which are linear and spiral tubes. Channels containing a porous medium will not be considered, due to the added complexity.

### Microchannels

The last influence on the Nusselt number discussed here are microchannels. According to Morini [50] (also seen in Das [26]), experiments show that the general Reynolds number limits used to distinguish laminar and turbulent flow can differ for very small channels with a hydraulic diameter lower than 1 mm. Das already mentioned the influence of small channels on the Reynolds number in her thesis [26].

#### Nusselt number for propellant convection

Now that the important aspects have been handled, the equations for the Nusselt number used in the model are presented. The equations will be primarily dependent on the Reynolds number. Because this number is dependent on the temperature of the flow (which is not known), the Reynolds number will be calculated based on the inflow temperature (often 298.15 K) using Equation 4.10. This number will then indicate what equation to use, see below.

First of all, the equations for flow in linear channels will be given. For laminar flow in circular channels, Stephan's Equation 4.18 can be used [51]. It is valid for  $Re_D \leq 2300$  and Prandtl numbers above 0.1.

$$Nu_D = 3.657 + \frac{0.0677 \left( Re_D Pr \frac{D}{L} \right)^{1.33}}{1 + 0.1 Pr \left( Re_D \frac{D}{L} \right)^{0.3}} \quad (4.18)$$

The equation takes the entrance region into account and is valid for uniform wall temperature. Notice that, for increasing channel length  $L$ , the Nusselt number value approaches the value given in Equation 4.17. Stephan's equation gives an average Nusselt number for the whole channel length. Its properties  $Re_D$ ,  $Pr$  and  $k$  (to calculate  $h$  in Equation 4.7) are evaluated at propellant bulk temperature  $T_b$  (see Equation 4.9).

For higher Reynolds number flows in linear channels, the well-known Gnielinski equation given by Rohsenow [52] and Bergman [48] is used to calculate the average Nusselt number. The equation (see 4.19) is applicable for both transitional and turbulent flow in circular tubes for  $0.5 \leq Pr \leq 2000$  and for  $2300 \leq Re_D \leq 5 \times 10^6$ . Other sources such as Taler [53] and Bergman [48] state a higher lower Reynolds number limit, namely  $1 \times 10^4$  and 3000 respectively. The latter source also indicates that the equation may be used for the UWT boundary condition and that errors are generally within 10 %.

$$Nu_D = \frac{\frac{f_{DB}}{8} (Re_D - 1000) Pr}{1 + 12.7 \left( \frac{f_{DB}}{8} \right)^{\frac{1}{2}} \left( Pr^{\frac{2}{3}} - 1 \right)} \quad (4.19)$$

Here,  $f_{DB}$  is the Darcy-Weisbach friction factor (dimensionless) and the subscript "D" stands for the channel circular diameter in m. Several equations exist to calculate the friction factor for transitional and turbulent flow. The one described by Bergman [48] is used, see Equation 4.20. It has an applicable range of  $3000 \leq Re_D \leq 5 \times 10^6$ , although it will be used in the Gnielinski equation downwards to Reynolds numbers of 2300.

$$f_{DB} = (0.790 \ln (Re_D) - 1.64)^{-2} \quad (4.20)$$

Notice that the Gnielinski equation is used for relatively long tubes, where the effect of the entrance region is negligible. Because this is not the case for the RACs considered in this model, the equation can

be modified as stated by Taler [53], see Equation 4.21. By modifying, the Nusselt number is calculated as an average for the whole pipe, including the entrance region.

$$Nu_D = \frac{\frac{f_{DB}}{8} (Re_D - 1000) Pr}{1 + 12.7 \left( \frac{f_{DB}}{8} \right)^{\frac{1}{2}} \left( Pr^{\frac{2}{3}} - 1 \right)} \left( 1 + \left( \frac{D}{L} \right)^{\frac{2}{3}} \right) \quad (4.21)$$

For increasing channel lengths  $L$ , the modified Gnielinski equation will approach the original equation. Also note that the properties dependent on temperature, being  $Re_D$ ,  $Pr$  and  $k$  for calculating  $h$ , are again considered at the bulk temperature  $T_b$ .

For turbulent flow in spiral tubing, Rohsenow [22, 52] states that the amount of accurate equations for the Nusselt number is limited. He shows a relation for developed turbulent flow, Equation 4.22, originally from Seban and McLaughlin [54]. It employs similar variables as the previous equations,  $D_c$  is the spiral diameter in m. Note that this relation is valid for  $1 \times 10^4 \leq Re_D \leq 1 \times 10^5$ . No Prandtl range is given.

$$Nu_D = 0.023 \cdot Re_D^{0.85} \cdot Pr^{0.4} \cdot \left( \frac{D}{D_c} \right)^{0.1} \quad (4.22)$$

For lower Reynolds numbers a relation by Kalb and Seader (from Zandbergen [22]) was found, see Equation 4.23. It is valid for  $0.7 \leq Pr_D \leq 5$ .

$$Nu_D = 0.913 \left( Re_D \left( \frac{D}{D_c} \right)^{0.5} \right)^{0.476} Pr^{0.2} \quad (4.23)$$

Again, both equations for spiral flow are evaluated at bulk temperature, which is a variable for  $Re_D$ ,  $Pr$  and  $k$  for calculating  $h$ . Ferreira gives more information about convection heat transfer in spiral ducts in his thesis [55].

### Propellant outflow temperature calculation

Eventually, all equations from this section will be combined to calculate the outflowing propellant temperature. The bulk temperature  $T_b$  will be taken as the only unknown variable. All equations, being Equations 4.6, 4.7, 4.8, 4.9, 4.10, 4.15 and one of the Nu equations 4.18-4.23, will be rewritten to have this temperature as the only unknown. Next to that, the properties used in these equations ( $k$ ,  $c_p$  and  $\mu$ ) which are added as bulk temperature-dependent equations as well. One last equation is needed to relate the power input from Equation 4.6 to the propellant temperature, which is Equation 4.24.

$$\Delta H = \frac{Q_{conv,x}}{\dot{m}} \quad (4.24)$$

Where  $\dot{m}$  is the mass flow (in  $\text{kg s}^{-1}$ ) and  $\Delta H$  is the change in enthalpy of the propellant in  $\text{J kg}^{-1}$ . This enthalpy increase can then be related to the propellant temperature increase via relations found in NIST<sup>1</sup>. Because there is no closed analytical solution, the Scipy Newton solver from Python will be used to numerically calculate  $T_b$ . Note that the script becomes unstable when the propellant inflow temperature  $T_{p,i}$  is higher than the RAC temperature  $T_{RAC}$ . This should thus be avoided in the inputs.

<sup>1</sup><https://webbook.nist.gov/>, accessed on 11-03-2019.

For small differences it can still be done, but higher differences (more than 50 K difference) will cause the script to crash.

### 4.2.2. Inner cavity convection

In a paper by Paitoonsurikarn et al. [56], a simplified correlation for  $h$  for free convection in cavities was found. The authors compared numerical simulation results (performed in Ansys Fluent) to experimental results. The equations hold for an evenly hot cavity which is horizontally oriented with a side opening, which means that the aperture is neither on the top nor bottom. This has influence on the way the hot air “escapes” the cavity. Starting with Equation 4.5, the Nusselt number can then be found using Equation 4.25. It is dependent on the Rayleigh number (dimensionless) which is defined by Equation 4.26.

$$Nu = 0.00324Ra^{0.447} \quad (4.25)$$

$$Ra = \frac{g\beta\Delta TL_s^3}{\nu\alpha} \quad (4.26)$$

$$T_f = \frac{T_w + T_\infty}{2} \quad (4.27)$$

In the latter equation,  $g$  is the gravitational acceleration in  $\text{m s}^{-2}$ ,  $\beta$  is the thermal expansion coefficient in  $\text{K}^{-1}$ ,  $\nu$  the kinematic viscosity in  $\text{m}^2 \text{s}^{-1}$  and  $\alpha$  the thermal diffusivity, also in  $\text{m}^2 \text{s}^{-1}$ . Note that the latter three are all for the surrounding fluid (air) at film temperature, which is the average of the wall or RAC temperature  $T_w$  and ambient temperature  $T_\infty$ , both in K (see Equation 4.27). The temperature difference mentioned in Equation 4.26 is the actual temperature difference between (bulk) ambient air and the RAC outer wall. Note that no range for Prandtl number is given in the paper, although the equations will only be applied for air as a surrounding medium, so it is assumed to be no issue.

The kinematic viscosity can be calculated by Equation 4.28 [3]. In turn, the found value is used in Equation 4.29 to calculate the thermal diffusivity. The dimensionless Prandtl number  $Pr$  used in that equation is then found by Equation 4.15. The symbols in the next two equations are the dynamic viscosity  $\mu$  (in  $\text{Pa s}$ ), the density  $\rho$  (in  $\text{kg m}^{-3}$ ), specific heat at constant pressure  $c_p$  in  $\text{J kg}^{-1} \text{K}^{-1}$  and  $k$  in  $\text{W m}^{-1} \text{K}^{-1}$ . Note that again, all these values are evaluated for air at the film temperature and ambient pressure, which is one atmosphere. They can be found in NIST<sup>2</sup>.

$$\nu = \frac{\mu}{\rho} \quad (4.28)$$

$$\alpha = \frac{\nu}{Pr} \quad (4.29)$$

The definition for the characteristic length  $L_s$  is given in Equation 4.30. Here,  $\phi$  is the cavity angle (in rad),  $D_{cav}$  the average cavity diameter in m,  $D_{ap}$  the aperture diameter (also in m) and  $L$  the cavity length in m.

<sup>2</sup><https://webbook.nist.gov/>, accessed on 11-03-2019.

$$L_s = (4.79 \cos^{4.43}(\phi) - 0.37 \sin^{0.719}(\phi)) D_{cav} + (1.06 \cos^{3.24}(\phi) - 0.0462 \sin^{0.286}(\phi)) D_{ap} + (7.07 \cos^{5.31}(\phi) + 0.221 \sin^{2.43}(\phi)) L \quad (4.30)$$

These equations hold for cavities with and without aperture and both for conical and cylindrical ones. However, the prediction error can be up to 50%. A recommendation is thus to find empirical relations that fit the experimental results from the paper better. For now, this is used in the theoretical model. Combining all equation from this subsection leads to  $h$ , which can then be used in Equation 4.4.

Note that dynamic viscosity  $\mu$  is dependent on temperature. It can be related via Sutherland's formula [57], see Equation 4.31.

$$\mu = \mu_0 \frac{T_0 + T_S}{T + T_S} \left( \frac{T}{T_0} \right)^{\frac{3}{2}} \quad (4.31)$$

Where  $\mu_0$  (in Pas),  $T_0$  (in K) and  $T_S$  (in K) are all constants and reference temperatures found in Crane [57]. The formula is valid for both propellants (not water) and surrounding air. For water, because it vaporizes at some point and thus the equation above cannot be applied, NIST data<sup>3</sup> was used to extract the relevant  $\mu$  values and create a polynomial in Microsoft Excel.

The specific heat at constant pressure  $c_p$  also changes with temperature for all materials and fluids involved. NIST provides the Shomate equation with coefficients to calculate  $c_p$  when the temperature is known, both for propellant and RAC material. The thermal conductivity  $k$  is seen as linear with respect to the temperature, and the gradients and intersects for the propellants and the material are both again from NIST and Excel. Because NIST does not provide air data, the temperature dependent values for  $c_p$  and  $k$  were extracted from The Engineering Toolbox<sup>4</sup> and polynomials were fitted to the data, again using Excel.

### 4.2.3. Outer wall convection

The convection coefficient for the outer wall is, similar to inner cavity convection, very susceptible to geometry, temperature, surrounding medium and so on. Equations 4.4, 4.5, 4.26, 4.28, 4.29 and 4.15 are reused, but another expression will be used to quantify the Nusselt number  $Nu$ . For a conical geometry this is Equation 4.32 [58], while for a cylindrical shape Equation 4.33 will be used [59]. The subscript "D" in the equations indicates that the used characteristic length  $L_s$  is the (base) diameter  $D$  in m of the cone or cylinder, because the cylinder is horizontal.

$$Nu_{con} = 0.7 + 0.35 (Ra_D)^{0.125} + 0.51 (Ra_D)^{0.25} \quad (4.32)$$

<sup>3</sup><https://webbook.nist.gov/>, accessed on 11-03-2019.

<sup>4</sup><https://www.engineeringtoolbox.com>, accessed on 07-08-2020.

$$Nu_{cyl} = \frac{2}{\ln \left( 1 + \frac{2}{\left( \left( 0.518 Ra_D^{\frac{1}{4}} \left( 1 + \left( \frac{0.559}{Pr} \right)^{\frac{3}{5}} \right)^{\frac{-5}{12}} \right)^{15} + \left( 0.1 Ra_D^{\frac{1}{3}} \right)^{15} \right)^{\frac{1}{15}}} \right)} \quad (4.33)$$

Note that the resulting Nusselt number will be used as an average for the whole outer area of the cone or cylinder, including any end caps and apertures present. The area  $A$  in Equation 4.4 will be adjusted to include these surfaces and exclude the apertures.

Again, the resulting outer wall convection heat transfer has its errors compared to the real experimental data. For now, the equations from this subsection are used, but it is recommended to update them accordingly.

## 4.3. Radiation

Radiation is the heat transfer from a hot to a cold object without the use of a medium, in contrast to conduction and convection which require a medium to transfer heat energy. One calculates the outgoing radiation heat transfer  $Q_{rad}$  (in W) of an object by Equation 4.34.

$$Q_{rad} = \epsilon \sigma A (T_1^4 - T_0^4) \quad (4.34)$$

Here,  $\epsilon$  is the object's emissivity (dimensionless), which is dependent on the material and coating used. A so-called blackbody has an emissivity of 1, while grey objects have one between 0 and 1.  $\sigma$  is the Stefan-Boltzmann constant ( $\text{W}/\text{m}^2/\text{K}^4$ ). The object of temperature  $T_1$  (in K) is completely surrounded by an object of temperature of  $T_0$  (in K) for this equation to be true.

Both cavity and outer wall will experience radiation. The outer wall will be hotter than its surroundings, so there will be outgoing radiation. The inner cavity will have the same, but it will also be the location where power flows in via focused (solar) radiation, which is the working principle for STP. First, the inner cavity radiation will be discussed (starting with the outgoing radiation and then the incoming irradiation), followed by the outer wall outgoing radiation.

Note that, in this section, it will be assumed that all walls are grey, meaning that all walls will radiate heat uniformly and diffusely (in all directions). This is in opposition to direct radiation, which is unidirectional.

### 4.3.1. Inner cavity radiation

The inside of the RAC will experience both outgoing radiation loss and incoming irradiation, as will be explained in the next two subsections.

#### Outgoing cavity radiation

Once the heat exchanger starts heating up, its inner wall will have a higher temperature when compared to its surroundings. It will start to radiate heat, which in this case can be considered diffuse (in all

directions). However, only the radiation going in the direction of the cooler aperture or opening will contribute to radiation loss. Thus, view factors need to be applied, which indicate the amount of radiation towards a specific wall. The factors  $F$  themselves are dimensionless. For various geometrical figures, Howell has derived the relevant view factor equations<sup>5</sup>.

### Cone

For the cone, only one surface (the inner cone wall, called surface 1) will radiate heat towards the base (surface 2), see Figure 4.1. If the aperture (or opening), called surface 3, does not cover the whole base, the remaining inner wall next to the aperture (still surface 2) will have the shape of a ring. The aperture is not shown in the figure, but it has a circular shape and is located in the middle.

The expression for the view factor from surface 1 to 1 (thus, to itself) is derived from Howell's expression C-110 and is shown as Equation 4.35. The expression for the view factor from surface 1 to surface 3 is derived from Howell's expression C-117 and is found in Equation 4.36. From deduction, the expression for the view factor from surface 1 to the remaining ring surface 2 is found in Equation 4.37. The inner surface 2 can only radiate towards surface 1, as it is in the same plane as the aperture, hence Equation 4.38.

In all those equations, the parameter  $r$  is the radius of the base,  $r_3$  is the aperture radius and  $h$  is the height (length) of the cone. All parameters are in m.

$$F_{1-1,cone} = 1 - \left( \frac{1}{1 + H^2} \right)^{\frac{1}{2}}, \quad H = \frac{h}{r} \quad (4.35)$$

$$F_{1-3,cone} = \frac{R^2}{(1 + H^2)^{\frac{1}{2}}}, \quad R = \frac{r_3}{r}, \quad H = \frac{h}{r} \quad (4.36)$$

$$F_{1-2,cone} = 1 - F_{1-1,cone} - F_{1-3,cone} \quad (4.37)$$

$$F_{2-1,cone} = 1 \quad (4.38)$$

### Cylinder

For a cylinder, two surfaces radiate towards the aperture: the cylinder inner wall (surface 2 in Figure 4.2) and the base wall (surface 3, not shown). Both their view factors towards the aperture (surface 1) have been derived from C-41 and C-82 from Howell and are displayed in Equations 4.39 and 4.40 respectively. All parameters are shown in Figure 4.2 and are again in m.

$$F_{2-1,cyl} = \frac{1 - H^2 - R^2 + (X^2 - 4R^2)^{\frac{1}{2}}}{4RH}, \quad R = \frac{r_1}{r_2}, \quad H = \frac{h}{r_2}, \quad X = H^2 + r^2 + 1 \quad (4.39)$$

$$F_{3-1,cyl} = \frac{1}{2} \left( X - \left( X^2 - 4 \left( \frac{R_3}{R_1} \right)^2 \right)^{\frac{1}{2}} \right), \quad R_1 = \frac{r_1}{h}, \quad R_3 = \frac{r_3}{h}, \quad X = 1 + \frac{1 + R_3^2}{R_1^2} \quad (4.40)$$

<sup>5</sup><https://web.engr.uky.edu/rtl/Catalog/>, accessed on 17-07-2020.

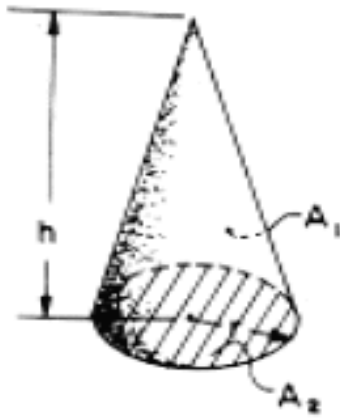


Figure 4.1: Cone with surfaces 1 and 2. Surface 3, the aperture, is not shown.

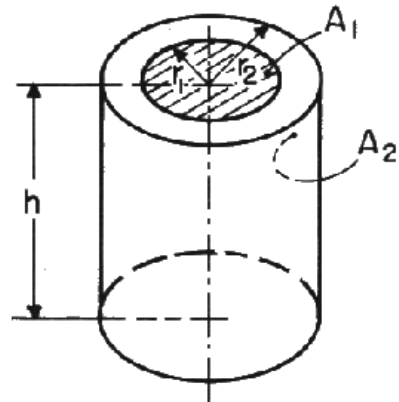


Figure 4.2: Cylinder with surfaces 1 and 2. Surface 3, the bottom wall is not indicated.

Now that the view factors are known for both geometrical figures, one can calculate the radiation loss using the general Equation 4.34, multiplied by the view factor. Note however, that outgoing radiation can also radiate towards other inner walls. Once it reaches this other wall, it will be partly absorbed and partly reflected, according to Equation 4.41 for opaque walls.

$$\rho + \alpha = 1 \quad (4.41)$$

Where  $\rho$  is the dimensionless reflectivity and  $\alpha$  is the dimensionless absorptivity. Note that, according to Kirchhoff's law,  $\alpha$  and emissivity  $\epsilon$  are equal at some specific known temperature and wave length [22]. However, if both are known, one can take the more accurate  $\alpha$ .

Thus, when using multiple inner walls, one starts off with radiation emission from multiple walls, which radiate diffusely and uniformly. The energy partly leaves the system via the aperture but can also fall upon another wall, where the process of absorption and reflection repeats. Python can loop a few times through this process numerically, to approach the final radiation loss from the inner cavity. Conversely, one could use Gebhart factors (also used by Leenders).

### Incoming cavity radiation

The incoming power of the RAC will be absorbed by the cavity wall according to Equation 4.42. Here,  $\alpha$  is the absorptivity (dimensionless), dependent on material, coating and radiation wave length.

$$Q_{in} = \alpha Q_{rad,in} \quad (4.42)$$

However, for an RAC it is not as simple as applying Equation 4.42. The non-absorbed energy will be reflected, as only opaque materials will be used which do not transmit the incoming radiation. The reflected energy will partly exit the system, but a part will again fall on an (opposite) wall, repeating the cycle. View factors  $F$  (dimensionless) again come into play here, as they indicate the amount of outgoing radiation which falls on another wall (to be absorbed). However, view factors are only applicable in case of a diffuse emitting wall, which radiates in all directions. Calculating the resulting radiation input can be achieved by making a ray tracing model (see e.g. the thesis by Das [26]), but

that will be out of the scope for this thesis. So, the assumption is made that the incoming irradiation will be reflected diffusely. In that case, the same method as in the previous subsection will be applied: Python will calculate the radiation gain by looping through a series of radiation absorption, reflection and loss per wall, using the view factors.

It is recommended for future users of this theoretical model to construct the aforementioned tool in order to find **RAC** shape influences on the radiation absorbed power. When that happens, design choices such as a spike can also be evaluated. Needless to say, reducing the aperture area will decrease the radiation and convection loss.

### 4.3.2. Outer wall radiation

For the outer wall, radiation is simply calculated by Equation 4.34. In case that no insulation is applied, the outer wall temperature is the **RAC** temperature. If insulation is present, the temperature of outer wall of the insulation layer is chosen.

### 4.3.3. Area

The involved area of heat transfer is very important, as the amount of power transferred depends on it linearly, see the sections on radiation and conduction. For the two geometrical figures discussed here, the inner and outer areas can easily be determined by simple formulas. However, often in real life the applicable area is much larger than the calculated area, due to the addition of connectors, thicker walls, more insulation etcetera. For instance, in the cases discussed hereafter in this chapter, the calculated outer **RAC** area was  $0.0028 \text{ m}^2$  while the actual area equaled  $0.0039 \text{ m}^2$ . This is a huge difference, which makes the model output inaccurate temperatures for **RAC** and propellant.

For this model, it is chosen to keep the calculation of areas in there. However, one can override these values by simply adding the areas themselves manually.

## 4.4. Conduction

Conduction  $Q_{cond}$  is the transfer of heat energy through a stationary medium because of temperature differences inside the medium [22]. It is dependent on a material's property, temperature variation and shape, see the next general Equation 4.43.

$$Q_{cond} = k \cdot A \cdot \frac{\Delta T}{t} \quad (4.43)$$

Where  $k$  is the material's thermal conductivity in  $\text{W m}^{-1} \text{ K}^{-1}$ ,  $A$  the area in  $\text{m}^2$ ,  $\Delta T$  the temperature difference (in K) between a hot and cold wall and  $t$  the wall thickness in m.

The conduction for this model will only be considered in case that insulation is applied. It is assumed that the spread of heat through the **RAC** will be instantaneous as it is made of high-conductive material. The assumption holds well in case copper is used, as the four thermocouples Leenders attached to his **RAC** all outputted temperatures close to each other [3].

In case insulation is used, an extra temperature parameter is added (the insulation wall temperature) to the model. In order to calculate this temperature and thus the outer wall losses in the form of convection and radiation, the conduction through the insulation wall will be equated to the outer wall convection and radiation losses. See Equation 4.44.

$$Q_{cond,insu} = Q_{conv} + Q_{rad} \quad (4.44)$$

For a cylinder, Equation 4.45 can be applied to calculate the conductive heat transfer [22]. Unfortunately, no such equation exists for conically shaped insulation, so this equation will apply for that as well.

$$Q_{cond,insu,cylinder} = \frac{2\pi k L}{\ln\left(\frac{R_o}{R_i}\right)} \Delta T \quad (4.45)$$

Where  $R_o$  is the outer cylinder radius (in m),  $R_i$  the inner one (in m),  $L$  is the cylinder length (in m). Note that  $k$  is the thermal conductivity of the insulation in  $\text{W m}^{-1} \text{K}^{-1}$ . It varies with temperature, Equation 4.46 was found by Leenders for the Saffil M-Fil insulation by fitting an exponential line using Excel.

$$k = 0.0665 \cdot e^{\left(0.0015 \frac{T_{RAC} + T_{insu}}{2} - 273.15\right)} \quad (4.46)$$

Equation 4.43 then can be transformed to Equation 4.47.

$$\frac{2\pi k L}{\ln\left(\frac{R_o}{R_i}\right)} (T_{RAC} - T_{insu}) = hA (T_{insu} - T_{amb}) + \epsilon_{insu} \sigma A (T_{insu}^4 - T_{amb}^4) \quad (4.47)$$

There is no closed analytical solution for Equation 4.47, but Python can solve it numerically for the insulation temperature  $T_{insu}$  (in K). Afterwards, the convection and radiation loss from the insulation wall can be calculated.

## 4.5. Pressure loss

The model will operate at a certain constant starting pressure as it enters the RAC channels, where it will experience a pressure loss. Note that only the pressure loss in the RAC tubes will be calculated. The pressure loss in the tubing between feed system inlet and RAC inlet and in the nozzle is not considered. This section is not verified nor is it validated, because attention is focused on the thermal part of the RAC. It will only show the pressure loss in the channels as a first estimate.

The pressure drop  $\Delta p$  (in Pa) in the channel(s) can be found using the Darcy-Weisbach equation (see 4.48) [22] for smooth piping.

$$\Delta p = f_{DB} \frac{L}{D} \frac{1}{2} \rho v^2 \quad (4.48)$$

Where  $f_{DB}$  is the Darcy-Weisbach friction factor (dimensionless),  $L$  is the characteristic length (here: tube length) in m,  $D$  is the tube inner diameter in m,  $\rho$  is the propellant density in  $\text{kg m}^{-3}$  and  $v$  is the velocity in  $\text{m s}^{-1}$ .

The friction factor is dependent on the Reynolds number  $Re$  (based on tube diameter) and several equations exist for both laminar and turbulent flow. For laminar flow in straight pipes (lower Reynolds numbers), the equation by Poisseuille [22, 60] is used, see Equation 4.49.

$$f_{DB} = \frac{64}{Re_D} \quad (4.49)$$

The equation for turbulent flow in straight pipes for range  $2300 \leq Re_D \leq 2 \times 10^4$  was given earlier in Equation 4.20, but will be repeated here in Equation 4.50 for clarity.

$$f_{DB} = (0.790 \ln(Re_D) - 1.64)^{-2} \quad (4.50)$$

For laminar flow in spiral tubing, Equation 4.51 from White is recommended by Guo [60] and Zandbergen [22].

$$f_{DB} = \frac{1}{1 - \left( 1 - \left( \frac{11.6}{Re_D \cdot \left( \frac{D}{D_c} \right)^{0.5}} \right)^{0.45} \right)^{\frac{1}{0.45}}} \cdot \frac{64}{Re_D} \quad (4.51)$$

For turbulent flow in spiral piping, the relation in Equation 4.52 will be used. It was found by Ito and recommended by Guo [60] and Zandbergen [22].

$$f_{DB} = 0.304 Re_D^{-0.25} + 0.029 \left( \frac{D}{D_c} \right)^{0.5} \quad (4.52)$$

$$Re_{D,cr} = 20000 \left( \frac{D}{D_c} \right)^{0.32} \quad (4.53)$$

Where  $Re_D$  can be found using Equation 4.10.  $D$  is the tube diameter in m and  $D_c$  is the spiral diameter in m. The division of the laminar and turbulent regions in spiral flow will be at the critical Reynolds number from Equation 4.53 [60], where laminar flow occurs below that number and turbulent flow above. The Reynolds number for the friction factor calculation will be evaluated at bulk temperature  $T_b$ .

## 4.6. Thrust

This section will deal with the generated thrust from the engine, for which IRT relations will be used [22]. IRT assumes (among others) that the propellant is a perfect gas, that the composition is homogeneous, that the nozzle flow is steady and isentropic and that the propellant experiences no external forces. Furthermore, the nozzle is assumed to experience choked flow. Again, this section is not verified nor validated, but serves just as an idea to know the ballpark of the generated thrust.

Note that nozzles are normally designed for one specific set of propellant properties. When the final propellant pressure, temperature and mass flow are known, one can calculate the nozzle dimensions (primarily throat and exit area) according to IRT. However, in this model the temperature will vary greatly at start-up, so the throat and exit area will follow this variation. In reality, the throat and exit area are fixed of course. At some point, the model will achieve thermal equilibrium, so when using the model for first nozzle dimension estimates, it is best to use the values associated with this equilibrium.

The thrust  $F$  in N is given as:

$$F = \dot{m}U_{eq} \quad (4.54)$$

$\dot{m}$  is the propellant mass flow in  $\text{kg s}^{-1}$ .  $U_{eq}$  is the equivalent exhaust velocity in  $\text{m s}^{-1}$  and can be calculated by:

$$U_{eq} = U_e + \frac{p_e - p_{amb}}{\dot{m}} A_e \quad (4.55)$$

Where  $U_e$  is the exhaust velocity in  $\text{m s}^{-1}$ ,  $p_e$  is the nozzle exit pressure in Pa,  $p_{amb}$  is the ambient pressure in Pa and  $A_e$  is the nozzle exit area in  $\text{m}^2$ . For the exhaust velocity, the equation is:

$$U_e = \sqrt{2 \frac{\gamma}{\gamma-1} \frac{R_A}{MM} T_c \left( 1 - \left( \frac{p_e}{p_c} \right)^{\frac{\gamma-1}{\gamma}} \right)} \quad (4.56)$$

Where  $\gamma$  is the specific heat ratio (dimensionless),  $R_A$  is the universal gas constant in  $\text{J mol}^{-1} \text{K}^{-1}$ ,  $MM$  is the molar mass of the propellant in  $\text{kg mol}^{-1}$ ,  $p_c$  is the chamber pressure in Pa and  $T_c$  is the propellant chamber temperature in K. This temperature equals the RAC propellant output temperature, as it is assumed that there are no thermal losses in the propellant flow from RAC to nozzle. The specific impulse  $I_{sp}$  can then be found by:

$$I_{sp} = \frac{U_{eq}}{g_0} \quad (4.57)$$

Where  $g_0$  is the sea level gravitational acceleration. For choked flow, one can calculate the throat area using Equation 4.58.

$$\dot{m} = \frac{\Gamma p_c A_t}{\sqrt{\frac{R_A}{MM} T_c}} \quad (4.58)$$

Here,  $A_t$  is the nozzle throat area (in m) and  $\Gamma$  is the Vandenkerckhove function (dimensionless), calculated by Equation 4.59.

$$\Gamma = \sqrt{\gamma} \left( \frac{2}{\gamma+1} \right)^{\frac{\gamma+1}{2(\gamma-1)}} \quad (4.59)$$

It is assumed that the nozzle has ideal expansion at SL, so the ambient pressure equals the exit pressure. The nozzle exit area  $A_e$  can then be found using Equation 4.60.

$$\frac{A_e}{A_t} = \frac{\Gamma}{\sqrt{\frac{2\gamma}{\gamma-1} \left( \frac{p_e}{p_c} \right)^{\frac{2}{\gamma}} \left( 1 - \left( \frac{p_e}{p_c} \right)^{\frac{\gamma-1}{\gamma}} \right)}} \quad (4.60)$$

One should note that the above equations are all based on IRT. No quality factors were applied, but they indicate that the "quality of the motor" will be around 80-98 % of the ideal situation [22]. Furthermore, especially at low thrust levels (and thus mass flows), one should take care to use the assumption of inviscous flow. When the Reynolds number (see Equation 4.61) drops below 10 000, a laminar boundary layer occurs in the throat and a corresponding discharge coefficient discharge coefficient  $C_d$  (dimensionless) will be applied. For the test cases, the throat Reynolds number is in the range of  $9000 \leq Re_t \leq 11\,000$ , depending on the propellant temperature. For now, the laminar boundary layer will not be considered. Further information for the quality factors can be found in Zandbergen [22] and Johnson [61].

$$Re_t = \frac{4\dot{m}}{\pi\mu D_t} \quad (4.61)$$

The model will take the chamber pressure, temperature and mass flow as inputs. From this, the nozzle throat area and then the nozzle exit area can be calculated. Then, the equivalent velocity will be calculated, which in turn gives the thrust and specific impulse. Note that ideal expansion at vacuum is, in reality, not possible as it requires an infinitely long nozzle to expand the gas to vacuum.

# 5

## Thruster design

This chapter will elaborate on the design of the STP engine, [STT2](#). First, the design process is laid out in a brief section, followed by an extensive part on the thruster design. This section will be divided into multiple subsections, each addressing a certain part of the motor. The aspects discussed are: the propellant, concentrator subsystem, the heat exchanger and nozzle. After the thruster is designed, an overview of the projected cost for manufacturing and testing is given. In the end, an [RAC](#) design mistake that will have a huge impact on the further course of the thesis will be brought forward.

### 5.1. Design process

When designing a thermal rocket, one usually starts off with the type of mission for which the system is meant. The mission will dictate a number of important factors, such as the needed change in velocity  $\Delta V$  (Tsiolkovsky Rocket Equation), mission duration, ambient properties and mass and volume restrictions. From those requirements, one can derive the thrust at which the engine should operate (most of the time) and the efficiency ( $I_{sp}$ ) at which the propellant is expelled. The higher the efficiency, the less propellant a spacecraft has to bring. Note that trade-offs are required here; saving 1 kg of mass in propellant is welcomed but not beneficial if the total thruster mass is increased by more than 1 kg to retrieve this reduction. This is not unthinkable in [STP](#) systems: one could increase the [RAC](#) mass and volume to heat the propellant to a higher temperature but this does not always pay-off.

Equation [2.8](#) relates the mass flow to the chamber pressure when the nozzle experiences choked flow. When designing an [STP](#) thruster system, one should take note that a chosen mass flow, from which the propellant temperature in the [RAC](#) can be derived, will dictate the chamber pressure at a certain throat area. Because the exit pressure should ideally be close to the ambient pressure, the area ratio and hence the nozzle exit area are also a result of the chamber pressure. Then, the chamber pressure "will work its way back" through the [RAC](#) (having a small pressure loss), which then sets the pressure at which the gas cylinder will release the propellant. In other words, the whole system is connected in terms of pressure and once the nozzle dimensions and mass flow are chosen, the pressure will follow suit. Altering certain variables, be it the mass flow, input power or ambient properties will see the engine not operating at the ideal conditions and thus suffer performance losses.

From the thrust and specific impulse, the mass flow and equivalent exhaust velocity are determined through [IRT](#). As explained above, one then aims for ideal nozzle expansion so that the nozzle exit pressure is equal to the ambient pressure. One should also start looking into possible propellants at this stage; the molar mass is especially important, but density, cost, storability, toxicity, heat capacity and other factors also play a role here, as could be seen in Chapter [2](#).

Only four main variables miss out at this point: chamber temperature, chamber pressure, throat area and exit area. The chamber temperature in **STP** is dependent on the mass flow, propellant's heat capacity (or better: enthalpy), the input power and the **RAC** thermal efficiency via Equation 2.6. Once the chamber temperature is known, the other three variables can be derived via Equations 2.1, 2.3 and 2.8. The feed pressure will simply be the chamber pressure plus the pressure loss occurring in the **RAC** and connection pieces. What becomes apparent is that a chosen mass flow for a thruster system will also mean that the feed pressure is a given factor, solely relying on the already designed thruster; this can be seen in Leenders's data (Table 2.1), where the increased mass flow also saw the feed pressure increased. Note that the propellant is to be stored at a higher pressure than the required feed pressure; in case it is not, the mass flow cannot reach the desired level and the user runs the risk of lower performance or even subsonic nozzle flow.

## 5.2. Thruster design

Per requirement, **STT2** will consist of three main components: concentrator, **RAC** and nozzle. This section will detail the designs for those parts, but it will kickoff by choosing a propellant. A separate heat storage is not considered because of the added complexity, but the heat exchanger could serve as some sort of heat storage on its own if it is first heated and then used to heat the propellant. Because of the same reason, the engine will not provide power, but solely focus on creating thrust.

### 5.2.1. Propellant choice

There are a number of recurring propellant options that are considered in literature. A propellant in solar thermal propulsion preferably has low molar mass, high density, low heat capacity and high thermal conductivity. A low molar mass ensures a higher specific impulse (Equation 2.3), while a high density is required in order to keep the volume low. For instance hydrogen is an excellent propellant in terms of efficiency, but is very hard to store due to its low density. To remedy this, the gas is liquefied by bringing it sub 20 K temperatures in combination with high pressure. This brings additional challenges in storing this propellant. A low heat capacity is important in that less power is required to bring the propellant to a certain temperature level; a high thermal conductivity ensures the fast heat transfer from **RAC** to propellant.

Next to the four aspects described above, cost, toxicity, corrosion, two-phase flow and availability also play a role when a propellant is selected. A small overview of the most-used propellants in **STP** demonstrators is given in Table 5.1, next to the more conventional water, nitrogen and carbon dioxide. Only molar mass, required enthalpy and density are considered, while most other aspects are reflected in the remarks column. Propellant properties are taken from **NIST** at room temperature and sea level pressure<sup>1</sup>. The enthalpy increase is the energy required to bring one kilogram of the propellant from room temperature to the aforementioned 835.3 K. The density of water naturally is a few magnitudes larger due to it being in a liquid state at room temperature; as such, latent heat is required to bring the propellant to a gaseous state, which accounts for a significant 64.1 % of the needed 3518 kJ kg<sup>-1</sup>.

The table immediately shows that hydrogen and ammonia are no option for this practical study. It is not allowed to test them in the **AE** cleanroom. Four other propellants remain. Helium does best when it comes to specific impulse followed by water, while carbon dioxide and nitrogen do better when it comes to thermal efficiency. Water has the disadvantage that it can be corrosive to the heat exchanger material and has hard-to-predict two-phase flow. All four are feasible as a propellant, but nitrogen is eventually chosen for testing because of three reasons: the availability (bottles are present in the **AE** cleanroom), low cost and to allow for comparison with Leenders's heat exchanger. However, the engine could also be used for other propellants, but the nozzle will most likely not be adapted in those tests due to the different propellant properties.

<sup>1</sup><https://webbook.nist.gov/>, accessed on 11-03-2019.

Table 5.1: Propellant properties (see NIST footnote).

Propellant	Molar mass [g/mol]	Enthalpy increase [kJ/kg]	Density [kg/m3]	Remarks
<b>Hydrogen (g)</b>	2.02	7814	0.082	Highly flammable
<b>Ammonia (g)</b>	17.03	1003	0.704	Toxic
<b>Helium (g)</b>	4.00	2789	0.164	Inert
<b>Carbon dioxide (g)</b>	44.01	561	1.808	-
<b>Water (l)</b>	18.02	3518	997.1	Corrosive, two-phase flow
<b>Nitrogen (g)</b>	28.01	557	1.145	Relatively inert

### 5.2.2. Concentrator subsystem design

The concentrator subsystem is interwoven with the choice for the heat source. As of now, three heat sources could be identified with the help of the literature study [62]: the Sun, a theater lamp and the high powered welding laser faculty at Faculty of Mechanical, Maritime and Materials Engineering (3mE).

In terms of power, solar irradiation is the most promising, as in theory a large concentrator system could be used to provide enormous amounts of power. On a sunny day, the global irradiation in The Netherlands is  $1000\text{-}1100 \text{ W m}^{-2}$  for multiple hours<sup>2</sup>. However, designing and constructing a dedicated solar collector is a time-consuming task, deserving of its own thesis. Pino concluded a project on an inflatable solar concentrator, but the result could only provide 6.1 W of power at an efficiency of 5.8 % with the theater lamp as a heat source [45]. It would thus not be viable to try Pino's design in a larger format, it would require an enormous area to collect the necessary 250 W. An uninflatable version of the design would relax the requirements, but if one succeeds to concentrate enough solar irradiation through the use of mirrors and lenses, other considerations arise; the use of solar light makes testing much more complex, as you become reliant on weather conditions. Furthermore, you cannot control the amount of power flowing in and equipment and test results could suffer from wind and rain if done outdoors. A huge advantage of using solar light would be that it naturally will be the power source once STP is implemented on spacecraft.

The theater lamp was used by Leenders and Pino in their theses and is rated at 1000 W. Leenders calculated that at a distance of 148 cm the lamp emits 240 W of power. However, only 49 W did reach the heat exchanger in Leenders's test runs when one lens was used. For Pino, the value that reached the relatively large concentrator was 106 W due to his setup. As such, reaching 250 W of input on a small object seems to be near impossible with the theater lamp.

The third and eventually chosen option was the use of the welding laser facility, located at the faculty of 3mE. The Nd:YAG laser can output a beam of 50 to 8000 W with steps of 1 W. The beam has a focus diameter of 0.20 mm but by placing an object in a defocused position along the beam the diameter can be as large as 50 mm. This is fortunate because delivering a large amount of energy in a small spot will likely cause melting issues. The wave length of the beam is 1064 nm. pocket meter (PMT 70icu) is present at the facility in order to determine the power output accurately. Next to that, the laser has the advantage that it does not require a concentrator subsystem but can directly heat the RAC. Furthermore, the power can be controlled and the expelled propellant can be dispersed of by the suction system. Two disadvantages are that the laser does not have a similar spectrum as solar irradiance and that the experiments have to be performed at 3mE, so the vacuum oven from AE cannot be used and the experiments have to be done in ambient. It was already doubtful if any system would fit inside the oven.

The advantages outshine the disadvantages so the laser will be chosen heat source. After consulting welding technician Jurriaan van Slingerland and Prof. Dr. Ian Richardson of the department of Materials Science and Engineering, they approved of the idea. Note that there are more facilities at DUT with

<sup>2</sup><https://solargis.com/maps-and-gis-data/download/netherlands>, accessed on 22-11-2020.

laser systems installed. See the literature study [27] for an overview. For this project, a concentrator subsystem will not be designed for this project. Instead, more attention can be given to the thermal heat exchanger and nozzle.

### 5.2.3. Receiver-Absorber Cavity design

This subsection will see the design of the heat exchanger. First, the material will be chosen, which is followed by the RAC configuration, shape and the dimensions.

#### RAC material

The material for the heat exchanger will be evaluated by the following criteria: thermal conductivity, density, melting point, heat capacity and manufacturability. Ideally, the material has a high thermal conductivity in combination with a low heat capacity so that heat can spread at a fast rate through the rate and the propellant can be heated at a larger area. Next to that, the material needs to withstand high temperatures without melting, have a low density in order to reduce mass and be manufacturable. The latter also incorporates the cost of the material. Emissivity is not a criterion, because the material can be coated in high-absorptive paint.

From literature, molybdenum, rhenium and tungsten are good candidates. Together with the more conventional steel, iron, copper, brass and aluminium, their properties are shown in Table 5.2. Properties are retrieved from The Engineering Toolbox<sup>3</sup>. At first glance, the more 'exotic' materials perform best. However, they are either expensive, hard to manufacture or hard to find in the right shape. From the conventional materials, brass and aluminium do not suffice due to their low melting points. Out of steel, iron and copper, copper has the best chances, due to its significantly higher thermal conductivity at the cost of higher density and thus mass. Its heat capacity is also lower, which allows the RAC to reach its maximum temperature earlier during start-up.

Table 5.2: Material properties (see footnote).

Material	Thermal conductivity [W/m <sup>2</sup> /K]	Density [kg/m <sup>3</sup> ]	Melting point [K]	Heat capacity [J/kg/K]
<b>Molybdenum</b>	139 (at 273 K)	10188	2893	272
<b>Rhenium</b>	48.6 (at 273 K)	20800	3459	140
<b>Tungsten</b>	182 (at 273 K)	19600	3673	132
<b>Steel (stainless)</b>	14.3 (at 293 K)	7480-8000	1783	490
<b>Iron (wrought)</b>	59 (at 293 K)	7750	1755-1866	449
<b>Copper</b>	401 (at 273 K)	8940	1357	385
<b>Brass (red)</b>	61 (at 293 K)	8400-8730	1000	375
<b>Aluminium</b>	236 (at 273 K)	2712	933	897

#### RAC configuration

For the heat exchanger, three main configurations are discussed [3, 26, 27]:

- Direct propulsion with direct absorption
- Direct propulsion with indirect absorption
- Indirect propulsion with indirect absorption

<sup>3</sup><https://www.engineeringtoolbox.com>, accessed on 07-08-2020.

The terms were already explained in Chapter 2; in direct absorption, the propellant is heated without any physical wall between the irradiation source and the propellant. One can think of a transparent windowed cavity with a rotating bed of seeds [63] (see also Chapter 2). Indirect absorption does have a barrier. Direct propulsion implies that the heat directly flows to the propellant and is not stored in RAC or dedicated thermal storage to release at a later stage. Indirect propulsion on the other hand profits from accumulated energy and the propellant can thus reach higher temperatures once fired, bringing higher specific impulses but at the cost of increased complexity and time constraints.

The literature study already explored the three configurations [62]: the direct propulsion with indirect absorption heat exchanger was chosen, because it is the least complex and it was recommended by multiple (student) researchers, including Shoji [63], Leenders [3], Preijde [64] and Das [26]. One of the mentioned reasons is that it is simpler because it does not have to have a transparent window nor does it need to have a separate heat storage. Instead, the heat exchanger can be of a single material, which reduces the risk of thermal stresses and connection issues. Indirect absorption also has less pressure drop than direct absorption [26]. A huge advantage of direct absorption with the help of the rotating bed of seeds is that higher temperatures than the wall material's melting point could be reached, which is in excess of 2500 K. However, this project will not handle temperatures higher than 1000 K, mostly due to the limitations in material manufacturing (see later subsection) and pressure sensor handling. The advantage is thus not valid here.

Choosing the direct propulsion with indirect absorption configuration will also leave some room to explore indirect propulsion, where the RAC is heated first while the propellant enters later. In that way, even higher efficiencies could be reached. One should stay aware of the possibility of material melting though.

### RAC shape

A direct propulsion with indirect absorption heat exchanger can be designed with or without a cavity (flat plate). Constructing the RAC without a cavity is not deemed feasible, due to the high reflectivity losses inherent to the option. Furthermore, the focused light will fall on one spot of the flat plate, which brings the problem of local heat build up with melting as a result or in other words, poor heat distribution. An advantage is that it is easy to manufacture. Literature however, favors the cavities [3, 26, 63, 64], often with fiber optic cables. This is due to the most important reason, the reduced mass.

For cavity heat exchangers, there are three options: a conical, cylindrical or spherical cavity. Cavities have the major advantage that the effective heating area is increased; the propellant needs to traverse a longer path around the RAC, which does not necessarily mean that the heat exchanger becomes heavier. One can simply leave the inner room empty. Furthermore, a cavity is an excellent shape for the current heat source, a laser with a tiny focal point. The beam can fall through an aperture in a lid which is located at the start of the cavity and then widen (remember that a laser is not entirely collimated), increasing the heat distribution width. As such, a lid with aperture will be part of the design, because the trade-off between the small mass increase due to the lid and the decreased convection and radiation losses is in favour of the latter. Preijde concluded so, but Leenders never mentioned a lid. That is mostly due to the heat source, which still had a sizable beam focus diameter of 2 cm, even after the lens was included in the system design. A lid would thus not be beneficial but even increase the heat losses, because part of the beam would fall on the outside of the lid and only increase radiation and convection losses. In general, the smaller the lid aperture, the lower the convection and radiation losses [56]. However, one needs to be aware that the aperture should allow (most of) the beam to pass to the cavity.

The three cavity options were extensively traded-off by both Shoji [63] as Preijde [64]. Both concluded that a cylindrical, lidded heat exchanger would be best option. It is not deemed necessary by the author to redo these trade-offs, but a summary will be given of what Preijde found. Shoji in this regard is less reliable, because he modelled the irradiation beam as non-focused; as such, he

invented unconventional shapes, such as a horn or outer disc, which only serves to increase the area upon which the beam falls. This only marginally increased the thermal efficiency though. Preijde on the other hand, did an extensive trade-off between six concepts, each of the cavity options twice with alternatingly ammonia and hydrogen as propellant. The trade-off had six criteria: specific impulse, system-specific impulse, thrust, wet system mass fraction, system volume and system complexity. Preijde built an optimization tool which, with the input of variables such as orbit altitude, solar flux and mass, could automatically calculate those criteria for each concept. For this thesis, the system-specific impulse, wet system mass fraction, system volume and system complexity are important. In the first three categories, the spherical RAC does outperform the other two by a small amount. This is due to the excellent temperature distribution and the high area-to-volume ratio of a sphere. However, when looking at system complexity, or in other words manufacturability, the spherical heat exchanger loses its advantage completely with regards to the other two shapes. Constructing a sphere with etched-out channels is extremely hard, especially when the maker has to rely on DUT workshop machinery. The high area-to-volume ratio of a sphere is also partly mitigated due to the fact that one can hardly fit anything else in the available space outside the sphere; it is not convenient at all.

The latter argument also holds for the conical cavity; although the light distribution is slightly better when compared to the cylindrical cavity, the available space outside the cone is not easy to use. Widening a cone to a cylinder will thus increase the mass by a small amount but increase the channel length, which increases the thermal efficiency. Furthermore, a cylinder is easy to construct on a lathe, while a cone is harder because you cannot secure it to the lathe easily. So mainly because of the low complexity combined with a more than reasonable performance, the lidded cylinder will be chosen as the RAC shape. This is also supported by Shoji and Preijde as earlier mentioned, but not by Leenders who designed a cone. In Leenders's trade-off, he did not include manufacturability as a criterion, which could be the cause of him leaning towards a cone. In any case, it will also be interesting to compare the results of the cylindrical RAC versus the conical heat exchanger.

### RAC dimensions

Unfortunately, the dimensions of the RAC were very reliant on the maker of the piece. It should be noted that at this point of the project, the author ran into issues regarding manufacturability. Especially the RAC formed a problem, because it would become a highly detailed small piece which would require a high amount of experience and man hours on lathes, mills and drills. From the requirements, only €500 is available to conclude a thesis project. While this is more than sufficient for a theoretical thesis, a practical study is different. Not only the manufacturing of RAC and nozzle is required, but also the material needs to be bought, next to expenses on propellant, connection pieces, hard soldering, sensors and other. An overview of the costs is found at the end of this chapter.

Because the author was not experienced at all regarding metal machining, DEMO was contacted. At various faculties at DUT, DEMO runs manufacturing workshops with high-end tools. They help out staff and students, but also any commercial institute that might knock on their door. When a sketch of the RAC design was shown to them, they estimated that the price would be €1600 for the heat exchanger alone. This was of course not viable. Reducing the amount of detail (for instance by decreasing the amount of channels) would not bring the price down, so another solution had to be found. Via other students and a DUT Dreamteam, a master student was found who was willing to manufacture the RAC for a price of €300. This was excellent, because it would leave room for the other expenses. However, because the used mills were manual and not CNC, many concessions needed to be made on the design. Especially the requirement that the thickness of the walls needed to be a minimum of 4 mm was a harsh constraint; for comparison, Leenders's RAC had walls of approximately 1 mm thick. At this point, it can thus already be stated that the mass requirement cannot be met.

In Section 2.3, it was seen that 175 W was needed to heat gaseous nitrogen from 298.15 K to 835.35 K at a mass flow of  $300 \text{ mg s}^{-1}$ . For a specific impulse of 90.0 s, a chamber pressure of 8.2 bar is then necessary. This would still satisfy requirements REQ-S-1, REQ-S-2 and REQ-S-3 while not exceeding the pressure constraint. The feed pressure would be higher than 8.16 bar to accommodate

for pressure losses in RAC and tubing, but this will not pose a problem to the experiments as the nitrogen cylinder can provide up to 200 bar. Leenders found pressure losses of 0.05 bar during his runs [7]. Note that higher chamber pressures or higher power input will lead to higher specific impulses, which could be needed to correct for any losses in nozzle or connection pieces.

In Chapter ??, a tool will be constructed that can predict the thermal efficiency of a heat exchanger accurately, as a function of channel shape, channel length, Reynolds number and so on. For now, the goal is to find a first estimate of the channel length. First of all, one needs to decide on the channel lay-out: this could either be linear, spiral or a porous medium. Spiral has the advantage of a longer channel length (thus the heat exchanger could be reduced), while linear is easier to manufacture. Porous has potentially the largest heating area, however it also requires a material that can withstand high temperatures. Next to that, the medium needs to be shaped to fit inbetween two heated walls. Furthermore, because the fluid 'hits' the medium constantly, the pressure loss will be larger than for the other two options. For now, porous is not considered, but it could be an interesting idea for further research. Leenders did recommend spiral tubing at the end of his thesis, while Preijde also made the recommendation. Thus, spiral will be chosen as the channel configuration.

For construction, it is impossible to make the channels out of the inside of a solid cylinder. So, the idea was picked up to make the RAC out of three pieces: an inner hollow cylinder with the channels etched out at the outside; an outer hollow cylinder (one end closed) that could fit smoothly over the inner cylinder, so that the channels would be closed off; a cap that would close of the other end of the cylinders. On both sides of the outer cylinder, holes would be made to connect the feed system and nozzle.

### Inner cylinder

The inner cylinder is first dimensioned at the hand of thermal convection. The convection heat transfer in one channel can be calculated using Equations 5.1 [22]. The assumption is that the RAC wall has a constant temperature for the whole length of the channel. This can be assumed because the heat exchanger has a high conductivity, so heat will spread at a high rate through the RAC.

$$Q_{conv} = h_p \cdot A_{conv} \cdot \frac{T_{p,out} - T_{p,in}}{\ln\left(\frac{T_w - T_{p,in}}{T_w - T_{p,out}}\right)} \quad (5.1)$$

Where  $Q_{conv}$  is the convective heat transfer in W,  $h_p$  is the convective heat transfer coefficient in  $\text{W m}^{-2} \text{K}^{-1}$ ,  $A_{conv}$  is the channel heating area in  $\text{m}^2$ ,  $T_{p,in}$  is the incoming propellant (here: 298.15 K) and  $T_{p,out}$  is the outgoing propellant temperature, equalling 835.4 K. For now it is assumed that the wall temperature  $T_w$  is slightly higher than the outgoing propellant temperature, so 850 K.

The convective heat transfer can be found using the dimensionless Nusselt number  $Nu_D$  (see Equation 5.2), which in turn can be calculated using the empirical Gnielinski formula (see Equation 5.3). The latter is valid for Reynolds numbers starting at 2300, although some sources dictate a lower limit of 3000 [48]. The Reynolds number  $Re_D$  can be found by using Equation 5.4, while the dimensionless Darcy Weisbach friction factor  $f_{DB}$  is calculated using Equation 5.5. The heating area per channel is found from Equation 5.6.

$$h_p = \frac{Nu_D k}{D} \quad (5.2)$$

$$Nu_D = \frac{\frac{f_{DB}}{8} (Re_D - 1000) Pr}{1 + 12.7 \left(\frac{f_{DB}}{8}\right)^{\frac{1}{2}}} \quad (5.3)$$

$$Re_D = \frac{\rho v D}{\mu} = \frac{\dot{m} D}{\mu A_{ch}} \quad (5.4)$$

$$f_{DB} = (0.79 \ln Re_D - 1.64)^{-2} \quad (5.5)$$

$$A_{conv} = \pi \cdot D \cdot L_{ch} \quad (5.6)$$

In case of a non-circular duct, the diameter  $D$  (in m) is replaced by the hydraulic diameter  $D_h$  in the same dimension, see Equation 5.7. In these equations,  $k$  is the propellant's thermal conductivity in  $\text{W m}^{-2} \text{K}^{-1}$  and  $\mu$  is the propellant's dynamic viscosity, both evaluated at the bulk temperature of the propellant, which is the average of the inlet and outlet temperatures (see Equation 5.8).  $A_{ch}$  is the channel cross-sectional area in  $\text{m}^2$  and  $L_{ch}$  is the channel length for a spiral around a cylinder, from Equation 5.9.

$$D_h = \frac{4A_{ch}}{S} \quad (5.7)$$

$$T_b = \frac{T_{p,in} + T_{p,out}}{2} \quad (5.8)$$

$$L_{ch} = \sqrt{\pi^2 D_{RAC}^2 + L_{RAC}^2} \cdot n_{turns} \quad (5.9)$$

Here,  $D_{RAC}$  and  $L_{RAC}$  are the heat exchanger's diameter and length respectively, both in m.  $n_{turns}$  is the number of turns.

Now that the equations are known, the RAC can be dimensioned. It should be noted that the student who manufactured the RAC advised to make the channels isosceles triangles (with 45 deg angles), with the hypotenuse pointing away from the centre of the cylinder. This was most easy to turn on a lathe according to him, as a chisel has this shape. A standard chisel of width 1.2 mm was chosen, so both sides in the material were 0.849 mm. As such,  $A_{ch}$  was  $0.36 \text{ mm}^2$  and  $D_h$  was 0.497 mm.

The number of channels was set at an arbitrary 6. This is because the Reynolds number would then equal 2428, just above the threshold for the Gnielinski formula. For this calculation, the propellant bulk temperature was assumed to be the average of the inlet propellant temperature and intended outlet propellant, so 566.8 K. The dynamic viscosity for nitrogen is equal to  $28.42 \times 10^{-6} \text{ Pa s}$  at that temperature<sup>4</sup>. A larger amount of channels would lead to lower Reynolds numbers, while a higher amount of channels would be detrimental to the pressure loss. Furthermore, more channels would also imply more work for the manufacturer. The pitch  $p$  in m between the channels would be twice the width of the channels, so 2.4 mm. The number of turns could then be found by dividing the RAC length by that number, see Equation 5.10.

$$n_{turns} = \frac{L_{RAC}}{p} \quad (5.10)$$

The diameter of the inner cavity was set at 8 mm to allow for some manufacturing space. The manufacturer agreed to have an outer diameter for the inner cylinder of 13 mm, so the channels were

<sup>4</sup><https://www.engineeringtoolbox.com>, accessed on 07-08-2020.

etched out to a maximum depth diameter of 11.8 mm. 175 W of power is needed, so the only unknown would be the length of the RAC channel section. Solving for all variables, the Nusselt number is 8.01, convective heat transfer coefficient is  $663 \text{ W m}^{-2} \text{ K}^{-1}$  and the resulting heat exchanger length is 31 mm. However, room is also left at the start and end of the inner cylinder to accommodate for the inlet and outlet. In those areas, the propellant can also heat up, so 10 % is subtracted of the length to reduce the size. A final 28 mm was the result. At that heat exchanger length, each of the six individual channels has a length of 0.090 m.

At the start of the inner cylinder, 5 mm is added to allow a 3 mm sized hole for the inlet. On the other side, 10 mm is added for an outlet of 8 mm. The reason that the outlet is larger is because it makes sure Leenders's nozzle can fit on there, should a dedicated nozzle be too expensive to build. The mass of the inner cylinder is 0.027 kg.

### Outer cylinder

The outer cylinder should fit around the inner cylinder and thus has an inner diameter of 13 mm. The outer diameter is 21 mm. The cylinder is open on one end, on the other end it is closed except for the aperture which has a diameter of 4 mm. That way, it allows for some adjustment to the laser focus height, while not being too large to let heat or reflection escape. On the side, the outer cylinder has one hole for the inlet (diameter: 3 mm) and one threaded hole (M8) for the outlet. The mass is 0.092 kg.

### Cap

The cap is used to close off the open end of both cylinders, once the inner cylinder is inserted in the outer. The cap is on the inlet side so it also features a 3 mm sized hole. Next to that, it has a threaded hole in the middle, size M6. This allows for a fourth part, which was added later in the design. The mass is 0.050 kg.

### Spike

A spike was added, in order to diverge the incoming laser beam and reflect it to the inner side walls. The idea was to make it as sharp as possible, but the manufacturer could only allow a minimum half angle of 20 deg. Furthermore, it was extended in the length because it could otherwise not be clamped in the lathe. The effect of the spike is not yet known, but the added mass of 0.004 kg was minor, so it was constructed as well.

### Result

The total volume of the heat exchanger amounts to  $19\,656 \text{ mm}^3$ , which gives a mass of 0.176 kg at a copper density of  $8978 \text{ kg m}^{-3}$ . This is more than double the amount of Leenders's RAC. As was expected, requirement REQ-S-4 is thus not met, due to the very thick walls required for construction. The outer area equals  $5008 \text{ mm}^2$ , the inner area is  $1462 \text{ mm}^2$ , including the spike area. See Appendix A for the technical drawings of STT2. An exploded view of STT2's heat exchanger is shown in Figure 5.1, pictures of the hardware results are available in Section 5.6.

## 5.2.4. Nozzle design

Originally, the nozzle was designed to be a simple conical one, with the throat and exit diameter determined from IRT. These values were 0.58 mm and 0.76 mm respectively. It would be constructed from a solid cylinder with a diameter of 5 mm and length of 20 mm. A hole of diameter 3 mm would be drilled out on one side (not to the end). Then, the nozzle would be drilled out on the other side. However, two issues prevented the final design and manufacturing of the piece: it could not be made accurately as a lack of appropriate tools, experience and funding. Leenders's nozzle had similar areas (0.58 mm for the throat and 0.68 mm for the exit), so it was decided to use his nozzle in testing and

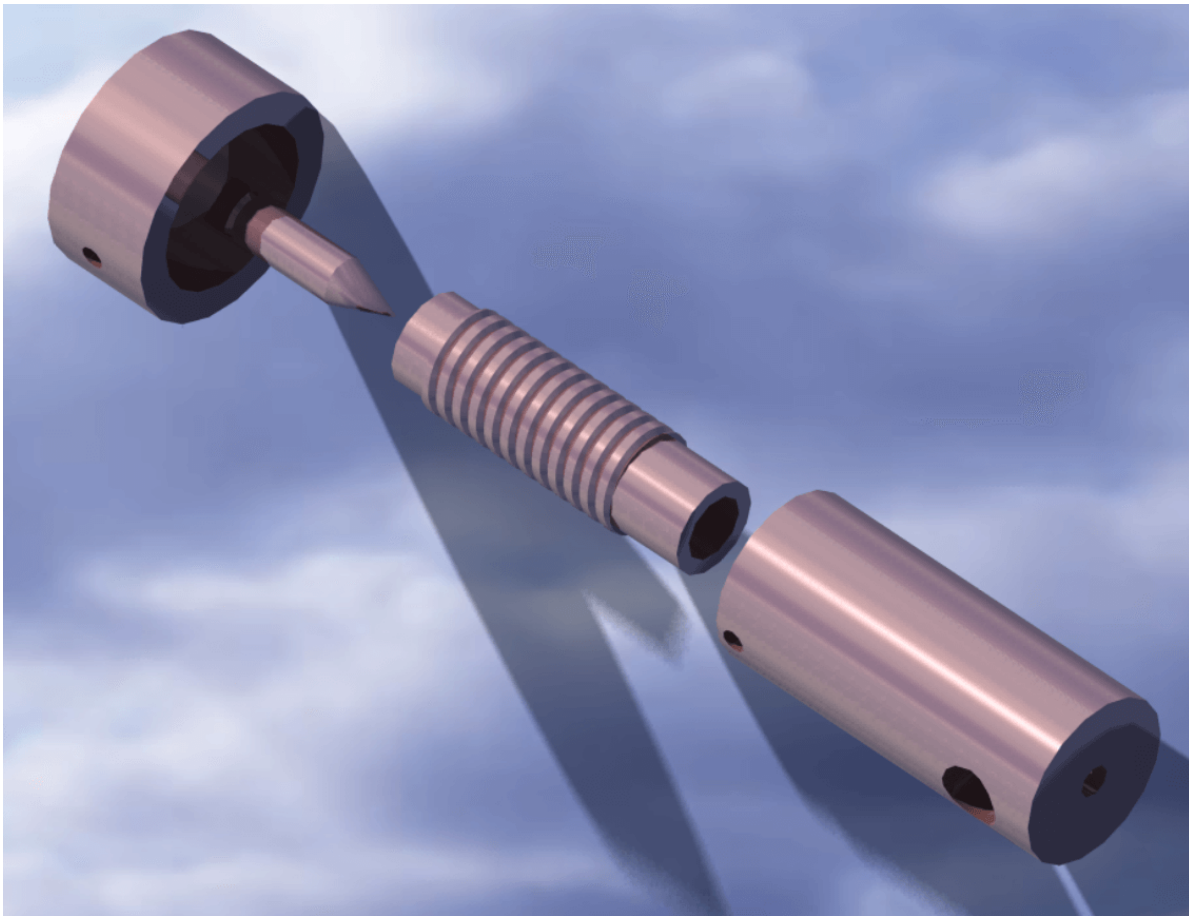


Figure 5.1: Exploded view of the STT2 heat exchanger.

accept the performance losses, which are only 1.2 %. A drawing of a dedicated nozzle for [STT2](#) was thus not made. However, a drawing of the copper nozzle can be found in [Appendix A](#).

### 5.3. Solar Thermal Thruster 2 performance

This section will focus on the performance of [STT2](#). Many inputs are retrieved from Chapter 5, see Table 5.3. Note that the number of channels is set at 6. No insulation is applied. With those inputs, the tool reaches a steady solution at an [RAC](#) temperature of 816.9 K, propellant temperature of 719.7 K, pressure loss of 0.10 bar, which gives a specific impulse of 84.0 s and thrust of 247 mN. This amounts to a thermal efficiency of 53.7 %, which is lower than the arbitrary 70 % which would bring the specific impulse to 90 s. As expected, the thermal losses at the outside are relatively high at such high temperatures. Radiation losses are dominating convection losses as well.

When the same cylindrical shaped insulation is applied as was for [STT1](#), the thermal efficiency dramatically increases to 88.2 %, which is more than enough to propel the specific impulse to 98.2 s at a thrust of 289 mN. Raising the power input to 400 W or more instead of using insulation would also raise the specific impulse, but at the cost of huge thermal losses. It is planned to have these values confirmed during testing.

Table 5.3: STT2 tool inputs.

Name	Symbol	Value	Unit
RAC type	-	"Cylindrical"	-
RAC material	-	"Copper"	-
Propellant	-	"Gaseous nitrogen"	-
Channel layout	-	"Spiral"	-
Number of channels	$n_{ch}$	6	-
RAC length	$L_{cav}$	0.051	m
RAC inner diameter	$D_{inner}$	0.008	m
RAC outer diameter	$D_{outer}$	0.021	m
RAC aperture diameter	$D_{ap}$	0.004	m
RAC inner cavity area	$A_{RAC,i}$	1.46e-3	$m^2$
RAC outer cavity area	$A_{RAC,o}$	5.01e-3	$m^2$
RAC mass	$M_{RAC}$	0.173	kg
Irradiation time	$n_i$	95	min
Incoming power	$Q_{in}$	250	W
Incoming power efficiency	$\eta$	1.00	-
Absorptivity oxidized copper	$\alpha_M$	0.70	-
Emissivity oxidized copper	$\epsilon_M$	0.65	-
Emissivity insulation	$\epsilon_{insu}$	0.09	-
Ambient temperature	$T_{amb}$	298.15	K
Ambient pressure	$p_{amb}$	101325	Pa
Propellant pressure	$p_p$	816000	Pa
Channel diameter	$D_{ch}$	0.0006	m

## 5.4. Cost

The following costs are associated with the development of the test motor:

- The heat exchanger will be manufactured at the DUT Dreamhall by a student at the price of €300. The nozzle is borrowed from Leenders. Various other connection pieces are manufactured by the author himself, see Section 5.6. One hard-soldered connection by DEMO costs €50.
- The heat exchanger will be constructed out of copper. It is more convenient to buy the copper in a round solid staff for manufacturing purposes. Also, a margin is necessary, in case of production errors or design changes. A margin of 3 mm is recommended. Because a significant amount of copper will be milled, the estimated length of the staff will be three times 82 mm, which is 246 mm. With a diameter of 30 mm it will cost €60.42 including taxes<sup>5</sup>.
- Some raw material (brass and steel) for the connection pieces (see Section 5.6) is also required and is bought at Firma Kokkelink in The Hague. It amounts to €26.07.
- A bottle of gaseous nitrogen is in the range of €50-€70 at the DUT Gassenteam<sup>6</sup>.
- All sensors can be borrowed from the the cleanroom at AE or the 3mE Meetshop.
- Some miscellaneous objects were also bought. An inlet tube, 3 mm outer diameter for €10.75 was purchased at Quartel, located in Pijnacker. Fireproof kit was bought for €14.41<sup>7</sup>. Bolts and nuts were acquired from a local hardware shop for €20.57.

<sup>5</sup>[metaalwinkel-metalen.nl](http://metaalwinkel-metalen.nl)

<sup>6</sup>[gassenteam-ictfm@tudelft.nl](mailto:gassenteam-ictfm@tudelft.nl)

<sup>7</sup>[kitcentrum.nl](http://kitcentrum.nl)

The total cost is projected to be €532-€552, which is already in excess of the available resources. It shows that executing a practical thesis can be very challenging and that workarounds and concessions to design are needed to complete the project.

## 5.5. Design mistake

During meetings with the manufacturer of the heat exchanger, it was indicated that the amount of channels would require extra man hours and would thus cost more. His request was to make one channel instead of six and increase the length sixfold. This was agreed, but the error was only discovered by the time test runs were initiated; by decreasing the amount of channels but not increasing the cross-sectional area, the pressure drop was tremendously high, nearing 25 bar for the mass flow level set in the objective. With six channels, this was a mere 0.20 bar. Essentially by having only one small channel, an extra nozzle was introduced in the engine which would be detrimental to its performance. As such, the heat exchanger could not be tested at the indicated mass flow level of  $300 \text{ mg s}^{-1}$ . No additional funding was available to commission a new heat exchanger, see the previous section.

The author realizes that this is a grave mistake which unfortunately renders the manufactured design almost useless. In Chapter 6, it will be explained that the channel design mistake is only one out of three reasons to divert the thesis into another path; during the initial tests, it was also discovered that the heat exchanger was plagued by leakages. Next to that, the COVID-19 crisis prevented any large-scale experiments at the faculty of 3mE. In the same chapter, a plan for the continuation of the thesis will thus be shown.

## 5.6. Hardware

These sections will focus on the hardware of STT2. First, the RAC hardware is presented, followed by a section on the connection pieces. In the end, recommendations will be given on how to tackle hardware issues in future theses. In Chapter 5, it was noted that no budget was left to manufacture a nozzle. This was kept in mind during the design of the heat exchanger, so the copper nozzle from Leenders could be connected to the RAC's outlet [3].

### 5.6.1. Receiver-Absorber Cavity hardware

As was shown in the design Chapter 5, the design was altered multiple times to allow for the RAC to be built. Finally, a design was chosen which could be made. It consisted of four parts which are shown in Computer Aided Design (CAD) drawings in Appendix A. All parts were constructed on Dreamhall manufacturing tools, primarily lathes and drills, by a student who was experienced in metal manufacturing.

Figures 5.2 and 5.3 show the disassembled and the assembled RAC respectively. Notice the threaded connections and the four parts out of which the heat exchanger is assembled: inner cylinder, outer cylinder, cap and spike. Also be aware of the extended spike, protruding out of the cap. This was necessary in order to clamp the spike in the lathe while the sharp part was made. In Tables 5.4 and 5.5, the dimensions and mass of the components are shown. As can be seen, the values do differ from the design values, but not by a significant amount. After the pieces were made and the inner cylinder was inserted in the outer cylinder, it was discovered that they could not be separated anymore. This was not seen as an issue, however the separate dimensions could not be measured.



Figure 5.2: Disassembled STT2.



Figure 5.3: Assembled STT2.

Component	Part	Design size	Actual size	Remarks
<b>Inner &amp; outer cylinder</b>	Outer diameter	21.00	21.81	-
	Inner diameter	8.00	7.78	-
	Length	47.00	46.76	-
	Channel diameter	13.00	12.82	-
	Inlet hole diameter	3.00	2.98	-
<b>End cap</b>	Outer diameter	29.00	28.98	-
	Inner diameter	21.00	20.70	-
	Length	14.00	15.20	-
	Laser hole diameter	5.00	5.00	-
	Inlet hole diameter	3.00	3.04	-
<b>Spike</b>	Diameter	6.00	5.96	-
	Length	22.24	30.06	Sticks out at the top. No influence on the design, except for mass.

Table 5.4: Component sizes (in mm)

### 5.6.2. Connection pieces hardware

Having the heat exchanger and nozzle was not enough to start the experiments. Some connection pieces still needed to be made. Because at this point there was no additional money available from the faculty, it was decided to follow two metal manufacturing courses, on milling and turning. Both were offered to freshmen student at the workshop at the faculty of [3mE](#) and the instructors did allow the author to follow the courses. Both had a time length of four hours, after which the manually operated lathe and mill could be used freely. The author recommends the courses wholeheartedly, as knowledge of the manufacturing process can only enhance the capabilities of an engineer in being.

After the courses, two main pieces were made: one was a brass object in order to connect the [RAC](#) inlet, first pressure sensor and nitrogen feed line; the other was a brass element to connect the second pressure sensor to the nozzle chamber. Both parts are shown in Figure 5.4 and are constructed on a lathe in the [3mE](#) workshop. Brass was chosen as it is cheap and easy to manufacture.

Next to that, a ceramic piece from some previous project was reused as a means to connect [STT2](#) to the test stand (see Chapter 6). The piece is made of Macor but could not be milled at the workshop, because of the detrimental effect of the material on the machinery. [DEMO](#) eventually manufactured the piece.

The [CAD](#) drawings of the connection pieces are shown in Appendix A.

<b>Component</b>	<b>Design mass</b>	<b>Actual mass</b>	<b>Remarks</b>
Inner & outer cylinder	0.119	0.125	Not possible to separate both pieces.
End cap	0.050	0.051	-
Spike	0.004	0.006	Longer spike than designed.
<b>Total</b>	<b>0.173</b>	<b>0.182</b>	-

Table 5.5: Component mass (in kg)

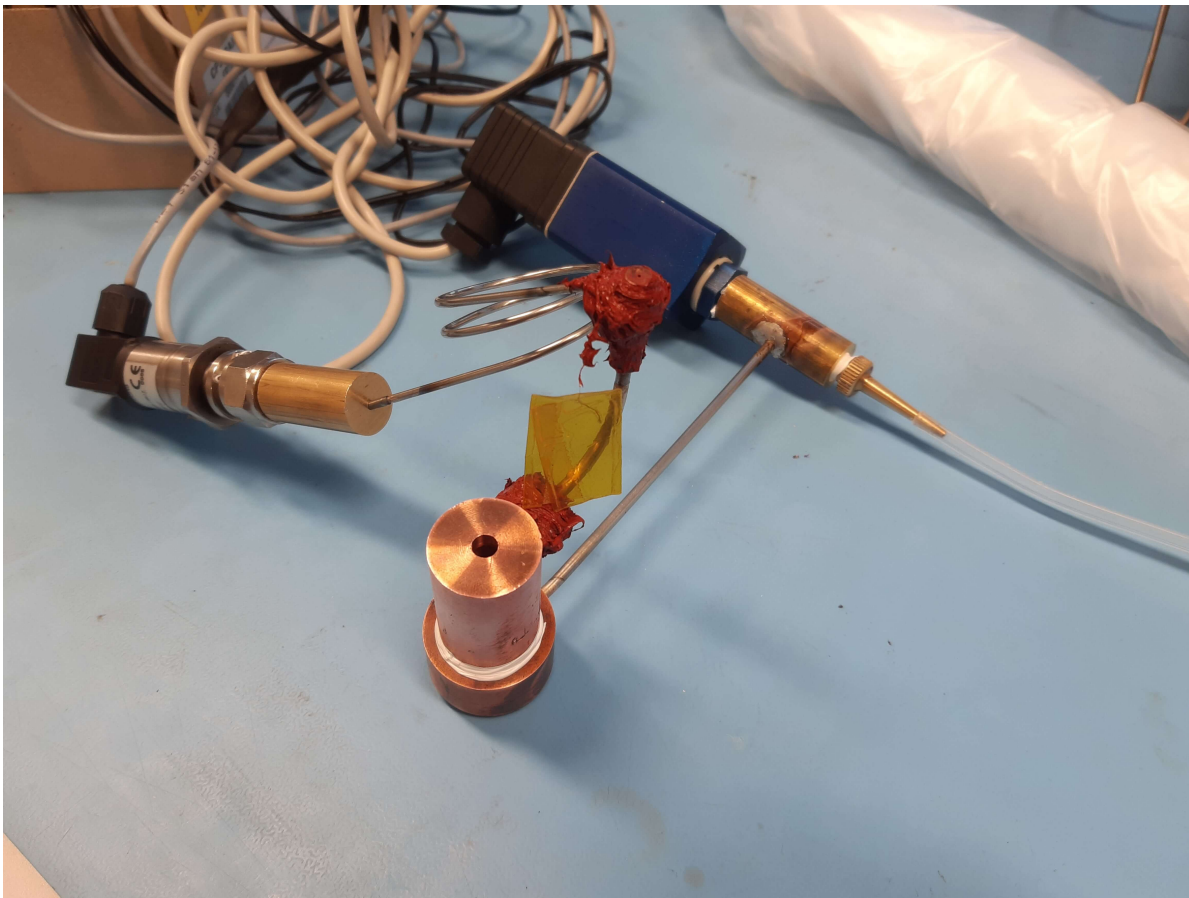


Figure 5.4: STT2 with both machined parts.

### 5.6.3. Construction recommendations

For hardware construction, recommendations are shown. They are listed here:

1. It is advised to have a high level of experience in the area of metal manufacturing before accepting a practical thesis in the area of STP. That way, one can focus on the design and testing instead of spending both time and money on the construction of especially the heat exchanger part of the engine. It was felt that the inexperience of the author held back the design by a large degree.
2. If an external party is chosen for the manufacturing, keep in mind to closely discuss the design with them, at every step. Most of the time, they can tell you what is possible and what is not.
3. Always choose hard-soldered connections over threaded connections. Hard-soldered connections are sturdy, high temperature resistant and leak tight. Furthermore, they are relatively inexpensive, see also Section 5.4.
4. The use of kit to remedy leakages is not preferred, due to it expanding and blocking of the inner piece tubes. Where possible, adjust the design to allow for hard-soldered connections.

# 6

## Experiment preparation

This chapter will explain what tests are going to be conducted (Section 6.1), the locations of testing (Section 6.2) and the required equipment (Section 6.3) to bring the experiments to a conclusive end. Next to that, a section is dedicated to the test stand hardware and its calibration. A few small test runs were done in the AE cleanroom, after which serious flaws were found which forced the alteration of this project in the later stages. Here, it was decided not to continue with the physical experiments. The last section of this chapter will discuss this change.

### 6.1. Planned experiments

In Chapter ??, it became apparent that the preliminary tool was still to be validated for simulations where propellant flow was present. Next to that, doing additional experiments when no propellant was flowing is also needed, as the tool was only validated by a few experiments Leenders conducted in his thesis [3]. During those experiments, the power input was not a constant, which makes the results less reliable to use.

Three types of experiments are planned for STT2:

1. Test 1: test with nitrogen flow without illumination.
2. Test 2: test without nitrogen flow with illumination.
3. Test 3: test with nitrogen flow with illumination.

The first test has to be performed in order to validate the performance results at room temperature. This is an excellent way, as no measures regarding heat shielding, thermocouples and suction have to be taken. The pressure at inlet and just before the nozzle (in the chamber) have to be measured. Together with the geometry of the nozzle, the mass flow and the load sensor readings and the nitrogen characteristics, it should be possible to assess whether design errors in the nozzle are present and how pressure is affected in the small channel of the RAC. It should be noted that the ambient pressure and the nitrogen chamber temperature are still required for this assessment. The second and third tests will be used to validate the preliminary tool, as told earlier. It should be noted that there is the advantage that the first test without the light source are more flexible locationwise. Instead of using the welding facility this can be done in the cleanroom, located at the eighth floor of the faculty of AE, where no technician is needed whatsoever (see Section 6.2). However, the second and third tests are

to be performed in the laser welding facility. During the testing, inputs such as input power and mass flow can be varied in order to see their respective impact on the engine performance.

## 6.2. Locations

Two main locations will be used for the experiments, the cleanroom at the 8th floor of **AE** and the welding facility at the **Materials Science and Engineering department (MSE)** of **3mE**.

### 6.2.1. Cleanroom

The cleanroom located at **AE** is an ISO 8 cleanroom with the purpose of, among others, providing a professional platform for students to work in<sup>1</sup>. It contains a vacuum oven, various sensors and computers and a nitrogen supply to conduct micro-propulsion experiments. The responsible contact person is Mehmet Şevket Uludağ. The cleanroom is accessible to **AE** students at all times, under the condition that they are granted access by the contact person from **Space Systems Engineering (SSE)**. A workshop is attached to the cleanroom, where various tools can be freely used. See Figure 6.1 for the cleanroom.



Figure 6.1: Cleanroom at **AE**.

<sup>1</sup><https://www.tudelft.nl/en/ae/organisation/departments/space-engineering/space-systems-engineering/facilities/>, accessed on 12-03-2020.

### 6.2.2. Welding facility

The welding facility can be found in another part of DUT, at 3mE. It is primarily used for research into welding. It is a closed-off area with a powerful laser which can go up to 8000 Watts in power. The reason it is listed here is because the laser will serve as the illumination source for tests 2 and 3.

## 6.3. Equipment hardware

In this section, the required equipment will be listed. The use for it will be explained, as well as various details such as the accuracy, disadvantages and shortcomings. All sensors will be connected to **National Instruments (NI) DAQ** devices which in turn deliver the data to a desktop or laptop. Most sensors and **DAQ** devices, if not all, are borrowed from 3mE's Meetshop.

### 6.3.1. Thermocouples

In order to measure the temperature of the propellant and RAC before, during and after heating, temperature sensors are needed. The data will be used to validate the predictions by the **RAC** model. As told before in the literature study [27], the temperature sensors will be thermocouples because of their high availability, medium accuracy and ease of use. The RS Pro 787-7835 is the chosen thermocouple (see Appendix C.3) because of its high temperature range, up to 1100 deg C (see Figure 6.2). The combined thermocouple and **DAQ** device may delay the signal by a second (a disadvantage of thermocouples), but that should pose no problem for the tests which will run for multiple minutes.

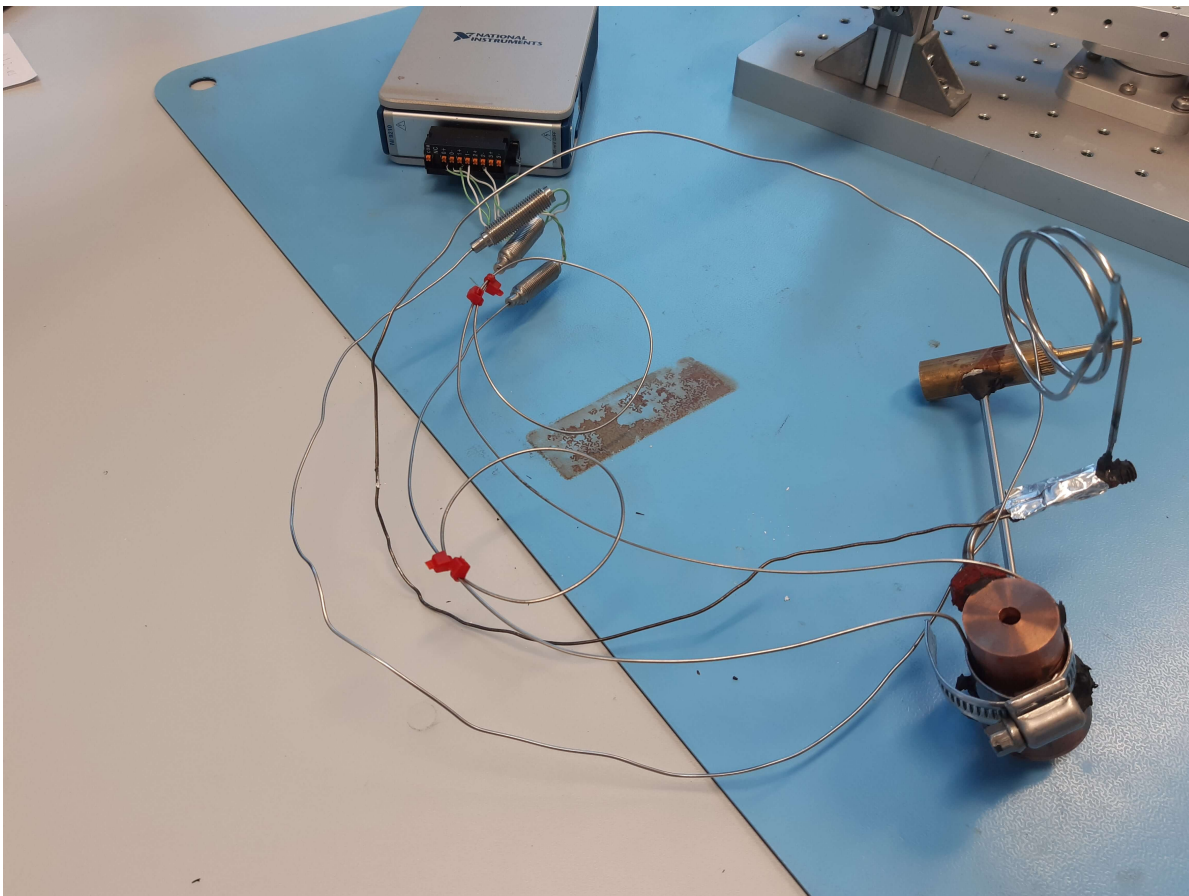


Figure 6.2: Thermocouples RS Pro 787-7835. In the background, the corresponding NI DAQ device is shown.

Because it is hard to directly measure the temperature of a gaseous flow, the sensors will be stuck to the outer and inner surfaces of the [RAC](#) and nozzle where possible. They will be connected to the engine using various methods, such as high temperature kit, steel clamps and hard soldering. Having these measurements, the propellant temperature can be determined or at least estimated.

### 6.3.2. Pressure sensors

The pressure sensors are necessary to measure the precise pressure of the propellant flowing through the engine. Combined with the temperature readings and mass flow, the pressure will determine what thrust should be delivered by the engine (what in turn is validated by the load sensor). Furthermore, two or more pressure sensors will give means to assess the pressure loss inbetween the two measuring points.

The pressures sensors will impact the design relatively more than the thermocouples, because they will have to be part of the flow to read the pressure. Thus, the amount of sensors will be limited to two, one before the [RAC](#) and one at the nozzle chamber. The sensors themselves have a physical connection in the form of a BSP female thread, G1/8" or G1/4" (see Figure 6.3). These will be connected via brass connection pieces to the engine, more information can be found in the latter subsection.



Figure 6.3: Pressure sensors 3300B16B0A01B000RS and DRTR-AL-20MA-R16B.

The pressure sensors used are the 3300B16B0A01B000RS and the DRTR-AL-20MA-R16B (see Appendix C.4 for the data sheets). The former is an absolute sensor, able to measure up to 16 bars of pressure. It outputs a current, which is converted via a constant resistor (468.8 Ohm) to a voltage which can be read by the [DAQ](#). The latter sensor is a relative one (to atmospheric pressure), again ranging up to 16 bars (over-pressure). A constant resistor of 559.7 Ohm is added to again convert the current output to a voltage output for the [DAQ](#). It should be noted that both sensors require a

connection to the grid and operate up to 80 deg C. It is thus adamant that both sensors are shielded from heat flux from the experiment irradiation or convection and radiation. One measure that is taken for the sensor placed after the RAC is to insert a coiled tube inbetween to allow the fluid to cool down (see Figure 6.4). Be aware that this brings the disadvantage of tubing pressure loss, making the sensor read a slightly decreased pressure than which is present in the nozzle chamber.

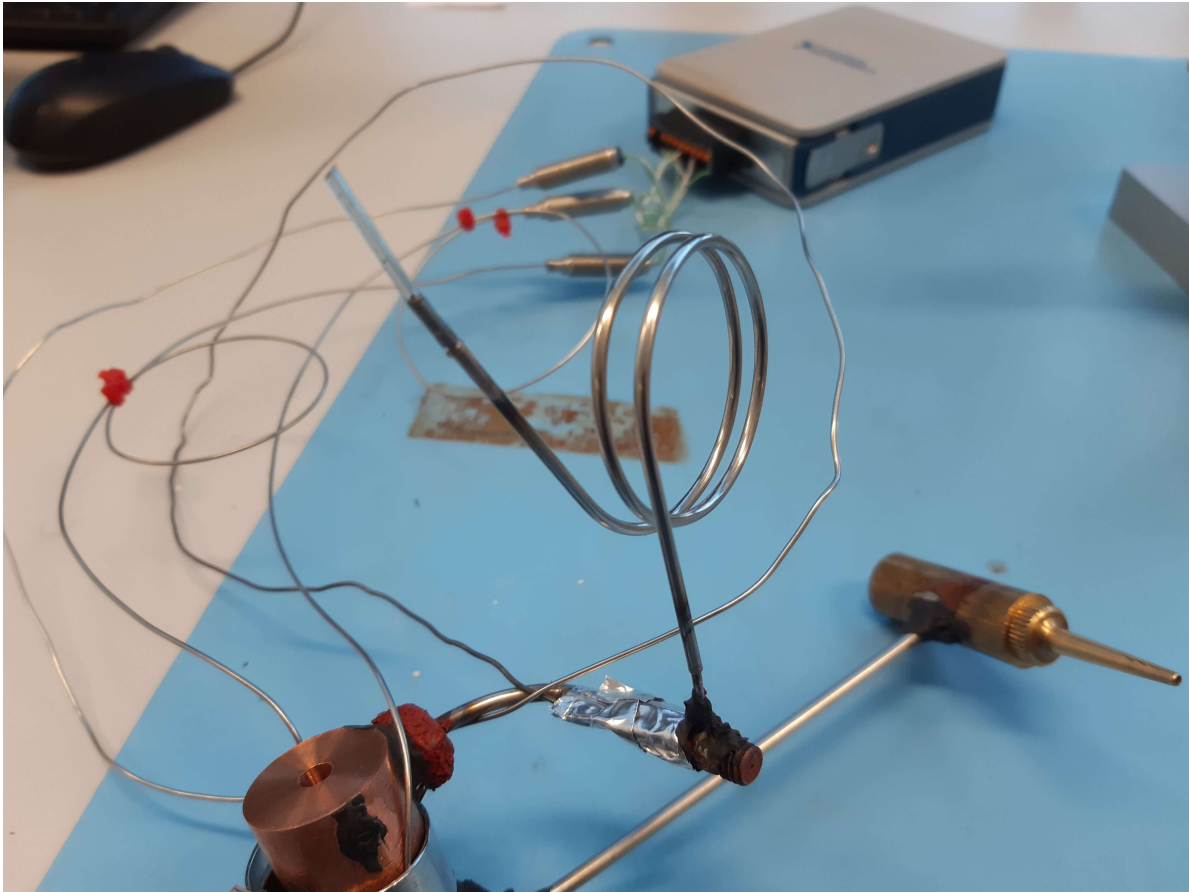


Figure 6.4: Coiled tube to allow the fluid to cool down for the pressure sensor.

### 6.3.3. Mass flow sensor

The mass flow sensor is a device which is aligned with the propellant flow and measures the mass flow. It is mounted just after the propellant outlet (most likely a gas cylinder). The faculty employs three Brooks mass flow sensors, each overlapping in range (see [27] for more information):

1. Brooks 5850S Smart Mass Flow. Range from 0-144 mln/min of nitrogen, or 0-3.00 mg/s.
2. Brooks 5850S Smart Mass Flow. Range from 0-2 ln/min of nitrogen, or 0-41.69 mg/s.
3. Brooks 5851S Smart Mass Flow. Range from 0-47.3 ln/min of nitrogen, or 0-860.83 mg/s.

All connections to the gas cylinder and the subsequent RAC are similar for the three sensors, which gives some flexibility. The accuracy is listed at 0.5%, but inaccuracy increases at the lower 10% of the range. Hence the overlap of the sensors, to accommodate for this. The sensors are connected to a DAQ device via a Printed Circuit Board (PCB) which is present in the AE cleanroom (see Figure 6.5. It automatically detects which mass flow sensor is connected and outputs a voltage for a similar DAQ as is used for the thermocouples. Note that the output of all three sensors is a current, in a nominal

range of 0-20 or 4-20 mA. This should be adjusted for in the voltage read-out, as it reads 0-5 or 1-5 V respectively. See Figure 6.6 for the 5851S version.

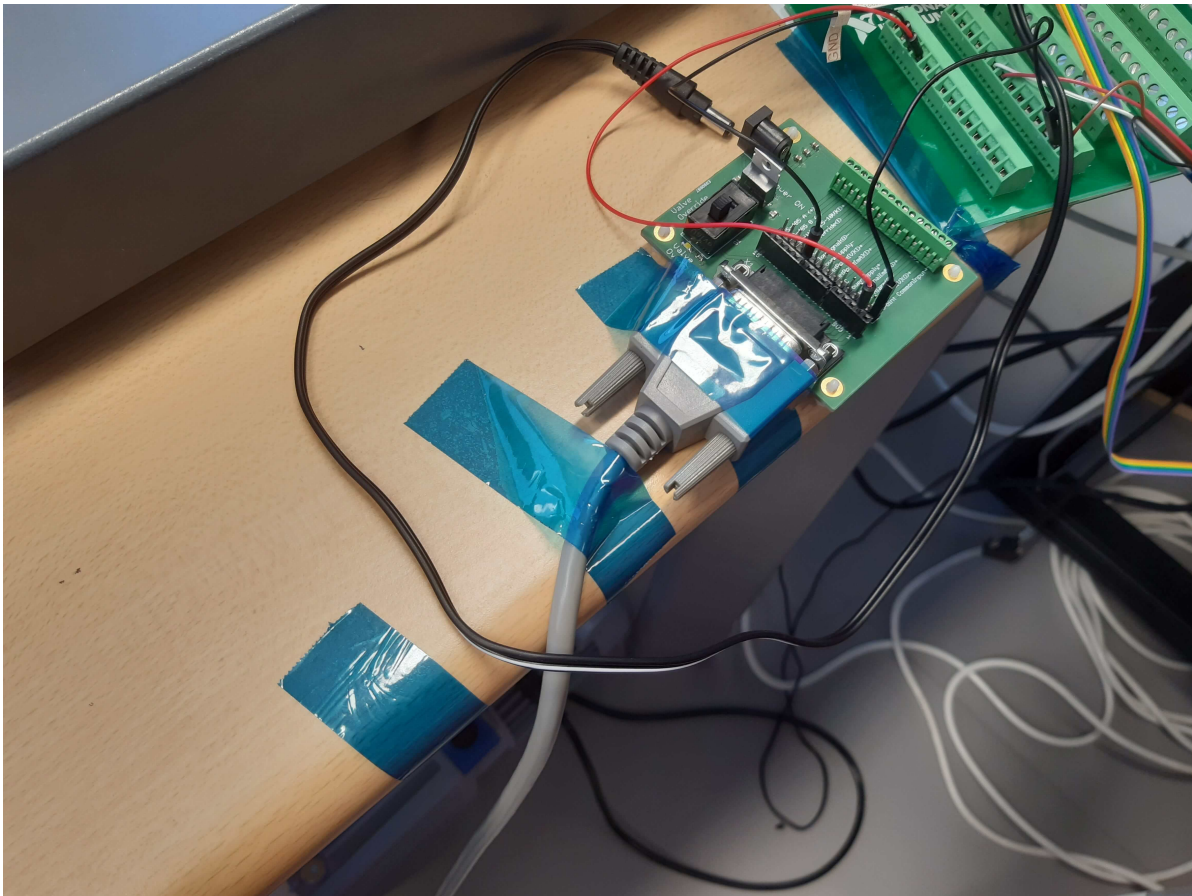


Figure 6.5: PCB connected to one of the Brooks mass flow sensors.

#### 6.3.4. Propellant supply

As stated in the report, gaseous nitrogen will be the designated propellant for the 'wet' experiments. It is cheaply available, has no corroding effects on the engine, no two-phase flow and yields intermediate performance in terms of thrust, temperature and specific impulse [27]. The propellant is held in cylinders and is delivered by the DUT Gassenteam. There are multiple purities available: 3.0, 5.0 and 6.0 in increasing purity order.

### 6.4. Test stand hardware

In the past, the department of SSE at the faculty of AE has developed multiple test stands in various thrust ranges in order to accurately measure the thrust exerted by microthrusters. Most of these were designed, verified, validated and enhanced by fellow thesis students throughout the years, found in Valente (2007) [4, 65], Koopmans (2007), Janssens (2009) [5], Grande (2010), Bijster (2014) [66], Jansen (2016) [46], Versteeg (2020) [67] and others. An overview can be found in the 2016 thesis of Jansen and shows four prominent test benches, all named AE-TB-X where the "X" represents the upper limit of range in Newtons. By that standard, the AE-TB-1.0 was developed (up to 1 N), followed by an enhanced TB-1.1 (a more accurate and less bulky 1.0), TB-50m (up to 50 mN) and TB-5m (maximum range of 5 mN). Because the TB-1.0 and TB-1.1 operate in the same range of thrust, the earlier has been decommissioned. It should be noted that, as Jansen mentions, the stands are not all available as



Figure 6.6: Brooks 5851S mass flow sensor.

of now as some are disassembled and rebuilt in other configurations. However, the parts are mostly available and are scattered throughout the department.

From Jansen, two main candidates are available for the STT2 experiments due to their range: the AE-TB-1.1 and the AE-TB-50m. It should be noted that Leenders measured a maximum hot gas thrust of 104.1 mN, using the then available AE-TB-1.0. From experience it is known that thrust sensors are less accurate in the lower range (about <5%). Indeed, Leenders shows a large discrepancy in the simulated thermal Matlab model thrust data and the experimental data. It is not apparent whether this is due to an inaccurate sensor or a lacking model validation, as Leenders does not elaborate on the differences.

However, both aforementioned stands will be evaluated hereafter. The thrust bench should adhere to a few requirements: it should be able to hold the engine and thrust sensor (naturally), not cause too much (background) noise and have a low mass and volume to be able to move it.

#### 6.4.1. Test bench AE-TB-1.1

Federica Valente built a thrust bench named AE-TB-1.1 (short: TB-1.1) for her thesis project in 2007 [4]. This thrust bench fulfilled some of the requirements, having low mass and fitting the engine and load sensor easily due to its modular build (using Boikon profiles). See Figure 6.7 for the thrust bench.

Valente reported a noise of 10-30 mN for the TB-1.1 with a standard deviation of 4.2 mN. The noise was explained by environmental influences, such as building vibrations and air currents. It can be cancelled out by averaging over the range of about five seconds, based on her graphs with

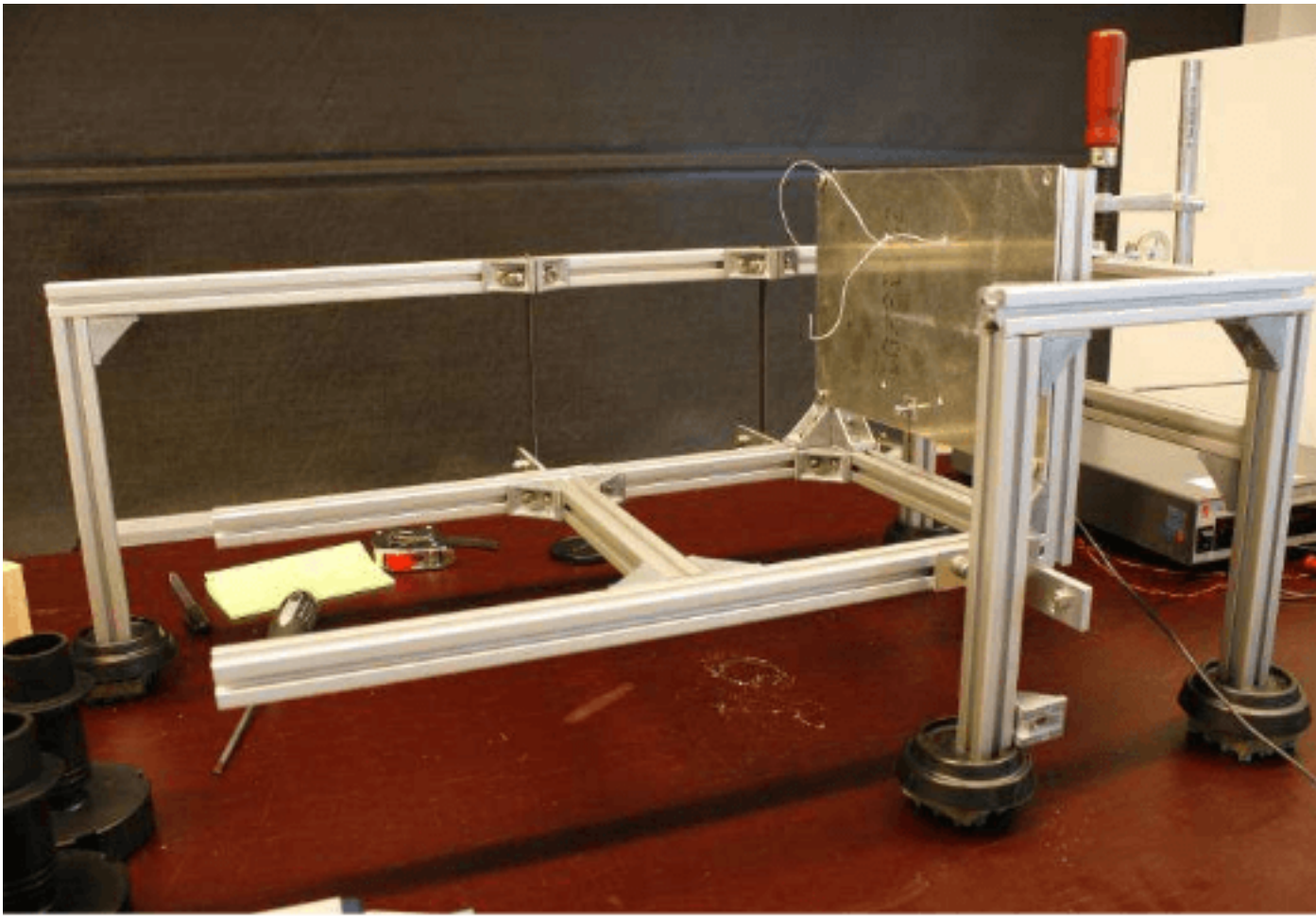


Figure 6.7: Thrust bench TB-1.1 [4].

experimental data. The bias (or accuracy) has an absolute value of 3 mN for a test case where the expected load was 951.57 mN. She attributes the difference to the visual leveling of the thrust sensor.

Because the thrust level for the current experiments will be in the range of 100 mN to 300 mN, the bias will affect the signal significantly. Hence, another bench was searched for.

#### 6.4.2. Test bench AE-TB-50m

Stef Janssens designed and built a thrust bench for micropulsion test applications, with a usable range of 0.5-4.2 mN [5]. He aptly named it the TB-50m, see Figure 6.8. The mechanics of the bench are simple: it has a bearing around which a beam revolves. The thruster is mounted on one side, while the thrust sensor will be at the other side. When the thruster fires, the beam will exert pressure on the thruster, which is then translated to a corresponding force. Special measures are to be taken to reduce friction in the beam bearing. This can be done by mounting relatively heavy engine parts directly above the bearing. Also, it should be noted that the thrust needs to be adjusted for the distance of the engine to the bearing relative to the distance of the bearing to the sensor. Using the law of moments where the distances along the beam are taken into account, the thrust of the engine can be calculated.

The used thrust sensor was the Futek LRF400 (L2338), having an upper limit of 100 mN and a reported accuracy within 2 % (for data sheet, see Appendix C.1). However, Janssens designed the stand for 50 mN, as the lower limit of the TB-1.0 was at that level. He does not elaborate on the

applicability of the bench in the 50-100 mN range, but it can be expected that extending the thrust arms would increase the range to 100 mN. Next to this, another issue arose: the bench was disassembled in the past decade. However, in 2015 Krusharev [6] rebuilt it for his own micro-thrust purposes (see Figure 6.9). Again, the LRF400 was the working sensor. Afterwards, again it was disassembled to allow other students to use the parts for their goals.

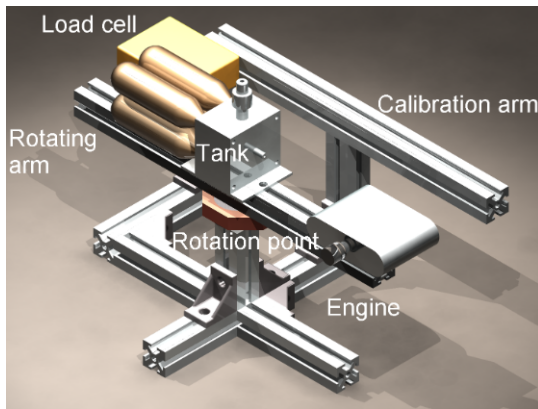


Figure 6.8: Thrust bench TB-50m, by Janssens [5].

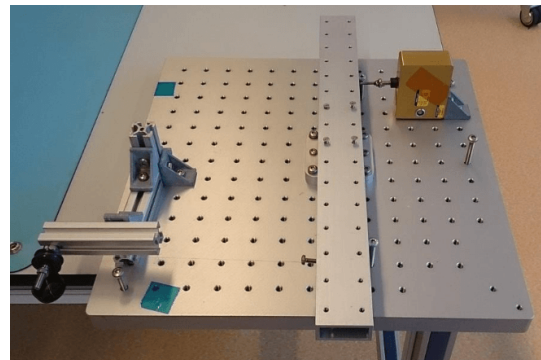


Figure 6.9: Thrust bench TB-50m, by Krusharev [6]. The LRF400 sensor is clearly shown in the top right corner.

Both Janssens and Krusharev reported extensively in their theses what components (including data sheets) were used, the capabilities of the bench and the methods of calibration, both for atmospheric conditions and vacuum. This serves as a way to reassemble the stand using the modular Boikons profiles. Again, the LRF400 will be built in but for flexibility, the Futek LSB200 (also advised by Janssens) is also present at the faculty of AE (see Appendix C.2 for the data sheet). This is a higher range thrust sensor, up to 100 g (or 1000 mN). However, the sensor appears to be inaccurate below 15 mN. For now, the lower range Futek LRF400 will be used in the thrust bench. Should it prove to be unsuitable, for example because of higher thrust ranges, the other sensor can be selected. Be aware the the bench will be rebuilt and calibrated around the LRF400; implementing the LSB200 instead is not complicated, as it has a simple thread connection on both sides, similar tot the LRF400. However, the standard thread is different, so another bolt will be necessary.

### Rebuilding AE-TB-50m

Thus, the TB-50m was (again) built out of the parts scattered in the AE cleanroom. It has a good resemblance to the Krusharev version, however a few adjustments can be spotted in Figure 6.10; extra Boikons profiles are added for more stability and for more flexibility in the alignment of thruster and sensor. The middle beam is mounted on the bearing used by Krusharev. Figure 6.11 shows the connection of the rotating beam to the sensor.

Because the test stand was rebuilt from scratch, the calibrations performed by earlier users were not valid. As such, they had to be redone. But first, the sensor output was calibrated, see next subsection.

### Relating LRF400 sensor output to force

As with Krusharev's stand, the LRF400 sensor will be measuring the thrust exerted by the engine. The sensor will be connected via an RS-232 cable to an NI DAQ USB-6008 device (see C.5 for the data sheet). In turn, the DAQ is connected via an USB cable to a computer. The sensor (Appendix C.1) will have a rated output of  $1 \text{ mV V}^{-1}$ . For an excitation voltage of 10 V which the DAQ provides, this will only amount to a measurable range of 10 mV, lower than the DAQ's absolute accuracy. As such the analog amplifier shown in Figure 6.12, named Scaime CPJ Rail (see Appendix C.6 for data sheet), was added to the circuit. It boosts the voltage (or current output, per user requirement) to 0-10V. In its data sheet, the gain is not displayed, but increasing the rated output from 10 mV to 10V will give a gain of 1000.

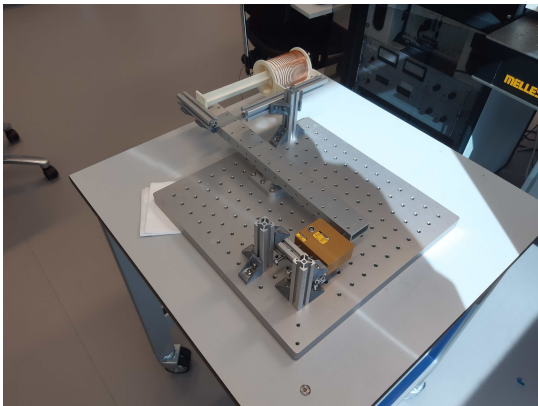


Figure 6.10: Thrust bench TB-50m, by Takken. Again, the LRF400 sensor is shown in the bottom.

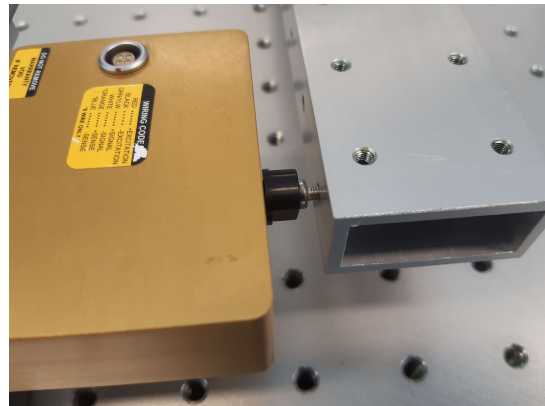


Figure 6.11: Connection of the rotating beam to the sensor.

Now, the sensor voltage values are to be related to force values. This will be a linear relationship in the order of  $y = ax + b$ , where the slope  $a$  and the intercept  $b$  need to be determined. In order to do this, a set of weights (with known masses) will be applied to the thrust sensor.

At first, a set of weights from the AE cleanroom will be weighed on the Mettler Coledo AG245 electronic scale (for data sheet, see Appendix C.7). The scale has a reported accuracy of 0.1 mg or  $1 \times 10^{-3}$  mN. Figure 6.13 shows the weighing setup and Table 6.1 presents the masses in the first two columns. Note that additional masses in the form of small bolts and nuts were added to the box by a fellow student, which are numbers 5 to 9 in the table. These were measured on the scale as well to increase the number of data points.

Then, those weights were laid on the upright (vertical) force sensor, see Figure 6.14. Using a simple [Laboratory Virtual Instrument Engineering Workbench \(LabVIEW\)](#) script, the voltage output of the sensor via the CPJ Rail and DAQ was read. This gave a relation between the mass and voltage, where the mass can be converted to a force by multiplying the mass with the local gravitational acceleration, assumed to be  $9.81 \text{ m s}^{-2}$ . See the third column in Table 6.1. Thus appeared a linear regression line between the weights' weight and voltage for the sensor in Equation 6.1. During this test, the sensor did not respond well to the lowest masses (downwards from 0.200 g or 2.0 mN); the readings were fluctuating between values, e.g. for an indicated mass of 0.002 g the readings were either 0.0048 mN or 0.0020 mN. This was not seen as an issue, see further below.

$$V_{LRF400} = 0.0972 \cdot F_{LRF400} - 1.4701 \quad (6.1)$$

For the range of 2-100 mN. Here the force  $F_{LRF400}$  is in mN and the voltage  $V_{LRF400}$  is in V with an  $R^2$  value of 0.999 998 7, see Figure 6.15. Thus, the regression line fits the data very precisely, despite the fluctuating voltage values for lower masses. Conversely, the force can be made dependent on the voltage, see Equation 6.2.

$$F_{LRF400} = 10.28 \cdot V_{LRF400} + 15.12 \quad (6.2)$$

Again, with force  $F_{LRF400}$  in mN and the voltage  $V_{LRF400}$  in V. It should be noted that the sensor will not be placed in an upright position in the test stand, but in a horizontal way. When the sensor was rotated 90° during testing, the sensor voltage under rest (so no applied load) did change from  $-1.47 \text{ V}$  (equivalent to 15.12 mN) to  $-4.09 \text{ V}$  (equivalent to 42.10 mN). The latter value in Equation 6.2, the intercept, is thus only valid for vertical measurements, for horizontal measurements the intercept should be adjusted to 42.10 mN. However, the test stand can still be calibrated for the slope value.

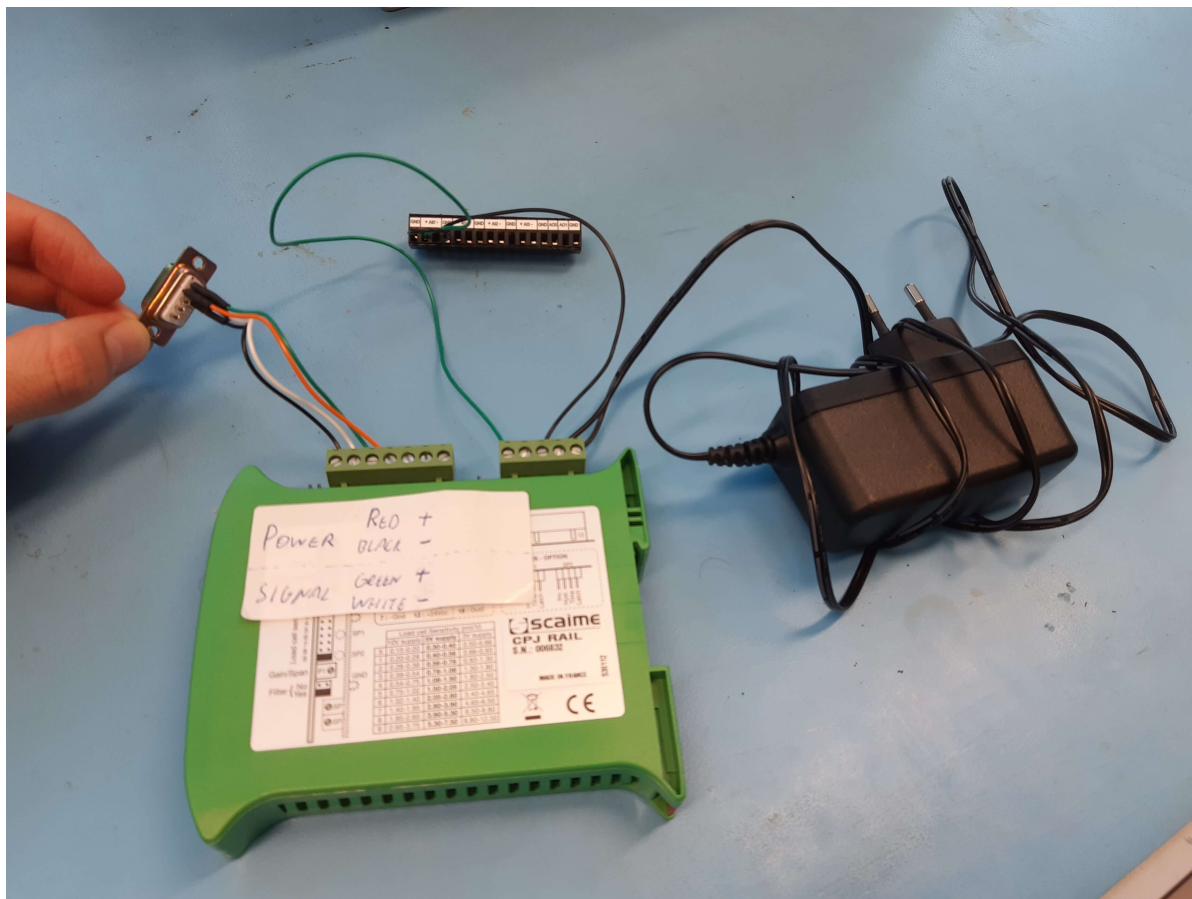


Figure 6.12: The analog amplifier Scaine CPJ Rail. It has three connections: the right to the power grid (230 V), the middle towards the DAQ device and the left to the RS232 cable of the thrust sensor.

### Calibrating AE-TB-50m

Now that there exists a relation between the sensor voltage output and force, the test stand as a whole can be calibrated. In order to this, two simple experiments were thought of: calibrating by using electromagnetic force, and calibrating by simple weights of which the masses are known (presumably the same weights as used before). Regarding the latter, some low friction pulley of some sorts should be added to the stand over which a wire attached to a basket is suspended. This was executed by Janssens as well, however those parts cannot be found at this instant. Thus, the other way, by electromagnetic force, was used.

At the faculty of AE exists a so-called [Variable-Turn Density Coil \(VTDC\)](#), developed by R. Bijster in 2014 [66]. It creates a homogeneous magnetic field while current runs through the coil which will induce a electromagnetic field if any magnet is inserted. For more details, see his thesis. In 2020, fellow students H. Versteeg [67] and A. Pappadimitriou related the current to the force, which turned out to be  $0.826 \text{ mN A}^{-1}$  with  $3\sigma$  confidence bounds of  $\pm 0.006 \text{ mN A}^{-1}$ , where  $\sigma$  is the standard deviation.

Both the [VTDC](#) and the actuator holding the magnet are available in the AE cleanroom. Thus, mounting the coil and actuator on the bench provided an easy method to calibrate the bench. In Figure 6.10, the coil and actuator are shown at the top.

The test was setup as follows: a [LabVIEW](#) script, created by Versteeg, would raise the current from 0 to 20 A in steps of 1 A. The current would be monitored at a sample rate of 100 Hz and each step would be held onto for 60 s, thus giving 6000 data points per step or 120 000 in total for the test. At the same time, another [LabVIEW](#) script would save the sensor force readings, adjusted by



Figure 6.13: Measuring the weights with the electronic scale Mettler Toledo.



Figure 6.14: Measuring the sensor voltage output with the use of the weights.

Table 6.1: Sensor voltage output versus mass.

#	<b>Indicated mass [g]</b>	<b>Measured mass [g]</b>	<b>LRF400 voltage output [V]</b>
<b>1</b>	10	10.0024	8.0705
<b>2</b>	5	5.0017	3.3025
<b>3</b>	2	2.0005	0.4397
<b>4</b>	1	1.0000	-0.5142
<b>5</b>	0.6290	0.6289	-0.8704
<b>6</b>	0.3872	0.3877	-1.1045
<b>7</b>	0.2872	0.2871	-1.1961
<b>8</b>	0.2142	0.2156	-1.2673
<b>9</b>	0.0725	0.0718	-1.3996
<b>10</b>	0.0451	0.0446	-1.4301
<b>11</b>	0.500	0.5002	-0.9925
<b>12</b>	0.200	0.1999	-1.2775
<b>13</b>	0.100	0.0998	-1.3691
<b>14</b>	0.050	0.0498	-1.4199
<b>15</b>	0.020	0.0200	-1.4505
<b>16</b>	0.010	0.0099	-1.4606
<b>17</b>	0.005	0.0048	-1.4708
<b>18</b>	0.002	0.0020	-1.4708

the aforementioned Equation 6.2 at a pace of 3 Hz, which then gave thrust information for 3,600 data points. These force readings were then adjusted according to Equation 6.3.

$$F_{EM} = F_{LRF400} \cdot \frac{d_1}{d_2} \quad (6.3)$$

Where  $F_{EM}$  is the electromagnetic force exerted by the coil-actuator pair in mN,  $F_{LRF400}$  is the outputted force of the sensor in mN,  $d_1$  is the distance of the sensor to the centre of the bearing (along the beam) in mm and  $d_2$  is the distance of the centre of the bearing to the actuator (along the beam) in mm. The latter were measured using a caliper and determined as  $d_1 = 175.00$  mm and  $d_2 = 167.70$  mm.

Then, the resulting adjusted  $F_{EM}$  would be averaged for each step of 1 A. The same was done for the current values recorded by Versteeg's script. Thus, these 20 data points were then plotted and a regression line was drawn to determine the slope of the graph. If the test stand adds no significant friction to the measurements and parts are properly aligned, this value should be close to the previously

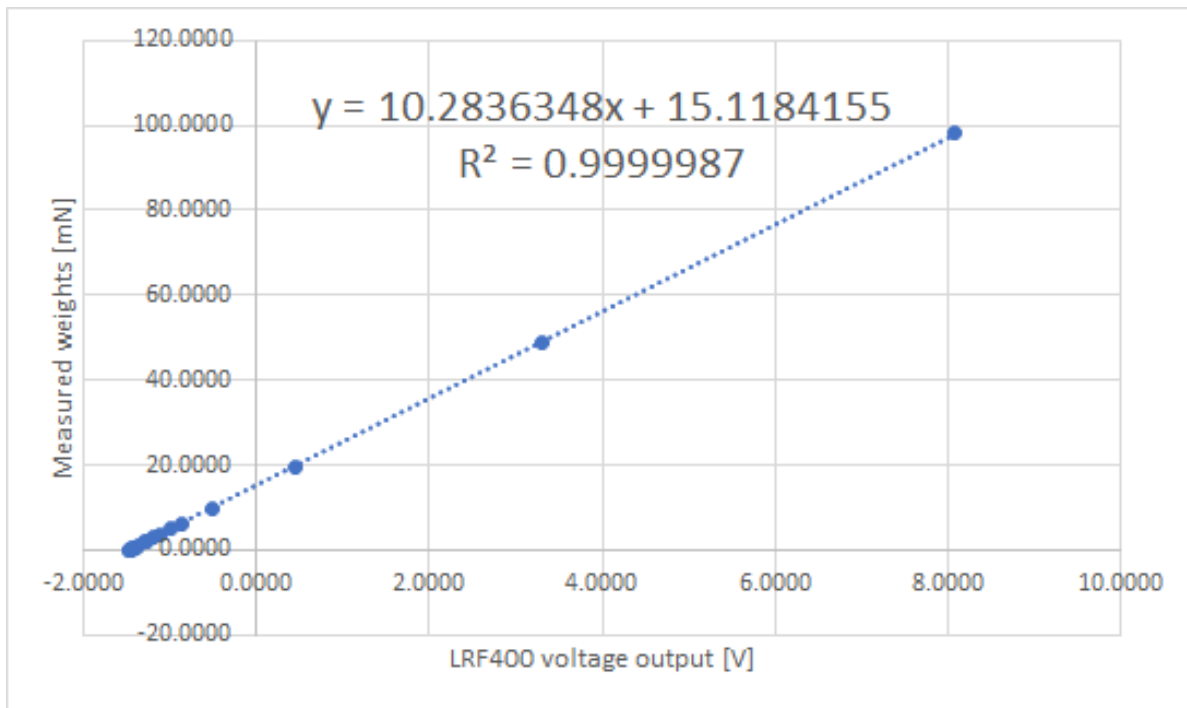


Figure 6.15: Weight on sensor versus voltage.

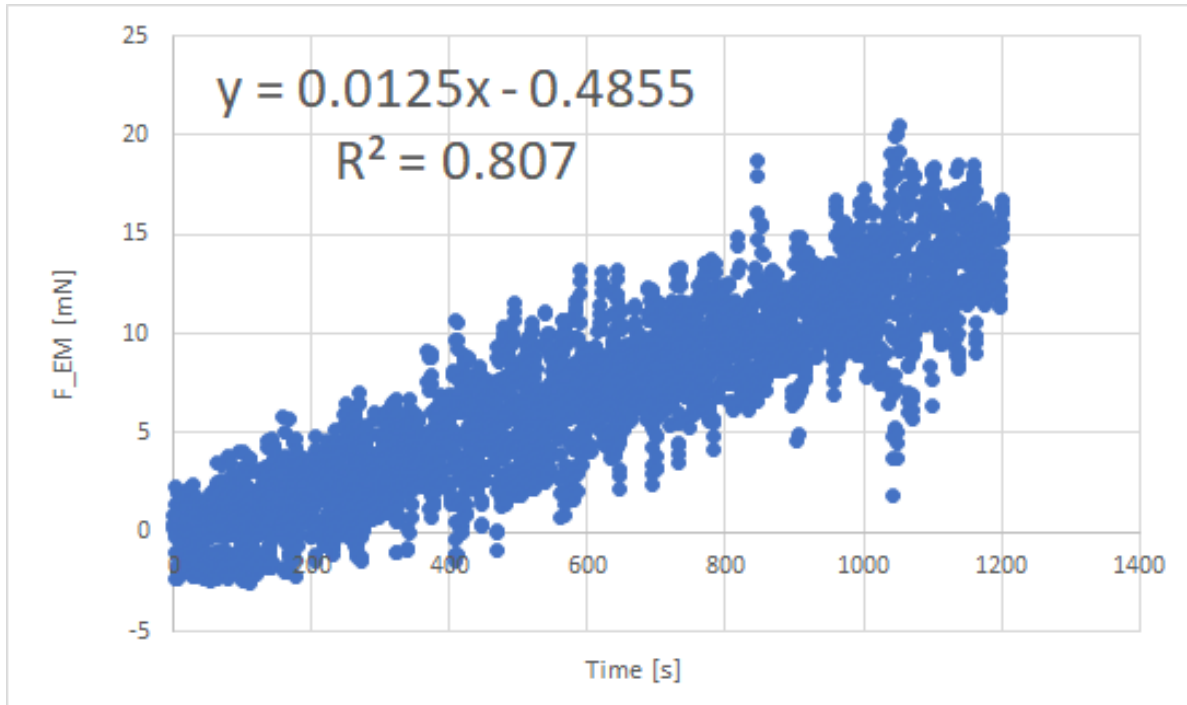
mentioned  $0.826 \text{ mN A}^{-1}$  value. Please note again that only the slope can be determined from the graph, the intercept is of no value as the sensor is turned sideways to be in the horizontal plane. By surveying previous test runs, the intercept value was manually entered at  $42.10 \text{ mN}$ , in contrast to the (vertically aligned) value reported in Equation 6.2 of  $15.12 \text{ mN}$ . As shown before, the intercept is not important as it can be easily determined at the start of experiments or during the analysis afterwards.

In Figure 6.16 the graph with the 3600 data points containing the  $F_{EM}$  values is shown versus the time which equaled 20 steps of 60 seconds each at a sample rate of 3 Hz. A significant amount of deviation is detected. Versteeg and Valente suggested that this is the noise induced by building vibrations and any by-passers. Figure 6.17 represents the averaged data per step versus the current. Note that the current was also averaged for the 20 steps, because the actual current running through the coil was not exactly equal to the integers 0, 1, 2.... The slope of this graph equals  $0.788 \text{ mN A}^{-1}$  with an  $R^2$  of 0.9994, which is 4.72 % off from the reported value by Versteeg and Pappadimitriou. Please note that the intercept value is not exactly zero, although the previously chosen value of  $42.10 \text{ mN}$  was apparently close.

What was later discovered is that, at the higher current range (from 16 A onwards), the coil will heat up and affect the magnetic field. Omitting the data points higher than 16 A would result in a more accurate slope value of  $0.800 \text{ mN A}^{-1}$ , which only differs by 3.26 % from the coil value.

However, it was decided to redo the test and add more Boikon profiles to secure the sensor and coil better to the base stand. A very precise alignment was also of importance as mentioned by Valente in her thesis [4]. Figure 6.10 depicts the stand ready for the second experiment. The test was conducted in the same way as test 1, however now steps of 0.5 A were taken. Distances  $d_1$  and  $d_2$  were measured at 175.00 and 170.91 mm respectively. The intercept (see Equation 6.2) was reset at  $53.95 \text{ mN}$ . Following the procedure described above, it resulted in the graphs depicted in Figures 6.18 and 6.19.

As seen from Figure 6.18, the noise of the unaveraged data is much lower in test 2 than it was in test 1. Some outliers are seen after 2000 s, this is likely caused by the author entering the cleanroom. Figure 6.19 depicts the slope value of  $0.803 \text{ mN A}^{-1}$ , already an improvement over the previous  $0.800 \text{ mN A}^{-1}$ .

Figure 6.16: Test 1:  $F_{EM}$  versus time.

from test 1. However, what is clearly seen in both pictures is again that the temperature has a large effect on the electromagnetic force; the second graph displays an offset starting at 16 A. In fact, at the end of test 2, a smell was detected in the cleanroom which was the coil overheating.

Only taking the force values up to 16 A, gave a precise ( $R^2$  equal to 0.9997) gradient of  $0.823 \text{ mN A}^{-1}$ , with a very minor difference of 0.31 % with respect to the coil slope of Versteeg and Pappadimitriou. Furthermore, for test 2  $\sigma$  was calculated for each step of 0.5 A, which consisted of 180 (or 3 Hz over 60 s) data points. These standard deviations were then averaged over the range of 0-16 A, which resulted in a  $\sigma$  of  $0.347 \text{ mN}$ . Comparing this value to the reported standard deviation of  $3.6 \text{ mN}$  of TB-1.1 by Valente [4] at a thrust of  $948.5 \text{ mN}$ , one can see that this is a huge improvement. Be aware that this standard deviation has been asserted for a small range. However, within this range no increase in standard deviation was noticed when increasing the current (and thus thrust). It is expected that the value is still significantly lower when approaching the upper limit of the TB-5m, which is  $100 \text{ mN}$ .

The standard deviation above is averaged for a varying range of current (and thus thrust). More interesting is to see test 2 as a combination of separate tests at different currents: to be precise a combination of 33 subtests, from 0 A to 16 A. These can be normalized to one and the same current, for instance 10.0 A. Please note that is not possible for the 0 A reading, leaving 32 tests. This allows us to calculate the  $3\sigma$  (99.7 %) confidence bounds for the mean of these experiments. This indicates that, if the test is redone, with 99.7 % confidence one can say that the mean of this test will fall within the confidence bounds. The mean  $\mu$  of the 32 subtests (all at 10 A) equals  $8.1699 \text{ mN}$ , with a  $\sigma$  of  $0.2210 \text{ mN}$ . Then, the confidence bounds are found by Equation 6.4.

$$F_{LRF,10A} = \left( \bar{\mu} \pm 3 \cdot \frac{\sigma}{\sqrt{n}} \right) = \left( 8.1699 \pm 3 \cdot \frac{0.2210}{\sqrt{32}} \right) = (8.1699 \pm 0.1172) = (8.1699 \pm 1.43\%) \quad (6.4)$$

Where  $n$  is the amount of samples to calculate the mean thrust.  $F_{LRF,10A}$  is in mN. Note that the mean is very close to the desired value of  $8.26 \text{ mN}$ . The difference is attributed to minor errors

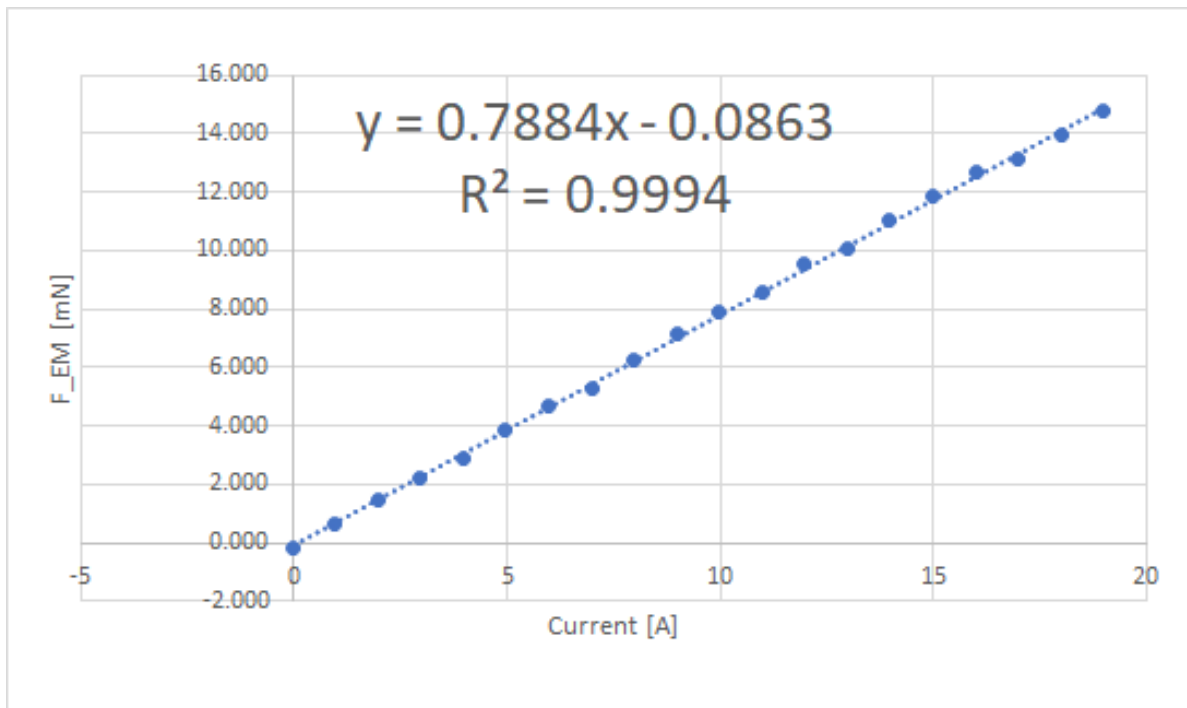


Figure 6.17: Test 1: averaged  $F_{EM}$  over steps of 1 A.

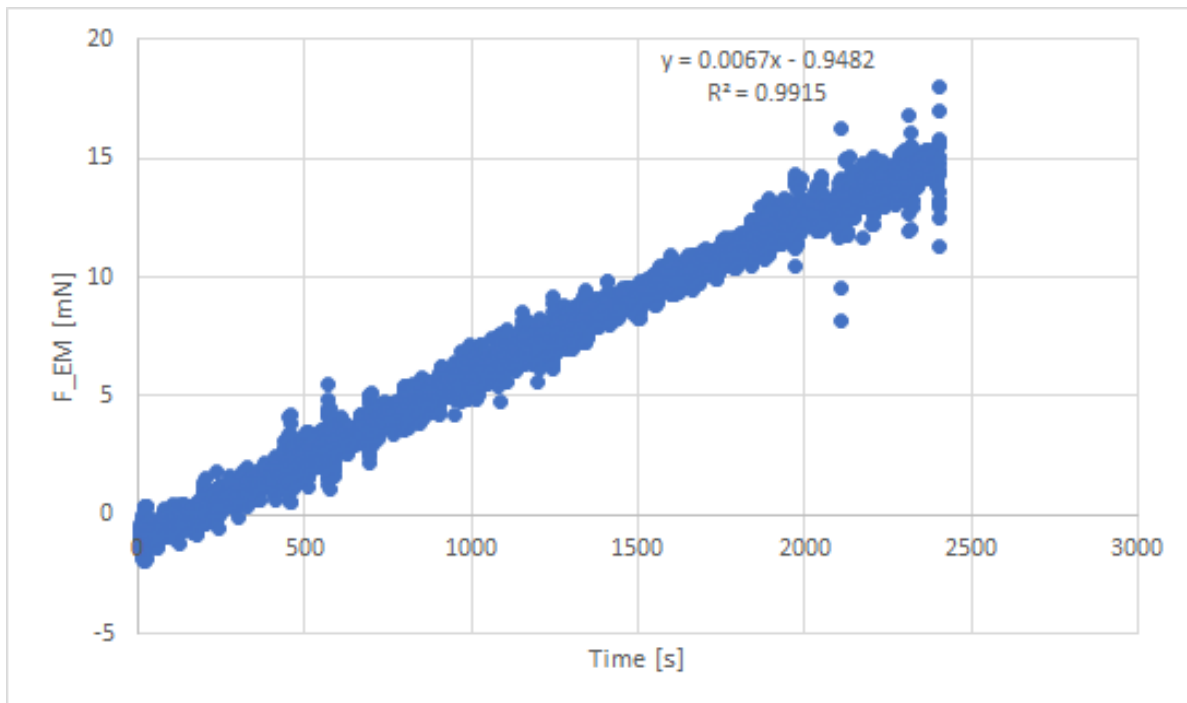
in hand measuring the distances and possible interference of the coil connections to the computer, causing variations in the magnetic field. A possible third explanation is that the bench was not leveled horizontally. For this, level sensors were needed but these were forgotten. It is known that tilting the sensor has an effect on the nominal measurements, however if the bench is tilted at the same angle these effects could be cancelled out in the gradient. See the recommendations for further improvements on this.

Because the difference is minor, the bench is considered to be calibrated up until 16 A or equivalently 12.3 mN. The intercept, set at 53.95 mN in the beginning, should be adjusted by 0.80 mN to a value of 54.75 mN.

#### 6.4.3. Test bench conclusions & recommendations

AE-TB-50m was rebuilt and calibrated for the range of 0-12.3 mN. Two possible methods to calibrate the bench were discussed in this section. The first one is by electromagnetic force with the use of a combination of coil and magnet actuator, the second is by hanging weights from a wire and (low-friction) pulley. It is recommended to alter the first method to be able to measure higher forces, because the upper limit of the current combination is 20 A or approximately 16.5 mN for a bench which could potentially go to 100 mN. Furthermore, the coil overheats if kept at higher currents ( $>16$  A) for extended periods of time. Altering can be achieved in a number of ways: one can install an actuator having more or stronger magnets or elongate the rotating beam in the direction of the coil.

It is also advised to recalibrate the bench when a thruster is fit onto the bearing arm. It is not known what the effect would be of the added mass. The two methods described above would be suitable for this. Furthermore, it would be interesting to see what the influence of room temperature would be on the bench output, as Valente already reported an influence of temperature on the readings for her TB-1.1. Next to that, looking into the tilt of the bench would be an improvement, as this could have an influence on the output. Last thing to mention is that the bench can be calibrated in combination with the LSB200 sensor, to see if its range can be extended to 1000 mN.

Figure 6.18: Test 2:  $F_{EM}$  versus time.

## 6.5. Thesis alteration

This section will detail the reasons to not commit to further experiments and the subsequent change in plan to finish the project.

### 6.5.1. Experiment stop

What became apparent in Section 5.5 was that the reduction of the number of channels from 6 to 1 proved disastrous to the usefulness of the heat exchanger; the cross-sectional area through which the propellant had to pass was simply too small, which resulted in enormous pressure losses or the feed system not delivering enough pressure to overcome the heat exchanger barrier. Next to that, the channel was so small that it approached the nozzle throat area; effectively, an extra nozzle was created inside the [RAC](#), which had again a negative impact on the thrust and specific impulse.

Next to that flaw, another was discovered during the few test runs that were done in this chapter: the heat exchanger leaked, especially at the inlet and outlet and at the outlet side of the cavity. The latter was because the holes in both cap and outer cylinder should line-up, but when they did, the cap was not entirely screwed on the cylinder. It was tried to remedy this problem with gas tape (teflon) and heat resistant fireplace kit, which helped to some extent. However, after a few days the kit was hardened and it appeared to block the channel; unfortunately, the piece could not be opened because of the same kit. This problem could be mitigated in the design by excluding thread connections and allowing hard-soldered connections. When trying to disassemble the [RAC](#) with brute force, the connection to the copper nozzle was broken as well.

A third reason to stop the experiments was because of the COVID-19 pandemic. As such, access to all faculties at [DUT](#) was restricted and no experiments could be carried out at the faculty of [3mE](#) anymore.

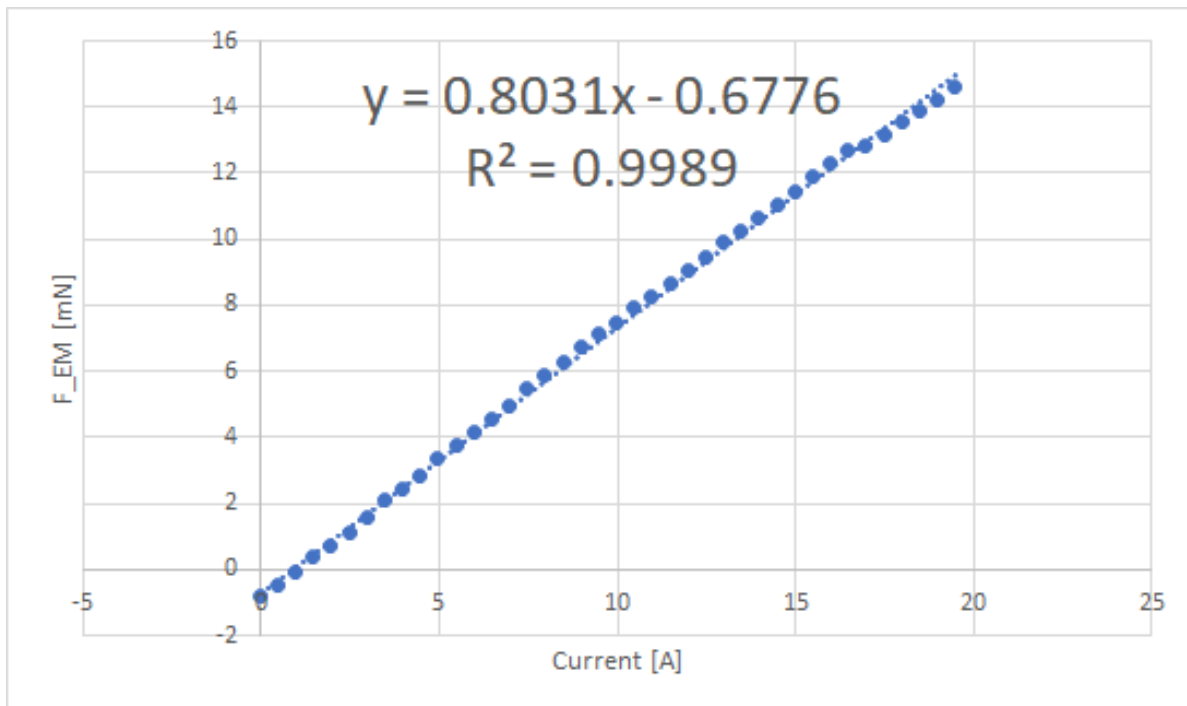


Figure 6.19: Test 2: averaged  $F_{EM}$  over steps of 0.5 [A].

### 6.5.2. Plan for continuation

All the flaws and setbacks combined, it was decided to decommission STT2 and start looking for alternatives to validate the preliminary model presented in the previous chapter. It is a pity that a project which took a lot of resources could not continue, but a new plan was setup.

In order to check if the designed solar thermal thruster would meet the goal and requirements from Chapter 2, the physical experiments were altered to simulation, by CFD. These simulations could accurately show what thermal efficiency was gained and what pressure losses would be experienced by the propellant flow. An additional benefit is that the simulations could also serve as a validation for the preliminary tool. Furthermore, the knowledge gained from the simulations could be used to make a final thruster design, dubbed STT3. Chapter 7 will show the CFD setup, analysis and STT2 results while Chapter 8 will focus on that final design.

# 7

## Computational Fluid Dynamics modelling

As explained in the previous chapters, the experiments could not be carried out in this thesis. So, it was decided to make a new **STP** thruster design with the knowledge gained during the design and manufacturing phase of **STT2**. In addition to that, **CFD** analyses will be used to assess the engine's performance.

The current chapter will describe the setup and execution of multiple **CFD** models. When constructing the preliminary tool in Chapter ??, it became clear that analytically analysing the thermal performance of an **RAC** outputs results that do not entirely match the actual data from experimental study. This was especially the case in the tool when forced convection (flowing propellant) was applied, see the third case in that chapter. Because the outgoing propellant temperature is one of the crucial pieces (next to propellant pressure and nozzle dimensions) to calculate the **STP** specific impulse, a better method had to be found. Thus, **CFD** models were constructed.

The **CFD** models will be used to assess the heat flows in the **RAC**. The equations relating to those heat flows, being convection, radiation or conduction, were explained in Chapter ???. Using the **CFD** method, the heat losses can be confirmed and a better view can be acquired regarding the convection heat flow from **RAC** to propellant. When this is done, the impact of altering design choices on the propellant temperature can be assessed. One can think of a different propellant, aperture size, wall thickness, channel layout and heat exchanger length. The ultimate goal of this chapter will be to optimize the design of both Leenders' and Takken's heat exchangers in terms of mass and propellant temperature.

In this chapter, the general workings and uses of **CFD** will first be explained. Then, the use for this project will be given, followed by a section showing what program was chosen for the numerical calculations. Afterwards, multiple sections on the cases from the preliminary tool chapter are presented. These cases will be setup, executed and post-processed. When the cases confirm the validity of the **CFD** models, the **CFD** method will be used to assess the performance of the **RAC** designed by the author. In the end, Leenders' **RAC** design will be changed in order to increase its performance.

### 7.1. Computational Fluid Dynamics workings and uses

**CFD** is the numerical analysis of a flowing fluid (gas or liquid) and its properties (temperature, pressure etc.) using computational power. The fluid flow and related heat transfer are governed by the

**Navier-Stokes (equations) (NS)** or simpler Euler equations [68]. The NS equations are partial differential equations consisting of inertial, viscous, external force and pressure terms, derived from the mass, momentum and energy conservation laws [69]. They can be analytically solved for simple cases, such as laminar pipe flow or the flow between two parallel plates. However, for more difficult geometries, approximate solutions can be found using numerical methods, which can be performed using computational power. As such, CFD emerges as a contender versus the more traditional two methods, which are experimental fluid dynamics and analytical fluid dynamics. The latter can prove sufficient for more simple heat transfer problems, for instance to calculate the natural convection heat loss at the outside of a simple geometric figure. This was already seen in the preliminary tool chapter. An experimental approach can potentially give the most accurate results in fluid flow and heat transfer problems. However, experiments are often expensive, time-consuming and not flexible when it comes to altering the setup. CFD could be a good addition to those two methods, as it is more accurate than an analytical approach and more flexible in terms of setup than testing.

Starting in the 70s of the previous century, researchers of CFD would often write their own computer code in order to numerically analyse the fluid flow and its properties. It was tedious, time-consuming and not very user-friendly. As such, companies and academia asked for better available software packages, which can be both commercial and non-commercial. Nowadays universities concerned with topics on aerodynamics, hydrodynamics and other often offer courses on CFD using these packages.

In general, CFD analysis follows a procedure where first the physical object which is subject to the simulation is defined. This can be done using CAD software and is the start of the so-called pre-processing. Then, solid and/or fluid regions are discretized or divided into small elements, which form the mesh. Next, the models that are applicable to the simulation are defined. One can think of the flow type (laminar, turbulent) which needs to be set, if thermal models need to be applied, if radiation is present and so on. Afterwards, the boundary conditions, such as the fluid flow velocity, starting temperatures and applied thermal loads are given. Then, the solver is chosen and the simulation commences. The software computes the relevant equations for each individual element in the mesh and tries to approach a solution (converge) where the differences or residuals between the elements are lowest. Once the simulation has converged, the user can extract the relevant data in the post-processing phase.

CFD has many applications in many areas. One can think of the fluid flow and subsequent pressure fields around an aircraft wing, the aerodynamic forces acting on driving vehicles, the smoke pattern in a fire, the thermal efficiency of a heat exchanger and so on. It is a very powerful tool on the conditions that the user has knowledge of CFD and the package he or she is using.

## 7.2. Goal of Computational Fluid Dynamics for this project

As was shown in Chapter ??, the preliminary tool could not accurately predict the heat transfer of the RAC to the flowing propellant in the channels. The losses by convection and radiation to the outside were accurately predicted by both Leenders' and Takken's analytical tool, but the empirical relations used in the propellant convection did not give the expected results when compared to the experimental thermal data from Leenders [3]. It was thus decided to utilize CFD analysis to get more insight in this part of the engine, especially because this heat flow determines the resulting fluid temperature.

The resulting fluid temperature is important as this is a major contributor to the efficiency of the thruster. An increase in propellant temperature theoretically raises the specific impulse by the square root of that same increase, according to Equation 4.56. Transferring as much as possible heat from the incoming radiation to the propellant is thus beneficial. When designing an STP thruster, which includes a feed system, heat exchanger or RAC and nozzle, the amount of thrust and the specific impulse are set as requirements, from which the mass flow follows. Once the ambient properties (background temperature, pressure) and the nozzle chamber pressure are known, one can calculate the required chamber temperature. This chamber temperature is then a requirement which, together with mass

flow, dictates the efficiency in which the heat exchanger needs to heat the propellant coming from the feed system. **CFD** can play an important role in this matter, as it could accurately predict the thermal performance of such a heat exchanger without the need for expensive and inflexible experiments.

Next to determining the amount of heat flowing towards the propellant, the heat flux losses towards the ambient can be quantified. They have been determined analytically but they could not be compared to Leenders' values, due to the lack of data in his thesis. It will be very interesting to see what losses are greatest and how those can be mitigated or decreased, for instance by insulation on the outer walls, use of paint with low emissivity or decrease of the aperture through which the radiation enters. Next to this, determining the pressure loss over the **RAC** is also useful information as the resulting outlet pressure is a contributor to the thruster system  $I_{sp}$ .

Note that, in this chapter, only the heat exchanger or **RAC** will be discussed. The nozzle and feed system, which together with the feed lines and connection line1s form the thruster system. The focus will be on the heat exchanger because analysing the system as a whole is considered out of scope for this project. For more information about **CFD** analysis on nozzles, see fellow students Krusharev [6] and Dickert (still conducting research).

The following will be executed in this chapter. At first Leenders' RAC, as part of **STT1**, will be physically modeled in the **CFD** software. Once this is done, an appropriate mesh is applied and boundary conditions are set. Three distinct cases, similar to those from Chapter ??, will be simulated with this model. From those cases, conclusions can be drawn on the validity of the model, see also next section. Once the thermal data from these simulations is deemed valid, the physical model will be changed to the design made by the author (**STT2**, see Chapter 5). This is especially important now that the current corona crisis and other issues hinder the execution of experiments (see Chapter 6). Again, simulations will be performed to assess the thermal efficiency of the **STP** design. After completion of these simulations, the results can be compared to the performance of Leenders' **RAC**. With the knowledge gained, a redesign of Leenders' **RAC** will be done with a focus on the channel layout and the aperture size. In a final simulation, the thermal performance of this redesign can be quantified and the potential  $I_{sp}$  increase will be given. As such, the **CFD** analysis can be a great addition to the preliminary tool as it can more accurately predict thermal efficiency and pressure losses in a designed **RAC**, without the need for costly and time-consuming experiments.

### 7.3. Verification and validation

Verification and validation are procedures to check if the intended design meets requirements and real-life performance. Verification for the **CFD** numerical simulation means that the outcome matches outputs from the analytical tool made in Chapter ???. The **CFD** results are deemed accurate enough once the maximum heat exchanger temperature lies within 10 %, which is the same requirement as stated in that chapter. A difference of 10 % in temperature will lead to a difference of 3.2 % in thruster specific impulse. Various parts of the simulation code can be verified, as the tool quantified all heat fluxes present in the system.

The same criterion will be used for validation, which for this case will be the comparison of outputs to experimental data. The experimental data from Leenders that exist for his three cases are to be used. Unfortunately, as stated before, these only exist in graphical form, so the relevant heat fluxes cannot be distinguished. Added to that, the documentation of the cases was not perfect, so errors could arise here.

Because the shape of the **RAC** of **STT1**, or especially its channel section, is unusual, verification and validation will be hard as no analytical or experimental results will be available of such a geometry. However, comparing temperature and heat flux results to various well-known cases from literature such as free convection from a plate and one phase flow through a circular pipe can be done. The results obtained from those cases will be compared to the cases presented in this chapter in order to check

"the sanity" of the results. In Section 7.8, a pipe flow verification case is executed in order to partly verify and validate the results in that section. Furthermore, various papers state the validity of Ansys Fluent in other cases, e.g. on natural convection along a vertical plate [70] or heat transfer in pipe flow [71].

The author is aware that verification and validation will be hard for the simulations performed here. It would be great if more experiments would be carried out to ensure the results found here are valid, but that will be out of the scope for this project. Note that previous users of CFD for microthruster systems, such as Das [26] and Krusharev [6] did not perform any verification nor validation (although Das did do comparisons to her Matlab model) so no help could be found there.

## 7.4. Computational Fluid Dynamics program choice

A number of CFD programs are available for the simulations described in this chapter. The most prominent ones among those are Ansys (Fluent or CFX), Comsol and OpenFoam. The first two are software packages from commercial companies, while the latter is an open-source program which is thus freely available. In previous theses at SSE and in papers related to STP those programs were used for a variety of tasks, such as ray tracing, conjugate heat transfer and nozzle performance. For instance, Krusharev utilized Ansys Fluent in his thesis to determine the thrust and subsequent specific impulse of four different nozzles [6]. Likewise, Ferreira recommended to replace his self-made analytical tool by an Ansys model which he thought could be more accurate [55]. Pino used Ansys not for CFD, but to structurally analyse his solar concentrator, which also happens to be in the area of STP [45]. In various handbooks, such as Tu et al [68], Rohsenow [52] and Zandbergen [22], Ansys (Fluent) is mentioned. Comsol was used by Das to model the incoming radiation of a solar thermal thruster [26] and is also mentioned in the handbooks. OpenFoam was used in the past by students Denies for rocket engine regenerative cooling thermal analysis [72] and Khamis for fluid flow analysis in MEMS thrusters [73]. OpenFoam is regarded by some to have a steeper learning curve, also because it lacks a dedicated Graphical User Interface (GUI) which Ansys and Comsol do possess.

It should be noted that the author of this thesis does not have any prior knowledge in CFD. Thus, after consulting some fellow students and staff at the faculty of AE, the choice was made to use Ansys Fluent. Be aware that this could also have been one of the others, it mainly depends on the experience a user has. A student version of Ansys Fluent can be downloaded from the DUT software website [software.tudelft.nl](http://software.tudelft.nl). This version has a maximum amount of 512 000 mesh elements. During simulation setup and running, the manual was used extensively [74]. To get a grip on the software, multiple tutorials were watched, both from Ansys and [youtube.com](https://www.youtube.com).

## 7.5. Quantification of losses to ambient

In this section, the quantification of thermal losses to the ambient is presented. As could be seen in Chapter ??, the heat exchanger loses heat because of convection and radiation to the ambient, both at the inner as the outer side of the RAC. This section will show the road map on how these losses are determined. Furthermore, this elaborate section will frequently be referred to in later sections, when the setup and execution of the individual cases is discussed. This section will thus show a step-by-step "recipe" on how to properly do a CFD analysis and produce useful results.

The heat exchanger will not be modeled in vacuum, but in air at room properties of 298.15 K and 1 atm. Modeling in vacuum would see the convection loss mitigated but the radiation loss increased dramatically, as the surrounding space is in general modelled at a temperature of 3 K.

Ansys Fluent has been chosen as the solver, but most of the tasks will be performed in Ansys Workbench which serves as a handy means to access all different Ansys modules. It consists of four tasks which are to be executed to complete a simulation: geometry, mesh, setup and post-processing.

All four will be explained in detail below.

### 7.5.1. Geometry

It starts off with the physical model of the **RAC** of **STT1**. The **CAD** drawings are available from Leenders' thesis [3]. Ansys DesignModeler is the **CAD** module that is integrated within the Workbench. Two **RAC** domains can be distinguished here: the **RAC** domain which is the material (in this case: copper) and the fluid or propellant domain (in this case: gaseous nitrogen). The material domain consists of the inner cone, outer cone and propellant ring. These are not modelled as separate entities but as one solid object. Any inconsistencies or minor gaps between the parts are thus not incorporated in the Fluent Model. After the material domain has been constructed, the fluid domain is etched out of the material.

In Figure 7.1, one can see the **RAC**. A cross-section is shown in Figure 7.2. The heat exchanger exit is slightly different than the drawings indicate. To simplify things here, the thread has not been modeled but simply constructed as a solid wall containing a hole with a diameter of 3 mm. In normal operations, a bolt containing a hole would be inserted in the exit, so it is expected not to have much impact in terms of mass or thermal performance. Figure 7.3 shows the fluid domain, with the propellant inlet at the left top and the exit at the right bottom. In Table 7.1, relevant sizes coming from the program are shown. Note that the **RAC** domain inner area is split into an inner cone wall and into an inner circular wall. Irradiation will only fall upon the earlier surface. The density of copper is taken from Fluent as  $8978 \text{ kg m}^{-3}$ . Note that the mass equals the sum of masses of the individual three parts as described by Leenders [3]. The outer surface area does differ significantly from the value given by Leenders (see also Table 3.1), which is mainly due to the fact that he did not take the ring into account for his calculations.

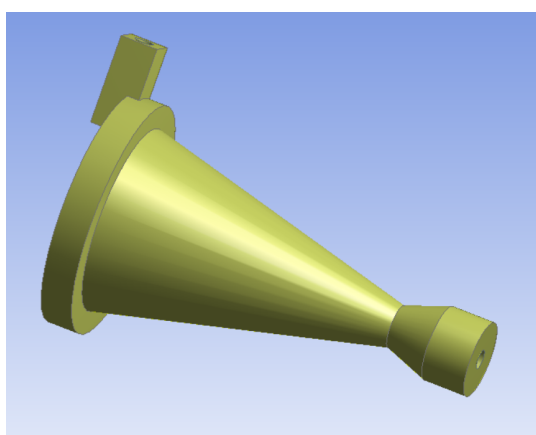


Figure 7.1: Solid domain of Ansys physical model of **STT1**.

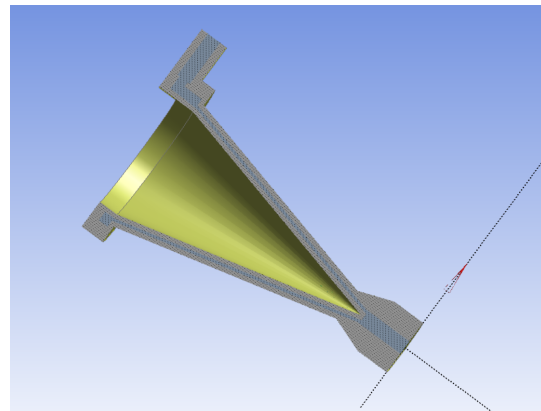


Figure 7.2: Cross-section of Ansys physical model of **STT1**. Note the smaller hole at the exit, which is on the right bottom of the picture. Furthermore, both inner walls (cone and circular) can be observed.

Table 7.1: **STT1** sizes by Ansys DesignModeler.

	<b>Size</b>	<b>Unit</b>
<b>RAC</b> domain inner cone area	2026	$[\text{mm}^2]$
<b>RAC</b> domain circular ring area	322	$[\text{mm}^2]$
<b>RAC</b> domain outer area	5124	$[\text{mm}^2]$
<b>RAC</b> domain volume	9732	$[\text{mm}^3]$
<b>RAC</b> domain mass (copper)	0.0866	[kg]
Fluid domain connection area	1995	$[\text{mm}^2]$

For the quantification of the convection and radiation losses, there are three options in Ansys Fluent: a surrounding ambient domain consisting of air combined with a radiation model, simple equations

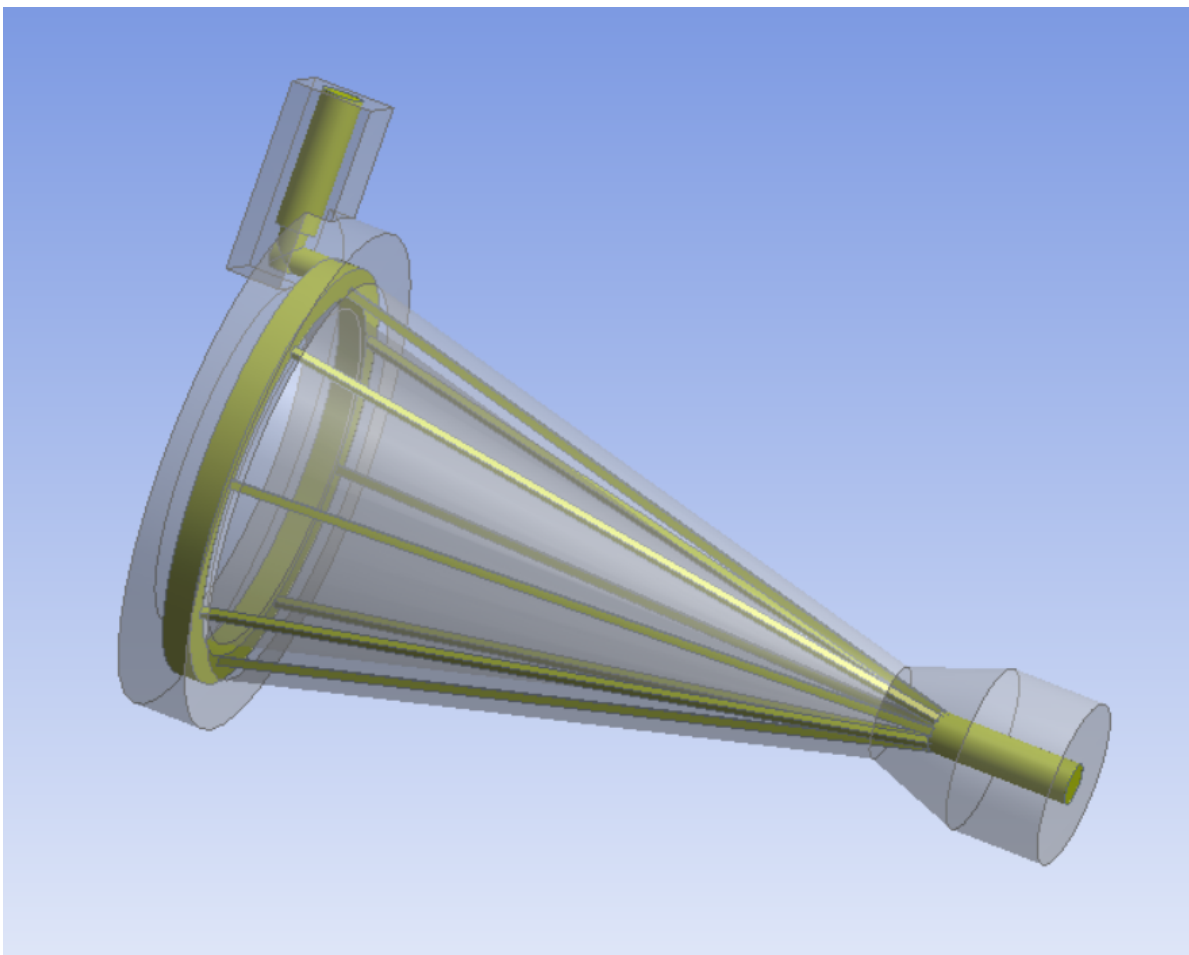


Figure 7.3: Fluid domain of Ansys physical model of STT1.

which require some inputs from the user or a mix of both. All three are explained below.

### 1. Ambient domain and radiation model

The first option is to build a rectangular "box" around the solid and fluid domain which will represent the surrounding air. See Figure 7.4 for an example. The upper wall of this box will be more distant from the RAC than the other walls, as natural convection from the heat exchanger to the ambient will be modeled as a loss. This way, the plume can develop and will not be hindered by the ambient domain "walls" before it leaves the ambient system. The size of the surrounding ambient domain is based on experience from the author and will be sufficiently large to allow the natural convection loss to develop but not be too large to prevent the amount of mesh cells becoming too large. The radiation is then calculated via the built-in Surface-to-Surface (S2S) radiation model from Fluent. The advantage is that it automatically implements the view factor (which is important for the inner cone) so the radiation loss is calculated accurately.

Downsides to this method are the increased computational time and the increase of complexity of the problem. Next to that, the inlet and outlet of the fluid domain need to be elongated so that the start and end outside of the ambient domain. This means that long tubing outside of the RAC is needed, which increases the complexity even further. It was surprising to see in a test run that this was needed, but the solver kept diverging because of the fluid "spilling" in the ambient domain. For the definition of divergence, see later in this section.

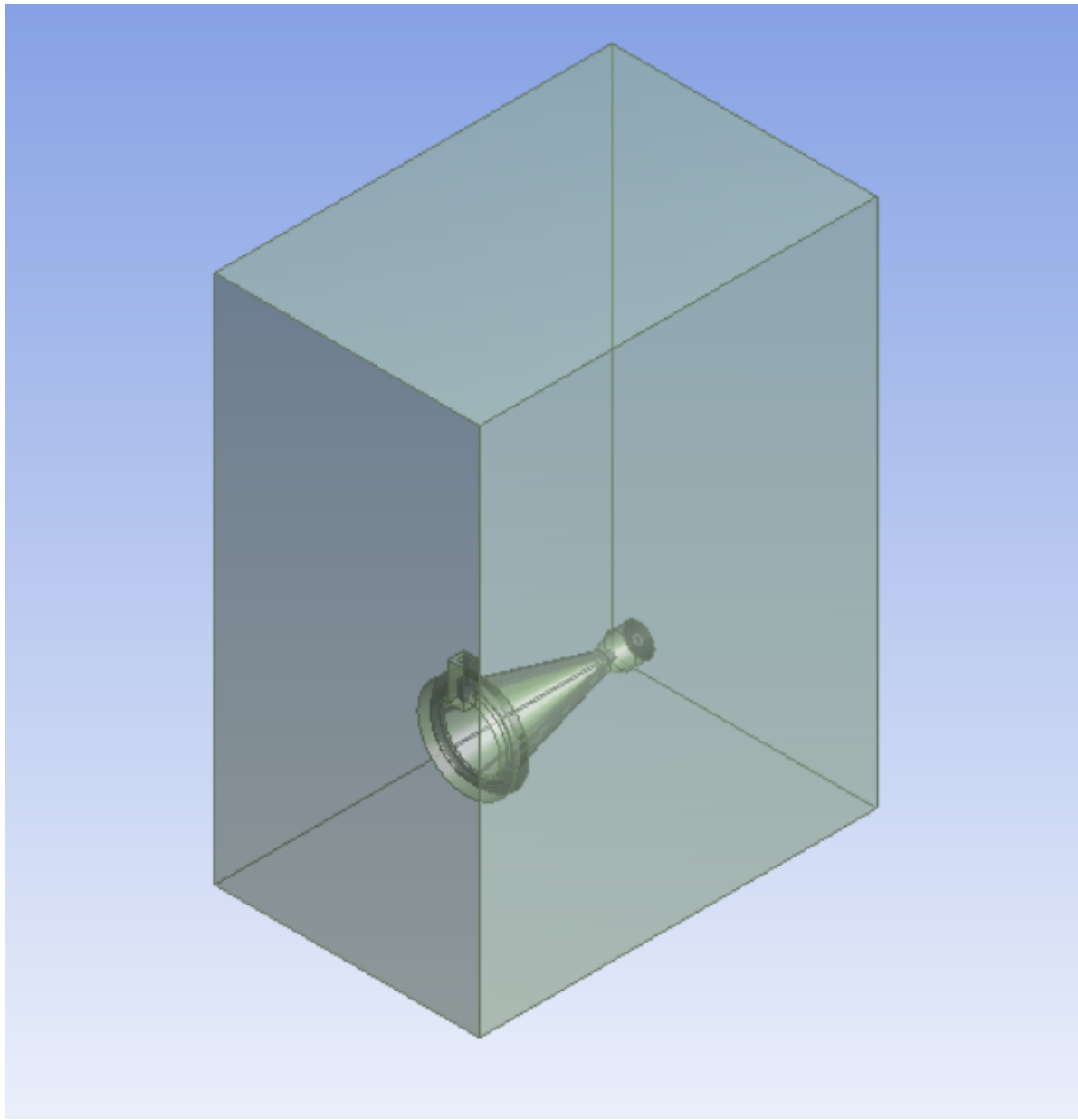


Figure 7.4: Air domain containing the RAC and fluid domain.

## 2. Equations with inputs from the user

Another option is to not model the ambient air surrounding the heat exchanger. This would save a lot of computational power and time and would allow the mesh in the solid and fluid parts to be more refined. Instead, Ansys hands the user the option to enter a convection heat coefficient  $h$  (in  $\text{W m}^{-2} \text{K}^{-1}$ ), free stream temperature  $T_{\text{inf},1}$  (in K), emissivity  $\epsilon$  (dimensionless) and external radiation temperature  $T_{\text{inf},1}$  (in K) for each surface. Using these four variables, the losses  $Q_{\text{conv}}$  and  $Q_{\text{rad}}$  (both in W) for each surface would be automatically calculated depending on the surface temperature  $T_{\text{surface}}$  (in K) according to Equations 7.1 and 7.2. In those equations,  $A$  is the surface area in  $\text{m}^2$  and  $\sigma$  is the Stefan-Boltzmann constant ( $\text{W/m}^2/\text{K}^4$ ). Although this is an easy solution which requires minimal computing power,  $h$  is usually hard to determine for natural convection (especially in non-standard geometric figures) and view factors are ignored in the radiation term. An approximation of  $h$  can however be found from literature. The absence of view factors can be handled by adjusting the emissivity factor if the view factor to the ambient is lower than 1, but it requires some hand calculations.

$$Q_{loss,conv} = hA(T_{surface} - T_{inf,1}) \quad (7.1)$$

$$Q_{loss,rad} = \epsilon\sigma A(T_{surface}^4 - T_{inf,2}^4) \quad (7.2)$$

### 3. A mix of both

A third option would be a mix of the two: at first the area-weighted average  $h$  is to be determined using the ambient domain but without fluid flow. Once this average is determined, the ambient domain can be deleted and the equations stated above can be used to determine the convection coefficient.

#### Choice for physical model

After some test runs with the physical RAC, the third option was chosen. The most prominent reason for this was that the solver did not converge when option 1 was followed. There simply were not enough elements present to both mesh the ambient and the fluid domain properly. Thus, first the convection coefficient  $h$  is determined without any propellant flow, then the ambient domain is deleted and the cases can be executed with the application of the earlier determined  $h$  to the outer RAC walls. The ambient domain will have a length of 110 mm, width of 50 mm and height of 100 mm. It will be placed around the heat exchanger symmetrically, except in the height direction; to account for heated air raising in the domain, it will extend more to the top than to the bottom.

### 7.5.2. Mesh

In Figure 7.5, a cross-section of the meshed ambient domain (the box), RAC domain and fluid domain (somewhat harder to see) is shown. One can see the density of the mesh increasing closer to the object of interest. This is also happening in Figure 7.6, which gives a closer look at the RAC and fluid domain. The areas of rapid changes in velocity and pressure of the fluid were automatically meshed denser by the program.

As told above, the mesh should not exceed 512 000 elements due to the student license DUT provided. During simulation running, the solution would often not converge because the mesh was too coarse. Convergence in this case is defined as the sum of the scaled residuals decreasing to some lower value, for instance  $1 \times 10^{-6}$ . These scaled residuals are calculated per element and then summed for each variable involved, such as energy (if the energy model is on) or fluid velocity in some particular direction. It is a great way to evaluate if the solution is a sane one. If the energy residuals are low, the solution can be deemed converged.

In order to remedy the divergence of the solution, it was tried to refine the mesh at physical points where the solver would show strange behaviour, such as elements having negative Kelvin temperatures or enormous velocities. This helped to some extent, but eventually applying a symmetry boundary condition was the most useful measure to reduce the number of elements. The object is reflectionally symmetrical and would even be twice symmetrical if not for the fluid inlet which prevents this. The elements that were "freed" were then used to refine the mesh, especially at the boundaries between RAC and ambient domain, both at the inner and outer side of the cone. Eventually, this gave way to a converged solution for the determination of  $h$ .

### 7.5.3. Setup

This subsection will deal with the setup of the simulation, including the models, boundary conditions and solver.

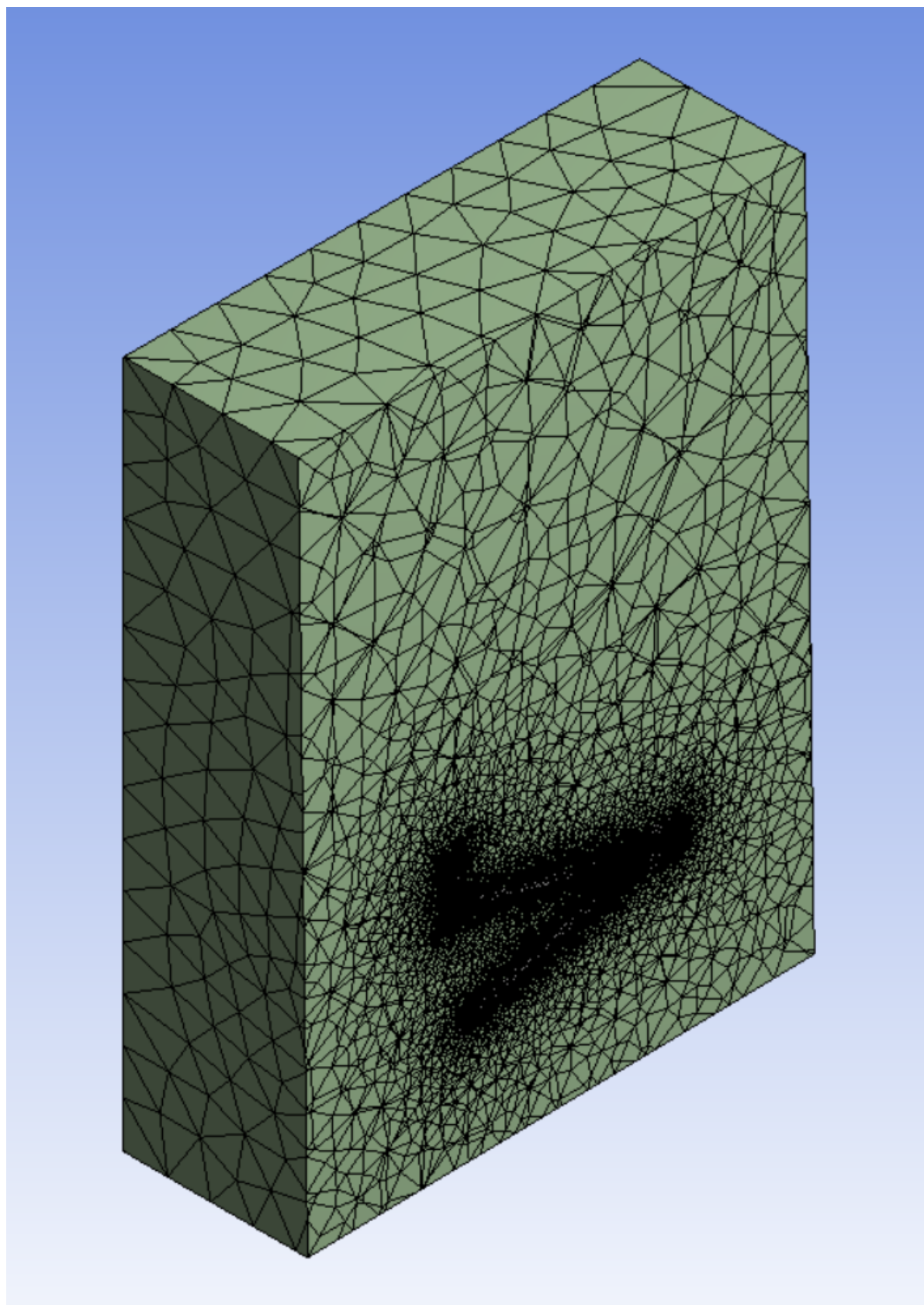


Figure 7.5: Cross-section of the meshed ambient, RAC and fluid domain.

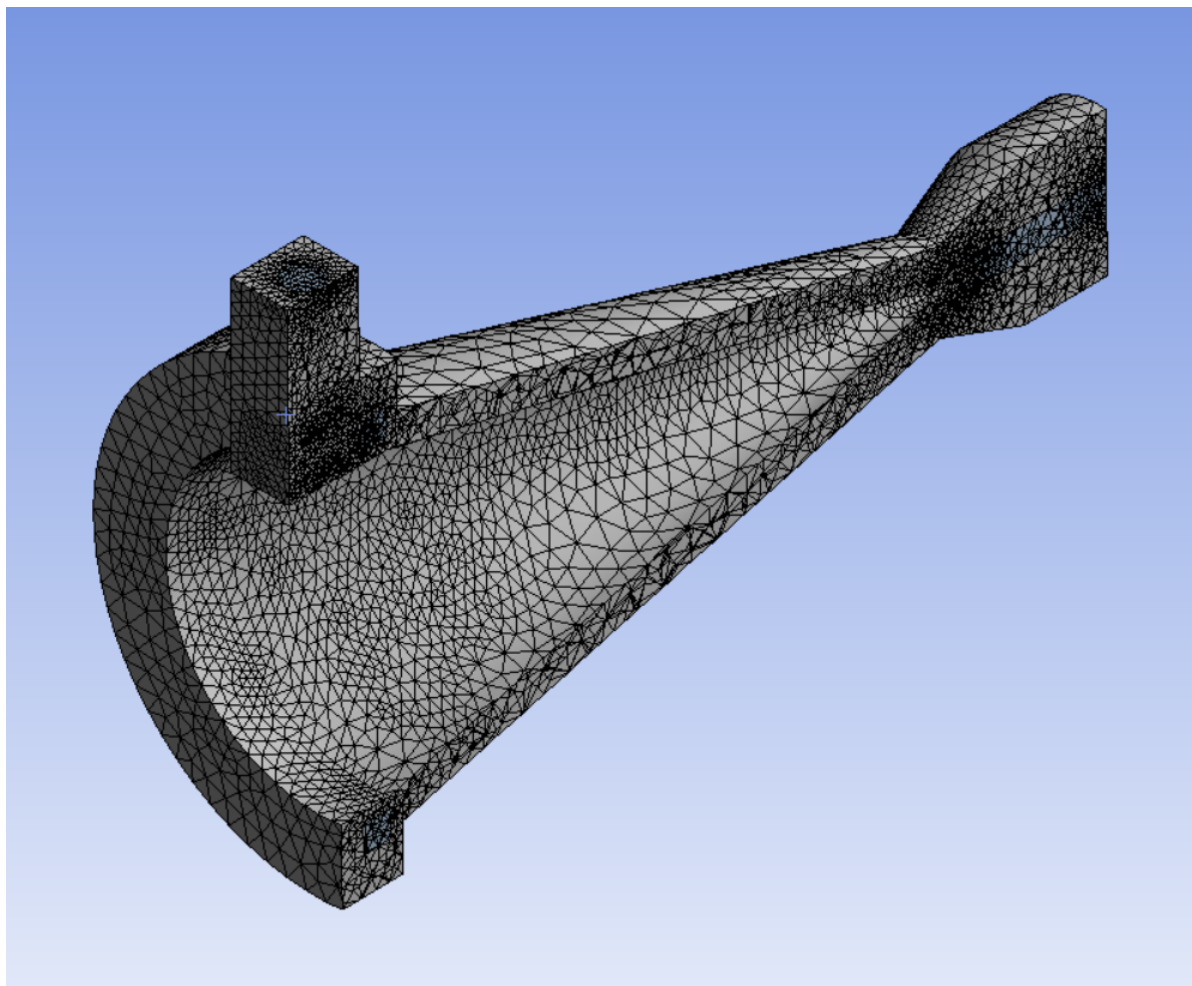


Figure 7.6: Closer cross-section of the meshed RAC and fluid domain. Note the two inner walls: the cone inner wall and the small circular inner wall.

### Gravity

The gravity will be toggled on, with value of  $9.81 \text{ m s}^{-2}$  in the negative y-direction. The positive y-direction is where the fluid enters the RAC. The gravity is amongst other important to the free convection, as free convection is buoyancy-based which simply means that heated air will rise because its density has been decreased.

### Transient or steady-state

The solver can be setup in two ways: the simulation can be done transient (unsteady) or steady-state. The former is a time-dependent simulation, where the applied heat fluxes that go in the system do not necessarily equal the outgoing heat fluxes. Ansys requires a time-step in this situation. Steady-state on the other hand will see the heat fluxes balanced out throughout the system. In steady-state simulations, the object(s) and fluid(s) involved will not change properties (e.g. temperature, pressure) with time. If a transient solver runs for an extended amount of time, it will approach the steady-state solution.

A transient approach will be done for this simulation, so the influence of RAC temperature on  $h$  can be discussed.

## Materials

Fluent offers a large variety of built-in materials, both fluid and solid. It is easy to rerun a simulation using a different material having e.g. a higher thermal conductivity or lower density to see its effects.

The **RAC** will consist of copper with a density of  $8978 \text{ kg m}^{-3}$ ,  $c_p$  of  $381 \text{ J kg}^{-1} \text{ K}^{-1}$  and  $k$  of  $387.6 \text{ W m}^{-1} \text{ K}^{-1}$ . Note that all three are constant and will not change with temperature.

The fluid domain would normally be filled with gaseous nitrogen, which has an ideal gas density (derived thus from the pressure and temperature),  $k$  of  $0.0242 \text{ W m}^{-1} \text{ K}^{-1}$  and dynamic viscosity  $\mu$  of  $1.663 \times 10^{-5} \text{ Pa s}$ . Again, the latter two are constant with temperature and pressure. However, in this simulation which will determine the convection coefficient  $h$ , no propellant will be present and the fluid domain will be filled with air, see properties below. It is modelled this way because it is assumed that no tubing is attached so that the channels can fill themselves with air.

The ambient domain consists of air with ideal gas density, constant  $c_p$  of  $1006.43 \text{ J kg}^{-1} \text{ K}^{-1}$ , constant  $k$  of  $0.0242 \text{ W m}^{-1} \text{ K}^{-1}$  and constant  $\mu$  of  $1.7894 \times 10^{-5} \text{ Pa s}$ . The density cannot be set constant, as heated air would not rise due to buoyancy in that case.

## Boundary conditions

The boundary conditions will define the constraints of the problem. The first boundary condition is the temperature at which the system will kick off. All domains will start at room temperature, which is  $298.15 \text{ K}$ . Then, the fluid inlet and outlet will be simple coupled walls which will conduct heat from fluid to ambient and the other way around (if applicable), because there is no propellant flow. The channel walls will also couple the **RAC** domain and fluid domain, so that heat transfers between those two. The inner and outer **RAC** walls will both be coupled with the ambient domain, so that convection occurs. Note that no radiation boundaries are applied, only convection and conduction is present in this simulation.

Now, there is a small issue. In an experiment, the room where the test is held is normally very large when compared to the test object. Thus, one can safely assume that the ambient is at a constant temperature. The heated air circulates and air at the starting temperature replaces the moved pocket. However, modelling such a vast room in Ansys is undoable, as it would require enormous amounts of mesh elements and computing power. To remedy this, three simulations will be run. In these simulations, the air domain side walls will have a somewhat arbitrary air velocity input of  $0.1 \text{ m s}^{-1}$ ,  $0.01 \text{ m s}^{-1}$  and  $0.001 \text{ m s}^{-1}$  and the air domain top wall will be the pressure outlet of the system. The results will be compared and commented on.

Finally, the inner cone area (one surface) will experience an incoming heat equal to  $27.18 \text{ W}$ . This was derived from the power input which was used in the cases in Chapter ???. It will be applied as a heat generation rate (in  $\text{W m}^{-3}$ ) over a very small thickness (in  $\text{m}^2$ ) because Fluent unfortunately does not allow a heat flux in a coupled wall.

## Initialization

The simulation will be started with an initial guess of all cells, which will be done via standard initialization. The starting temperature will again be set at  $298.15 \text{ K}$ . The operating pressure is  $101\,325 \text{ Pa}$  or  $1 \text{ atm}$ . The number of time steps will be 300 with 5 iterations per time step. Each time step will be  $20 \text{ s}$ . The software will thus simulate the model for  $6000 \text{ s}$  or  $100 \text{ min}$ .

## Solving

The solver ran for approximately 45 min per simulation. For all three simulations, the energy equation residual did converge to a value around  $1 \times 10^{-8}$ , with a very small oscillation. This is due to the natural convection, which brings some instability in the heat leaving via the air domain. It is also due to the fact that the transient solution approached steady-state, which is prevented by again the inherent instability of the natural convection. The temperature of both inner and outer wall did not increase after the 300 time steps for all simulations. Only the latter simulation (for an air speed of  $0.001 \text{ m s}^{-1}$ ) experienced backflow at the top, which means that air is flowing back in the air domain system. What the effect of this is is not known. In Figure 7.7, the scaled residuals of this simulation are shown. In the further figures down below, the results of the simulation with the lowest air speed will be shown.

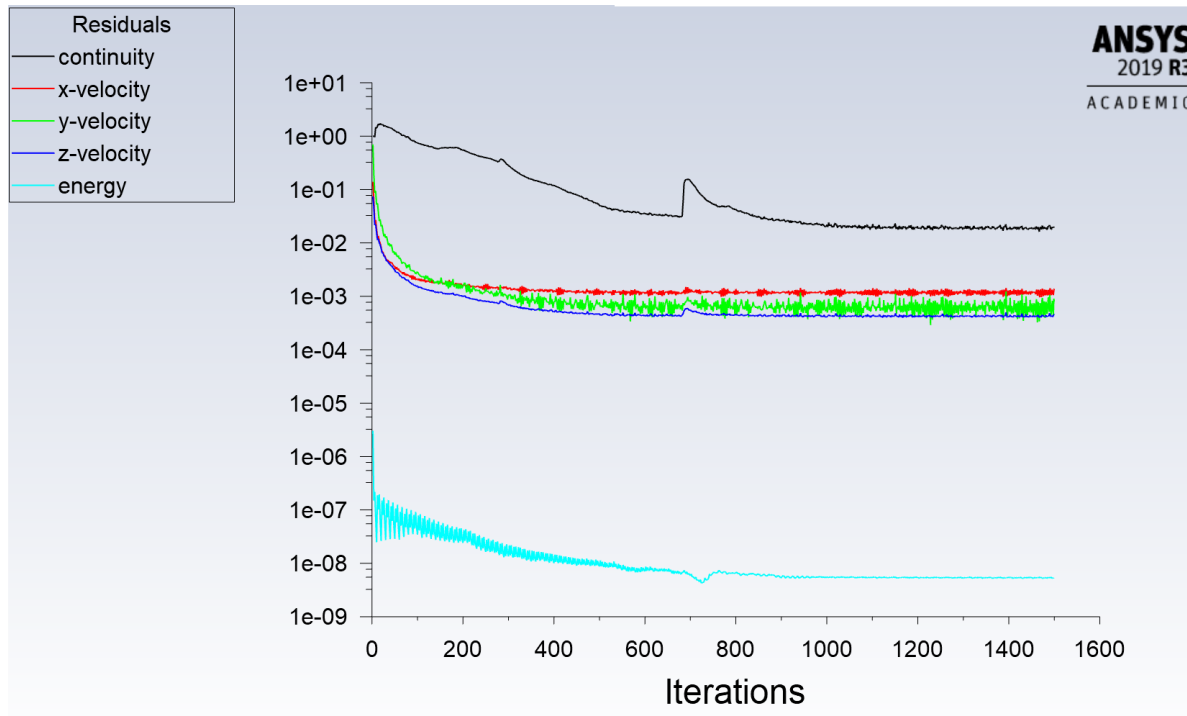


Figure 7.7: Scaled residuals of the simulation to determine convection losses for a case without insulation at an air speed of  $0.001 \text{ m s}^{-1}$ . Note the very small oscillation in the energy equation.

### 7.5.4. Post-processing

In Figures 7.8 and 7.9, the heated fluid domain is shown in side and fronts views respectively (air speed of  $0.001 \text{ m s}^{-1}$ ). The higher temperature area at the top of the cavity with respect to the bottom can clearly be seen. This is due to buoyancy, note that gravity is pointing down (in the negative y-direction) in the pictures. Next to this, Ansys Fluent outputs a ASCII file which can be read by Excel. Area-weighted averages of both temperature  $T$  (in K) and fluxes  $q$  (in  $\text{W m}^{-2}$ ) from the inner and outer walls are outputted. From these, the convection coefficient  $h$  in  $\text{W m}^{-2} \text{ K}^{-1}$  can be calculated using Equation 7.3. In this equation,  $T_\infty$  is the ambient temperature in K, which will be equal to 298.15 K. This temperature will also be used as an input for further simulations when it concerns the free-stream temperature related to convection heat transfer.

$$h = \frac{q}{T_{wall} - T_\infty} \quad (7.3)$$

In Figure 7.10, the temperature of both inner and outer walls are shown ( $0.001 \text{ m s}^{-1}$ ). The temper-

ature rises smoothly until 80 min, after which it seems to stabilize. Taking the last temperatures after 100 min of flow time, they are 748.42 K, 747.47 K and 747.64 K for the inner cone wall, inner circular wall and outer walls respectively. Be aware that the outer walls consist of multiple surfaces which are (area-weighted) averaged to obtain the current temperature. There will thus be some variation on these outer walls, which are all in connection with the ambient. The resultant temperatures are very close, with the largest temperature difference being 0.95 K. It proves that the assumption from Chapter ?? that the temperature throughout the RAC can be seen as equal in all locations due to the high thermal conductivity is valid.

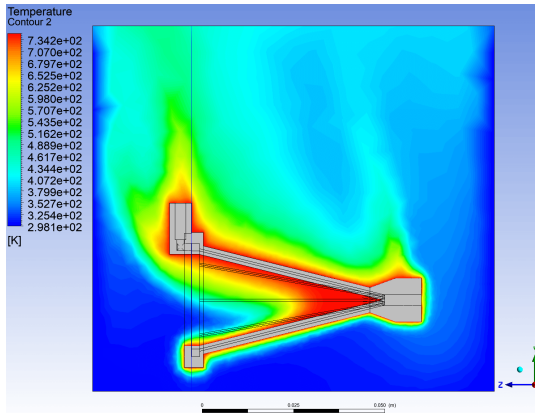


Figure 7.8: Side view of the heated air domain. Note how the upper part of the air in the cavity has a higher temperature than the lower part, due to buoyancy (gravity is pointed down, in the negative y-direction). Air speed is  $0.001 \text{ m s}^{-1}$ .

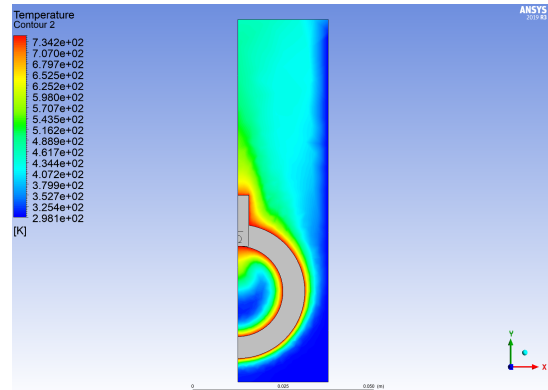


Figure 7.9: Front view of the heated fluid domain. Again, a small higher temperature pocket is seen at the top of the cavity, in the positive y-direction. Air speed is  $0.001 \text{ m s}^{-1}$ .

In Figure 7.11, the resulting  $h$  for both the inner cone and circular walls and outer walls for all three simulations are shown. Unsurprisingly, the values are higher for the outer than for the inner walls. Air tends to be “blocked” in the inner pocket, which acts as a buffer to cool air entering, thus lowering the convection. The convective heat transfer coefficient, after some initial differences, stabilizes after 40 min. Taking the average after this point yields the results shown in Table 7.2. The values do quite differ, with lower convection loss values with lower air speed. This is unsurprising, because with lower air speeds less cold air is forced into the domain. Incropera et al. [8] state a range of  $2\text{-}25 \text{ W m}^{-2} \text{ K}^{-1}$  for free convection in gases, so the numbers seem viable. Furthermore, calculations using Equation 7.3 showed that the simulations all outputted 27.10 W, so all approached steady-state.

Table 7.2: Convective heat transfer coefficients per air speed and emissivities. Results of three simulations with the air domain surrounding the RAC domain.

	$h [\text{W/m}^2/\text{K}]$ at air speed of <b>0.1 [m/s]</b>	$h [\text{W/m}^2/\text{K}]$ at air speed of <b>0.01 [m/s]</b>	$h [\text{W/m}^2/\text{K}]$ at air speed of <b>0.001 [m/s]</b>	View factor to ambient [-]	Adjusted emissivity to ambient [-]
<b>RAC inner cone wall</b>	4.59	3.59	3.29	0.176	0.114
<b>RAC inner circular wall</b>	7.59	7.04	6.44	0.426	0.277
<b>RAC outer walls</b>	13.60	10.48	10.06	1.000	0.650

The values were also compared with the outputs from the equations in the preliminary tool Section 4.2. The Python script outputted, for similar inputs, an  $h$  of  $1.72 \text{ W m}^{-2} \text{ K}^{-1}$  and  $13.63 \text{ W m}^{-2} \text{ K}^{-1}$  for the inner and outer walls respectively. There is no distinction in the two inner walls in the preliminary tool. Both values do not correspond very well. The paper from Paitoonsurikarn [56] was aimed at a cylindrical cavity, which can explain the difference in the conical cavity. For the outer walls, the preliminary tool assumed a geometrical cone, while in reality there is a ring at the inlet and a thickened

part at the end of the [RAC](#). For the case following after this subsection, the values for an air speed of  $0.001 \text{ m s}^{-1}$  will be used, as this air speed is more realistic than a higher air speed which would not be present in a laboratory during testing. However, it is recommended to redo these simulations if more powerful computers and a license allowing for more mesh elements is available. For now, the results here obtained are used, also because the interest lies mostly in the propellant convection domain.

Note that, when a steady-state simulation was executed for an air speed of  $0.001 \text{ m s}^{-1}$ , similar values for the temperatures and  $h$  were found after the solution stabilized around 600 iterations.

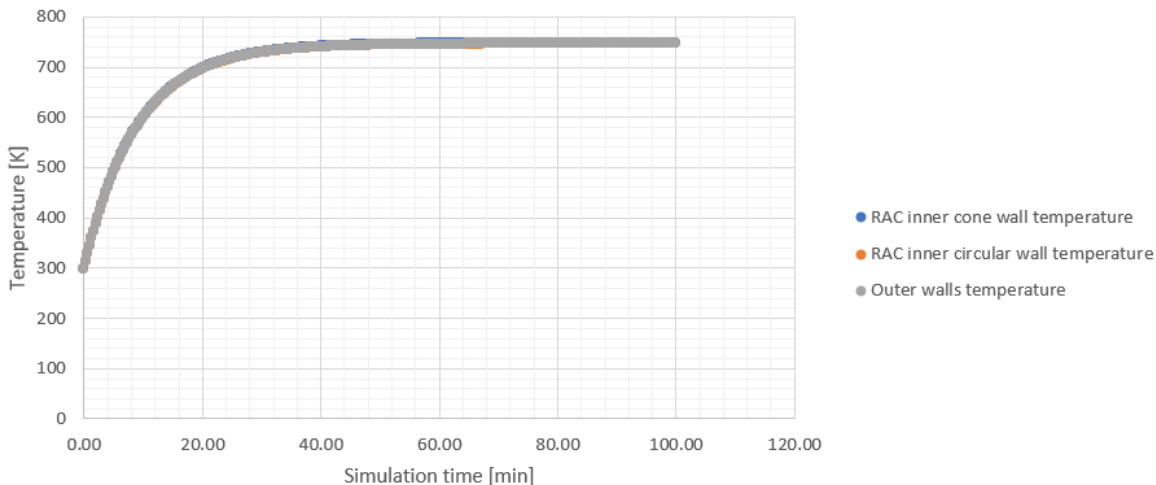


Figure 7.10: Area-weighted average temperatures for inner cone, inner circular and outer walls. Necessary to determine the convection losses for an [RAC](#) without insulation. Air speed is  $0.001 \text{ m s}^{-1}$ .

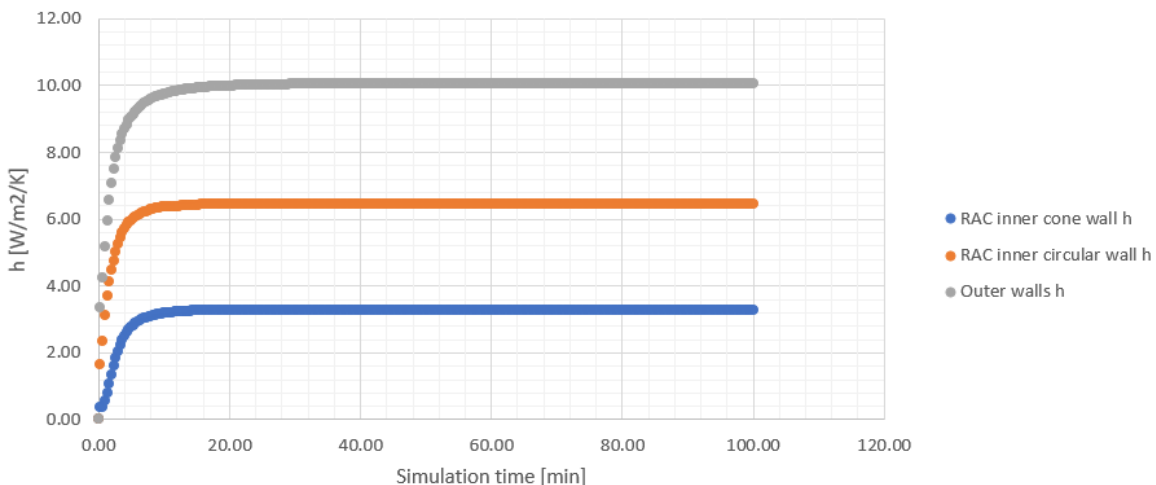


Figure 7.11: Convective heat transfer coefficients for inner cone, inner circular and outer walls, for a case without insulation. Air speed is  $0.001 \text{ m s}^{-1}$ .

Now that the convective loss values have been determined, the ambient domain can be deleted. From now on, the convection will be calculated from [Equation 7.1](#). For the other loss to the ambient, which is radiation, [Equation 7.2](#) is used. However, as already stated, no view factors are used by Ansys Fluent when using the boundary condition related to this equation. This is not so much an issue for the outer walls, which radiate towards an ambient of emissivity 1 and  $298.15 \text{ K}$  as it is for the inner wall (including the inner wall ring). The latter two surfaces will partly radiate back to themselves, which reduces the radiation heat loss. To remedy this, the emissivity of both inner wall surfaces will be multiplied by the calculated view factors for those surfaces. It will thus be assumed that any radiated

energy from a surface to itself will be fully absorbed and not reflected, to simplify matters. Note that the outer walls do not fully face towards the radiant; some small surfaces also radiate to other surfaces, but this will be ignored.

## 7.6. Case 1: Solar Thermal Thruster 1, no mass flow and no insulation

For the first case, which will be a physical RAC model of STT1 with no mass flow and no insulation, the setup from Section 7.5 is copied. The following inputs will differ or need explanation:

- The ambient domain will be deleted.
- All RAC domain walls will have a convection boundary condition with  $h$  equal to  $3.29 \text{ W m}^{-2} \text{ K}^{-1}$ ,  $6.44 \text{ W m}^{-2} \text{ K}^{-1}$  and  $10.06 \text{ W m}^{-2} \text{ K}^{-1}$  for the inner cone, inner circular and outer walls respectively. The free-stream temperature is set at 298.15 K.
- All RAC domain walls will radiate energy towards the ambient. The emissivity of the walls will be 0.65. For the inner two walls (the cone wall and the circular ring), this number will be lower to account for the reabsorbing of the radiated heat. For the cone wall, the view factor to the ambient equals 0.176. Thus, the emissivity will equal 0.114 for this wall. For the circular wall, the view factor to the ambient is 0.426, which gives a resulting emissivity of 0.277 for that wall. The view factors were calculated with the same equations that were used in Subsection 4.3.1.
- The input power on the inner cone wall will equal 27.18 W. This is similar to the input in Chapter ??'s cases, where the original input of 60 W would partly miss the RAC, partly be absorbed and partly be reflected back to the ambient (thus lost). See Subsection 4.3.1 for details.
- No propellant is flowing. The fluid domain is filled with air which will be heated by the RAC.
- The solver will still be transient and will run for 150 time steps of 20 s each. The number of iterations per time step is 5.

The solution converges very well (down to an energy residual of  $1 \times 10^{-9}$ ), which was to be expected because there is no moving fluid. In Figure 7.12, one can see the temperatures of the three surfaces approaching steady-state around a temperature of 520 K. Again, the three temperatures lie very close to each other, proof of the high copper conductivity.

In Table 7.3, the inputs and outputs of the Ansys case 1 simulation are shown for the last time step, which is at 3000 s or 50 min. The radiation and convection heat flow have been checked using Equations 7.1 and 7.2. One can see the results in the last row of the table, they resemble the values outputted by the Fluent simulation.

Table 7.3: Inputs and outputs for Ansys case 1.

		<b>Inner cone wall</b>	<b>Inner circular wall</b>	<b>Outer walls</b>	<b>Unit</b>
<b>Input power</b>	Input	27.18	0.00	0.00	[W]
<b>Convective heat transfer coefficient</b>	Input	3.29	6.44	10.06	[W/m <sup>2</sup> /K]
<b>Emissivity</b>	Input	0.114	0.277	0.65	[-]
<b>Final temperature</b>	Output	522.27	521.18	521.49	[K]
<b>Radiation &amp; convection losses</b>	Output	2.36	0.80	23.99	[W]

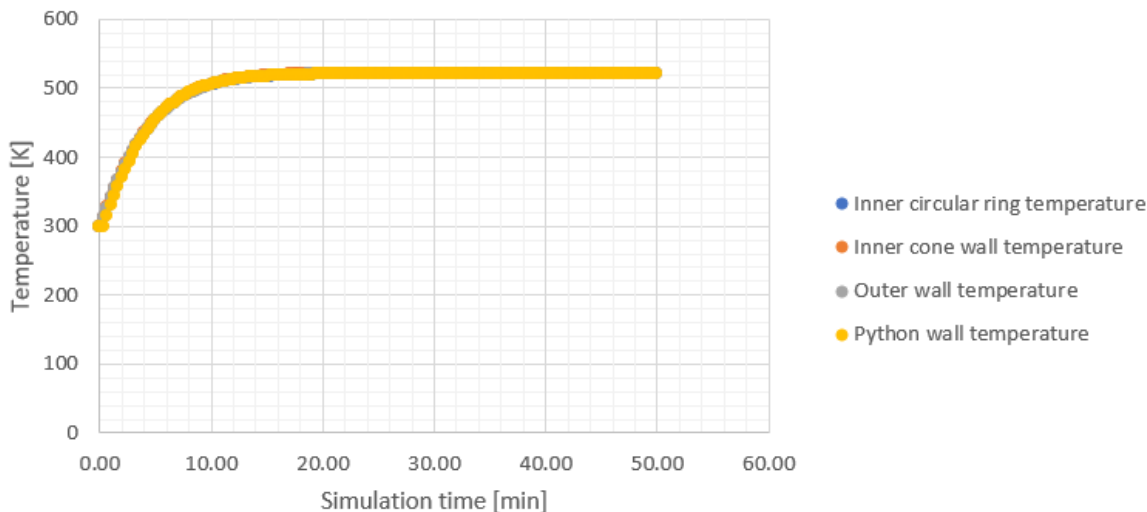


Figure 7.12: Case 1: area-weighted average temperatures for inner and outer walls. Note the overlaying Python wall temperature.

Summing the heat flows in last row yields 27.15 W, which is slightly lower than the power input. This means that the solution almost reached steady-state. Comparing the results with case 1 from the preliminary tool in Chapter ??, the final (which is almost steady-state) temperatures quite differ: 543.11 K calculated by the preliminary tool versus the 521.18–522.27 K from the Fluent simulation. However, bear in mind that the area and mass inputted in the preliminary tool script was significantly lower than the area in the simulation. When this is adjusted for, the final temperature by the tool suddenly equals 506.07 K, already closer. The difference completely disappears once the convective heat transfer coefficients are manually altered to the values from Ansys Fluent, see also Figure 7.12. So, unsurprisingly, Ansys Fluent does very well on simple heat problems with fixed convection and radiation coefficients and a constant power input.

## 7.7. Case 2: Solar Thermal Thruster 1, no mass flow and insulation

Case 2 introduces a thick insulation layer around the RAC with a very low conductive heat coefficient. Leenders indicated a cylindrical insulation layer with a diameter of 11 cm and length of 10 cm. He did not exactly state how this layer was placed with respect to the RAC. In the current simulation, the symmetry axis will coincide with the heat exchanger's symmetry axis (without the ring). Lengthwise, the layer will be placed so that on both ends it will stick out equally. A hole is made in the insulation towards the RAC aperture, with a diameter equal to that of the cone base diameter, which is 0.025 m. There are now three inner areas instead of two: the RAC inner cone and the RAC inner circular walls were already known, the circular inner insulation wall is the third. They will all be treated as a separate surface.

At first, the convection coefficients  $h$  need to be determined again. The same approach as in Section 7.5 will be used, with the difference that now an insulation layer is applied. The insulation is added as a material in Fluent, with a density of  $100 \text{ kg m}^{-3}$  and  $C_p$  of  $1000 \text{ J kg}^{-1} \text{ K}^{-1}$ . These two properties are constants, but the thermal conductivity  $k$  in  $\text{W m}^{-1} \text{ K}^{-1}$  of the Saffil M-Fil will be dependent on temperature in K (see Appendix C.9 for the data sheet). A trendline, Equation 7.4, was created out of the three data points provided using Excel.

The ambient domain will have a length of 155 mm, width of 170 mm and height of 300 mm. It will

again be placed around the heat exchanger symmetrically, except in the height direction; to account for heated air raising in the domain, it will extend more to the top than to the bottom.

The input power on the RAC inner cone wall will equal 27.18 W. The air speed will be  $0.001 \text{ m s}^{-1}$ , coming from the air domain side walls. For the determination of  $h$ , the fluid domain will be united with the RAC domain so that more elements are freed up for critical areas, such as the RAC-insulation and insulation-ambient boundaries.

$$k = 3.125 \cdot 10^{-7}T^2 - 3.232 \cdot 10^{-4}T + 0.2065 \quad (7.4)$$

The solution converges nicely to a residual between  $1 \times 10^{-5}$ - $1 \times 10^{-6}$ , again with a small oscillation. After 350 time steps of 20 s each (5 iterations per time step) the simulation is stopped. Figures 7.13 and 7.14 show the temperatures and convective heat coefficients respectively of the three earlier mentioned inner surfaces and the outer insulation surface. The coefficients become constant after 40 min. Averaging them from this time on, the coefficients displayed in Table 7.4 are obtained. The sum of the found coefficients are multiplied with the wall area and temperature difference between wall and ambient equals 27.15 K, which is very close to the inputted 27.18 K. The solution is thus almost steady-state. The highest temperature is reached at the inner copper cone wall and equals 796.1 K.

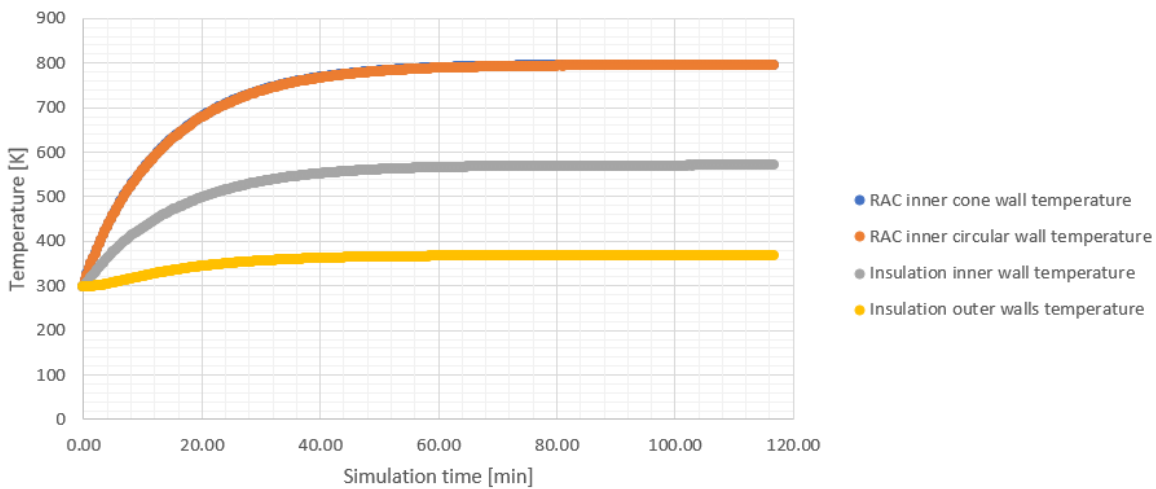


Figure 7.13: Area-weighted average temperatures for inner and outer walls, with insulation. Air speed is  $0.001 \text{ m s}^{-1}$ .

Table 7.4: Convective heat transfer coefficients, view factors and resulting emissivities for case 2.

	$h [\text{W/m}^2/\text{K}]$ at air speed of <b>0.1 [m/s]</b>	$h [\text{W/m}^2/\text{K}]$ at air speed of <b>0.01 [m/s]</b>	$h [\text{W/m}^2/\text{K}]$ at air speed of <b>0.001 [m/s]</b>	View factor to ambient [-]	Adjusted emissivity to ambient [-]
<b>RAC inner cone wall</b>	1.16	2.81	2.76	0.045	0.029
<b>RAC inner circular wall</b>	2.99	4.99	4.93	0.196	0.127
<b>Insulation inner wall</b>	0.44	2.75	2.90	0.243	0.158
<b>Insulation outer walls</b>	11.15	6.56	6.03	1.000	0.090

Figures 7.15 and 7.16 show side views of the air domain and the insulation and RAC domains respectively. Note that, in the left picture), the grey mass is the insulation with the hole towards the RAC. As expected, there is a temperature gradient in the insulation due to low thermal conductivity.

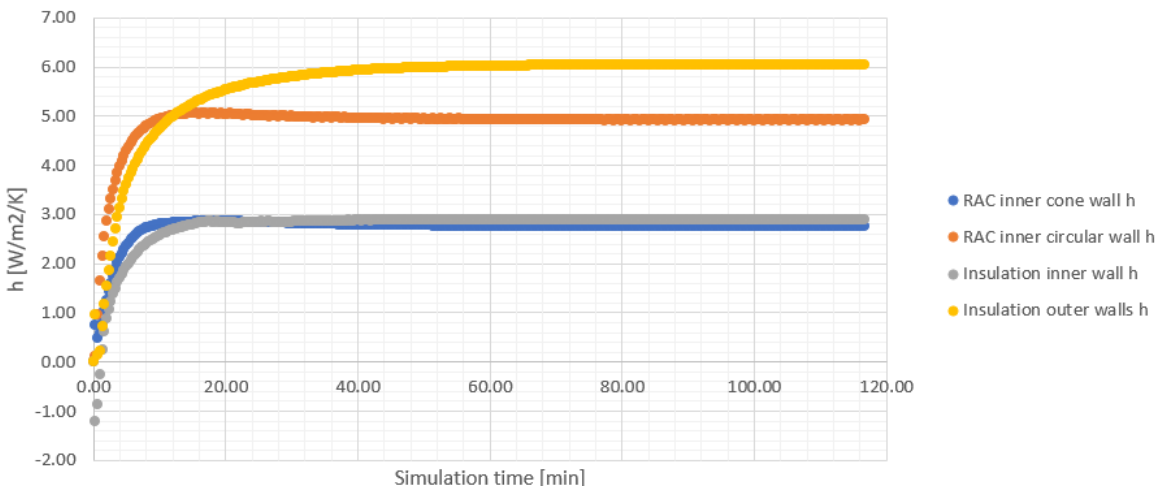


Figure 7.14: Area-weighted average convective heat transfer coefficients for inner and outer walls, with insulation. Air speed is  $0.001 \text{ m s}^{-1}$ .

The heat exchanger on the other hand has a somewhat constant temperature throughout. Notice the asymmetry in the cavity due to buoyancy (gravity is pointing down in the pictures). Next to that, the corners of the insulation do not seem to reduce the convection losses by a large extent, because the are at low temperatures (close to room temperature). So, when optimising, cutting of the corners to reduce mass is an option.

The velocity of the incoming air from the sides was  $0.001 \text{ m s}^{-1}$ . However, to see what the influence of the velocity is, also cases with  $0.1 \text{ m s}^{-1}$  and  $0.01 \text{ m s}^{-1}$  were executed. The results are shown in Table 7.4. Both simulations almost reached steady-state, both with convection losses of  $27.14 \text{ K}$ . The initial air speed does affect the loss coefficients by a large extent. The focus for this chapter will be more on the convection towards the propellant than the convection to the ambient. For now, the values corresponding with an air speed of  $0.001 \text{ m s}^{-1}$  will be used. It is recommended, for future calculations, to increase the size of the air domain to allow for a more accurate assessment of the convection losses.

In the preliminary tool, the equations from Section 4.2 returned a steady-state value of  $5.11 \text{ W m}^{-1} \text{ K}^{-1}$  for the outer insulation walls and  $1.73 \text{ W m}^{-1} \text{ K}^{-1}$  for the inner walls. There was no distinction between the different inner walls. The values are close, but not entirely similar to the values found during CFD. This can be due to the different physical model which was inputted in the Python model, because the ring was absent in that case. Next to that, as was previously mentioned, the equations used to determine the value for the preliminary tool were mainly applicable to cylindrical cavities, not conical ones.

Now the view factors for the inner three surfaces need to be calculated again. They are added to Table 7.4 and multiplied with the base emissivity, which in this case is still 0.65. However, for the outer insulation walls, the base emissivity is low (0.09 to be precise) because Leenders wrapped the insulation with aluminium foil [3]. As expected, the walls that lie more to the inner side of the system have the lowest view factor and thus emissivity.

So, to execute case 2, boundary conditions for both convection and radiation will be applied to the walls, according to the values in Table 7.4. These values are all with respect to the free stream temperature and room temperature of  $298.15 \text{ K}$  and a blackbody surrounding (emissivity equal to 1), so no outgoing radiation is reflected back. Again, the ambient domain is deleted to free up computational room for the heat exchanger, fluid and insulation domains. However, the solver did not converge for the aforementioned values. Again, the fluid domain had to be merged with the solid RAC domain, so no channels are present for this case. After these adjustments the solution converged to a scaled residual below  $1 \times 10^{-9}$ . The maximum temperature that was attained was  $751.3 \text{ K}$ , which is unsurprisingly a

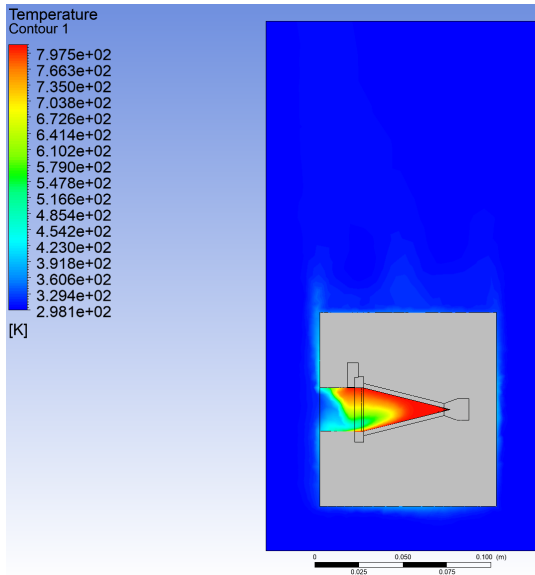


Figure 7.15: Side view of the heated air domain. Note how the upper part of the cavity has a higher temperature than the lower part, due to buoyancy (gravity is pointing down).

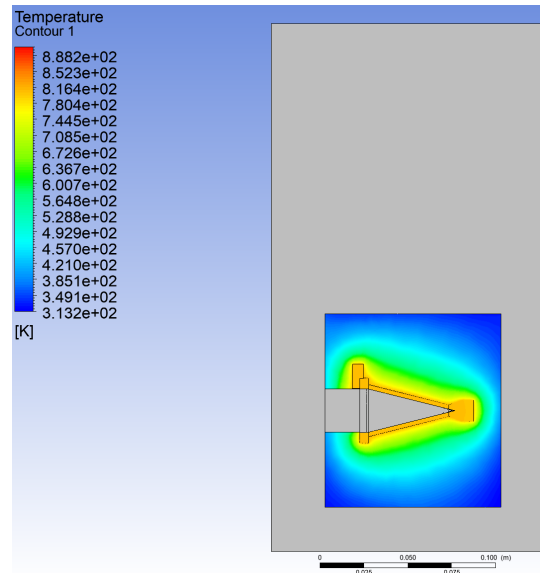


Figure 7.16: Side view of the heated RAC and insulation domains.

bit lower than the value that was read from the plot in Figure 7.13, 796.1 K. This is due to the radiation loss, which was not modelled during the simulations where  $h$  was determined.

Comparing the maximum temperature with the temperature attained during case 2 in Chapter ??, which is 728.11 K, there is a difference. This is explainable because the emissivity is much higher for the inner cavity in the Python tool than it is in the current simulation. The emissivity is higher because it was not corrected for the insulation which decreased the view factor of the cone to the ambient. Because the cone attains a very high temperature, radiation becomes more dominant than convection losses, and the heat loss becomes more significant when the emissivity is not adjusted for.

## 7.8. Case 3: Solar Thermal Thruster 1, mass flow and insulation

In the previous two cases it could be seen that the simulations output other values for wall temperatures and convection losses than the preliminary tool from Chapter ???. This is not necessarily an issue, as the differences had mainly to do with different inputs to both tools; the physical models differed, subsequently the areas varied and the boundary conditions in the form of emissivity and convection coefficients were not equal. Only the latter is hard to remedy. From experience, the most accurate results for the convection losses would be from CFD with a large enough air ambient domain. However, with the current computer power and license used for the simulations this is not possible. It is thus a recommendation to redo the simulations in order to produce more reliable convection loss results.

For the third case, which sees propellant mass flow and insulation, various simulation were tried but they all failed due to divergence. When diverging, the outputs were not reliable, due to them going either approaching 1 K or 5000 K. As such, case 3 cannot be executed as planned. However, another case was thought of, see next section.

Before proceeding to the next section, a test case is run. Verifying and validating the results of the heat transfer to the propellant is near impossible due to the lack of experimental results. However, a well-known test case, regarding flow through a circular high temperature duct, can be executed because the propellant temperature increase can be analytically derived. Comparing the results with an Ansys Fluent simulation, the solver can be verified and validated for this particular case. Although

it does not resemble the channel section from STT1 exactly, the comparison can still prove the added benefit of the method.

Equations from Subsection 4.2.1 were used to analytically predict the heating of nitrogen propellant flowing through a circular pipe. Both a laminar and turbulent case are performed, see Table 7.5. The only differences are the mass flow and hence the Reynolds numbers.

Table 7.5: Inputs for verification cases, both laminar and turbulent.

	Laminar case	Turbulent case
<b>Mass flow [kg/s]</b>	0.00025	0.0025
<b>Pipe length [m]</b>	1.5	
<b>Pipe diameter [m]</b>	0.01	
<b>Wall temperature [K]</b>	500	
<b>Propellant inlet temperature [K]</b>	298.15	
<b>Thermal conductivity [W/m/K]</b>	0.02583	
<b>Dynamic viscosity [Pa s]</b>	$1.76 \cdot 10^{-5}$	
<b>Specific heat at constant pressure [J/kg/K]</b>	1040	
<b>Reynolds number</b>	1808.6	18086.8

From theory, one phase flow heat transfer can be predicted when the wall temperature is constant. In that case, for laminar flow Stephan's Nusselt number equation (4.18) can be applied and the modified Gnielinski equation (4.21) is applicable to the turbulent test case. The resulting heat transfer values are shown in Tables 7.6 and 7.7 for the laminar and turbulent case respectively. For the simulations, the tube wall was held at a constant temperature of 500 K. The steady-state simulations ran for 400 iterations, after which they were deemed converged. For the turbulent case, the  $k-\omega$  model was used (see next section).

Table 7.6: Comparison between theoretical and Ansys Fluent results, for the laminar test case.

Laminar flow	Ansys Fluent	Theory	Difference [%]
<b>Power input [W]</b>	45.73	46.61	-1.9
<b>Convective heat transfer coefficient [W/m<sup>2</sup>/K]</b>	11.33	12.08	-6.2
<b>Nusselt number</b>	4.39	4.68	-6.2
<b>Propellant outlet temperature [K]</b>	474.0	477.4	-0.7

Table 7.7: Comparison between theoretical and Ansys Fluent results, for the turbulent test case.

Turbulent flow	Ansys Fluent	Theory	Difference [%]
<b>Power input [W]</b>	487.76	473.17	3.1
<b>Convective heat transfer coefficient [W/m<sup>2</sup>/K]</b>	146.25	127.93	14.3
<b>Nusselt number</b>	56.62	49.53	14.3
<b>Propellant outlet temperature [K]</b>	485.75	480.14	1.1

The differences are minor, especially for the propellant outlet temperature. The Nusselt number differences are larger, which can be attributed to the fact that a natural logarithm term is incorporated in Equation 4.6, which inflates the differences in outlet temperature. However, as the temperature differences are within the 10 % range, the criterion stated at the beginning of the chapter is satisfied. Thus, Ansys Fluent is expected to output valid results for the cases following hereafter. However, experiments to support this statement are strongly suggested but are out of the scope for this thesis.

## 7.9. Case 4: Solar Thermal Thruster 1, mass flow and no insulation

For case 4, the focus lies on the propellant convection, the insulation domain will be deleted and the convection and radiation values from case 1 will be used to evaluate the heat flow to the propellant. Unfortunately, this also implies that the results cannot be compared to anyone of Leenders' cases, as he tested the [RAC](#) with insulation.

Originally, Leenders designed his heat exchanger so that the outlet temperature reached 373.15 K for a mass flow of  $300 \text{ mg s}^{-1}$  and power input of 29 W, at an efficiency of 80 %, so only 20 % is lost to the surroundings due to convection and radiation.

This case will be redone in Ansys Fluent, as case 4. The boundary conditions will be set as before, with a change in power input and an applied mass flow. The goal of this case is to check the efficiency value and study the effect of laminar and turbulent flow on propellant outlet temperatures. Next to that, it will be interesting to see what the pressure loss is in the [RAC](#). Furthermore, the obtained Nusselt numbers can be compared to literature. The case will be done in steady-state, because the solver unfortunately has a tendency to diverge for transient solutions.

The flow type is very important for the amount of heat that is transferred to the propellant. The flow can be laminar ( $\text{Re}$  lower than 2300), turbulent ( $\text{Re}$  higher than 10 000) or transitional (inbetween Reynolds numbers). For the case at hand, the Reynolds number equals 4550 for gaseous nitrogen at room temperature. Equations [4.10](#) and [4.16](#) were used to calculate this number for the channels, which have a square cross-section of 0.6 mm per side.

That means that the flow will have a transitional flow type in the small channels, in theory. However, the flow could also experience turbulent behaviour due to the sharp 90 deg corners at the inlet of the [RAC](#). As such, two simulations will be carried out: one where the propellant is assumed laminar and one where the flow is turbulent. For the latter, a model has to be found; it requires too much computational effort, even for the current generation supercomputers, to solve the [NS](#) equations for every eddie at every length scale in the flow [69]. Instead, one uses the [Reynolds-averaged Navier-Stokes \(equations\) \(RANS\)](#), in which the velocity and pressure are time-averaged, dramatically reducing the simulation time. Ansys Fluent has many of these RANS-models available. Looking at previous theses done in the area of [STP](#) at the faculty of [AE](#), no advice on turbulent models was found unfortunately. In literature, for internal flow, the  $k-\omega$  model is known to perform well. In this model,  $k$  is the turbulent energy in  $\text{m}^2 \text{ s}^{-2}$  and  $\omega$  is the specific turbulent dissipation rate in  $\text{s}^{-1}$ . For details on this, see Argyropoulos et al. [69]. Because the solver is very sensitive to the initial values, they are to be calculated using the equations in [7.5<sup>1</sup>](#). Here,  $v$  is the velocity of the flow (in  $\text{m s}^{-1}$ ),  $I$  is the turbulence intensity (dimensionless),  $C_\mu$  is a turbulence model constant (dimensionless) and  $l$  is the turbulence length scale (in m).

$$k = \frac{3}{2} (v \cdot I)^2 \quad (7.5a)$$

$$I = 0.16 Re_D^{-\frac{1}{8}} \quad (7.5b)$$

$$\omega = C_\mu^{-\frac{1}{4}} \frac{\sqrt{k}}{l} \quad (7.5c)$$

$$C_\mu = 0.09 \quad (7.5d)$$

$$l = 0.070D \quad (7.5e)$$

Following this, initial values of  $38.69 \text{ m}^2 \text{ s}^{-2}$  and  $270\,394 \text{ s}^{-1}$  for  $k$  and  $\omega$  respectively were calculated.

<sup>1</sup>[https://www.cfd-online.com/Wiki/Turbulence\\_free-stream\\_boundary\\_conditions](https://www.cfd-online.com/Wiki/Turbulence_free-stream_boundary_conditions), accessed on 07-10-2020.

To further speed up convergence for the turbulent simulation, inflation layers were applied at the inside of the channels. These are necessary, because the flow close to the walls sees quick changes in temperature and pressure. To accurately capture this, a high-density mesh is needed in those areas.

For this case, the walls bordering the fluid and RAC domains were split up in three regions: the entrance region, where the propellant flows in and is distributed among the eight channels; the channel region, where the propellant goes through the very small channels; the exit region, where the eight separate flows converge again and leave the system. Doing this, it is possible to see the contribution of each region regarding the heat flow to the propellant. It would be very interesting to see to what extent the flow heats up in each region. Again, the values for convective and radiative heat loss from case 1 were applied to the walls bordering the fictive ambient.

The laminar subcase converged relatively fast in 1000 iterations, which took about 30 min. There was a small oscillation in the temperature and flux terms, so averages were taken starting at 400 iterations. The results are shown in Table 7.8. The first three rows display the losses to the surroundings, the last three rows show the heat flow to the propellant for each region.

Table 7.8: Averaged wall temperatures and heat flows for case 4.

	Case 4: laminar		Case 4: turbulent	
	Temperature [K]	Heat flow [W]	Temperature [K]	Heat flow [W]
<b>Inner cone wall</b>	381.40	0.73	369.13	0.61
<b>Inner circular wall</b>	379.29	0.23	366.97	0.19
<b>Outer walls</b>	380.45	6.71	368.22	5.59
<b>1. Entrance region</b>	378.87	11.13	366.47	11.41
<b>2. Channel region</b>	381.62	9.90	369.47	11.17
<b>3. Exit region</b>	381.20	0.29	369.64	0.00
<b>Sum of heat flows</b>	-	<b>28.98</b>	-	<b>28.98</b>

Similarly, the turbulent subcase was executed with the  $k$  and  $\omega$  values shown above. It took more than one hour to stabilize the temperatures and fluxes. The results are shown in Table 7.8. There one can observe that the heat flow to the propellant is higher for the turbulent subcase than for the laminar one, which was to be expected. So unsurprisingly, the propellant outlet temperature for the turbulent subcase is also higher, see Table 7.9. The third row displays the propellant temperature after passing the last region, the exit region. The last row shows the efficiency of the heat exchanger; it is almost the predicted 80 % Leenders stated in his thesis [3]. As a result, the outlet propellant temperature approaches the aforementioned 373.15 K.

In Table 7.9, Nusselt numbers for the turbulent case are partly missing. That is due to the propellant temperature at the end of the region surpassing the average wall temperature of that region by a small amount. In that case, the natural logarithm from Equation 4.6 yields invalid results. An explanation for this is two-fold: either the solution is not accurate or the wall temperature is higher at the start of the region, heating the propellant to a temperature which is higher than the wall temperature at the end of the region.

Table 7.9: Averaged propellant temperatures and Nusselt numbers for each region, case 4.

	Case 4: laminar		Case 4: turbulent	
	Nusselt number [-]	Resulting propellant temperature [K]	Nusselt number [-]	Resulting propellant temperature [K]
<b>1. Entrance region</b>	4.70	333.44	6.16	334.38
<b>2. Channel region</b>	7.67	365.10	N/A	370.11
<b>3. Exit region</b>	4.23	366.03	N/A	370.11
<b>Efficiency</b>		73.5%		77.9%

In Table 7.10, the Nusselt numbers are displayed for the channel region. The Reynolds number

equals 4550 and the Nusselt numbers are calculated using different methods. Incropera et al. gives the Dittus-Boelter equation (see 7.6) [8]. The coefficient  $n$  (dimensionless) equals 0.4 for heating and 0.3 for cooling. It is valid for  $0.7 \leq Pr \leq 160$  and  $Re_D \geq 10\,000$ .

$$Nu_D = 0.023 Re_D^{\frac{4}{5}} Pr^n \quad (7.6)$$

Similarly, the Stephan equation is only applicable for laminar flow. That can directly be seen in Table 7.10, as the Nusselt number from the Stephan equation is significantly lower. Comparing the values with the Nusselt numbers from Table 7.9, there is some discrepancy in the laminar subcase. A strong thermal entrance effect was expected in the channels, raising the Nusselt number, but apparently the thermal boundary layer developed quicker than expected, bringing the value closer to the theoretical 3.66 from Equation 4.17. Unfortunately, the values cannot be evaluated by experiments; Leenders did not state the input power for his tests with mass flow, so those results cannot be used.

Table 7.10: Nusselt number calculations for channel flow, at a Reynolds number of 4550.

Method	Equation	Nusselt number [-]
Gnielinski	4.19	15.24
Gnielinski (modified)	4.21	15.97
Dittus-Boelter	7.6	16.83
Stephan	4.22	9.51

For the turbulent subcase, a temperature contour of the fluid domain in side view was taken, see Figure 7.17. Here it can be noticed that the fluid flowing through the lower channel is already more heated than the propellant in the upper channel. This is also seen when plotting the temperature along two lines (sample size of 1000), one through the middle of the upper channel and the other through the middle of the lower pipe, see Figure 7.18.

Furthermore, which is also supported by the very low contribution of the third region in terms of heat input, the area at the end of the RAC does not see much heat flow. This means that the RAC can be designed smaller, reducing the area (and thus losses to the ambient) and reducing the mass, which is one of the key design criteria for spacecraft propulsion. This reduction of mass will be the subject of the next chapter, where the RAC will be optimized in terms of mass.

The total pressure loss in the RAC for the turbulent subcase is 37 082 Pa (at an outlet pressure of 101 325 Pa or 1 atm, while for the laminar subcase it is 28 785 Pa). This is quite substantial. From Equations 4.48 and 4.50, one can calculate that the losses in the channels are 18 029 Pa (at room temperature and sea level pressure). This value is for both laminar and turbulent flow. Outside of the channels, there is some additional pressure drop, also due to the bends and corners. Leenders reported a pressure loss in his experiments around 5000 Pa. However, this was for a much lower mass flow,  $175 \text{ mg s}^{-1}$ . The pressure loss values are thus not validated, but they are in the right direction. Again, experiments on STT1 at a mass flow of  $300 \text{ mg s}^{-1}$  could validate these results.

## 7.10. Case 5: Solar Thermal Thruster 2, mass flow and no insulation

In Chapter 5, a new STP design was made, called STT2. Section 5.6 showed that grave errors were made in the design and build process. For this case, these errors will be partly mitigated by increasing the number of channels from 1 to 8 while increasing the spiral pitch by a factor 8. Due to this correction, the cross-sectional area of the combined channels is equal for both STT1 and STT2 and a comparison can be made on the thermal efficiency and pressure losses.

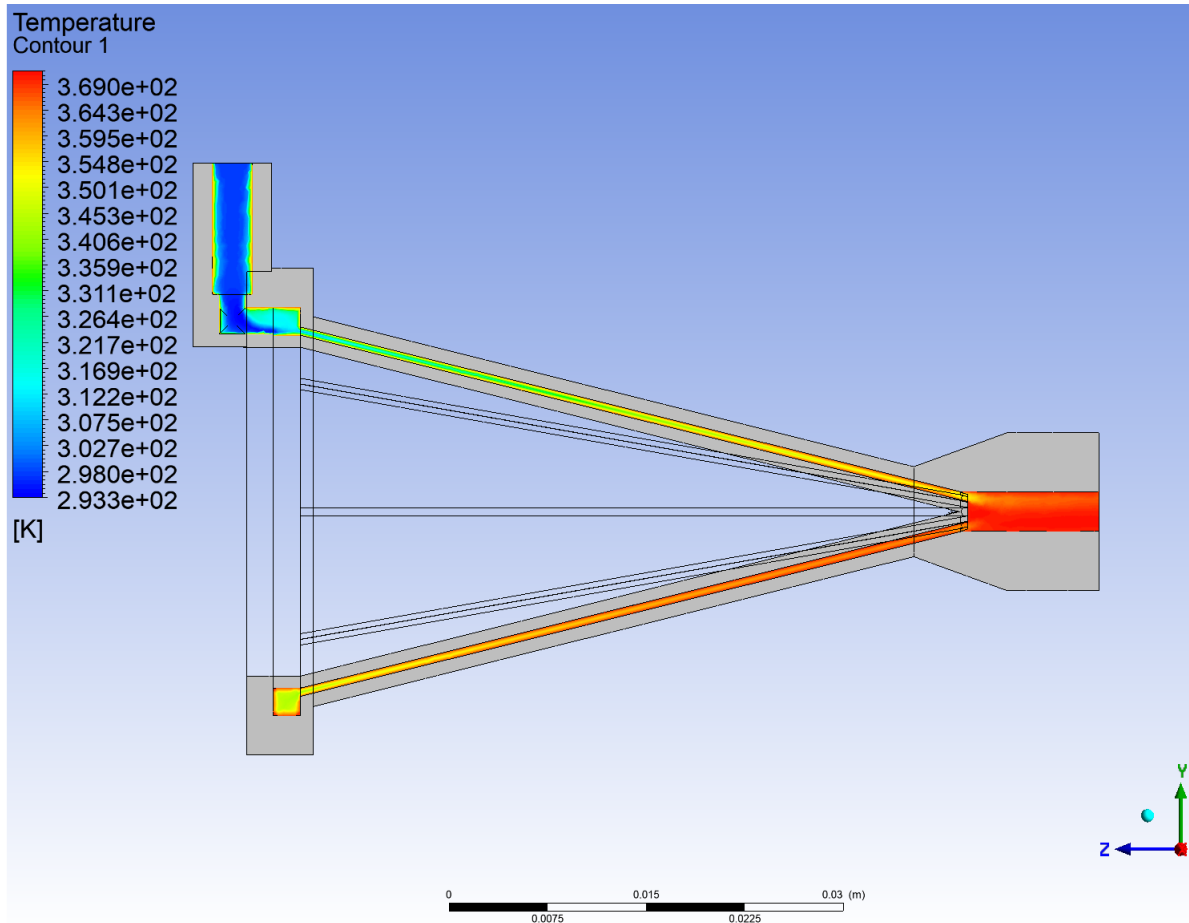


Figure 7.17: Turbulent subcase. Temperature contour of the fluid domain in side view.

At first, the convection losses were simulated per the procedure shown for case 1, see Section 7.5. Similarly, the view factors of all involved surfaces were calculated. Table 7.11 shows the results. Again, the view factor of 0.65 is multiplied with the view factor. It is assumed that the outer walls all have a view factor of 1, despite having some sharp corners. Next to that, the spike walls are assumed to radiate zero power to the ambient.

Table 7.11: Averaged convective heat transfer coefficients, view factors and emissivities for each surface, case 5.

	<b><math>h</math> [W/m<sup>2</sup>/K]</b>	<b>View factor [-]</b>	<b>Emissivity [-]</b>
<b>Entrance ring</b>	0.075	0.2071	0.135
<b>Heated wall</b>	0.005	0.0115	0.007
<b>Bottom ring</b>	0.075	0.0021	0.001
<b>Top ring and spike</b>	0.075	0	0
<b>Outer walls</b>	8.494	1	0.650

Entering the values from Table 7.11 as boundary conditions, laminar and turbulent subcases were run, yielding the results from Table 7.12. Note that the Reynolds number in the channels is equal to 5492. According to Equation 4.53, this is in the laminar region, because the critical Reynolds number lies at 7259. However, still both cases are run to see the differences in performance. It was not possible to apply a symmetry boundary due to the spiral channels rendering the heat exchanger asymmetrical. As such, elements were sparse and had to be carefully applied in the small channel region. Again, an inflation layer was applied, a high-density mesh as quick temperature and pressure changes are seen close to the walls.

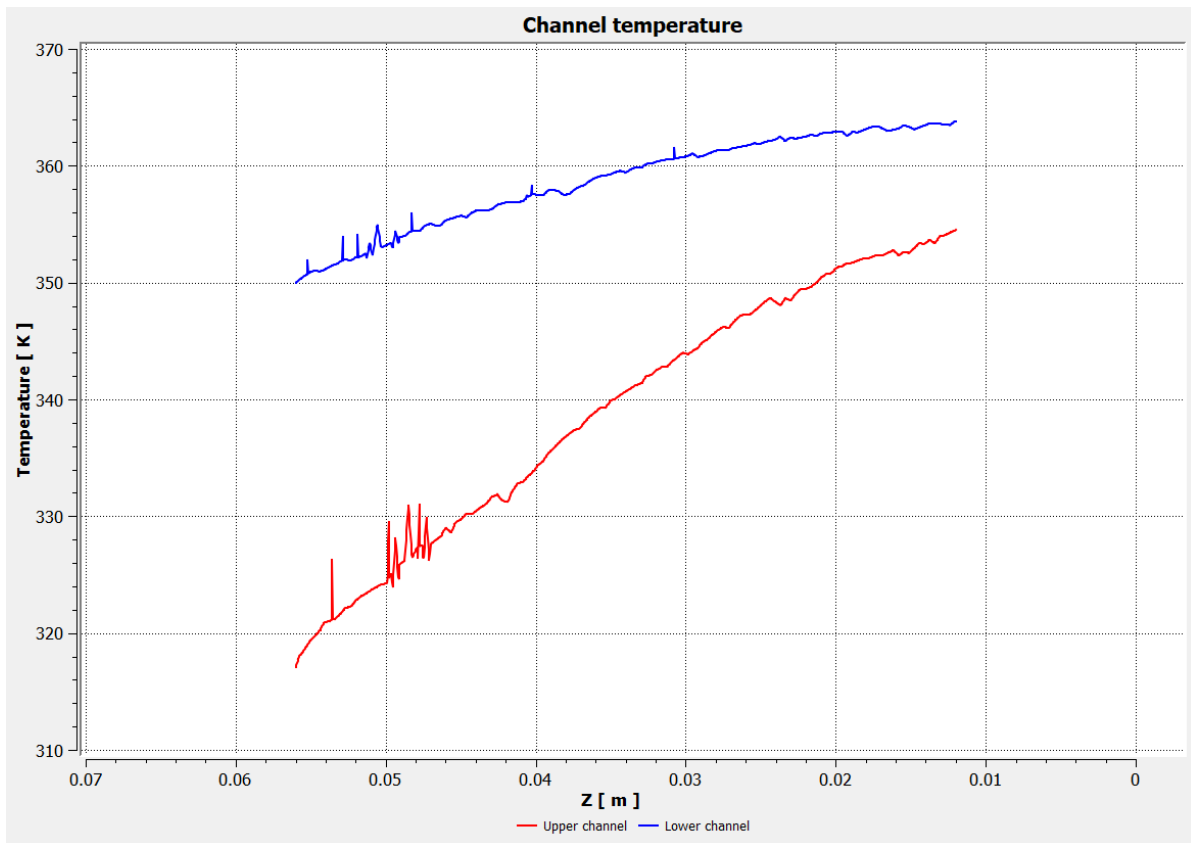


Figure 7.18: Temperature along both the upper and lower channel, turbulent subcase. Note that the x-axis, which is in the positive Z-direction, is reversed.

What immediately becomes apparent is the raise in thermal efficiency for both subcases when compared to [STT1](#). This can mainly be attributed to the lower convection and radiation losses on the outer surfaces of the heat exchanger, despite the almost equal outer wall area (the difference was a mere 2.2 %). However, the total channel area (including entrance and exit regions) is 26.4 % larger for [STT2](#) than it is for [STT1](#). What is furthermore noticeable is that the propellant temperature again came very close (or even exceeded the average wall temperature) for the turbulent subcase. This heat exchanger is thus superior in terms of thermal efficiency but will not be favoured because of its higher mass in comparison to Leenders' [RAC](#). The mass of 103 % higher for [STT1](#) than it is for [STT2](#). This is mainly attributed to the relatively thick walls which were required to manufacture the piece. If manufacturing allows, decreasing the wall thickness would make this design very competitive, especially when the aperture is kept at a minimum diameter.

In Figure 7.19, a cross-section of [STT2](#) is shown for a turbulent flow. Clearly, the heating of the propellant in the channel area can be observed. Again, the propellant that traversed through a channel that "started" further away from the propellant inlet is already more heated. Especially in the turbulent subcase the entrance region, which is the area before the fluid enters the channels, greatly heats up the fluid. This part is very hard to analyse, as its shape is not a convectional one.

Regarding the pressure loss of the heat exchanger, the loss is 54 402 Pa and 76 761 Pa for laminar and turbulent flow respectively. This is almost double the values when compared to [STT1](#). Inputting the channel dimensions and sea level properties, Equations 4.48, 4.51 and 4.52 yield 25 263 Pa and 23 423 Pa for laminar and turbulent flow cases respectively. Again, some pressure is also lost in the entrance and exit regions, but the exact values can again neither be verified nor validated unfortunately.

Table 7.12: Averaged propellant temperatures and Nusselt numbers for each region, case 5.

	Case 4: laminar		Case 4: turbulent	
	Nusselt number [-]	Resulting propellant temperature [K]	Nusselt number [-]	Resulting propellant temperature [K]
<b>1. Entrance region</b>	3.44	315.47	6.39	326.38
<b>2. Channel region</b>	9.23	368.52	16.98	370.62
<b>3. Exit region</b>	3.57	371.72	N/A	373.11
<b>Efficiency</b>		80.8%		81.9%

## 7.11. Case 6: Solar Thermal Thruster 2, mass flow and no insulation, high power

In order to compare the results to the last case in Chapter ??, the power was increased to 250 W and the number of channels was reduced to 6. As a result, the laminar Ansys Fluent run showed a propellant temperature of 775.3 K at a thermal efficiency of 61.2 % and pressure loss of 1.23 bar. The RAC reached temperatures between 800.3-813.7 K. The assumption of uniform wall temperature is thus less valid at higher power inputs. The turbulent case unfortunately did not converge; the temperatures oscillated over a large range of more than 100 K. This can be attributed to the fact that the decrease in channels increases the kinetic energy in the channels as the mass flow stays the same. Apparently, this requires a finer mesh in order to converge. Unfortunately, the Fluent student license does not allow for more elements. It is expected though that the thermal efficiency for the turbulent case would be higher (by 1-4 %), as this was also what was seen in the previous cases.

In Section 5.3, the thermal efficiency of a similar case was found by using the preliminary Python tool. It was equal to 53.7 %, which is considerably lower than the value reported by Ansys Fluent. However, the tool could not take into account the heat transfer in the entrance and exit of STT2. Without the heat transfer in those areas, Ansys Fluent would only report a thermal efficiency of 59.6 %. The values do differ and again, both preliminary tool and Ansys Fluent would benefit from experimental results, especially where it concerns propellant convective heat transfer.

## 7.12. Conclusions & recommendations

This chapter proved that CFD can be a welcome addition in the designing process of the RAC of an STP engine. Although the use is limited due to a student license, it is recommended to carry out CFD simulations to confirm analytical results regarding heat transfer. Especially in entrance and exit areas where it is often hard to predict what the implications of the intended design are, numerical analysis can help. However, due to the fact that relations from literature are near impossible in these regions, it is also very hard to verify the results from the analysis. Commercial software programs, such as the used Ansys Fluent, are very well verified and validated for well-known cases, but leave a blind spot in non-trivial simulations. To mitigate the risk that results gained from the simulations are deemed useless, the following is recommended. First, the results can be sanity checked by comparing them to literature. If anomalies, when present, can be explained by literature, one can already assume that the outcomes have more value. What is even better is to perform a mesh sensitivity analysis, in which the influence of the mesh is quantified by step wise going from a more coarse to a more fine discretization. Last recommendation for validation is to perform an experiment, after which the results can be compared to the simulation outcome.

The first and third recommendations were partly carried out in this chapter. However, the recommendation still stands to execute more experiments and check the influence of finer meshes, if resources allow. For this thesis that will be out of the scope. Next to that, the designed spike, intended to scatter the incoming radiation, could not be evaluated. Implementing a ray tracing module (as done by [26]), which is possible in Fluent, would also increase the validation of the simulation results.

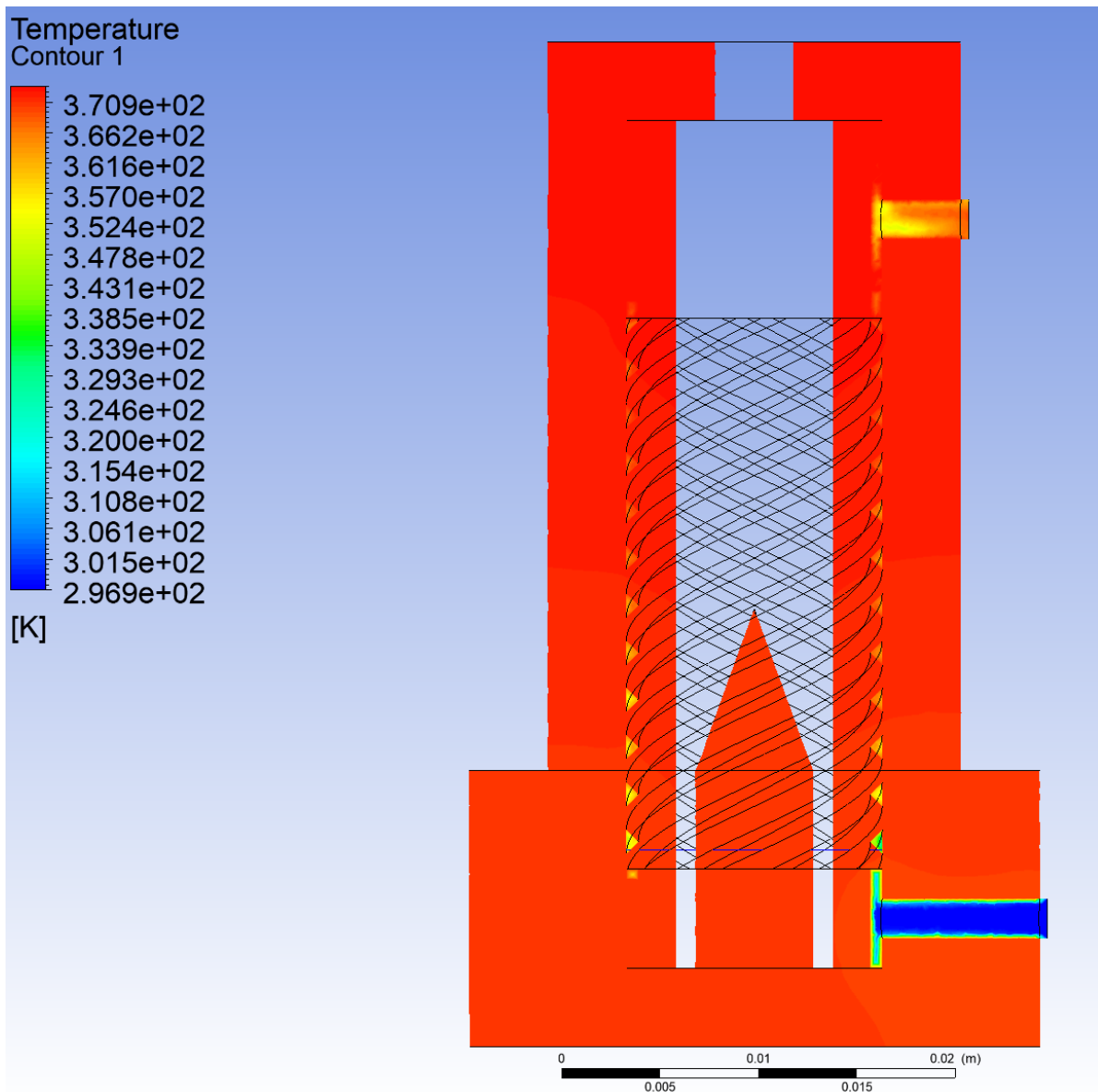


Figure 7.19: Case 5: cross-section of STT2 showing the temperature in RAC and propellant in turbulent flow.

Next to the question whether CFD analysis can be used in STP design, a comparison between the heat exchangers of Leenders and the author was made. The latter was modified to correct for the errors from the earlier design process. While the modified STT2 heat exchanger had a slightly higher performance due to the lower outside area and the reduced losses from the inner cavity, its mass was significantly higher than Leenders' RAC. The findings from this chapter will be carried over to the next chapter, where a new design will be proposed.

# 8

## Final solar thermal thruster design

This chapter will describe the final design of the solar thermal motor. The design will be built on the findings from the previous chapters and be named **STT3** in order to distinguish it from the previous two engines. In the first section, recommendations will be given that were found out during the design, manufacturing and performance analysis of both **STT1** and **STT2**. It will be followed by a section where the resulting design is presented, followed by a performance analysis using both preliminary tool and **CFD** simulation, to assess if the thermal performance meets the requirements set in Chapter 2. Finally, conclusions will be drawn on the results.

To reason to redesign the solar thermal engine is because previous chapters showed that STT2 does not meet the requirements in both performance and mass. Ultimately, the aim of this chapter is that the design will be the input for a new thesis, wherein the validity of the design is researched by subjecting it to testing. Eventually, raising the nitrogen specific impulse to a **SL** specific impulse of 90.0 s at a mass flow of 300 mg s<sup>-1</sup> set in Chapter 2 is the goal of the redesign.

### 8.1. Recommendations from previous chapters

As was explained in Section 6.5, the **STT2** design was designed with a few serious flaws, which disallowed the use of experiments to validate its performance. These flaws need to be prevented in future designs; as such, the preliminary tool from Chapter ?? was fitted with an option to check if the fluid velocity would not become too high in the channels (see Equation 8.1 where  $\rho$  is the propellant density in kg m<sup>-3</sup>).

$$v_{max} = 175 \left( \frac{1}{\rho} \right)^{0.43} \quad (8.1)$$

Next to this, Section 5.6 recommended to omit the use of threads in any design because of leakage issues. Hard-soldered connections are recommended as they are more reliable in that area but suffer from a maximum temperature constraint of 933 K.

From Chapter 5, it became clear that the limited resources at **DUT** are very influential on the design. Thesis students often have to rely on favours to make the design possible or need to learn how to manufacture themselves. Both heat exchangers discussed in this thesis are good examples of this aspect; Leenders somehow did manage to make his prototype small and lightweight, while for **STT2**

the Dreamhall maker did ask for a relatively thick wall to make the design possible and prevent any faults.

Manufacturing such a delicate and small heat exchanger yourselves is a challenge. Only students that have multiple years in experience in metal machining on lathes, drills and mills are expected to have the knowledge to execute such a design. Another solution is to deliver the drawings to the indoor workshop **DEMO**. They are experts on metallurgy and have high-grade **CNC** machinery, while students often only have access to manual mills and lathes. However, the required designs are very expensive and cannot be made within the budget of €500,- provided by the faculty, given that other expenses on propellant and material also need to be within budget.

It became clear from the preliminary tool in Chapter ?? that accurately predicting the enthalpy increase of the flowing propellant was very hard, because the channel regions were made up out of differing cross-sectional shapes. Likewise, the pressure loss was also hard to assess. In Chapter 7, it was researched if **CFD** analysis would be an asset to an **STP** designer on a limited budget. The careful conclusion from that chapter is that it could, given that the designer performs sanity checks, mesh sensitivity analysis and ultimately simple experiments.

In Chapter 7 it was furthermore seen that the pressure loss in the heat exchanger can become as high as 1.23 bar for STT2 and 0.46 bar for STT1. This is not acceptable, as Chapter 2 shows that a limited amount of pressure loss is allowed to keep the feed pressure below 10 bar which is the maximum pressure for nanosatellites. Next to that, some of the pressure sensors have 10 bar as the upper limit. These can be replaced by sensors having a larger pressure range, but this will affect the budget. Remember that the design pressure for the nozzle chamber equals 8.16 bar, so any pressure loss before the nozzle is added up to that. An arbitrary 0.50 bar maximum of pressure loss in the heat exchanger is thus set as additional requirement, **REQ-S-5**. This value will allow for some additional pressure loss in tubing outside the heat exchanger and also some flexibility in altering the mass flow in experiments.

## 8.2. Solar Thermal Thruster 3 design

STT3 will largely follow the design set in Chapter 5: the heat source, heat exchanger type and shape, heat exchanger material and propellant will remain the same as the choice for those aspects was already discussed in that chapter. As such, the heat source for STT3 will be an indirect absorbing, direct propulsion type with nitrogen as the propellant. Next to that, the heat exchanger will be cylindrical with spirally-shaped channels and made out of copper.

One issue with **STT2** was the high mass. As was pointed out before, the wall thickness of **STT2**'s heat exchanger can be reduced from 4 mm to Leenders's 1 mm. Doing this, the mass will dramatically reduce, which probably brings it within acceptable ranges. Another major problem of **STT2** was the channel section. Only one channel with a cross-sectional area of  $0.36 \text{ mm}^2$  was erroneously designed, which proved to be detrimental to both pressure loss and heat transfer. The amount of channels thus has to be increased, as well as its cross-sectional shape (which is triangular) revised.

### 8.2.1. Heat exchanger dimensions

The goal of 70 % in thermal efficiency (with input power 250 W) results in a final propellant temperature of 835.3 K at a mass flow of  $300 \text{ mg s}^{-1}$  and an inlet temperature of 298.15 K. Because of the high thermal conductivity of copper, it is assumed that the wall temperatures are equal in every location. This seems valid, because according to the analysis in Chapter 7 for **STT2** the walls had a maximum difference of 13.4 K. So, the outer walls have to have a temperature of at least the final propellant temperature. Only the outer walls of **STT2** experienced significant losses (97.7 W), while the other walls did lose a maximum of 0.38 W in total. 153.1 W is currently transferred to the propellant, which

is 61.2 %. 70 % amounts to 175 W which needs to be used to heat the propellant. This leaves 75 W for losses. At a convective heat transfer coefficient of  $8.494 \text{ W m}^{-2} \text{ K}^{-1}$ , wall temperature of 835.3 K, emissivity of 0.65 and ambient temperature of 298.15 K, the outer wall area can be  $0.00338 \text{ m}^2$  at most. This is a reduction of 32.5 % when compared to the original  $0.0050 \text{ m}^2$ , which is drastic.

**STT1** can be roughly seen as two cylinders, the first having diameter 21 mm and length 37 mm, the second (which is the end cap) diameter 29 mm and 14 mm. The outer wall area then amounts to  $0.0050 \text{ m}^2$ , a bit more than the aforementioned value due to the aperture. As said before, the thicknesses can and will be reduced (under sufficient manufacturing knowledge), analogous to Leenders' **RAC**. The outer wall thickness for the smaller cylinder will be reduced from 4 mm to 1 mm, which reduces its diameter by 6 mm and its length by 3 mm. The end cap will have its wall thickness reduced from 4 mm to 2 mm. The resulting outer area is then  $0.0029 \text{ m}^2$ , which is more than sufficient to reduce the heat loss. It leaves a margin for an increase in convective heat transfer coefficient and a higher outer wall temperature. Next to that, the channel region heating area is not affected by these changes, so the thermal efficiency could only increase; the channel section length of 28 mm will be unchanged as well as the inner diameter of 11.8 mm where the channels start.

### 8.2.2. Channel shape and dimensions

In Section 7.10, it became clear that 6 channels for **STT2** would lead to unacceptable pressure losses but high thermal efficiency as well. This also becomes clear from the Darcy-Weisbach equation for pressure loss (see 8.2) and the Reynolds number equation (see 8.3). As a rule of thumb, the higher the Reynolds number, the higher the amount of heat flowing to the propellant. This is supported by the analysis in Chapter 7, where the turbulent flow sees a higher thermal efficiency than the laminar one, which is also seen in the equations in Subsection 4.2.1. To raise the Reynolds number (with fixed mass flow), one could lower the cross-sectional area by decreasing the diameter (in circular channels). However, this would increase the flow velocity in the channels, which would increase the pressure loss by that same amount squared. Pressure loss versus thermal efficiency is the trade-off here, which is also visible in Incropera et al.'s Table 8.1 [8]. There we observe that a higher Nusselt number is approximately proportional to the pressure loss in a channel, for laminar flow. Because turbulent flow, above Reynolds numbers of 2300 is still wanted but, this number will be kept as the minimum for channel flow Reynolds numbers.

$$\Delta p = f_{DB} \frac{1}{2} \frac{L}{D_h} \rho v^2 \quad (8.2)$$

$$Re_{channel} = \frac{\rho v D_h}{\mu} \quad (8.3)$$

Three distinct shapes can be distinguished for the channel: circular, square and triangular. As for **STT2**, they will be milled at the outside of the inner cylinder, at a diameter of 11.8 mm. Incropera's table shows that circular channels have the highest Nusselt number at uniform wall temperature and laminar flow. This is also depicted in Table 8.1, second column. However, the Nusselt number does not incorporate the effect of channel area. Looking at the inner heat exchanger cylinder where the channels have to be made in, a circular cross-section would waste a lot of room on this cylinder; in the same  $0.6 \times 0.6 \text{ mm}^2$  "box", the circular channel takes less "room" than the square one. The triangular shape does even worse, see the table's third row where the wetted perimeter  $S$  in m is shown. When corrected for this area (perimeter) difference and also for the hydraulic diameter, the triangular channel comes out on top in terms of heat transfer, see last column. For this calculation, the channel length  $L_{ch}$  is taken as 1 m and the thermal conductivity as  $0.02583 \text{ W m}^{-2} \text{ K}^{-1}$ . The heat transfer  $Q_{conv,T}$  in  $\text{W K}^{-1}$  is calculated using Equation 8.4.

$$Q_{conv} = \frac{Nuk}{D_h} \cdot S \cdot L_{ch} \quad (8.4)$$

Table 8.1: Comparison between channel shapes in terms of heat transfer [8].

Channel shape	Nu <sub>D<sub>h</sub></sub> at uniform wall temperature [-]	S [mm]	D <sub>h</sub> [mm]	Q <sub>conv</sub> [W/K]
<b>Circular</b>	3.66	1.88	0.60	0.297
<b>Square</b>	2.98	2.40	0.60	0.308
<b>Triangular</b>	2.49	1.88	0.35	0.331

However, the effect of pressure loss is far greater for the triangular cross-section. In Table 8.2, the second column shows the values taken from Incropera [8]. The Reynolds number is shown in the third column for an arbitrary 10 channels using Equation 8.3 ( $\mu$  equals  $1.76 \times 10^{-5}$  Pa s), so the mass flow through each channel is  $30 \text{ mg s}^{-1}$ . With the use of the cross-sectional area  $A_{cs}$  in  $\text{m}^2$  and taking the density as  $1.135 \text{ kg m}^{-3}$ , the flow velocity  $v$  in  $\text{m s}^{-1}$  can be calculated. This eventually gives the pressure losses in the last column of the table using Equation 8.2 for a channel of 1 m in length. There, it can be seen that the triangular option has a far higher pressure loss when compared to the other two.

Table 8.2: Comparison between channel shapes in terms of pressure loss [8].

Channel shape	f <sub>DB</sub> · Re <sub>D<sub>h</sub></sub> [-]	Re <sub>D<sub>h</sub></sub> [-]	f [-]	A <sub>cs</sub> [mm <sup>2</sup> ]	v [m/s]	Δp [bar]
<b>Circular</b>	64	3617	0.0177	0.283	93.5	4.90
<b>Square</b>	57	2840	0.0201	0.360	73.4	3.11
<b>Triangular</b>	53	3788	0.0140	0.156	169.6	20.12

Because of the low pressure losses and medium thermal efficiency, the square cross-section is chosen as the channel shape. Note that the square option is harder to manufacture than a triangular one, but easier than the circular option. The dimensions of the channel cross-section will be 0.6x0.6 mm<sup>2</sup> to allow for comparison with Leenders's RAC.

In order to reduce the amount of pressure loss the most, the number of channels needs to be increased. With the current cross-section, the Reynolds number minimum of 2300 allows for 12 channels, which give a Reynolds number of 2367 in each channel. The width between each channel will be 1 mm, so the pitch is 1.6 mm times 12 is 19.2 mm. The width is similar to the wall thickness, so it is expected that this can be manufactured. As said before, the channel section total length is 28 mm, which gives a channel spiral length of 60.8 mm.

### 8.2.3. Other changes

Next to the changes in heat exchanger dimensions and channel section, the holes at start and end will both have a diameter of 5 mm. That way, tubes with an outer diameter of 5 mm and an inner diameter of 3 mm can be connected. The latter value ensures that the pressure losses are low in these tubes, because the cross-sectional area is 19.6 times the area of one channel. The holes will be extended by 5 mm at a diameter of 5 mm to allow for a solid connection. Simultaneously, both ends of the inner cylinder will be shortened to a length of 3 mm. Threads present in STT2 will be substituted by hard solder connections to prevent leakages. According to DEMO, these connections can withstand 933 K at most, which is sufficient. The spike will be removed, because its use cannot be verified in the upcoming analysis. It could be placed back if a ray tracing tool is used. Now that the spike is removed, one end of the inner cylinder will be closed to prevent leakage on that side.

A nozzle with a throat diameter of 0.58 and an exit diameter of 0.76 mm is designed. It will be made of copper as well, due to the high melting point, easy manufacturability and medium cost.

### 8.2.4. Results

In Appendix B, the CAD drawings of STT3 are shown. The resulting design has an outer wall area of  $0.00274 \text{ m}^2$ , which is smaller than the maximum  $0.0038 \text{ m}^2$ . The extra reduction allows for a small increase in coefficient of convective heat transfer to the ambient. The total volume of the RAC amounts to  $4852 \text{ mm}^3$ , which gives a mass of  $43.6 \text{ g}$  at a copper density of  $8978 \text{ kg m}^{-3}$ , meeting the requirement. In Figures 8.1 and 8.2, both designed heat exchangers of STT2 and STT3 are shown respectively. Note the considerable difference in size, while the scale is equal. Furthermore, the increased hole diameter for both inlet and outlet in STT3 is shown, so that tubes can be connected more easily. An exploded view of STT3's heat exchanger is shown in Figure 8.3.

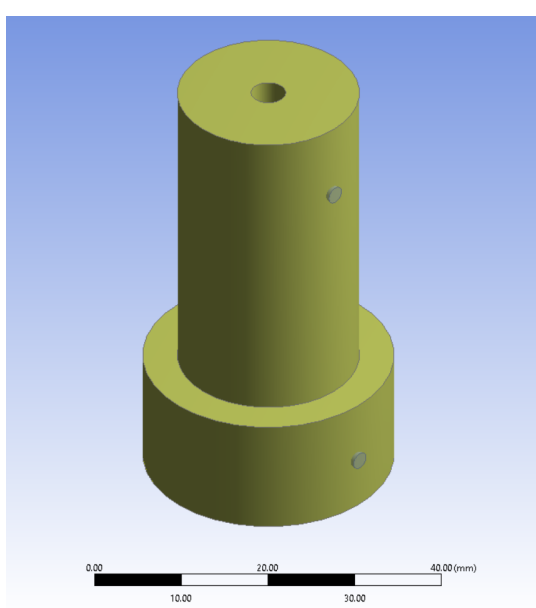


Figure 8.1: View of STT2.

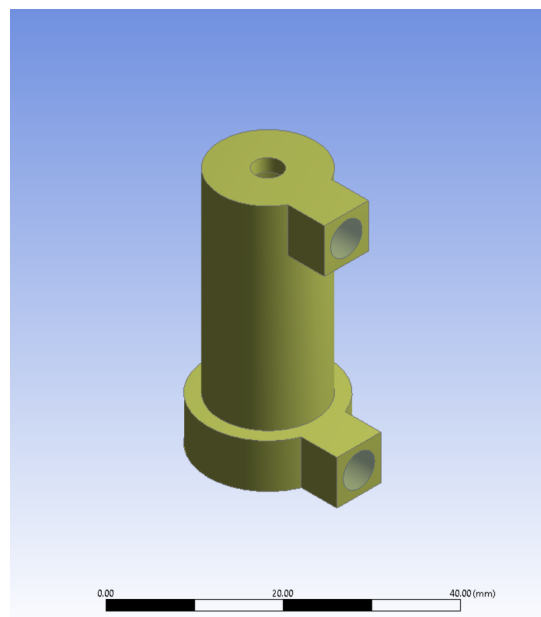


Figure 8.2: View of STT3.

## 8.3. Solar Thermal Thruster 3 performance

The inputs from Section 5.3 were used for the PDT simulation. The differences in inputs are the RAC mass and dimensions and the number of channels and its dimensions. From those inputs, the tool calculated a thermal efficiency of 61.1 % and a pressure loss of 0.02 bar for the heat exchanger.

The same procedure as in Chapter 7 was taken for the STT3 CFD simulation. First, the wall coefficient of convective heat was calculated by creating a "box of air" around the heat exchanger. Again, the fluid domain is integrated in the RAC domain to allow for more mesh elements to be placed on critical connecting surfaces, such as the outer walls. The air velocity from the sides is again  $0.001 \text{ m s}^{-1}$ . The simulation was deemed converged after 500 iterations and outputted a convective heat transfer coefficient of  $9.358 \text{ W m}^{-2} \text{ K}^{-1}$  at an ambient temperature of  $298.15 \text{ K}$ , when averaged over the last 100 iterations. This value is a little higher than the value for STT2, but the decrease in outer wall area fully mitigates this extra loss. Thus, it is to be expected that the total loss (in Watts) for the current design will be less than for STT2. The radiation view factors are calculated for each inner surface. The outer surface is assumed to have a view factor of 1 towards the ambient.

Then, the air box is deleted and the convective and radiative boundary conditions are applied to each wall. The inner cylinder surface will experience a power input of  $250 \text{ W}$ . After 500 iterations, a thermal efficiency of 68.6 % was reached, which resulted in an outlet propellant temperature of  $830.3 \text{ K}$ , which is almost the desired value for a specific impulse of  $90 \text{ s}$ . The pressure loss amounts to  $0.43 \text{ bar}$ .



Figure 8.3: Exploded view of the STT3 heat exchanger.

## 8.4. Conclusions

Table 8.3 shows the properties and results of both PDT and CFD analysis for all three engines. The results are from simulations with 250 W of input power, nitrogen mass flow of  $300 \text{ mg s}^{-1}$  and SL ambient properties. PT here stands for preliminary tool.

The first thing that is visible is the large differences in preliminary tool outcomes and CFD results. This is mostly explained by the influence of the entrance and exit regions of the heat exchangers, which are not taken into account in the tool. These regions are quite sizable in STT2 and STT3, hence the differences. For STT1, an interesting detail is that the thermal efficiency is lower for the CFD analysis than for the preliminary tool results. This could perhaps be due to varying Reynolds numbers in the channels; however, validation experiments could be of great assistance here, as could it be for all results.

Another thing that becomes apparent is that STT2 is not at all competitive with respect to STT1 because of the higher mass. However, the thermal efficiency is higher for STT2 than for STT1 at the cost of more pressure loss when looked at the CFD results. STT3 on the other hand outperforms STT1 and STT2 on all areas, be it size, mass or performance. So, this new design is recommended for future

manufacturing and testing at DUT. The most prominent downside for the engine are the small details. However, STT1 could be built at DUT and STT3 does not have any smaller details than Leenders's RAC, so it is believed that STT3 can one day be tested at this university.

Table 8.3: Properties and results for all three engines.

	<b>STT1</b>	<b>STT2</b>	<b>STT3</b>
<b>RAC material [-]</b>	Copper	Copper	Copper
<b>RAC mass [g]</b>	87	182	44
<b>RAC length [mm]</b>	69	51	38
<b>RAC largest diameter [mm]</b>	37	29	19
<b>RAC number of channels [-]</b>	8	6	12
<b>Channel cross-sectional shape [-]</b>	Square	Isosceles triangle	Square
<b>Channel length [mm]</b>	52.5	77.3	60.9
<b>Channel cross-sectional area [mm<sup>2</sup>]</b>	0.36	0.36	0.36
<b>Nozzle throat diameter [mm]</b>	0.58	0.58	0.58
<b>Nozzle exit diameter [mm]</b>	0.68	0.68	0.76
<b>Propellant</b>	Nitrogen	Nitrogen	Nitrogen
<b>PDT: Thermal efficiency [%]</b>	53.2	53.7	61.1
<b>CFD: thermal efficiency [%]</b>	50.4	61.2	68.6
<b>PDT: pressure loss [bar]</b>	0.10	0.10	0.02
<b>CFD: pressure loss [bar]</b>	0.46	1.23	0.43

# 9

## Conclusions & recommendations

This chapter will describe the conclusions, followed by the recommendations.

### 9.1. Conclusions

The project was kicked off as a practical study towards STP thrusting. The goal was to, with DUT resources, construct and successfully test an engine and bring the SL specific impulse to 90.0 s at a continuous nitrogen mass flow of  $300 \text{ mg s}^{-1}$ . This goal was set with accordance to the only practical STP predecessor at DUT who executed the same idea in 2008 with a specific impulse of 49.6 s under a heat input of 49 W and thermal efficiency of 52 %. A SL specific impulse of 90.0 s was still thought to be achievable when looking at the melting points of the used materials and the sensor equipment involved. The goal would be supported by three main subgoals: the thermal efficiency of the heat exchanger would be increased to 70 %; the input power to the heat exchanger would be increased to 250 W; and a preliminary tool would be built in order to determine the STP thruster performance.

The thruster STT2 was designed to be of a direct propulsion, indirect absorber type. The realized RAC was a windowless cylindrical copper piece with one spiral channel with a triangular cross-sectional area of  $0.36 \text{ m}^2$ . The part had a manufactured mass of 0.182 kg, total length of 51.0 mm and largest diameter of 28.98 mm. It also featured a 4 mm aperture to reduce inner cavity losses and a spike which would scatter the incoming radiation. For the manufacturing phase, executed by a fellow student for a reduced price, many concessions had to be made on the design of the cavity. The most influential one was that the cavity walls needed to be thicker than designed, which caused the design to be heavier than its predecessor. No budget was left for the nozzle, so the copper nozzle from Leenders was projected to be used in the experiments. The heat source would be a 8000 W welding laser at the faculty of 3mE. The laser emits a beam that can be controlled in 1 W steps. The smallest focus diameter is 0.20 mm while the beam diameter can become as large as 50 mm. Gaseous nitrogen was the propellant choice due to its relative inert nature, medium performance and cheap availability.

A preliminary tool was built in Python in order to evaluate the thruster performance. The tool allowed for flexibility in inputs such as propellant, heat exchanger shape and dimensions, insulation, mass flow, pressure and available power. It was validated for cases where no mass flow was present, but it proved to be hard to find the convective heat transfer from heat exchanger to propellant because no reliable validation cases were available. Predicting this heat transfer would be hard, due to the sharp corners, varying cross-sections and entrance effects of the channel section in heat exchangers. Nonetheless, the tool foresaw that the heat exchanger would have a thermal efficiency of 53.7 % under a solar load of 250 W. This would not be sufficient to reach the first subgoal. However, the tool predicted a thermal

efficiency of 88.2 % when a cylindrical insulation layer (diameter of 11 cm and length of 10 cm) was placed around the heat exchanger.

When experiments were prepared to validate these findings, three main reasons were found to discontinue the physical experiments: the first was that STT2's heat exchanger was erroneously designed with one instead of six channels. This proved to be a huge problem, because at a mass flow of  $300 \text{ mg s}^{-1}$  the pressure drop over the heat exchanger would be more than 25 bar. The second reason to reconsider the experiments was that the RAC was leaking on multiple sides due to the thread connections. When trying to tackle this issue with teflon tape and kit, the heat exchanger's channel section was blocked by the kit. A third reason was the COVID-19 pandemic, which prevented the laser facility at 3mE to be used for the experiments.

As such, a new plan was made: the preliminary tool would be validated by CFD analysis in Ansys Fluent. Furthermore, the CFD analysis would provide the designer with a more accurate prediction of the thermal performance and the pressure loss in the heat exchanger. Next to that, a new design would be made based on the knowledge gained during the manufacturing phase. The CFD analysis saw a thermal efficiency of 61.2 % and pressure loss of 1.23 bar for STT2's heat exchanger. This is significantly higher than the preliminary tool outputted, which is partly explained by the fact that Ansys Fluent took the heat transfer in the entrance and exit region of the heat exchanger into account. However, still some discrepancies remained, which could not be explained. In order to validate these findings, dedicated experiments should be done.

With the knowledge gained from the CFD analysis, STT2 was redesigned into a more competitive STT3. One requirement was added for this engine: it would have a maximum pressure loss of 0.50 bar over the heat exchanger. Furthermore, the motor still had to adhere to Chapter 2's requirements. STT3 was again of a direct propulsion, indirect absorber type with a windowless cylindrical copper RAC with an aperture of 4 mm. The number of channels was increased to 12 and its cross-section was altered to a square shape of 0.6 mm by 0.6 mm. The overall length was reduced to 38 mm and the overall diameter was brought back to 19 mm. The reduction was mostly due to the lower wall thickness, which would be brought from 4 mm to 1 mm in most locations. The increase in channels would lower the Nusselt number due to lower flow velocities, but it was predicted that this would be more than compensated for by the lower losses to the surroundings. Furthermore, it would reduce the amount of pressure loss. The spike was removed as its influence could not be predicted. The total heat exchanger mass amounted to 43.6 g. The nozzle was designed with a throat diameter of 0.58 mm and an exit diameter of 0.76 mm.

The preliminary tool predicted a thermal efficiency of 61.1 % with an input power of 250 W and only a pressure loss of 0.021 bar. The CFD analysis outputted a thermal efficiency of 68.6 % and a pressure loss of 0.43 bar. This efficiency almost meets the desired 70 %, while the pressure loss is lower than the desired 0.50 bar maximum. The large discrepancies in preliminary tool and CFD analysis were mostly explained due to the fact that Ansys Fluent did take the entrance and exit regions into account. Because the heat exchanger design incorporated the heat transfer in these regions as well, the thermal efficiency is much higher from the CFD simulations. Again, both tools would benefit from experimental validation cases.

The current project had the goal to show that a solar thermal engine could reach a SL specific impulse of 90.0 s at DUT. This objective is not reached entirely; the experiments could not be continued as expected. However, with the help of CFD simulations, it was shown that the subgoals were partly met for STT2: the thermal efficiency of 61.2 % was lower than 70 %, but the input power can be increased with the use of the laser welding laboratory. Next to that, a preliminary tool did allow for useful results, although some parts still require validation. STT3 was the result of the redesigned STT2 and met all subgoals set: the CFD analysis gave a thermal efficiency of 68.6 %, almost meeting the SL 90.0 s specific impulse mark. Next to that, it had a lower mass and volume than its two predecessors and could still be made and experimented on at DUT.

The expectation is thus that this thesis serves as the input for a next master student who is willing

to pick up the STT3 design, manufacture the pieces and test them in the laser welding facility at [3mE](#) when possible again.

## 9.2. Recommendations

The foremost recommendation that is to be given is to construct [STT3](#) and validate both the preliminary tool and [CFD](#) simulation results. This is most needed in the area of convective heat transfer to the propellant, as the losses to the surroundings were already quantified at a good level. When this is done, the results could help to improve the Python tool while also showing if the extensive effort needed for the [CFD](#) analysis pays itself back.

Next to this recommendation, another list is given below. It will consist of recommendations to any student and of advice for the project itself.

- It would be interesting to see how other propellants than nitrogen (water, carbon dioxide) would influence the performance. Two-phase flow is not incorporated in the preliminary tool, so that would be an improvement.
- Quantifying the losses on the outer sides of the heat exchanger is an area which has not been explored extensively in this thesis. The convective heat transfer for losses should be validated.
- Incorporating a thermal heat storage, fiber optic cables or a power subsystem in the engine would bring the [STP](#) thruster more up-to-date with the research nowadays.
- A thorough understanding of metallurgy is a huge advantage for a practical thesis into [STP](#). The pieces are expensive to manufacture, so any work that can be done by the student itself will increase the options in other areas, such as sensor equipment.
- Any experience on experimenting (at [DUT](#)) is also an advantage. One needs to be aware that practical issues will arise during testing and that a problem-solving mindset is required.
- Additional funding is required in order to order externally built pieces. Try the department of [AE](#) or look for other sponsors outside of the university.

# Bibliography

Most of the TU Delft thesis reports are retrievable from <https://repository.tudelft.nl/>.

- [1] Bryce Space & Technology, *SmallSats by the Numbers 2019*, (2019).
- [2] H. P. Gerrish Jr, *Solar Thermal Propulsion at MSFC*, Tech. Rep. (Marshall Space Flight Center, 2016).
- [3] H. C. M. Leenders, *Development of a solar thermal propulsion system*, Tech. Rep. (MSc thesis report TU Delft, 2008).
- [4] F. Valente, *Development and verification of test set up for microthrusters testing*, Tech. Rep. (MSc thesis report TU Delft, 2007).
- [5] S. Janssens, *Design of a micro propulsion test bench*, Tech. Rep. (MSc thesis report TU Delft, 2009).
- [6] I. Krusharev, *Micro - Thruster Development: Propulsion System for the DelFFi Mission*, Tech. Rep. (MSc thesis report TU Delft, 2015).
- [7] H. Leenders and B. Zandbergen, *Development of a Solar Thermal Thruster System*, 59th International Astronautical Congress (2008).
- [8] F. Incropera, D. Dewitt, T. Bergman, and A. Lavine, *Fundamentals of Heat and Mass Transfer (6th edition)* (John Wiley & Sons, 2007).
- [9] S. W. Janson, *25 Years of Small Satellites*, 25th Annual AIAA/USU Conference on Small Satellites (2011).
- [10] A. Freeman, *Exploring our solar system with CubeSats and SmallSats : the dawn of a new era*, *CEAS Space Journal* **12**, 491 (2020).
- [11] F. Leverone, A. Cervone, and E. Gill, *Cost analysis of solar thermal propulsion systems for microsatellite applications*, *Acta Astronautica* **155**, 90 (2019).
- [12] A. Perera-Webb, A. Da Silva Curiel, and V. Zakirov, *The changing launcher landscape - A review of the launch market for small satellites*, in *IAC* (2017) pp. 11987–11990.
- [13] A. Poghosyan and A. Golkar, *CubeSat evolution: Analyzing CubeSat capabilities for conducting science missions*, *Progress in Aerospace Sciences* (2017), [10.1016/j.paerosci.2016.11.002](https://doi.org/10.1016/j.paerosci.2016.11.002).
- [14] T. A. Grönland, P. Rangsten, M. Nese, and M. Lang, *Miniaturization of components and systems for space using MEMS-technology*, *Acta Astronautica* **61**, 228 (2007).
- [15] M. A. Silva, D. C. Guerrieri, A. Cervone, and E. Gill, *A review of MEMS micropropulsion technologies for CubeSats and PocketQubes*, *Acta Astronautica* **143**, 234 (2018).
- [16] D. B. Scharfe and A. D. Ketsdever, *A Review of High Thrust , High Delta-V Options for Microsatellite Missions*, in *45th AIAA/ASME/SAE/ASEE Joint Propulsion Conference*, August (2009) pp. 1–14.
- [17] P. Tortora, *Small satellites beyond boundaries*, *CEAS Space Journal* **12**, 489 (2020).
- [18] A. R. Tummala, *An Overview of Cube-Satellite Propulsion Technologies and Trends*, *MDPI* (2017), [10.3390/aerospace4040058](https://doi.org/10.3390/aerospace4040058).

- [19] K. Lemmer, *Propulsion for CubeSats*, in *Acta Astronautica* (Elsevier Ltd, 2017) pp. 231–243.
- [20] F. Etheridge, *Solar Rocket System Concept Analysis*, Tech. Rep. (AFRPL, 1979).
- [21] F. G. Kennedy, *Solar Thermal Propulsion for Microsatellite Manoeuvring*, Tech. Rep. (University of Surrey, Surrey, 2004).
- [22] B. Zandbergen, *AE4S01 Thermal Rocket Propulsion reader (version 2.06)* (TU Delft, 2017).
- [23] J. C. Mankins, *Technology Readiness Levels*, White Paper (April) Advanced Concepts Office. Office of Space Access and Technology. NASA. , 5 (1995).
- [24] F. Leverone, A. Cervone, M. Pini, E. Gill, and P. Colonna, *Feasibility of an Integrated Solar Thermal Power and Propulsion System for Small Satellites*, IAC (2017).
- [25] C. C. Selph, AFRPL, Tech. Rep. (AFRPL, 1981).
- [26] K. Das, *Design and Thermal Analysis of a Solar Thermal Thruster*, Tech. Rep. (MSc thesis report TU Delft, 2018).
- [27] A. Takken, *Literature study*, Tech. Rep. (TU Delft, 2019).
- [28] A. Takken, *Project Proposal and Plan*, Tech. Rep. (TU Delft, 2019).
- [29] T. Nakamura, D. Sullivan, J. A. Mcclanahan, J. M. Shoji, R. Partch, and S. Quinn, *Solar Thermal Propulsion for Small Spacecraft*, (2004) pp. 1–11.
- [30] P. Henshall, P. Palmer, and A. Baker, *Solar Thermal Propulsion Augmented with Fibre Optics: A System Design Proposal*, 41st AIAA/ASME/SAE/ASEE Joint Propulsion Conference & Exhibit , 1 (2005).
- [31] M. R. Gilpin, *Phase-Change Thermal Energy Storage and Conversion : Development and Analysis for Solar Thermal Propulsion*, in *48th AIAA/ASME/SAE/ASEE Joint Propulsion Conference*, August (2012) pp. 1–11.
- [32] K. A. Ehricke, *The solar-powered space ship*, Convair Astronautics (1956).
- [33] F. G. Kennedy and P. L. Palmer, *Preliminary design of a micro-scale solar thermal propulsion system*, in *38th AIAA/ASME/SAE/ASEE Joint Propulsion Conference & Exhibit*, July (2002) pp. 1–11.
- [34] F. Kennedy, P. Palmer, and M. Paul, *Results of a Microscale Solar Thermal Engine Ground Test Campaign at the Surrey Space Centre*, in *40th AIAA/ASME/SAE/ASEE Joint Propulsion Conference and Exhibit*, July (2004) pp. 1–11.
- [35] H. Sahara, K. Watanabe, M. Shimizu, and Y. Nakamura, *Single-Crystal Molybdenum Solar Thermal Propulsion Thruster*, *Trans. Japan Soc. Aero. Space Sci.* **46**, 180 (2003).
- [36] H. Sahara, M. Shimizu, K. Osa, K. Watanabe, and Y. Nakamura, *Solar Thermal Propulsion for Microsatellites End-of-Life De-Orbiting*, (2003) pp. 1–8.
- [37] H. Sahara and M. Shimizu, *Solar Thermal Propulsion System for Microsatellites Orbit Transferring*, in *40th AIAA/ASME/SAE/ASEE Joint Propulsion Conference and Exhibit*, July (2004) pp. 1–7.
- [38] M. R. Gilpin, D. B. Scharfe, A. P. Pancotti, and M. P. Young, *Molten Boron Phase-Change Thermal Energy Storage to*, in *Distribution* (2011).
- [39] P. Henshall and P. Palmer, *Solar Thermal Propulsion Augmented with Fiber Optics: - Technology Development*, in *42nd AIAA/ASME/SAE/ASEE Joint Propulsion Conference & Exhibit*, July (2006) pp. 1–12.
- [40] T. Nakamura, R. Krech, J. McClanahan, J. Shoji, R. Partch, and S. Quinn, *Solar Thermal Propulsion for Small Spacecraft - Engineering System Development and Evaluation*, in *41st AIAA/ASME/SAE/ASEE Joint Propulsion Conference & Exhibit* (2005).

- [41] J. D. M. Malloy, R. F. Rochow, and J. B. Inman, *Hybrid solar rocket utilizing thermal storage for propulsion and electrical power*, (1994).
- [42] B. Xing, K. Liu, M. Huang, and M. Cheng, *High efficient configuration design and simulation of platelet heat exchanger in solar thermal thruster*, *Journal of Thermal Science* **23**, 246 (2014).
- [43] H. C. M. Leenders and P. Batenburg, *Thermal control of a solar thermal propulsion system*, Tech. Rep. October (TU Delft, 2006).
- [44] H. C. M. Leenders, *Solar thermal propulsion Literature study*, Tech. Rep. (TU Delft, 2007).
- [45] D. M. Pino, *Solar Concentrator Demonstrator for PocketQubes*, Tech. Rep. (MSc thesis report TU Delft, 2016).
- [46] E. Jansen, *Improvement and validation of test stand performance for novel micropulsion systems*, Tech. Rep. (MSc thesis report TU Delft, 2016).
- [47] A. Cervone, B. Zandbergen, D. C. Guerrieri, M. A. Costa, I. Krusharev, and H. Zeijl, *Green micro-resistojet research at Delft University of Technology: new options for Cubesat propulsion*, *CEAS Space Journal* (2016), [10.1007/s12567-016-0135-3](https://doi.org/10.1007/s12567-016-0135-3).
- [48] T. Bergman and A. Lavine, *Fundamentals of Heat and Mass Transfer (8th edition)*, 8th ed. (Wiley, 2017).
- [49] J. Meyers, *ME 144 : Heat Transfer Internal Convection (v1.0)*, (2011).
- [50] G. L. Morini, *Laminar-to-turbulent flow transition in microchannels*, *Microscale Thermophysical Engineering* **8**, 15 (2004).
- [51] H. Baehr and K. Stephan, *Heat and Mass Transfer* (Springer, 2006).
- [52] W. M. Rohsenow and J. R. Hartnett, *Handbook of heat transfer* (McGraw-Hill, 1999).
- [53] D. Taler and J. Taler, *Simple heat transfer correlations for turbulent tube flow*, *E3S Web of Conferences* **13**, 1 (2017).
- [54] R. A. Seban and E. F. McLaughlin, *Heat transfer in tube coils with laminar and turbulent flow*, *International Journal of Heat and Mass Transfer* **6**, 387 (1963).
- [55] R. Ferreira, *Development and Testing of a Water Microresistojet*, Tech. Rep. (MSc thesis report TU Delft, 2008).
- [56] S. Paitoonsurikarn and K. Lovegrove, *On the study of convection loss from open cavity receivers in solar paraboloidal dish applications*, *Proceedings of ANZSES* **0**, 154 (2003).
- [57] Crane Company, *Flow of fluids through valves, fittings and pipe* (Crane Company, 1979).
- [58] P. Oosthuizen, *Free Convective Heat Transfer From Horizontal Cones*, ASME , 5 (1973).
- [59] R. J. Goldstein, U. Madanan, and T. H. Kuehn, *Simplified correlations for free convection from a horizontal isothermal cylinder*, *Applied Thermal Engineering* **161**, 113832 (2019).
- [60] L. Guo, Z. Feng, and X. Chen, *An experimental investigation of the frictional pressure drop of steam-water two-phase flow in helical coils*, *International Journal of Heat and Mass Transfer* **44**, 2601 (2001).
- [61] A. N. Johnson, P. I. Espina, G. E. Mattingly, and C. L. Merklet, *Numerical characterization of the discharge coefficient in critical nozzles*, Tech. Rep. (University of Tennessee Space Institute, 1998).
- [62] A. Takken, *Thesis Proposal and Plan*, Tech. Rep. (TU Delft, Delft, 2019).
- [63] J. M. Shoji, *Solar Rocket Component Study*, Tech. Rep. (Rockwell International, Canoga Park, 1985).

- [64] J. J. Preijde, *Design of a Solar Thermal Power-Propulsion System for a Small Satellite*, Tech. Rep. January (MSc thesis report TU Delft, 2015).
- [65] F. Valente, *Development and verification of test set up for microthrusters testing*, Tech. Rep. (TU Delft, 2007).
- [66] R. Bijster, *Design, Verification and Validation of a Micropulsion Thrust Stand*, Tech. Rep. (MSc thesis report TU Delft, 2014).
- [67] H. Versteeg, *Novel fabrication method for a hot gas supersonic micro-thruster*, Tech. Rep. (MSc thesis report TU Delft, 2020).
- [68] J. Tu, G.-H. Yeoh, and C. Liu, *Computational Fluid Dynamics* (Elsevier, 2008).
- [69] C. D. Argyropoulos and N. C. Markatos, *Recent advances on the numerical modelling of turbulent flows*, *Applied Mathematical Modelling* **39**, 693 (2015).
- [70] T. H. Kuehn and R. J. Goldstein, *Correlating equations for natural convection heat transfer between horizontal circular cylinders*, *International Journal of Heat and Mass Transfer* **19**, 1127 (1976).
- [71] K. Das and D. Basu, *Software Validation Test Plan and Report for Ansys-Fluent Version 12.1*, Tech. Rep. November (US Nuclear Regulatory Commission, 2010).
- [72] L. Denies, *Regenerative cooling analysis of oxygen/methane rocket engines*, Tech. Rep. (MSc thesis report TU Delft, 2015).
- [73] K. Khamis, *Comparative Study between MEMS and Conventional Thrusters for Small Spacecraft Micropulsion*, Tech. Rep. (Msc thesis report TU Delft, 2019).
- [74] ANSYS Fluent Tutorial Guide 18, *ANSYS Fluent Tutorial Guide 18*, *ANSYS Fluent Tutorial Guide 18 15317*, 724 (2018).



# A

## Technical drawings Solar Thermal Thruster 2

The [CAD](#) drawings of Solar Thermal Thruster 2 are shown in this appendix. It consists of the following eight drawings:

1. Figure A.1: the inner cylinder of the [RAC](#) part.
2. Figure A.2: the outer cylinder of the [RAC](#) part.
3. Figure A.3: the cap of the [RAC](#) part.
4. Figure A.4: the spike of the [RAC](#) part.
5. Figure A.5: the connection piece for connecting the inlet of the [RAC](#) part to the feed line and inlet pressure sensor.
6. Figure A.6: the connection piece for connecting the outlet of the [RAC](#) part to the outlet pressure sensor.
7. Figure A.7: the Macor piece for securing the [RAC](#) part to the thrust bench.
8. Figure A.8: the copper nozzle. Note that this drawing is taken from Leenders [3].

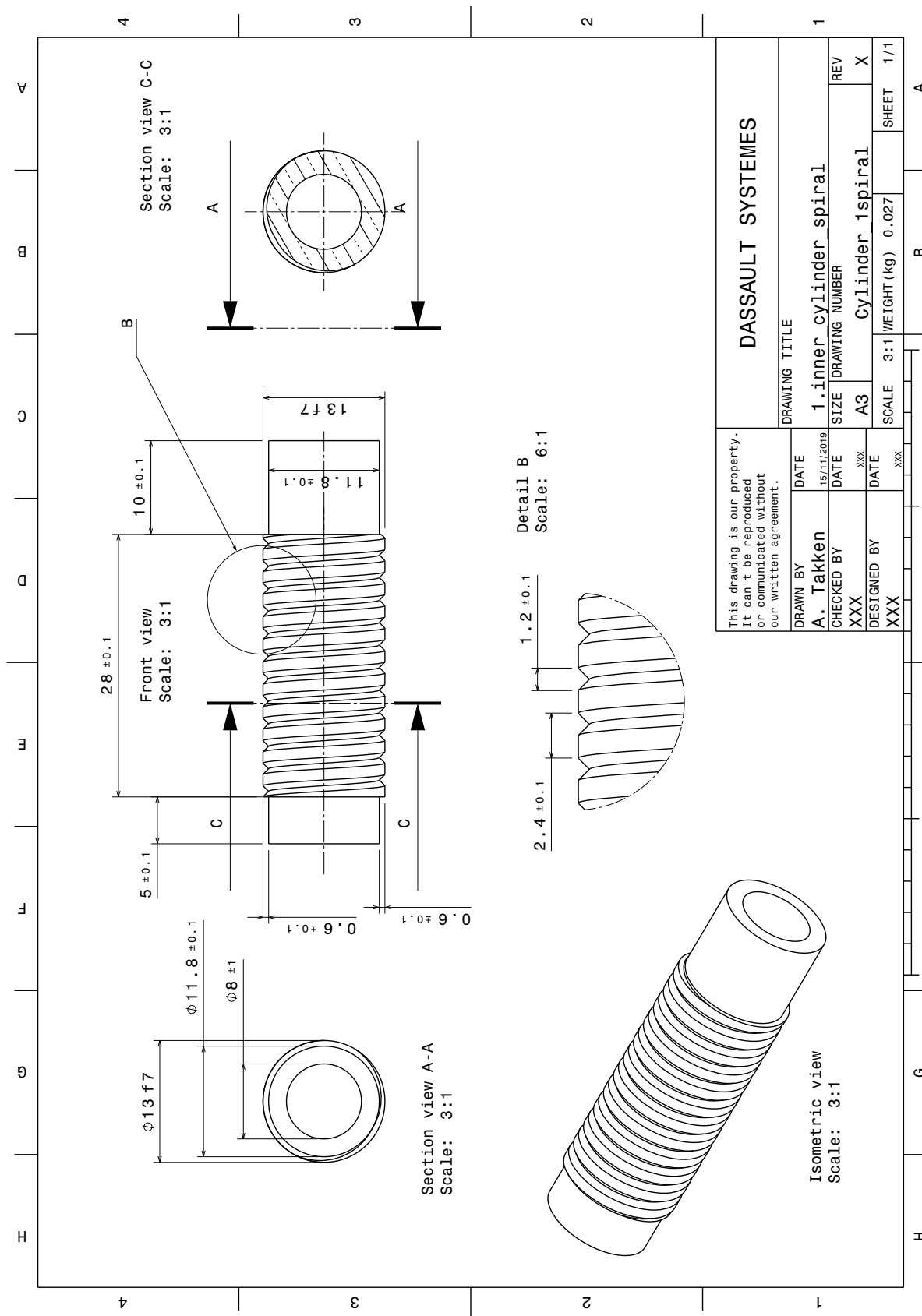


Figure A.1: Drawing of STT2 inner cylinder.

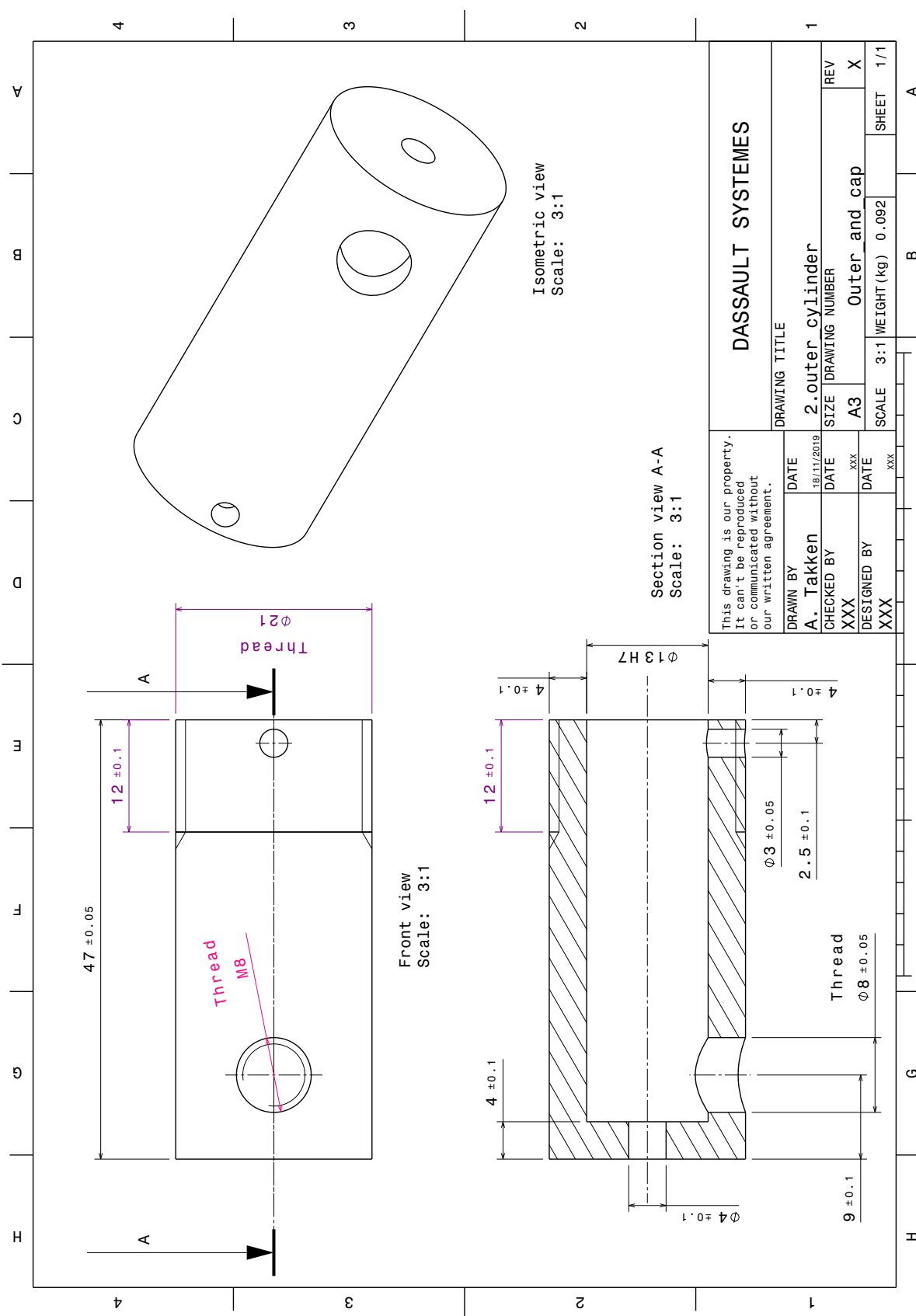


Figure A.2: Drawing of STT2 outer cylinder.

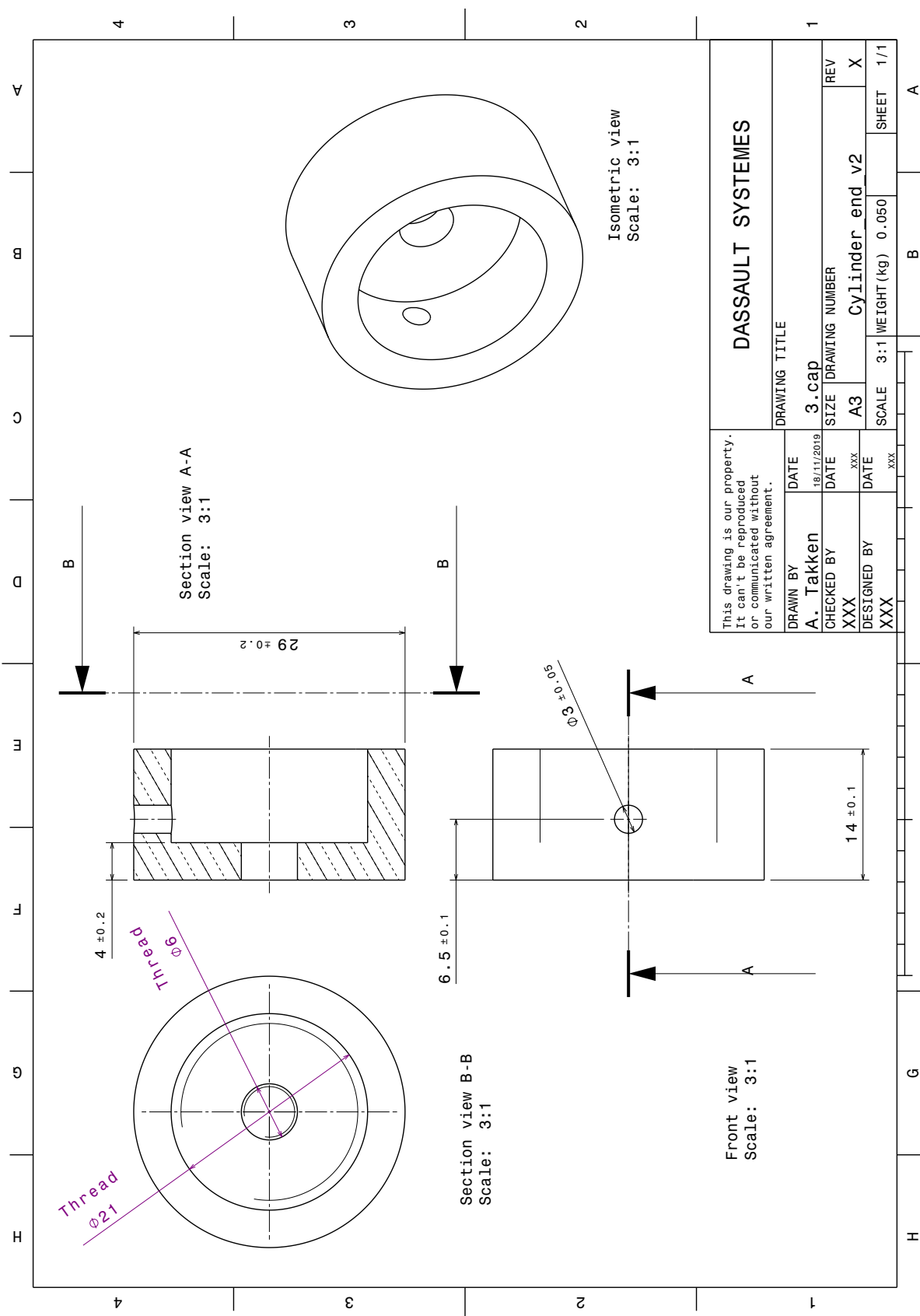


Figure A.3: Drawing of STT2 cap.

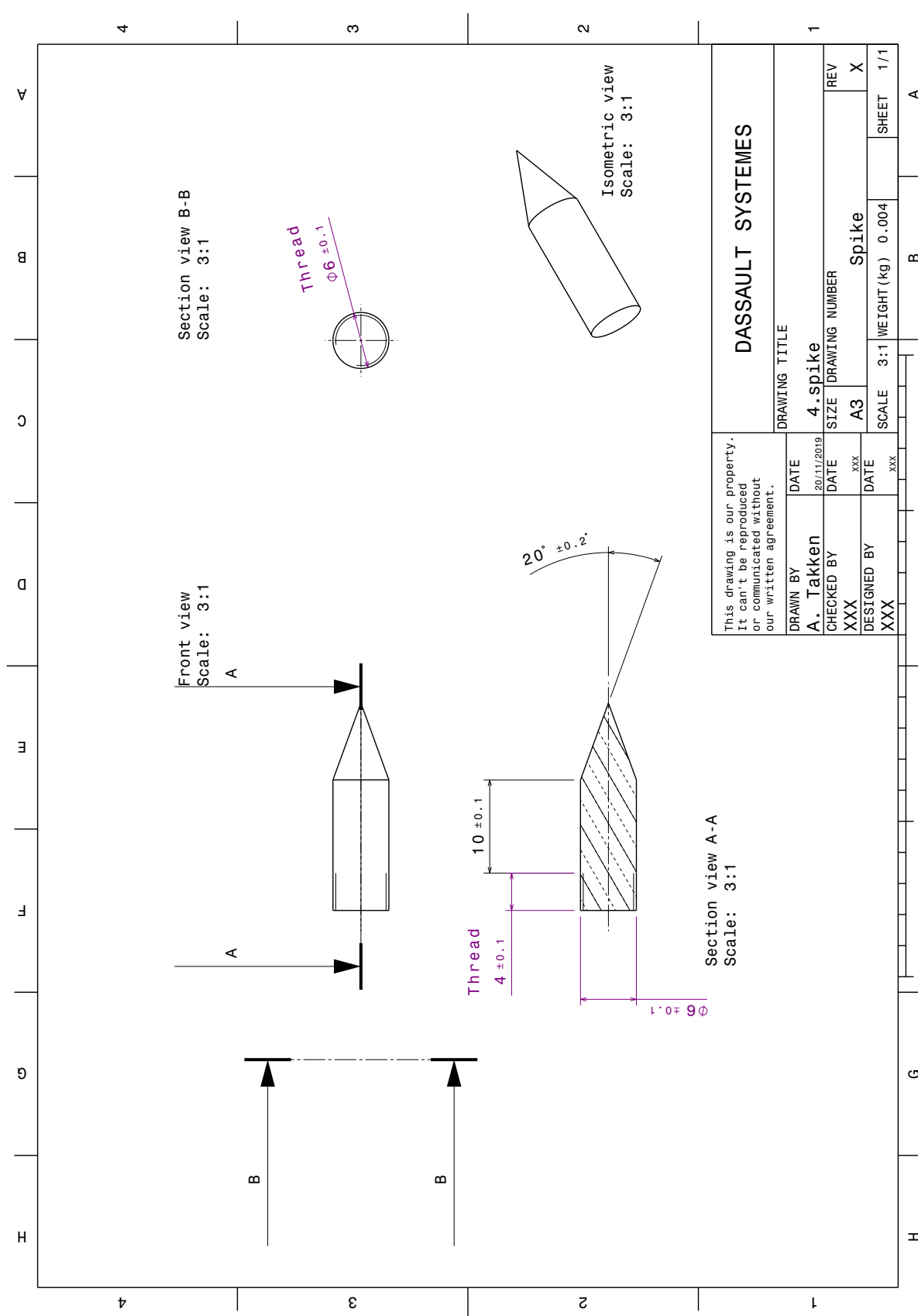


Figure A.4: Drawing of STT2 spike.

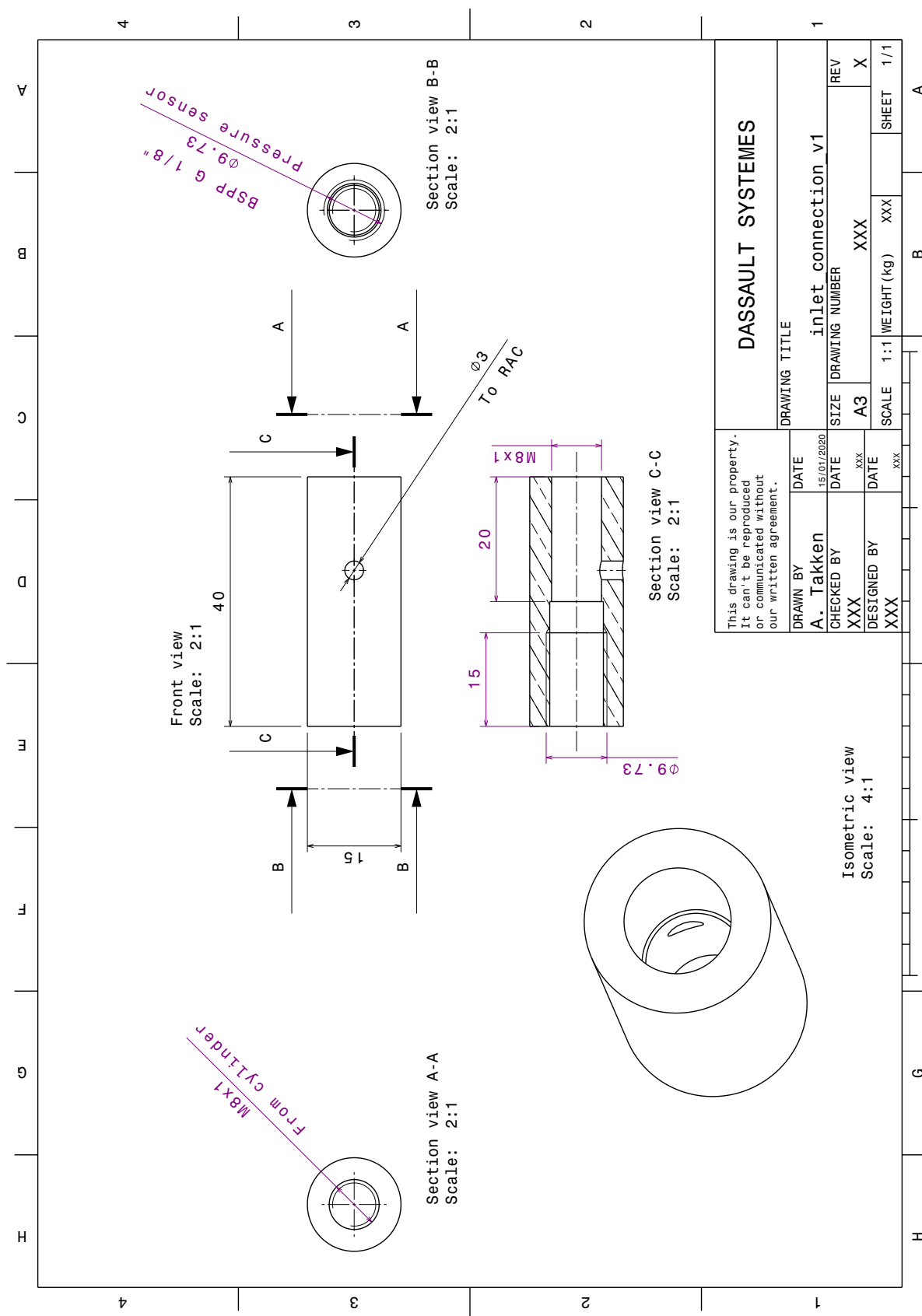


Figure A.5: Drawing of STT2 inlet connection piece.

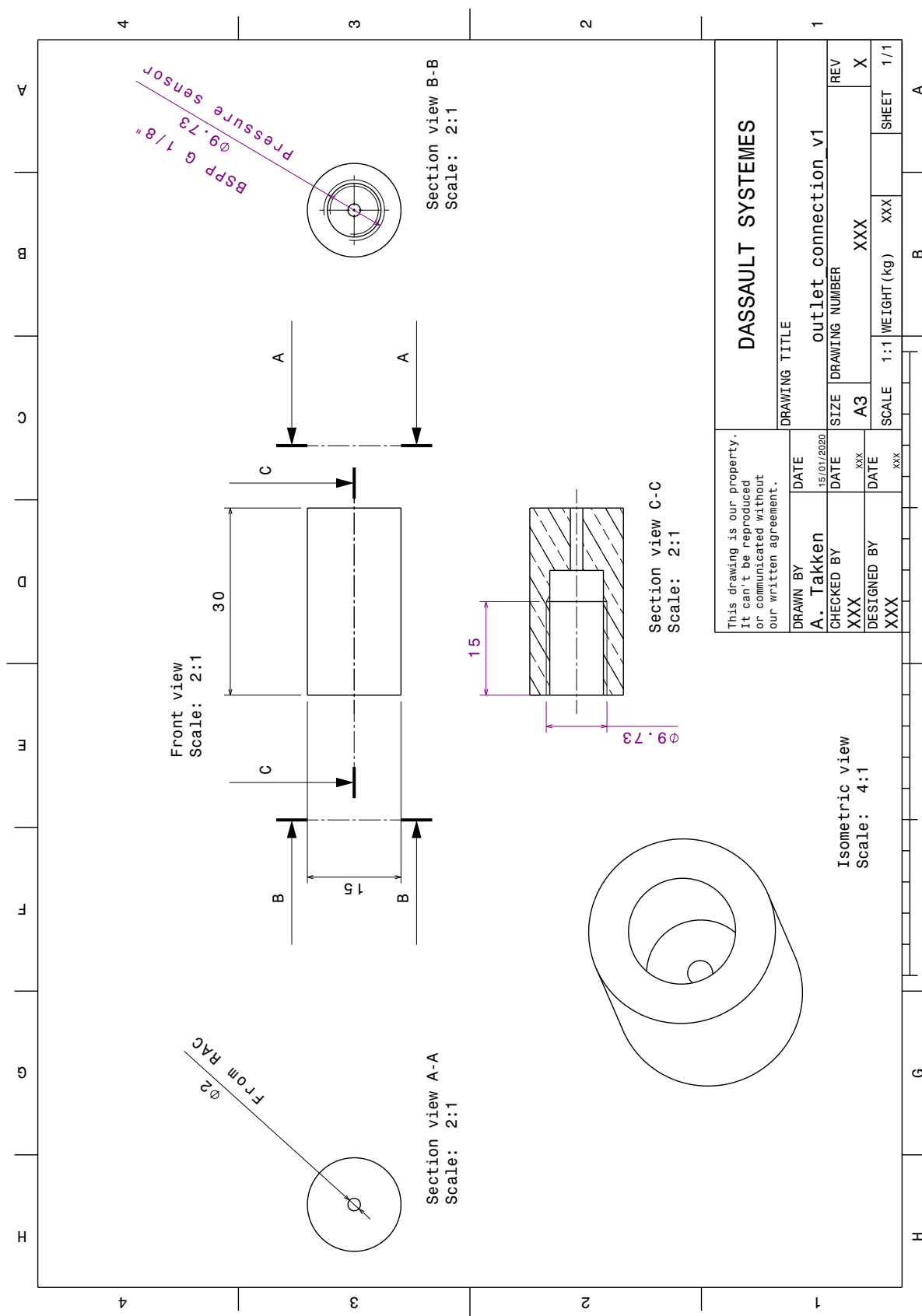


Figure A.6: Drawing of STT2 outlet connection piece.

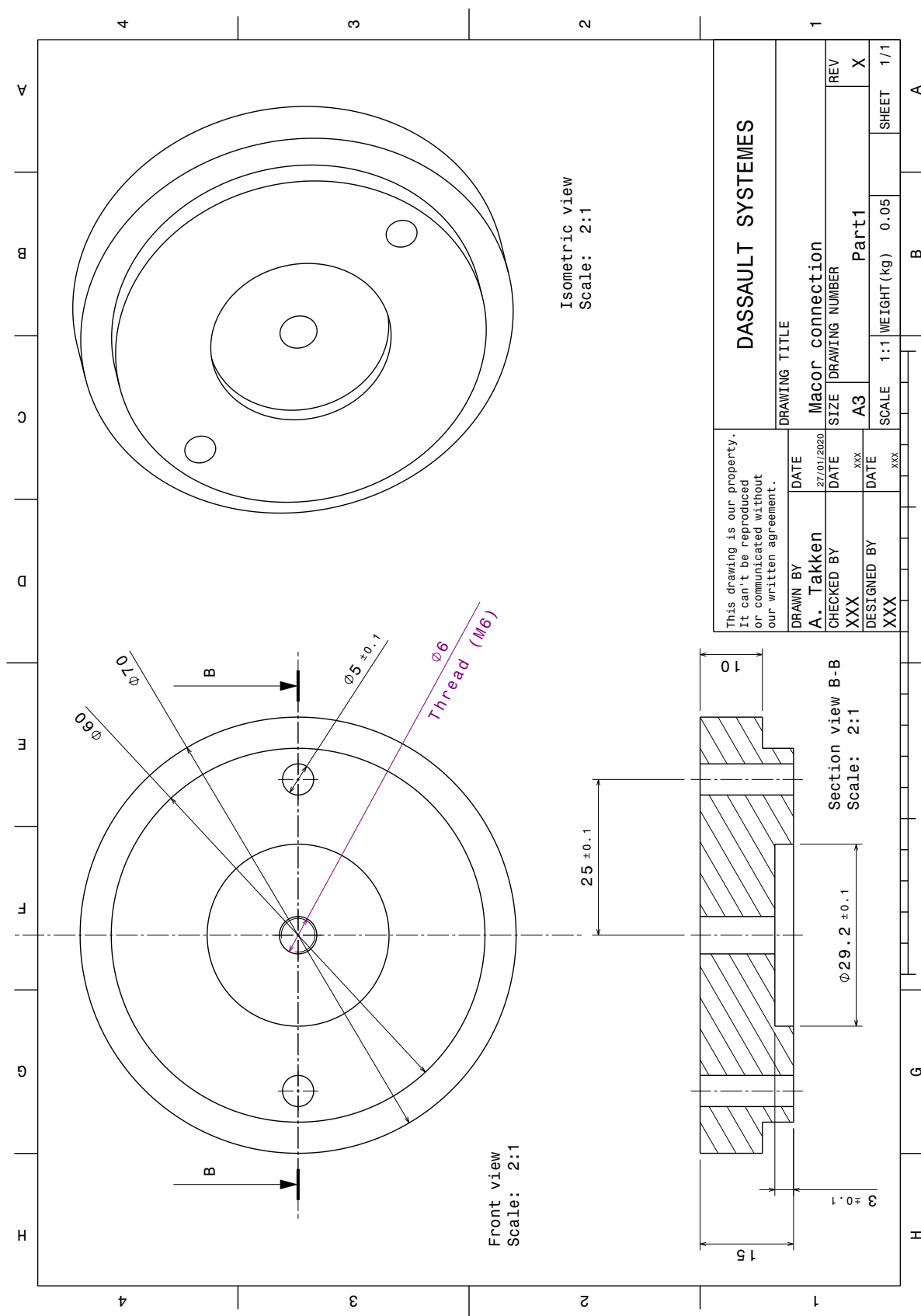


Figure A.7: Drawing of STT2 Macor connection piece.

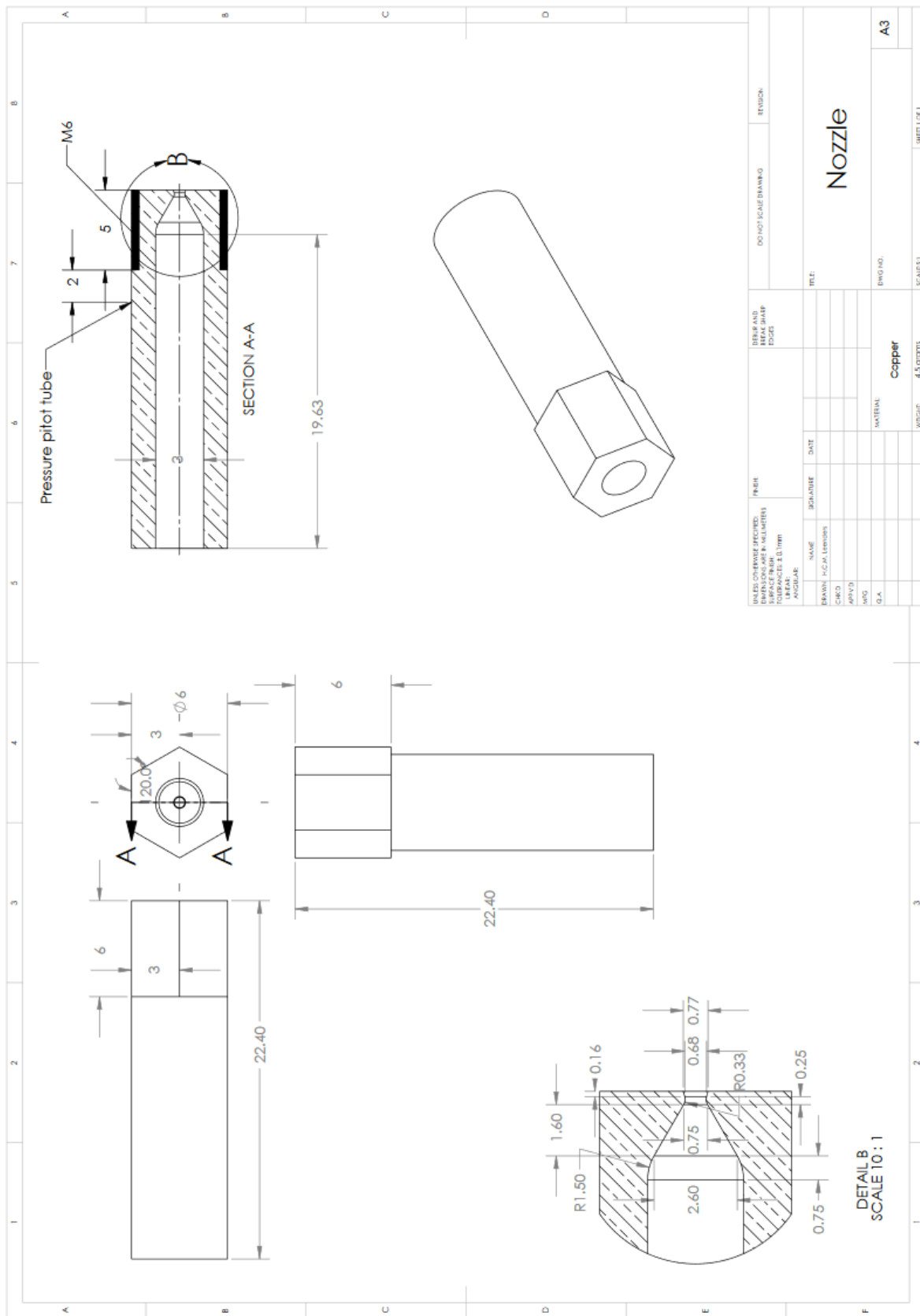


Figure A.8: Drawing of the STT2 copper nozzle, from Leenders [3].

# B

## Technical drawings Solar Thermal Thruster 3

The [CAD](#) drawings of Solar Thermal Thruster 3 are shown in this appendix. It consists of the following four drawings:

1. Figure [B.1](#): the inner cylinder of the [RAC](#) part.
2. Figure [B.2](#): the outer cylinder of the [RAC](#) part.
3. Figure [B.3](#): the cap of the [RAC](#) part.
4. Figure [B.4](#): the nozzle.

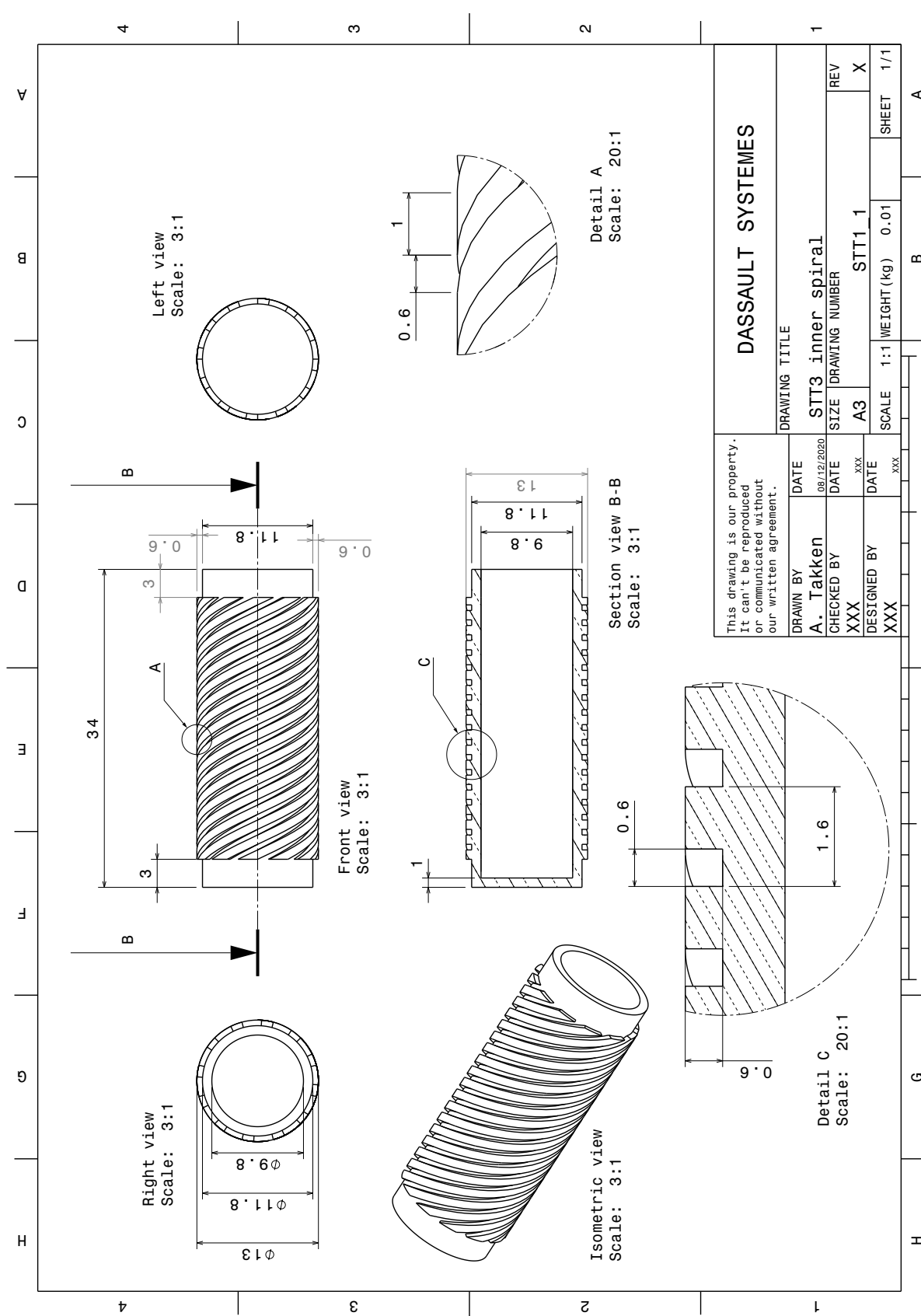


Figure B.1: Drawing of STT3 inner cylinder.

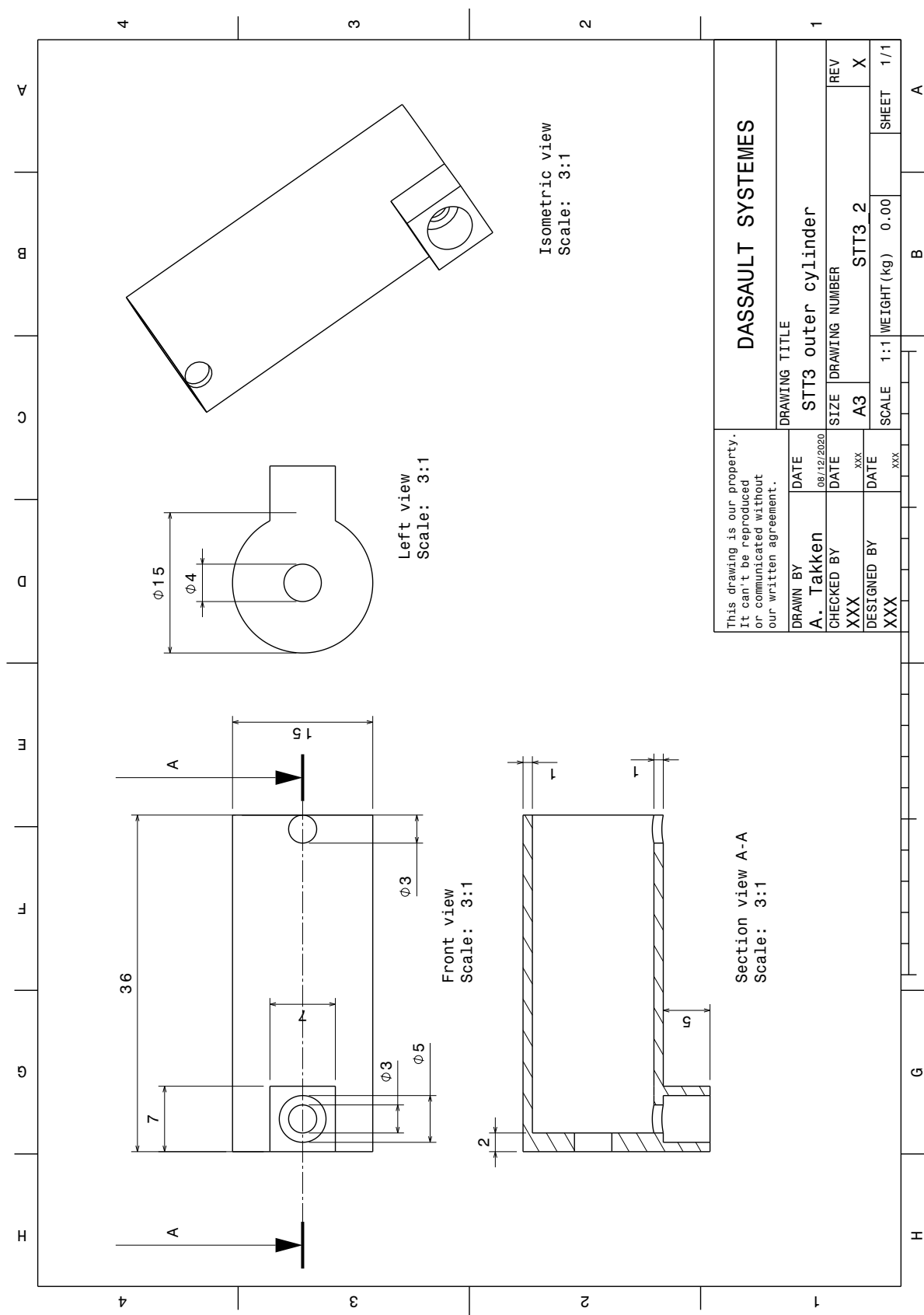


Figure B.2: Drawing of STT3 outer cylinder.

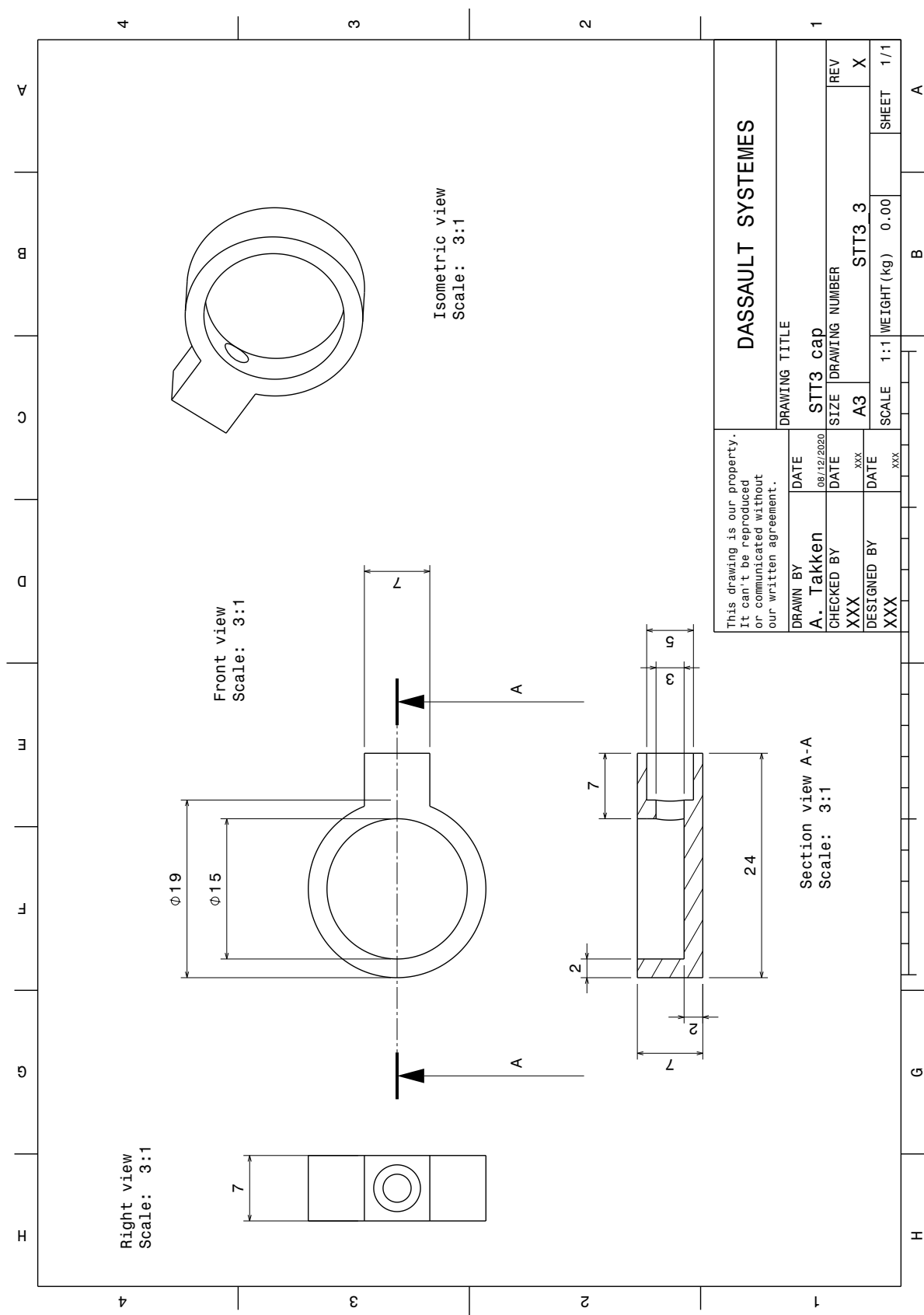


Figure B.3: Drawing of STT3 cap.

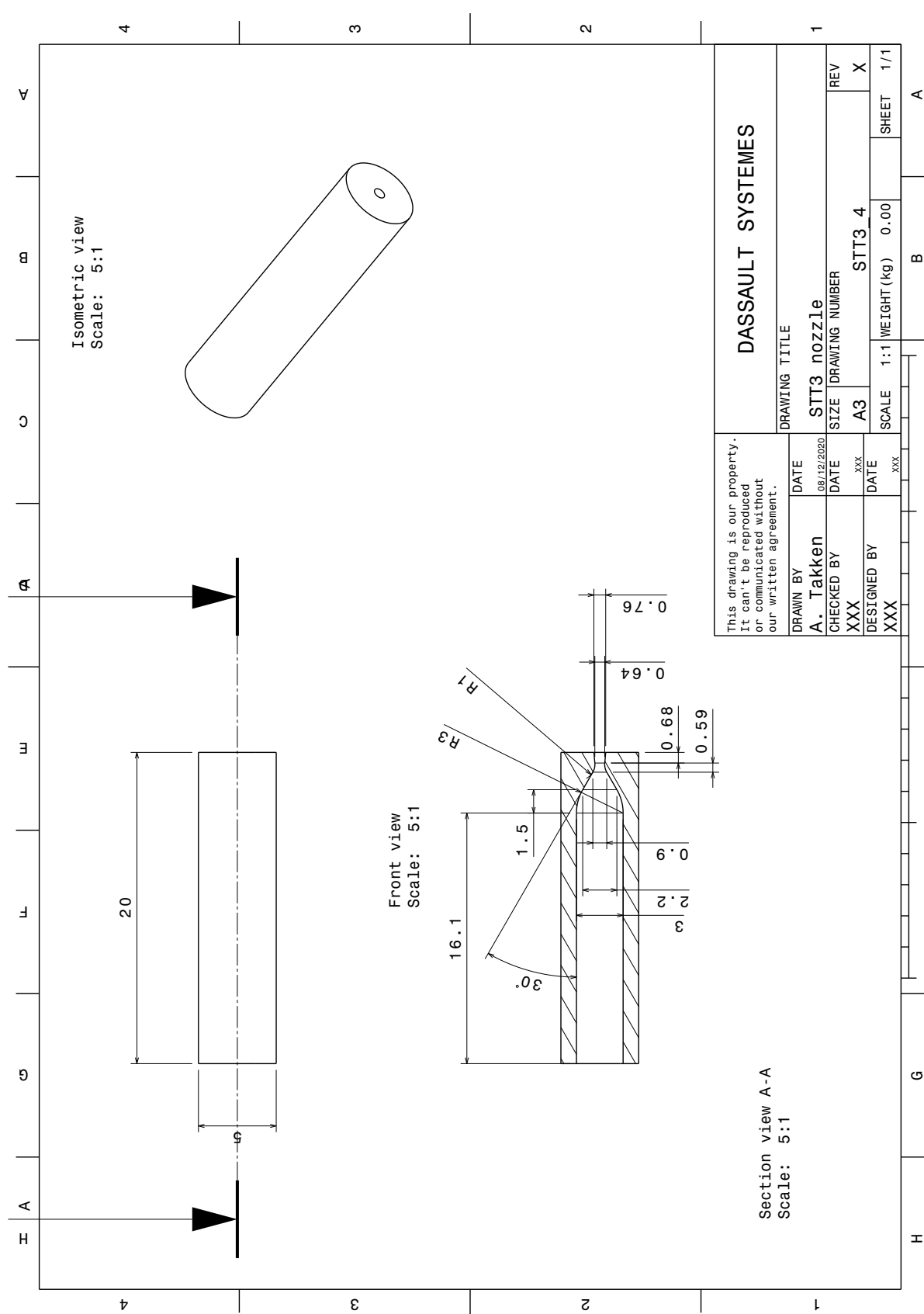


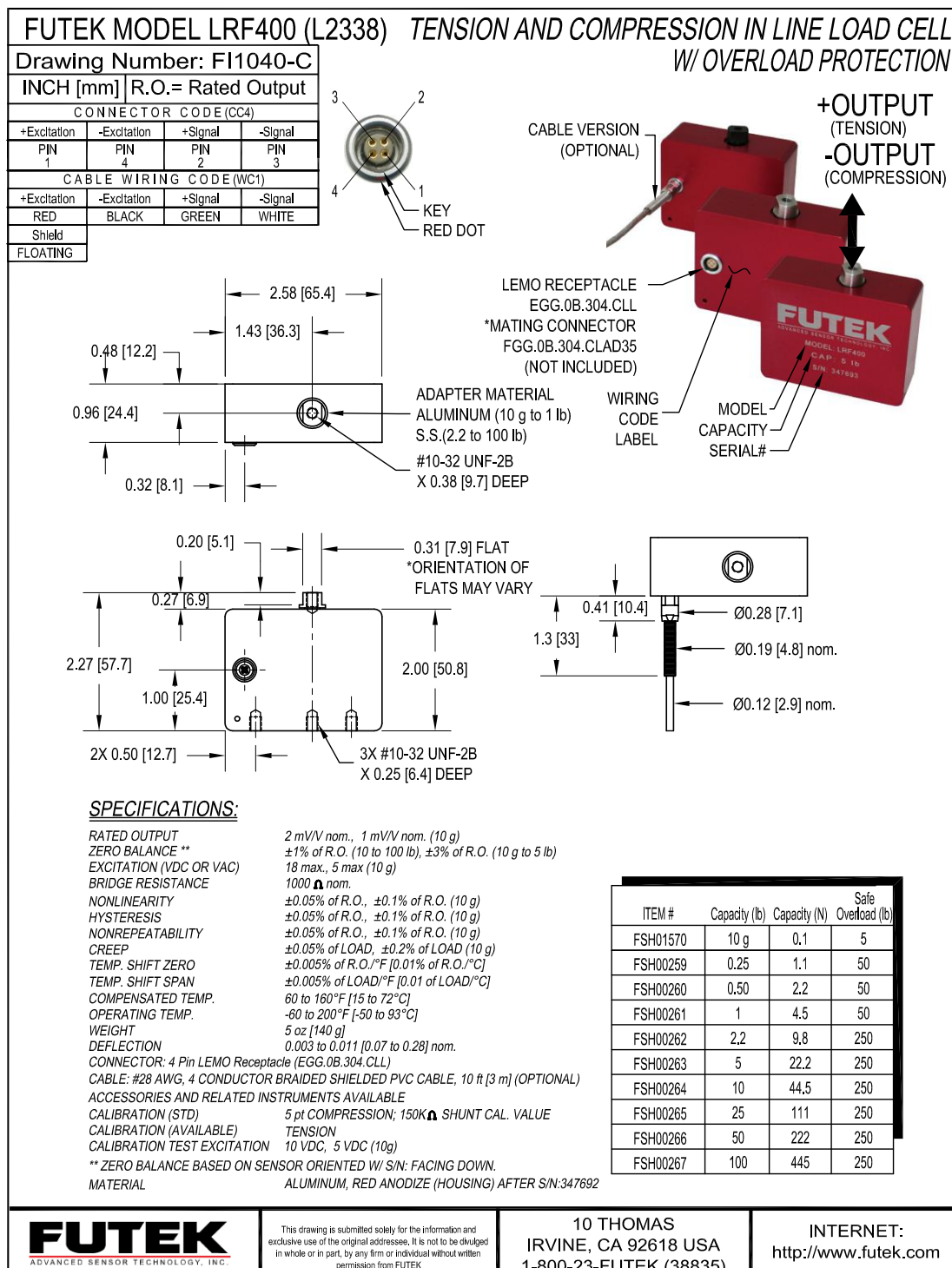
Figure B.4: Drawing of STT3 nozzle.

# C

## Experiment hardware

Below, the data sheets of all used sensor equipment, insulation and kit are shown. They were all used in the test runs at some point, except for the insulation. Most sensor equipment is borrowed for free from the Meetshop, located at the faculty of [3mE](#).

## C.1. Futek LRF400 (L2338) data sheet



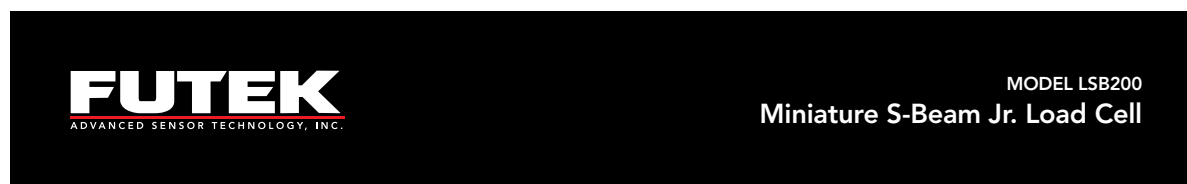
**FUTEK**  
ADVANCED SENSOR TECHNOLOGY, INC.

This drawing is submitted solely for the information and exclusive use of the original addressee. It is not to be divulged in whole or in part, by any firm or individual without written permission from FUTEK

10 THOMAS  
IRVINE, CA 92618 USA  
1-800-23-FUTEK (38835)

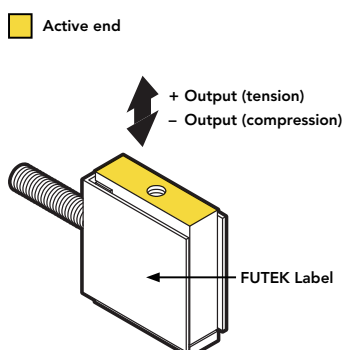
INTERNET:  
<http://www.futek.com>

## C.2. Futek LSB200 data sheet



### FEATURES

- Up to 10 times the overload protection
- Overload is available in Tension and Compression
- Light weight
- Notable nonlinearity
- Loads up to 100 lb (445 N)
- Miniature size



SPECIFICATIONS	
PERFORMANCE	
Nonlinearity	±0.1% of RO
Hysteresis	±0.1% of RO
Nonrepeatability	±0.05% of RO
ELECTRICAL	
Rated Output (RO)	See chart on third page
Excitation (VDC or VAC)	10 max
Bridge Resistance	See chart on third page
Insulation Resistance	≥500 MOhm @ 50 VDC
Connection	#29 AWG, 4 conductor, spiral shielded silicone cable, 5 ft [1.5 m] long
Wiring Code	WC1
MECHANICAL	
Weight (approximate)	0.3 oz [9 g]
Safe Overload	1000% of RO 200% tension only (50–100 lb)
Material	Aluminum (10 g–10 lb), stainless-steel (25–100 lb)
IP Rating	IP40
TEMPERATURE	
Operating Temperature	-60 to 200°F [-50 to 93°C]
Compensated Temperature	60 to 160°F [15 to 72°C]
Temperature Shift Zero	±0.01% of RO/°F [0.018% of RO/°C]
Temperature Shift Span	±0.02% of Load/°F [0.036% of Load/°C]
CALIBRATION	
Calibration Test Excitation	5 VDC
Calibration (standard)	5-pt Tension
Calibration (available)	Compression

## C.3. RS Pro data sheet

**ENGLISH****Datasheet**

### **IEC Mineral Insulated Thermocouples with Threaded Pot**

Type 'K' with threaded pot & tails – 310 stainless steel or Inconel® Alloy 600 sheath



- Mineral insulated Type 'K' Thermocouple
- Choice of 310 stainless steel or Inconel® Alloy 600 sheath
- Highly flexible, sheath can be bent/formed to suit many applications and processes
- 0.5mm diameter fast response option, other diameters include 1.0, 1.5, 3.0 & 6.0mm
- Insulated hot junction
- Probe temperature range -40°C to +1100°C
- M8 x 1.0mm fine pitch threaded pot seal (200°C)
- M8 locknuts available as an option (see below)
- 100mm tails, PFA twin twisted 7/0.2mm, colour coded to IEC 584

**Specifications**

Sensor type:	Type 'K' (Nickel Chromium/Nickel Aluminium) to IEC 584
Construction:	Flexible mineral insulated probe with 310 stainless steel or Inconel® Alloy 600 sheath with M8 x 1.0mm fine pitch threaded pot seal & tails
Element/hot junction:	Single element, junction insulated from sheath (offers protection against spurious electrical signals)
Termination:	100mm PFA twin twisted 7/0.2mm tails, +green/-white colour coded in accordance with IEC 584
Probe temperature range:	-40°C to +1100°C >1.0mm diameter -40°C to +750°C – 1.0mm diameter and below
Pot seal rating:	200°C

RS014/0816

## C.4. Pressure sensor data sheets

# OPERATION MANUAL

## Industrial pressure transmitter with voltage or current output



### Description



### Characteristic features

- Product variants from vacuum to 100 bar FS
- For measurement of relative pressure
- Output standard signal of 0...10 V or 4...20 mA
- Temperature compensated
- Robust, medium resistant models
- Simple assembly
- Water and oil resistant
- Enclosure IP65

### Typical areas of application

- Food technology
- Pneumatics
- High pressure
- Fuel pumps
- Gases
- Fuel cells

### Features

The pressure probe of series DRTR convert the measured values in the form of calibrated and temperature compensated standard signal of 0...10 V or 4...20 mA. The delivery spectrum covers a wide pressure range from vacuum to 100 bar FS with 12 variants of different measuring ranges (see table).

Through a precise calibration at 7 measuring points, an outstanding accuracy and a very low temperature residual error is achieved.

The probes are ideally suitable for measurement of static and dynamic relative pressure in liquids or gases. Typical areas of application are in the field of pneumatics, hydraulics and other industrial applications.

The robust probe housing with enclosure type IP 67 is made of anodised aluminium and is provided with a 1/4" internal thread for connection to the medium.

The electric connection is done with an industrial plug as per DIN 43650. The model with current signal is connected through a current loop. The model with voltage output requires an auxiliary supply.

Besides the standard variants, customer specific models for absolute pressure with other type of calibration, ratio metric voltage output and also with digital output signal are also available. Further information on OEM-models can be obtained on request!

In general the B+B pressure sensors are medium resistant. However we recommend to prove the media compatibility with critical mediums such as electroplating applications (iron trichloride) or oils with undefined additives .

### Technical Data

#### Industrial pressure transmitter

Measuring range	0...+100 bar, 6 types
Bursting pressure	See table
Residual error linearity / hysteresis	< ±0,2 % FS
Temperature coefficient	TCO < ±0,015 % FS / K
Operating temperature range	-20...+80 °C
Sensor material	Ceramics, Al2O3
Housing material	Aluminium AlMgPbCu, blue anodised
Seal	Viton
Pressure connection	1/4" female thread
Dimensions	30 x 30 x 89 mm
Connection	4-pole industrial connection, DIN 43650
Protection	IP65
<b>Model 4...20 mA</b>	
Output signal	4...20 mA, Two-Wire
Permissible load	R <sub>A</sub> [Ω]=(U <sub>V</sub> [V]-10V)/0,02 A
<b>Model 0...10 V</b>	
Output signal	0...10 V, Three-Wire
Auxiliary power	12...30 V DC / 5 mA

Technical changes reserved  
0141 0316-180 14.08.2015

B+B Thermo-Technik GmbH | Heinrich-Hertz-Straße 4 | D-78166 Donaueschingen  
Fon +49 771 83160 | Fax +49 771 8316-50 | info@bb-sensors.com | bb-sensors.com



# OPERATION MANUAL

## Industrial pressure transmitter for measuring absolute pressure DRTR-ED-XX\_A



### Description



### Technical data

#### DRTR-ED-R

Measuring range	1...+50 bar, 6 Types
Overload	See table
Residual error Linearity/Hyst.	< ±0.4 % FS
Temperature coefficient	TCO < ±0.015 % FS / K TCG < ±0.010 % FS / K
Application temp. range	-20...+80 °C
Sensor material	Ceramics, Al <sub>2</sub> O <sub>3</sub>
Housing material	Stainless steel 1.4305 optional 1.4571
Seal	Viton
Pressure connection	G 1/4" male thread
Dimensions	(LxWxH) 89x50x30 mm
Power supply connection	4-pole industrial plug, DIN 43650
Protection	IP65
CE-conformance	2014/30/EU
EMV-noise emission	EN 61000-6-3:2011
EMV-noise withstanding	EN 61000-6-1:2007
<b>Model 4...20 mA</b>	
Output signal	4...20 mA, 2-wire
Permissible load	R <sub>a</sub> [Ω]=(U <sub>v</sub> [V]-10V) 0.02 A
<b>Model 0...10 V</b>	
Output signal	0...10 V, 3-wire
Power supply	12...30 V DC / 5 mA

### Characteristic features

- Variants from vacuum to 50 bar FS
- For measuring absolute pressure
- Output standard signal 0...10 V or 4...20 mA
- High-quality industrial design in stainless steel
- Robust, media-resistant design
- Temperature compensated
- Easy to install
- Water and oil resistant
- IP65 protection

### Areas of application

- Pneumatics
- Hydraulics
- Industrial applications
- Machinery and plant technology
- Automation technology

### Features

The stainless steel series pressure sensor DRTR-ED transfer the measured value as a calibrated and temperature compensated standard signal 0...10 V or 4...20 mA. The product range covers 6 graded measuring range variants of the pressure range from vacuum to 50 bar Full Scale (FS) (See table).

From a precise calibration of 7 measurement points at 3 different temperatures, an excellent precision and a very low temperature residual error is achieved. The sensors are ideal for measuring both static and dynamic absolute pressure in liquids and gases. Typical applications for this sensor is in the field of pneumatics, hydraulics and other industrial applications.

The robust housing of the sensor with IP65 protection is made out of stainless steel and has a G 1/4" male thread media port.

The electrical connection is an industrial plug according to DIN 43650. The version which needs current signal gets this through the power loop. The version with voltage output requires a separate power supply. In addition to the versions with 4...20 mA and 0...10 V variants with digital output signal and stainless steel case, relative pressure versions are also available.

Technical changes reserved  
0141 0316-140 20.04.2016

B+B Thermo-Technik GmbH | Heinrich-Hertz-Straße 4 | D-78166 Donaueschingen  
Fon +49 771 83160 | Fax +49 771 8316-50 | info@bb-sensors.com | bb-sensors.com



1/2

## C.5. National Instruments USB-6008 data sheet

### SPECIFICATIONS

# USB-6008

8 AI (12-Bit, 10 kS/s), 2 AO (150 Hz), 12 DIO USB Multifunction I/O Device

### Definitions

*Warranted* specifications describe the performance of a model under stated operating conditions and are covered by the model warranty.

The following characteristic specifications describe values that are relevant to the use of the model under stated operating conditions but are not covered by the model warranty.

- *Typical* specifications describe the performance met by a majority of models.
- *Nominal* specifications describe an attribute that is based on design, conformance testing, or supplemental testing.

Specifications are *Typical* unless otherwise noted.

### Conditions

Specifications are valid at 25 °C unless otherwise noted.

### Analog Input

#### Analog inputs

Differential	4
Single-ended	8, software-selectable
Input resolution	
Differential	12 bits
Single-ended	11 bits
Maximum sample rate (aggregate)	10 kS/s, system dependent
Converter type	Successive approximation
AI FIFO	512 bytes
Timing resolution	41.67 ns (24 MHz timebase)



Timing accuracy	100 ppm of actual sample rate
<b>Input range</b>	
Differential	$\pm 20\text{ V}^1, \pm 10\text{ V}, \pm 5\text{ V}, \pm 4\text{ V}, \pm 2.5\text{ V}, \pm 2\text{ V}, \pm 1.25\text{ V}, \pm 1\text{ V}$
Single-ended	$\pm 10\text{ V}$
Working voltage	$\pm 10\text{ V}$
Input impedance	$144\text{ k}\Omega$
Overtoltage protection	$\pm 35\text{ V}$
Trigger source	Software or external digital trigger
<b>System noise<sup>2</sup></b>	
Differential	
$\pm 20\text{ V}$ range	$5\text{ mV}_{\text{rms}}$
$\pm 1\text{ V}$ range	$0.5\text{ mV}_{\text{rms}}$
Single-ended, $\pm 10\text{ V}$ range	$5\text{ mV}_{\text{rms}}$

**Table 1.** Absolute Accuracy at Full Scale, Differential

Range (V)	Typical at 25 °C (mV)	Maximum over Temperature (mV)
$\pm 20$	14.7	138
$\pm 10$	7.73	84.8
$\pm 5$	4.28	58.4
$\pm 4$	3.59	53.1
$\pm 2.5$	2.56	45.1
$\pm 2$	2.21	42.5
$\pm 1.25$	1.70	38.9
$\pm 1$	1.53	37.5



**Note** Input voltages may not exceed the working voltage range.

<sup>1</sup>  $\pm 20\text{ V}$  means that  $|\text{AI+} - (\text{AI-})| \leq 20\text{ V}$ . However, AI+ and AI- must both be within  $\pm 10\text{ V}$  of GND. Refer to the *Taking Differential Measurements* section of the *NI USB-6008/6009 User Guide* for more information.

<sup>2</sup> System noise measured at maximum sample rate.

## C.6. Scaime CPJ Rail data sheet

**Conditionneur de signal analogique**  
Analog signal conditioner

# CPJ / CPJ2S

**±10 V/0-10 V / 4-20 mA**



Version Rail DIN  
DIN Rail Version

- Conditionne jusqu'à 4 capteurs à jauge de contrainte ( $350 \Omega$ )
- Capteur 4 ou 6 fils
- Sortie tension ( $\pm 10 \text{ Vdc}$  ou  $0-10 \text{ Vdc}$ ) et sortie courant ( $4-20 \text{ mA}$ )
- Signal d'étalonnage par shunt
- 2 seuils sur relais en option (CPJ2S)

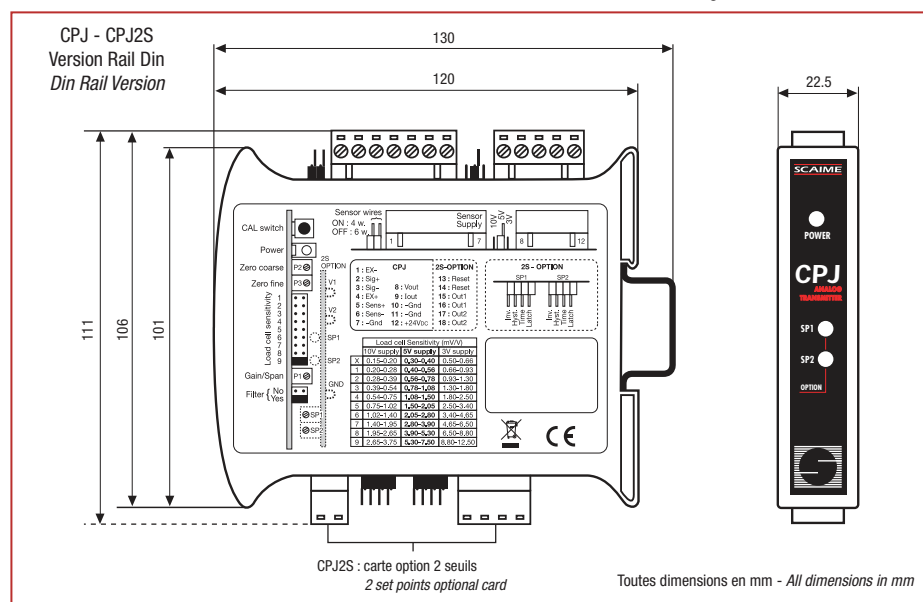
- The CPJ is able to run up to 4 strain gauge load cells ( $350 \Omega$ )
- 4 or 6 wire load cell
- Voltage output ( $\pm 10 \text{ Vdc}$  or  $0-10 \text{ Vdc}$ ) and current output ( $4-20 \text{ mA}$ )
- Shunt calibration signal
- 2 set points on relays optional version CPJ2S



Version Carte  
Board Version



Version Boîtier IP65  
IP65 Housing Version



## C.7. Mettler Toledo AG245 data sheet

Technical data and optional equipment

**68**

# 7 Technical data and optional equipment

## 7.1 Technical data of the AG balances

### Power supply

Power supply with AC/AC adapter national power cable	115 V, -20%+15%, 50/60 Hz, 230 V, -20%+15%, 50/60 Hz,	195mA 90mA	Sec: 12V, 50/60Hz, 1.25A Sec: 12V, 50/60Hz, 1.25A
---	--	---------------	--

### Fusing

Temperature switch

### Power supply AG balance

9.5–17.5 V, 50/60 Hz, 7 VA or 9–20 V =, 7 W



Use only with a tested AC adapter with SELV output current.

Ensure correct polarity  $\ominus$ — $\odot$ — $\oplus$

### Ambient conditions for AG balances

Height above sea level

Use AG balances only in closed rooms

up to 4000 m

Temperature

5–40 °C

Atmospheric humidity

80% RH @ +30 °C

Oversupply category

II

Pollution degree

2

### Standard equipment

Balance complete with feedthrough for weighing below the balance, fitting for antitheft device and integrated short-form operating instructions, protective cover for keypad and display, cleaning brush, AC adapter, holder for AC adapter, power cable, operating instructions, draft shield element (AG135, AG285 only)

<b>Technical data</b>	<b>AG64</b>	<b>AG104</b>	<b>AG135</b>	<b>AG204</b>
Readability	0.1 mg	0.1 mg	0.1 mg/0.01 mg <sup>1)</sup>	0.1 mg
Maximum capacity	61 g	101 g	101 g/31 g <sup>1)</sup>	210 g
Taring range	0...61 g	0...101 g	0...101 g	0...210 g
Repeatability (s)	0.1 mg	0.1 mg	0.1 mg/0.02 mg <sup>1)</sup>	0.1 mg
Linearity <sup>2)</sup>	±0.2 mg	±0.2 mg	±0.2 mg/±0.03 mg <sup>1)</sup>	±0.2 mg
Stabilization time (typical)	3 s	3 s	3 s/12 s <sup>1)</sup>	3 s
Adjustment	internal, fully automatic motorized initiation (FACT) and test possibility for checking the sensitivity			
• with internal weight	100 g	100 g	100 g	200 g
• with external weights	50 g	50/100 g	20/50/100 g	50/100/200 g
Sensitivity				
• Temperature drift <sup>2)</sup>	±1.5 ppm/°C	±1.5 ppm/°C	±1.5 ppm/°C	±1.5 ppm/°C
• Long-term drift <sup>3)</sup>	±0.003 %	±0.003 %	±0.003 %	±0.003 %
Display	backlit LCD	backlit LCD	LCD, not backlit	backlit LCD
Interface	LocalCAN universal interface			
Weighing pan	ø 85 mm, stainless steel			
Effective height above pan	240 mm			
Dimensions (w/d/h) balance	205 x 330 x 310 mm			
Net weight/with packaging	4.9 kg/7.25 kg			

<b>Technical data</b>	<b>AG204 DR®</b>	<b>AG245**</b>	<b>AG285</b>
Readability	1 mg/0.1 mg <sup>1)</sup>	0.1 mg/0.01 mg <sup>1)</sup>	0.1 mg/0.01 mg/0.01 mg <sup>1)</sup>
Maximum capacity	210 g/81 g <sup>1)</sup>	210 g/41 g <sup>1)</sup>	210 g/81 g/41 g <sup>1)</sup>
Taring range	0...210 g	0...210 g	0...210 g
Repeatability (s)	0.5 mg/0.1 mg <sup>1)</sup>	0.1 mg/0.02 mg <sup>1)</sup>	0.1 mg/0.05 mg/0.02 mg <sup>1)</sup>
Linearity <sup>2)</sup>	±1 mg/±0.2 mg <sup>1)</sup>	±0.2 mg/±0.03 mg <sup>1)</sup>	±0.2 mg/0.1 mg/±0.03 mg <sup>1)</sup>
Stabilization time (typical)	3 s	3 s/15 s <sup>1)</sup>	3 s/15 s <sup>1)</sup>
Adjustment	internal, fully automatic motorized initiation (FACT) and test possibility for checking the sensitivity		
• with internal weight	200 g	200 g	200 g
• with external weights	50/100/200 g	40/100/200 g	40/100/200 g
Sensitivity			
• Temperature drift <sup>2)</sup>	±1.5 ppm/°C	±1.5 ppm/°C	±1.5 ppm/°C
• Long-term drift <sup>3)</sup>	±0.003 %	±0.003 %	±0.003 %
Display	backlit LCD	LCD, not backlit	LCD, not backlit
Interface	LocalCAN universal interface		
Weighing pan	ø 85 mm, stainless steel		
Effective height above pan	240 mm		
Dimensions (w/d/h) balance	205 x 330 x 310 mm		
Net weight/with packaging	4.9 kg/7.25 kg		

<sup>1)</sup> Values in the fine range (AG135, AG245, AG285) or DeltaRange (AG204 DeltaRange®)

<sup>2)</sup> In the temperature range 10 ... 30°C

<sup>3)</sup> Sensitivity deviation/year after first-time startup with self-calibration FACT switched on

\*\* Production phaseout form June 2000

## C.8. Zwaluw Fire Sealant 1200 °C data sheet

**Den Braven**

Technische Datasheet

### Zwaluw Fire Sealant 1200 °C Hittebestendige pasta



#### Product Omschrijving

Zwaluw Fire Sealant 1200 °C is een pastavormig product dat door droging uithardt tot een niet elastische afdichting die bestand is tegen hoge temperaturen.

#### Voordelen

- Bestand tegen hoge temperaturen tot 1200 °C
- Lijmen en voegen van vuurvaste stenen

#### Applicaties

Zwaluw Fire Sealant 1200 °C is ontwikkeld voor het afdichten van aansluitvoegen in kachels, open haarden en ovens. Fire Sealant 1200 °C is een verhardend, niet elastisch product geschikt voor toepassingen waar geen beweging optreedt.

#### Gebruiksaanwijzing

Bij de eerste blootstelling aan hoge temperaturen wordt geadviseerd om de temperatuur geleidelijk op te voeren. Eventueel nog aanwezig vocht in de Fire Sealant 1200 °C kan tot blaasvorming leiden.

#### Aanvullende informatie

Applicatie temperatuur	+ 5 °C to + 40 °C
Basis	Sodium Silicate
Dichtheid	2,0 g/ml
Temperatuur bestendigheid	+ 1200 °C
Uithardingstijd	1 - 4 days
Vorstbestendigheid gedurende transport	Up to - 15 °C

Deze waarden zijn typische eigenschappen en kunnen variëren van +/- 3%

#### Beperkingen

- Niet geschikt voor PE, PP, PC, PMMA, PTFE, zachte kunststoffen, neopreen en bitumineuze ondergronden
- Niet geschikt voor continue waterbelasting

#### Oppervlakte voorbereiding en afwerking

Aanbrengtemperatuur: + 5 °C tot + 40 °C (geldt voor omgeving en ondergronden). Ondergronden dienen schoon, droog, vet- en stofvrij en draagkrachtig te zijn. Ondergronden goed ontvetten met Zwaluw Cleaner. Bijzonder poreuze ondergronden dienen licht bevochtigd te worden. Ondergronden vooraf altijd testen op hechting. Glad afwerkbaar met Zwaluw Finisher.

#### Schoonmaken

Vers materiaal en gereedschap kunnen worden gereinigd met behulp van Zwaluw Cleaner. Uitgehard materiaal kan alleen mechanisch worden verwijderd. Handen kunnen worden gereinigd met Zwaluw Wipes.

#### Kleur(en)

- Zwart

#### Verpakking

- Koker

Voor productspecificaties, raadpleeg de Product Detail Pagina



Den Braven Benelux B.V.  
Denariusstraat 11, 4903 RC Oosterhout  
+31 (0) 162491000 info@denbraven.nl

28-06-2018 13:44:01 UTC



**Den Braven**

## Technische Datasheet



### Zwaluw Fire Sealant 1200°C

Hittebestendige pasta

#### Houdbaarheid

In ongeopende originele verpakking, tussen + 5°C en + 25°C, tot 9 maanden houdbaar na productiedatum mits bewaard op een droge plaats.

#### Gezondheid & Veiligheid

Het productveiligheidsblad dient te worden gelezen en begrepen voor gebruik. Productveiligheidsbladen zijn beschikbaar op aanvraag en via de Den Braven websites.

#### Waarborg & Garantie

Den Braven garandeert dat haar product, binnen de houdbaarheidstijd, in overeenstemming is met de specificaties.

#### Disclaimer

Alle informatie in dit document en in al onze gedrukte en digitale publicaties is gebaseerd op onze huidige kennis en ervaring en is het uitsluitend (intellectuele) eigendom van Den Braven. Het document (en de daarin vervatte vinding (en)) mag uitsluitend met de uitdrukkelijke schriftelijke toestemming van Den Braven worden gekopieerd, aangedaan getoond of op andere wijze worden vervelvuldigd, openbaregemaakt en/of gebruikt. De technische gegevens in dit document worden gegeven bij wijze van indicatie en zijn niet uitputtend. Den Braven is niet aansprakelijk voor enige (directe of indirecte) schade als gevolg van eventuele (redactionele) fouten, onvolledigheden of onjuistheden in de inhoud van dit document. Daaronder wordt mede verstaan, maar is niet beperkt tot, onjuistheden of onvolledigheden die het gevolg zijn van technologische veranderingen of onderzoek tussen de datum van publicatie van dit document en de datum waarop het product wordt verkregen. Den Braven behoudt zich het recht voor om wijzigingen aan te brengen in formuleringen. Den Braven is niet aansprakelijk voor enige (directe of indirecte) schade als gevolg van het gebruik van het in dit document weergegeven product. Voor het aanbrengen en gebruiken van het product dient de gebruiker de informatie van dit document en andere documenten met betrekking tot onze producten, te lezen en te begrijpen. De gebruiker is verantwoordelijk voor het uitvoeren van alle nodige tests om er zeker van te zijn dat het product geschikt is voor de wijze van toepassing. Wij hebben geen invloed op de wijze van aanbrengen van het product en de omstandigheden tijdens opslag en



Den Braven Benelux B.V.  
Denariusstraat 11, 4903 RC Oosterhout  
+31 (0) 162491000 info@denbraven.nl

28-06-2018 13:44:01 UTC

## C.9. Saffil M-Fil data sheet



### SAFFIL M-FIL PRODUCT DATA SHEET



#### **Introduction**

M-FIL blanket is formed from high temperature MULLITE fibres. It has been specifically designed for demanding applications and has a classification temperature of 1600°C. M-FIL blanket utilises an innovative stitching/self needling process, which produces a product with significantly improved gas erosion characteristics.

These and other properties make M-FIL suitable for the most demanding high-end insulation applications.

#### **Health and Safety**

Mullite fibres are not subject to European legislation 97-69EC. M-FIL has been designed and made to give not only a narrow band of fibre diameter distribution but also does not form crystobalite when exposed to high temperatures.

#### **Properties and Benefits**

M-FIL blanket exhibits all the benefits associated with SAFFIL products. It's lightweight, low thermal mass properties enables it to cope with the most demanding industrial insulation applications.

#### **Thermal conductivity**

Controlled fibre diameter and low-shot has a direct bearing on thermal conductivity of fibre products. M-FIL is a significantly better insulator than other fibres by up to 50% in some cases. M-FIL is increasingly being used as fuel costs escalate and cost saving solutions are required. M-FIL more than meets these needs by cost effectively providing a stable, long lasting thermal barrier.

#### **Chemical Resistance**

M-FIL shows a good resistance to chemical attack and shows very good resistance to alkali and low Ph.

#### **Thermal Shock Resistance.**

The low heat storage and fibrous structure avoid the problems normally caused by thermal shock. Faster cycle times are possible that offer advantages in the form of reduced fuel consumption and increased capacity.

#### **Typical Applications.**

M-FIL blanket can be used in most module configurations. Modules can be supplied to any specification and anchoring systems installed / designed to your specific requirements.

M-FIL blanket is flexible and resilient and can be used for expansion gaps, seals and thermal backing in kilns.



# SAFFIL

## M-FIL - Technical Data

Classification Temperature	°C	1600		
<b>Properties measured at ambient (23°C / 50% RH)</b>				
Colour		White		
Solubility in water		Insoluble		
Odour		Odourless		
Fibre diameter (median)	Micron	3.0 - 3.5		
Shot content (Non fibrous material)		negligible		
Tensile Strength	kPa	38		
Bulk Density	g/cm³	0.1		
<b>Properties when exposed to high temperature</b>				
Melting Point	°C	2000		
Thermal Conductivity				
Temp	800	1000		
W/mK	0.22	0.30		
	1200	0.41		
	1400	0.54		
<b>Standard Availability</b>				
Rolls (Nominal)	Density (Kg/m³)	Length (mm)	Width (mm)	Thickness (mm)
	100	7200	620	25

Standard Packaging:- M-FIL is supplied in rolls packed in cardboard cartons (570 x 570 x 670mm)

The values given herein are typical average values obtained in accordance with accepted testing methods and are subject to normal manufacturing variations. They are supplied as a technical service and are subject to change without notice.

### Head Office Address

SAFFIL Ltd  
 Pilkington Sullivan Site,  
 Tanhouse Lane,  
 Widnes,  
 Cheshire.  
 WA8 0RY  
 UK

Tel + 44 (0) 151 422 6700  
 Fax + 44 (0) 151 422 6701  
 Web <http://www.saffil.com>

